UNIVERSIDAD MICHOACANA
DE SAN NICOLAS DE HIDALGO

FACULTAD DE INGENIERIA ELECTRICA
DIVISION DE ESTUDIOS DE POSGRADO

THESIS

ADVANCED WIND TURBINE ELECTRO-MECHANICAL MODELLING INCLUDING ASYMMETRIES FOR POWER SYSTEM DYNAMIC ANALYSIS

by

Luis Alberto Fajardo Ruano

Thesis submitted to fulfill partial requirements for the Degree of

DOCTOR IN SCIENCES
IN ELECTRICAL ENGINNERING

Thesis Advisor

Doctor en Ingeniería Eléctrica *J. Aurelio Medina Ríos*

Morelia, Michoacán de Ocampo, Mexico, November 2013

ADVANCED WIND TURBINE ELECTROMECHANICAL MODELLING INCLUDING ASYMMETRIES FOR POWER SYSTEM DYNAMIC ANALYSIS

Los Miembros del Jurado de Examen de Grado aprueban
la **Tesis de Doctorado en Ciencias en Ingeniería Eléctrica, Opción en Sistemas Eléctricos** de ***Luis Alberto Fajardo Ruano***

Antonio Ramos Paz

Dr. Antonio Ramos Paz
Presidente del Jurado

Dr. J. Aurelio Medina Rios
Director de Tesis

Dr. Claudio Rubén Fuerte Esquivel
Vocal

Dra. Elisa Espinosa Juárez
Vocal

Dr. Juan Felipe Soriano Peña
Revisor Externo, FIM-UMSNH

Dr. J. Aurelio Medina Rios
Jefe de la División de Estudios de Posgrado
de la Facultad de Ingeniería Eléctrica, UMSNH
(Por reconocimiento de firmas)

UNIVERSIDAD MICHOACANA DE SAN NICOLÁS DE HIDALGO
Octubre 2013

Acknowledgement

I want to express my gratitude to this thesis supervisor Dr. J. Aurelio Medina Rios, for his help, friendship, tolerance, patience and understanding.

Thanks to Professor Frede Blaabjerg at Aalborg University, Aalborg, Denmark, for accepting me to be part of his research group in Wind turbine - Power Electronics, as a guest PhD student, 2006-2007. I also gratefully appreciate the advices and scientific support to this research given by the Professor Florin Iov, even beyond my staying at Aalborg University.

I also acknowledge the financial support given by the Coordinación de la Investigación Científica, at the Universidad Michoacana de San Nicolás de Hidalgo, Mexico.

Abstract

This thesis focuses in a detailed electromechanical model, as a DAE (Differential-Algebraic Equations) mathematical structure, in state variables. The model integrates, the *123* characteristics of the mechanical subsystem with large pre-bent blades, and the phases *abc* characteristics of the electric subsystem, including meaningful electromagnetic phenomena in large (MW) squirrel cage induction generators. These both side effects are applied to the wind turbine shaft system.

The deterministic wind speed component is calculated using a feedback computational scheme, where gravitational, inertial and aerodynamic mechanical loads at each blade interact with the wind shear and tower transference. Wind shear includes atmospheric stability and tower transference parameters are computed considering the blade-tower geometry for an operative condition. This deterministic wind speed feeds the mechanical subsystem, as represented by a modified two-mass drive-train model, where the moment of inertia of the wind turbine rotor instead of a constant input is computed as blade length, mass-density and mechanical loading dependent. The induction generator, as represented in phase *abc* coordinates, involves also non-linear *abc* models for main path magnetic saturation, stator/rotor iron losses and deep-bar effect. If all these effects are partially or totally neglected, this thesis model reproduces the results of approximate models, as used in industrial tools.

This detailed electromechanical modelling is intended to be useful to test industrial based power electronics models, control strategies and protection schemes. Research contributions are made for both subsystems. They highlight the individual effects of large pre-bent blades and the individual effects of the electric phases, on the shaft system during transient operation. Matlab/Simulink® is used as the computational platform with S-functions modules in C code. Computational requirements were supplied with a personal computer, DELL, i-7, Q-720, 1.6 GHz.

Key Words: Wind Turbine, Wind Energy Conversion System, Renewable Energy

Resumen

Esta tesis se concentra en un modelo electro-mecánico detallado como una estructura matemática DAE (Differential-Algebraic Equations, por sus siglas en inglés), en variables de estado. El modelo integra, las características *123* del subsistema mecánico con palas largas y pre-curveadas, con las características de fases *abc* del subsistema eléctrico, incluyendo fenómenos electromagnéticos significativos in generadores de inducción grandes (MW). Estos efectos desde ambos subsistemas, se aplican al sistema de ejes de la turbina eólica.

Para la componente determinística de la velocidad del viento, las cargas gravitacional, inercial y aerodinámica sobre cada pala, interactúan con los efectos debidos a la altura y la transferencia de la torre. El efecto de la altura incluye la estabilidad atmosférica y los parámetros para el efecto de transferencia de la torre se calculan considerando la geometría pala-torre, para una condición operativa. Esta velocidad del viento alimenta el subsistema mecánico, representado por un modelo de dos-masas modificado, donde el momento de inercia del rotor de la turbine eólica en lugar de ser una entrada constante, se calcula como una función de la longitud de la pala, su densidad de masa y su cargabilidad mecánica. El generador de inducción se representa en coordenadas de fase *abc*, e incluye modelos no-lineales para la saturación magnética de la ruta principal, perdidas en el hierro en estator y rotor, y el efecto de barra profunda.

Si estos efectos se desprecian parcial o totalmente, el modelo produce los resultados de modelos aproximados de herramientas industriales.

El modelamiento electromecánico detallado aquí propuesto, se concibe útil para la prueba de modelos que involucren equipos con base en electrónica de potencia, estrategias de control y esquemas de protección. Las contribuciones de esta investigación son hechas para ambos subsistemas mecánico y eléctrico. Ellas resaltan los efectos individuales de las palas largas pre-curveadas y los efectos individuales de las fases *abc* del sistema eléctrico, sobre el sistema de ejes durante una operación transitoria.

Para el desarrollo se utiliza Matlab/Simulink®, como plataforma computacional con funciones S en código C. Los requerimientos computacionales se suplen desde un ordenador personal, DELL, i-7, Q-720, 1.6 GHz.

Palabras clave: Turbine Eólica, Sistema de Conversión de Energía con base en el viento, Energía Renovable

Table of Contents

Symbols and Acronyms

J	Moment of inertia. In the text it is applied to different masses
Kij	Stiffness between masses i and j
Dij	Damping between masses i and j
$Twt,123$	Mechanical Torque of the wind turbine at each blade
Te	Electromagnetic Torque
ω	Rotor speed. In the text it relates to wind turbine or induction generator
Rs,abc	Phase Distinguished Stator resistance
Rr,abc	Phase Distinguished Rotor resistance
Xs,abc	Phase Distinguished Stator leakage reactance
Xr,abc	Phase Distinguished Rotor leakage reactance
L,abc	Phase Distinguished Inductance. In the text it is applied for self and mutual magnetic effects
$L\sigma,abc$	Phase Distinguished Leakage Inductance. In the text it is applied for stator and rotor windings.
i	Instantaneous current intensity. In the text it is applied for stator and rotor windings.
v	Instantaneous Voltage. In the text it is applied for stator and rotor windings.
ψ	Instantaneous Magnetic Flux. In the text it is applied for stator and rotor windings.
u	Wind Speed. In the text it is applied to include different characteristics
z	Height above sea or land.
p	Heaviside operator (d/dt).
BML	Blade mechanical loading
S2M	Standard two-mas model
BB2M	Blade based two-mass model
ABC, *abc*	Stator/rotor phase coordinates
PCC	Point of Common Coupling
LLL	Three-phase fault
LG	Single-phase fault
IEEE	Institute of Electrical and Electronic Engineering
RISØ	National Laboratory, Denmark
NREL	Nationl Renewable Energy Laboratory, USA
SCIG	Squirrel Cage Induction Generator
OSF	One Saturation Function
TSF	Three Saturation Functions
TESF	Three Equidistant Saturation Function
TnESF	Three Non-Equidistant Saturation Function

List of Figures

List of tables

List of Publications

Publications associated with this research are:

International IEEE Conferences

1. **L.A. Fajardo-R.**, A. Medina, "Per-Blade equivalent wind speed function for high order drive-train modelling," Presented to IEEE PES-General Meeting, Detroit, Michigan (USA), July, 2011. Digital Object Identifier:10.1109/PES.2011.6039447

2. **L.A. Fajardo-R.**, A. Medina, F. Iov, "Dynamics of *abc* and *qd* Constant Parameters Induction Generator Model: Wind Park application," Presented to IEEE International Conference of Electric Machines and Systems, ICEMS´09, Tokyo, Japan, Nov. 15-18, 2009. Digital Object Identifier:10.1109/ICEMS.2009.5382680

3. **L.A. Fajardo-R**., A. Medina, F. Iov, "Transient stability with Grid Connection and Wind Turbine Drive-Train Effects," , Presented to IEEE International Conference of Electric Machines and Systems, EPEC´09, Montreal, Canada, Oct. 22-23, 2009. Digital Object Identifier:10.1109/EPEC.2009.5420768

4. **L.A. Fajardo-R.**, F. Iov, F. Blaabjerg and A. Hansen. "Advanced induction machine model in phase coordinates for wind turbine applications," Aalborg University, Institute of Energy Technology, Denmark. Presented to IEEE International Conference of Electric Machines and Drives IEMDC´07, Antalya, Turkey, May 3-5, 2007. Digital Object Identifier 10.1109/IEMDC.2007.383599

5. **L.A. Fajardo-R.**, F. Iov, J.A. Medina-Rios, F. Blaabjerg, and A. Hansen. "An advanced model in phase coordinates of induction generator for studying the fault ride-through capabilities of wind turbines," Aalborg University, Institute of Energy Technology, Denmark. Presented to IEEE International Conference of Power Electronics, EPE'07. ISBN 9787075815108. Aalborg, Denmark., September 2-5, 2007.

International Journal

6. **L.A. Fajardo-R.**, A. Medina, F. Iov. “Upgraded Two-mas Model Including Large Pre-Bent Blades,” Submitted to International Journal of Electrical Power and Energy Systems, Science Direct, ELSEVIER, 2014

◆

1

Introduction

In order to efficiently make the most of the wind speed energy, wind turbines rotor technology trends to increment blade length and flexibility, and additionally pre-bend them. However, that the wind speed producing blade movement be symmetrically applied at each blade is a suitable idealization only. Additionally, the electrical side is always exposed to grid-connection disturbances, and statistics further show that the asymmetrical electrical faults are the most expected [Iov *et al*. 2007]. In transient operation, both mechanical and electrical excitations are going to act on the wind turbine rotor axis system, which is linked to very small low-speed shaft stiffness, as compared to conventional power plants [Hinrichsen and Nolan 1982]. These features makes possible to ask: How the mechanical and electrical models should be modified and improved to quantify the individual electro-mechanical effects on this wind turbine rotor axis system?

To make an answer, a detailed wind turbine electromechanical modelling $123 \leftrightarrow abc$ is conceived in this thesis, where the individual effects from both sides can be taken into account, as acting on the rotor axis system. As the wind power penetration increases, this modelling will help to make more consistent decisions on control strategies and protection schemes, to efficiently attend future grid code requirements on voltage and frequency.

1.1 Background

The most significant information for the specific objectives is used to write the background in this Section. Behind them there are several and maybe tens of technical reports and papers, which are used to describe the specific background for specific topics in each Chapter of this thesis.

1.1.1 Wind

Three precedent research works are selected as noteworthy for this chapter. Two are related to Risø National Laboratory in Denmark [Sørensen *et al*. 2002], [Carvalho 2003], and a third to the University of Toronto in Canada [Dolan and Lehn 2006]. In [Sørensen *et al*. 2002], [Carvalho 2003], it is defined a "weighted wind speed of all wind speeds as instantaneously seen by the wind turbine along the blade". The total wind field *u* entering to the disk area has deterministic and stochastic components. The deterministic component is understood to exist all around the neighbourhood of the hub height in the rotor disk, to be strictly no time dependant and to directly influence the dynamics of the wind turbine because of the rotating blades. While the turbulence effect is represented by the highly time dependant, very small and multi-frequency, stochastic wind speed component.

With the focus on the wind shear effect, it is established in [Carvalho 2003] that: i) the wind speed is strongly affected by the aerodynamic roughness length, ii) the mechanical torque has sinusoidal waveform which oscillates between 0.96 and 1.03 p.u., leaving an approximated 1.0 p.u. value at the hub height, and iii) the blade mechanical loading is highly influenced although the shear effect on the electrical power is negligible. The inclusion of this wind shear paradigm is formulated in [Dolan and Lehn 2006], having the power-law wind profile as the starting point for small or medium size wind turbines, where the hub height is equal to the measuring height. Some questions appear: How to efficiently compute the seed wind speed at 10 m height?, What is expected if as usual, the measuring height is lower than the hub height, for large wind turbines?, What kind of influential atmospheric properties are missed in the power law wind profile?, What is expected if the order in Taylor series expansion is incremented?, and What is expected if the problem of wind shear is seen from the logarithmic law wind profile?

The tower transference effect, as formulated in [Sørensen *et al*. 2002] and used in [Dolan and Lehn 2006], relates a wind speed drop mostly due to the short distance between blade-tip and the tower axis, each time a blade passes in front of it. This distance, is assumed constant and also the corresponding tower radius. The result is wind speed 3p frequency pulsations producing mechanical torque vibrations, which appear reflected on the electrical generator variables. A question is how to include the actual blade bending to efficiently estimate the approach of the blade to the tower, including the blade mechanical loading?

1.1.2 Aerodynamics and Drive-Train

Pioneering work about the 2-mass model was presented in [Akhmatov 2003], based on field experiments in [Pedersen *et al*. 2000], [Pedersen *et al*. 2003]. They correspond with a measured fluctuating behaviour of the electric frequency, when a wind farm (Rejsby Hede, 40x600 kW) was tripped from the electrical network. This standard 2-mass model successfully represents rigid blades, and wind turbine rotor and generator rotor moments of inertia, are manufacturers supported. If blades increase and mechanical flexibility is taken into account, this model is not able to directly represent their details.

The increase in flexibility of drive-train representation has been recognized as a very important aspect to include embedded wind turbine electrical generation in power system dynamic studies. Furthermore, flexibility has also been identified as essential for large-blade wind turbine dynamics including power quality [Salman *et al*. 2000], [Li and Chen 2008]. However, blade parameters are beginning to be only recently available. In this way, the stiffness at each blade body-section is tabulated for a 61.5 m blade length, 5MW wind turbine and it is obtained by physical test [Jonkman *et al*. 2009]. Other blade parameters as structural twist angle, mass density, chord, lift and drag aerodynamic coefficients and torsional stiffness are also reported. Based on this fact a blade-based 2-mass model is proposed in this research. In this model the blade mechanical properties reinforcing the rotor flexibility, can be directly included, which is not possible in the standard 2-mass model [Akhmatov 2003]. In this way this proposed blade based 2-mass model is greatly promising to represent the always increasing wind turbine technology.

1.1.3 Phase-coordinates (*abc*) Induction Generator

The phase coordinates, conventionally named *abc* reference frame, has been traditionally taken as a base concept to obtain the orthogonal *d-q* representation of passive and active electrical elements in circuit theory [Krause *et al*. 2002]. The electromagnetic behaviour through Maxwell's equations of any electrical element, seen as voltages, currents and magnetic fluxes, can be represented with two variables only. In this way, symmetric three-phase electric machines are expanded concepts where the variables are transferred between both *abc* and *dq* reference frames through transformations matrices [Park 1929], [Krause *et al*. 2002]. Being the *dq* modelling the target, the above paradigm is usually found in research publications about induction machines in the last nine decades.

Basic induction machine model in phase coordinates, including special associated electromagnetic phenomena, has been occasionally reported and it appears oriented to small and medium size induction machines [Akbaba and Fakro 1992], [Donescu *et al*. 1999], [Seyoum *et al*. 2003], [Seman *et al*. 2003]. It is assumed that those phenomena should produce time-varying parameters. This is extensively reported in [Seman *et al*. 2003], [Babau *et al*. 2007], [Tu *et al*. 2008], [Ranta *et al*. 2009], using supplementary to the standard test, instrumentation technology, measurements and strategies. It is known in addition that the assessment of electromagnetic behaviour affecting the operation of small commercial machines is not applicable in large machines [Akbaba and Fakro 1992].

A relatively recent research approach concerning induction machine *abc* modelling was formulated in [Bolik 2004], where magnetic saturation was approached by an $L_m = f(I_m)$ function following the no-load equivalent circuit operation concept. Also in [Iov *et al*. 2003], [Iov *et al*. 2004], a *dq* induction machine model is formulated with deep-bar effects through correction factors for rotor resistance and inductance parameters following [Akbaba and Fakro 1992], and using blocks in Simulink/Matlab environment. In the final report [Iov *et al*. 2003] it is recommended "…to include saturation and iron losses in all electrical machines models, based on standard data sheets".

This research models the magnetic saturation, synthetizing a standard no-load test based $L_m = f(V_m)$ saturation function and creating the possibility to have three instead of only one, saturation functions. This proposal assumes a simple break to use the phase test data, i.e. without voltage average, which is perfectible possible. The result is a time varying magnetizing inductance parameter. The iron losses are represented by a time-varying non-linear resistance involving the effect of non-sinusoidal voltage supply, as produced by the power converter interface, in a grid-connected wind turbine [Boglietti *et al*, 2003], [Ranta *et* *al*. 2009]. The deep-bar effect modelling is referenced to previous experimental result publication in [Babau *et al*. 2007], and is formulated as a time-varying non-linear slip dependent function to represent rotor resistance and leakage reactance.

1.2 Motivation

At the time this research started, it was found that previous related research proposed a physical based wind turbine model are limited to low flexibility. This conventional model, includes for instance, a rigid 44 m. blade length, a 2-mass drive-train model, an equivalent rotor wind speed model with wind turbine mechanical torque to be evaluated at the rotor axis, gear-box as a mechanical transformer, and *d-q* reference frame induction generator model. Typical commercial wind turbines were in the range between 1 to 2 MW. At the end of this thesis, blade lengths are of the order of 60 m for commercial 3 to 5 MW wind turbines, and they tend to increase to more than 100 m, for 10 or even 20 MW wind turbines.

1.3 Problem Statement

For low voltage fault ride-through assessment, electrical faults are relevant for the mechanical behaviour of wind power plants [Iov *et al*. 2007], [Cutululis *et al*. 2008]. Researchers use a rotor wind speed model beating the rotor axis at the hub height, the standard two-mass model with constant input moments of inertia and a *d-q* reference frame model for the induction generator. Studies were made using industry DIgSilent and academy $HAWC_2$ computational tools, where the conventional paradigm of electro-mechanical symmetry is used. Symmetrical faults are most relevant than the asymmetrical, despite these are statistically more often than those. The reason seems to be the Dy connection in the power transformer.

However, wind speed beats in a no-symmetric way today large blades, producing mechanical vibrations, which together to their structural flexibility and mass distribution, makes them be continuously waving. These features among other mechanical properties are not directly represented in the conventional two-mass model, with constant wind turbine rotor moment of inertia input. This model was used for the researchers to identify the mechanical behaviour after a faults was applied at the power grid. Also, the *abc* → *dq* → *abc* transformation in the induction machine has been widely controversial about its reliability, representing asymmetrical operation.

1.4 Objectives

1.4.1 Main objective

To design an advanced wind turbine modelling to suitably represent:

- The deterministic component of a per-blade equivalent wind speed, to include wind shear and tower transference as affected by mechanical blade loading.
- The aerodynamic influence of large pre-bent blades on the 2-mass model.
- A phase coordinates *abc* induction generator to include time-varying parameters due to main path magnetic saturation, iron losses and deep-bar effect.

1.4.2 Specific objectives

Wind speed model:

a) To define an engineering approach to wind speed seed at 10 m height
b) To improve the definition of aerodynamic roughness function model for wind shear model
c) To include the atmospheric stability in the wind shear model
d) To improve the definition of clearance distance between blade-tip and tower in the tower transference effect model, considering the blade-tower geometry. This feature should include the mechanical pre-bent blade properties.
e) To include the blade mechanical loading modelling in order to look for instantaneously updated azimuthal angle corrections and blade deflections. These variables will influence wind shear and tower transference modelling.

Drive train model:

a) To define a time dependent inertia moment of a pre-bent blade, as a function of its mechanical properties and the instantaneous position of the blade-sections.

b) To compare the behaviour of this research proposed blade-based 2-mass model to the standard 2-mass model.

c) To compare the behaviour of the rotor axis computed wind turbine rotor speed from the standard 2-mass model to the composed rotational speed from the blade-based 2-mass model.

d) To compare the behaviour of the rotor axis computed wind turbine torque from the standard 2-mass model to the wind turbine torque from the blade-based 2-mass model, in order to integrate the effects of the improved wind and drive-train models.

Squirrel-cage induction generator model:

a) To identify a main path magnetic saturation non-linear model, in the context of phase coordinates *abc* modelling. The model should be based on no-load test.

b) To identify an iron loss non-linear model to include eddy and hysteresis losses and stator and rotor components. The model should support non-sinusoidal effects from the power electronic interface, and also be consistent with the standard IEEE.

c) To identify a deep-bar effect non-linear model.

d) To compare the disturbed induction machine behaviour with the time-dependent parameters from these electromagnetic effects, and that with constant parameters.

1.5 Methodology and Simulation Tool

To suitably support the developments in Section 1.4.2, a wind turbine power system setup as shown in the Section B.2 of the Appendix B, is constructed. A 2 MW wind turbine is grid connected to PCC-busbar (Point of Common Coupling) at 31.5 kV. The 2 MW 31.5/0.96/√3, 50 Hz Dy11 power transformer, is between PCC and the induction generator. The 2 MW / 0.96 kV / 50 Hz. induction generator, has the option to be used as squirrel cage or wound rotor. At 5 s a symmetric or asymmetric fault is inserted, and after 0.5 s, it is cleared. The fault duration time agrees with European Grid Codes [Hansen *et al*. 2011] for low voltage fault ride-through computational purposes, involving wind power. This research uses larger than 40 m. blade, as described in [Jonkman *et al*. 2009], 2-mass drive-train tuned parameters as published in [Akhmatov 2003], [Ackermann 2005] and a data-sheet corresponding to standard tests on a 2 MW/ 0.96 kV/50 Hz induction machine.

Having access to technical data bases through the Universidad Nacional de Colombia, as a retired Associate Professor, the background of the wind speed modelling, the aerodynamic modelling and the phase coordinates induction generator modelling, is assessed. The emphasis is made on large wind turbines and particularly on off-shore applications. These aspects include technology of the last 20 years.

However, Conference and Journal papers since 1960 are reviewed to find original seed references, as used by researchers in the last 20 years. Data bases are IEEE/IET, Science Direct – ELSEVIER, SPRINGER VERLAG and direct internet access to e.g. RISO NATIONAL LABORATORIES, NREL-USA ENERGY DEPARTMENT, is also done. Sometimes using searching machines with specific references, papers directly come and access to journals is possible.

The most old research area is all about the wind speed model, with meteorological research. Its engineering point of view and for wind turbine application is proposed until 2002, and pre-bent blades are only 4 years old. The mechanical modelling of wind turbines is a relatively novel topic, despite its applications in other technologies. It is in 2000's where a two-mass model breaks the use of the up to then used one-mass model for airplanes. And relative to the induction machine, despite the existence of large motors, it is only in 2000's they are proposed as special designs to be used as induction generators. The 3 MW wind turbine applications are 4 years old approximately and the 5 MW wind turbine is in few places in the world just now. Other emerging designs of 10 and 20 MW are still in the desk.

Matlab/Simulink is selected to develop a physically based Wind Turbine Model. The Simulink arrangement for this research looks as depicted in the Section B.2 of the Appendix B. Blocks are supported as S-functions in C-code, and they are designed in state variables. In the simulation parameters window a variable-step (minimum step size = 1e-6 and maximum step size = 100e6) is elected with ode15s (stiff/NDF) method, corresponding to DAE systems. Simulation time is an open parameter in dependence of the analyst interest. The stochastic wind component is in frequency domain inside the WIND block. Its formulation is taken from the public blockset development at the Department of Energy Technology (AAU-DET).

Using C-language is a plus in this development because, with specific code and computational adjustments, each model can be transferred to an industrial tool.

Although initially conceived for an Active Stall Wind Turbine with SCIG, the model is able to support grid connected through full power converter and double fed architectures. The modelling conception using SCIG is according to the trend as the wind turbine size increases [Babau *et al*. 2007], due to among other reasons, short circuit characteristics.

1.6 Contributions

The main contributions of this thesis are in the field of time-varying parameters and variables. On the mechanical side they are associated to individual blade rotor structure (*123*), and on the electrical side to the induction generator in phase coordinates (*abc*).

- ***On the wind model (123)***. Based on: i) an engineering wind speed concept at 10 m height instead of the meteorological based friction velocity, ii) the blade-tower geometry to produce a variable operative clearance distance instead of a constant value, and iii) the blade mechanical loading taking into account gravitational, inertial and aerodynamic loads, wind shear and tower transference effects are significantly improved. Expanding the rotor wind speed concept, a per-blade equivalent wind speed is constructed. It allows magnifying non-linear and magnitude characteristics of the effective wind speed, otherwise hidden by the wind speed calculated at the rotor axis. The resultant model more reliably takes into account the effective wind speed all along large pre-bent blades.

- ***On the drive-train model (123)***: Based on the beam theory and taking into account the mechanical properties of large pre-bent blades, the computation of the moment of inertia for one blade. It allows improving the estimation of the whole wind turbine rotor moment of inertia and the low-speed shaft stiffness, for any operative conditions. As a consequence, the standard 2-mass model is empowered to directly include the blade length, its mass density and its pre-bent characteristics. This features together to the per-blade equivalent wind speed model, constitutes a robust whole aerodynamic model. It targets the blade enlargement and flexibility tendency, for large MW size (10, 20 MW) wind turbines.

- ***On the induction generator (abc)***: In order to combine the aerodynamic model with a very detailed model for large induction machines, it is proposed to include: i) A promissory three-saturation function of the $L_{m,abc}$-V_{abc} type, which assumes phase processing data in the standard no-load test, instead of averaging them, ii) A non-linear iron-loss resistance model, as voltage and flux dependent, and involving non-sinusoidal voltage supply, iii) The definition of a test based methodology to successfully represent rotor resistance and leakage reactance, as non-linear slip dependent function. The resultant model remarks non-linear electromagnetic features and their effects on magnetizing and rotor parameters. It makes the model suitable to detail *abc* phase contributions of electric events, coming from the electric side of the wind turbine.

The wind turbine electromechanical model in this way constructed is intended to be useful to test associated models for power converter and reactive power compensator, control strategies and protection schemes. Research contributions highlight the individual effects of large pre-bent blades and the individual effects of the electric system phases, during electro-mechanical transient operation. They promote the idea that, sensing and observing the performance of the *123* ↔ *abc* interaction in one specific transient event will help to make decisions, to make three or individual mechanical/electric control compensation, and/or to prevent three or individual mechanical/electrical adjustments of tolerable limits in protection schemes.

1.7 Thesis Outline

In addition to this Introduction Chapter, six additional Chapters and two Appendices configure the text of this thesis. Chapters 2 and 3 constitute the aerodynamic part of the wind turbine, and Chapters 4, 5, 6 and 7 constructs the electrical part. Both parts supplement their contents in the construction of a whole wind turbine model.

Chapter 2 describes a per-blade equivalent wind speed model, based on the previously published rotor wind model. The proposed per-blade deterministic wind speed component is able to represent the effects of large pre-bent blades on the effective wind speed, including their blade mechanical properties like length, pre-bent and mass-density. A blade mechanical loading function is used to reinforce the influence of wind shear and the tower transference effects.

Chapter 3 presents a beam theory based methodology to compute the blade inertial moment in pre-bent blades and by extension an operational dependent rotor inertia moment. The standard 2-mass model, which was successfully used to represent wind turbine rotor with rigid blades, is taken into account to parametrically compare and validate the new modelling. The modified 2-mass model can directly represent blade length, its pre-bent and mass density, together to operational conditions, which is not possible with the standard 2-mass model. This modelling together to the wind speed model in Chapter 2, configure a robust wind turbine aerodynamic model, where individual blade effects are remarked.

Chapter 4 refers to a proposed feedback methodology to include outside computed electromagnetic effects, valid for large squirrel cage induction machines. The basic *ABC*/*abc* induction generator model is the classical paradigm in [Krause *et al*. 2002], with fluxes as state variables. The main path magnetic saturation comes from the Chapter 5, iron losses from the Chapter 6 and deep-bar effect from the Chapter 7. These three developments are non-linear *abc* models producing time-varying parameters. A data-sheet of standard tests for a 2 MW – 690 V – 50 Hz induction machine, is used as a parametric guide.

Chapter 5 constructs a new paradigm to represent the main path magnetic saturation, by three saturation functions instead of an only one. It is based on the standard no-load test, where instead of averaging the phase measurements, they remain like that. These saturation functions are represented by the voltage dependent magnetizing inductance [Donescu *et al*. 1999], [Seyoum *et al*. 2003]. Due to the time-varying voltage supply changes due to electrical disturbances, the saturation model produces time-varying *abc* magnetizing inductance parameters.. These parameters modify the inductance matrix.

Chapter 6 structures a modified non-linear iron losses resistance, to represent iron-losses in the induction machine. It is in addition corrected to involve the effect of non-sinusoidal voltage supply from the power converter interface [Boglietti *et al*. 2003], [IEEE Std-120-2004], [Ranta *et al*. 2009]

Chapter 7 synthetizes a non-linear slip dependent deep-bar effect function, to produce time-varying *abc* rotor resistance and leakage inductance parameters. It is based on previously published experimental results [Babau *et al*. 2007].

Chapter 8 summarizes the work made in this thesis and the most meaningful conclusions and recommendations about expected future work.

These electromagnetic effects modelled in Chapters 5, 6 and 7, act individually or together on the basin induction generator, presented in Appendix B. All of them constitute a robust induction generator model, where individual phase effects are remarked.

Appendix A supplements definitions about the wind model.

Appendix B supplements induction generator model and power system setup

Bibliography is listed at the end of the text.

* * *

2

Per-Blade Equivalent Wind Speed

2.1 Introduction

If the rotor wind speed results from the addition of the per-blade mechanical effects [Sørensen *et al*. 2002], then, a **per-blade equivalent wind speed** concept can be retained as primary torque source due to flexible and pre-bent large blades. It includes: i) an improved engineering perception of the wind seed at 10 m height and the sea aerodynamic roughness function as fetch and wind seed dependent, ii) a detailed representation of wind shear and tower transference effects together to a logarithmic law wind profile with atmospheric stability and blade-tower geometry, respectively, and iii) the effect on them of blade angle deformations and deflections due to blade mechanical loading. As a consequence of this modelling, non-linear wind speed characteristics are retained as seen at each blade, the magnitude is larger than the resultant rotor wind speed as seen at the hub height, and both of them presents a more reliable waveform and magnitude.

2.2 Wind Speed as a Total Inflow

The total wind field entering to the disk area described by the rotating blades is conceived as an air flow function from computational fluid dynamics, defined as the result of deterministic and stochastic components [Sørensen *et al*. 2002], [Carvalho 2003], given by:

$$u(x,y,z,t)=u_{\mathrm{det}}(x,y,z)+u_{stoch}(x,y,z,t) \tag{2.1}$$

where x, y, z are rotor coordinates and the time t. The $x-z$ coordinates are in the rotor plane with Cartesian sign convention and y is positive in the downstream direction.

Figure 2.1 shows a block diagram of the total wind according to (2.1).

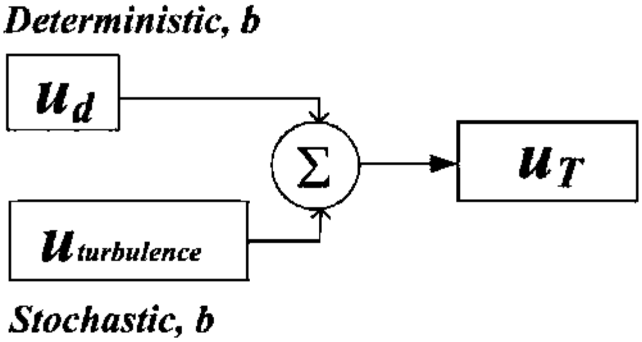

Figure 2.1. Schematic diagram representing the total wind speed

These components have been formulated in the past with emphasis on their hub height effects. But the fast increase of wind turbine power size with large blades, seems to suggest a paradigm change. By this reason a per-blade '*b*' (*b* = 1,2,3) discriminator to the stochastic and deterministic components in Figure 2.1, has been added.

The wind components are developed in what follows focusing the research on a per-blade assessment of the deterministic part, given its direct influence on the dynamics of the wind turbine because of the blade rotation, and in that way with power system stability.

The previously developed stochastic part as upstream turbulence in [Sørensen *et al.* 2002], [Carvalho 2003], is computationally oriented in this research to affect the per-blade performance.

2.3 Improving the Modelling of the Deterministic Wind Speed Component

This research targets an advanced point of view to be consistent to the advanced wind turbine simulation software HAWC2 [Larsen and Hansen 2007]. Figure 2.2 is a schematic diagram of this research proposal, where the deterministic component considers the following features:

i) The upstream wind speed u_z is constructed following the logarithmic law. It is the result of combining the wind speed at 10 m height u_{10}, the stochastic wind component and the effect of gusts. The associated aerodynamic roughness length, instead of a constant value is a function, which discriminates its use at sea or land, and includes atmospheric stability.

ii) Tower-blade specific geometry improves the blade-tower clearance distance and tower radius effects on the wind shear and tower transference, and

iii) Both wind shear and tower transference phenomena are modified in order to include the operational blade angle deformation θ_l and deflection δ_l effects, fed back from the blade structural loading.

Thus, the deterministic part of the total wind speed is a mean wind speed at some specific height of a blade section, as affected by the wind shear u_{ws} and tower transference u_{tt} effects. In polar coordinates the deterministic wind speed is expressed as:

$$u_d(r,\theta) = u_{ws}(r,\theta) + u_{tt}(r,\theta) \qquad (2.2)$$

where the azimuthal reference θ angle feedbacks from the drive train model [Sørensen *et al.* 2002], and r is the distance to the place where the wind is applied, as measured from the blade-root. This deterministic component is conceived to exist all around the neighbourhood of the hub height in the rotor disk, to be strictly no time dependant and to directly influence the dynamics of the wind turbine, because of the blade rotation [Carvalho 2003]. In the simplest way u_d is usually selected as a constant value in the traditional engineering practice.

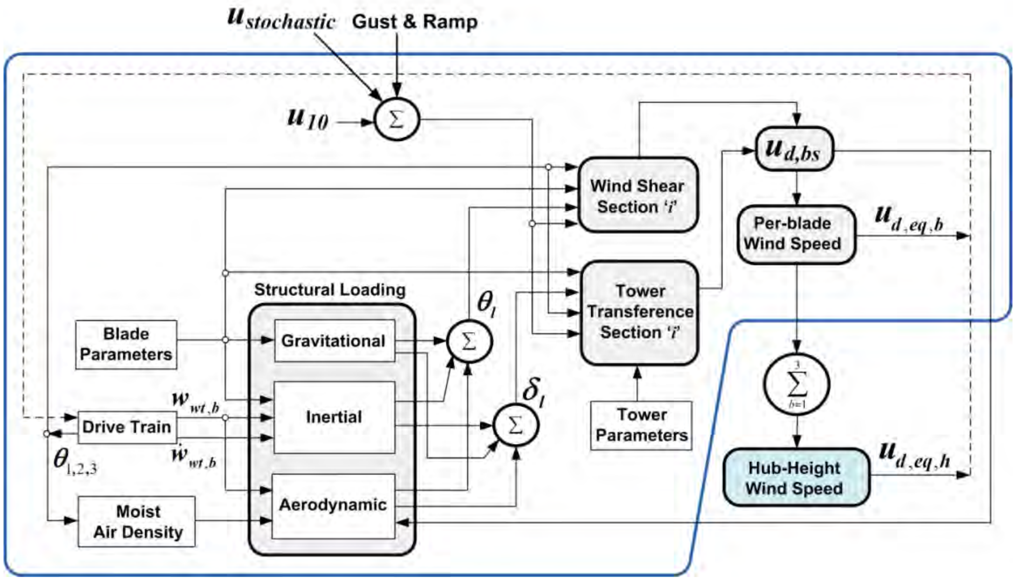

Figure 2.2. Systematic computation for the proposed per-blade deterministic mean wind speed

Figure 2.2 close the wind-blade interactive dynamics, i.e. the wind u_d and rotational speed produce blade loads, which at a time produce blade deformation and deflection to affect u_{ws} and u_{tt}, and so on. Additionally the inclusion of CO2 air component, reinforces this proposal for present world moist air density [Picard *et al*. 2008].

2.3.1 Upstream Wind Speed u_z

Despite the fact that increased uncertainty is introduced by extrapolating data, the mean wind speed as measured at 10 m height u_{10}, is a usually available realistic basin value. The z height extrapolation is done by using either logarithmic law or power law. The power law based on the wind shear α parameter and the Von-Karm κ constant [Madsen *et al*. 1984] appears to be not enough to represent the Atmospheric Boundary Layer (ABL) characteristics, and particular air-water and air-land interaction, which determine a more realistic description of atmospheric stability of the wind profile. Meanwhile the logarithmic law further involving these features has been historically in continuous development [Madsen *et al*. 1984], [Gryning *et al*. 2007].

Two up to date alternatives to compute u_z are presented. First, as detailed in Appendix A, an up to date approach to the logarithmic law involving atmospheric stability can be expressed by,

$$u_z = \frac{u_*}{\kappa}\left(Z_1 + Z_2 + Z_3\right) = \frac{u_*}{\kappa} Z_\psi \tag{2.3}$$

where, u_* is the friction velocity, z is the height of interest, and

$$Z_1 = \ln\left(\frac{z - d_{om}}{z_{om}}\right),\quad Z_2 = -\Psi_m\left(\frac{z - d_{om}}{L}\right),\quad Z_3 = \Psi_m\left(\frac{z_{om}}{L}\right) \tag{2.4}$$

where Ψ_m function represents the atmospheric stability function [Dyer 1974], [Large and Pound 1981], L is the Obukhov length [Monin and Obukhov 1954] associated to the measuring technology. Both are the result of a computational process highly influenced by statistical correlations of meteorological variables. It introduces an inherent analytical error in (2.3) as the height z increases. Also z_{om} is the aerodynamic roughness length and d_{om} is a height correction factor for on-land applications.

Second, a relevant recent model has been proposed in [Gryning *et al*. 2007] and it has demonstrated a more realistically data following experiment as reported in [Peña *et al*. 2008]. As detailed in Appendix A, Gryning establishes that in (A.1) the length scale $1/\ell$ can be significantly redefined using three layers instead of one, as in (2.3). This layers are named from ground to top in the ABL, surface, middle and upper boundary layers. This three-layer model can be expressed as a function of Obukhov's length L, the highest possible boundary layer depth z_i, and empirical constants. For stable conditions ($L > 0$) the three-layer length scale results

$$u_z = \frac{u_{*o}}{\kappa}\left[\ln\left(\frac{z-d_{om}}{z_{om}}\right) + b\frac{z}{L}\left(1-\frac{z-d_{om}}{2z_i}\right) + \frac{z-d_{om}}{\ell_{MBL}} - \frac{z-d_{om}}{z_i}\frac{z-d_{om}}{2\ell_{MBL}}\right] \qquad (2.5)$$

and for unstable atmospheric condition (L < 0)

$$u_z = \frac{u_{*o}}{\kappa}\left[\ln\left(\frac{z-d_{om}}{z_{om}}\right) - \Psi_{mG}\left(\frac{z-d_{om}}{L}\right) + \frac{z-d_{om}}{\ell_{MBL}} - \frac{z-d_{om}}{z_i}\frac{z-d_{om}}{2\ell_{MBL}}\right] \qquad (2.6)$$

where the Ψ_{mG} function is defined as,

$$\Psi_{mG}\left(\frac{z}{L}\right) = \frac{3}{2}\ln\left(\frac{1+\chi_G+\chi_G^2}{3}\right) - \sqrt{3}\arctan\left(\frac{1+2\chi_G}{\sqrt{3}}\right) + \frac{\pi}{\sqrt{3}} \qquad (2.7)$$

and,

$$\chi_G = \left(1 + a\frac{z}{L}\right)^p$$

Parameters a, b and p in (2.5) and (2.6) are selected according to the theoretical limit for convective conditions [Carl *et al*. 1973], [Grachev *et al*. 2000], [Gryning *et al*. 2007].

For the time dependent stochastic wind component $\boldsymbol{u}_{\boldsymbol{stochastic}}$, this research uses a modelling based on Kaimal's power spectra, according to RIS∅'s National Laboratories at Denmark University [Sorensen *et al*, 2002], [Carvalho 2003]. It optionally can include Ziggurat's white noise generator [Marsaglia and Tsang 2000], [Iov *et al*. 2004], to represent rotational sample turbulence. Furthermore, instead of using it as hub height referenced, it is applied here at each blade body-section height. Also the wind gust component $\boldsymbol{u_{gust}}$, uses the modelling approach in [Anderson and Bose 1983].

2.3.2 Averaged Mean Wind Speed $\bar{u}_{10}$

As it is seen in Section 2.3.1 the friction velocity u_* is the usual basin wind speed. But this value for engineering purposes is not directly available by measurements. However, it can be computed at any height and its trend is to vanish as z increases [Yokoyama *et al.* 1979], [Zilitinkevich and Essau 2005], [Gryning *et al.* 2007]. Consequently its value u_{*10} at 10 m height exists and it can be related to u_{10}, as it is found in [Taylor and Yelland 2001].

In [Peña and Gryning 2008] the friction velocity is expressed equal to mean value plus an increment. The same approach can be used to define an averaged mean wind speed $\bar{u}_{10}$ value, as obtained from the usually known data set of mean wind speeds u_{10} in a planning scenario (hour, day, week, month, year). Accordingly, the mean wind speed u_{10} can be conceived as an incremental deviation around its averaged $\bar{u}_{10}$ value. It is expressed by,

$$u_{10} = \bar{u}_{10} + \Delta u_{10} \tag{2.8}$$

where the increment Δu_{10} can even be a mean value too. Joining (2.8) and Peña's approach, it results,

$$u_{*10}^2 = C_{d10} \bar{u}_{10}^2 \xi_{u10} \tag{2.9}$$

where,

$$\xi_{u10} = \left(1 + 2\frac{\Delta u_{10}}{\bar{u}_{10}} + \left(\frac{\Delta u_{10}}{\bar{u}_{10}} \right)^2 \right)$$

Or if u_{10} in (2.3) is taken to (2.8), it result,

$$u_{*10}^2 = \kappa^2 \bar{u}_{10}^2 \xi_{u10} \frac{1}{Z_{\psi 10}^2} \tag{2.10}$$

Because of $\bar{u}_{10}$ can be larger or smaller than u_{10} for a specific time span, if $\bar{u}_{10} > u_{10}$ the deviation Δu_{10} is negative and the factor ξ_{u10} becomes less than 1.0.

If $\bar{u}_{10} < u_{10}$, Δu_{10} is positive and ξ_{u10} is bigger than 1.0. If $\Delta u_{10} = 0$, $\xi_{u10} = 1.0$.

2.3.3 Aerodynamic Roughness Length On Sea Application

The aim of this section is on the z_{om} parameter in (2.4). Instead of a constant parameter what is a common use, it is improved as a wave age $\bar{u}_{10}$ dependent function. Pioneering research has established that:

- The z_{om} parameter is proportional to the Charnock parameter honouring Charnock [Charnock 1955].
- The Charnock parameter is a function of wave age [Maat *et al.* 1991], [Smith *et al.* 1992],[Taylor and Yelland 2001], [Saint-Drenan 2009]. An inverse wave age functionality was defined by Kitaigorodskii's ratio, which relates inverse wave age and fetch *x* [Kitaigorodskii 1962].

Taking into account the proposal in Section 2.3.2, the Charnock parameter is proposed to be expressed as a function of u_{*10} instead of u_{*o}. By definition it result to be [Taylor and Yelland 2001],

$$\alpha_c = A\left[\frac{1}{C}\left(\frac{u_{*10}^2}{gx}\right)^D\right]^B \tag{2.11}$$

and consequently,

$$z_{om} = \frac{A}{(Cx^D)^B}\left(\frac{u_{*10}^2}{g}\right)^{1+BD} \tag{2.12}$$

Equations (2.11) and (2.12) based in u_{x10} have the basic structure to implement u_{10} in Charnock parameter based models. Explicit Charnock parameter and aerodynamic roughness length functions appear, when replacing (2.9) in (2.11) and (2.12), i.e.

$$\alpha_c = A\left[\frac{1}{C}\left(\frac{C_{d10}\bar{u}_{10}^2\xi_{u10}}{gx}\right)^D\right]^B \tag{2.13}$$

$$z_{om} = \frac{A}{(Cx^{D})^{B}} \left(\frac{C_{d10}\overline{u}_{10}^{2}\xi_{u10}}{g} \right)^{1+BD} \tag{2.14}$$

while implicit functions appear when replacing (2.10) in (2.11) and (2.12) resulting on,

$$\alpha_{c} = A \left[\frac{1}{C} \left(\frac{\kappa^{2}\overline{u}_{10}^{2}\xi_{u_{10}}}{gxZ_{\psi 10}^{2}} \right)^{D} \right]^{B} \tag{2.15}$$

$$z_{om} = \frac{A}{(Cx^{D})^{B}} \left(\frac{\kappa^{2}\overline{u}_{10}^{2}\xi_{u_{10}}}{gZ_{\psi 10}^{2}} \right)^{1+BD} \tag{2.16}$$

It is found by simulation that, if u_{*10} is defined as dependent on the averaged mean wind speed $\bar{u}_{10}$, the resultant α_c and z_{om} functions are within a reliability region defined by available methods [Jhonson *et al.* 1998], [Lange and Højstrup 2000], [Taylor and Yeeland 2001], [Fairal and Bradley 2003]. A general expression for the aerodynamic roughness length function is

$$z_{om} = \frac{\overline{u}_{10}^{2(1+BD)}}{x^{BD}} F(u_{10}) \tag{2.17}$$

where for an explicit function takes the form,

$$F(u_{10}) = \frac{A}{(C)^{B}} \left(\frac{C_{d10}\xi_{u10}}{g} \right)^{1+BD} \tag{2.18}$$

and for an implicit function is,

$$F(u_{10}, x) = \frac{A}{(C)^{B}} \left(\frac{\kappa^{2}\xi_{u_{10}}}{gZ_{\psi 10}^{2}} \right)^{1+BD} \tag{2.19}$$

The modelling from (2.11) to (2.19) allows reasoning in two ways: i) The z_{om} function is taken to (2.3). If an explicit function is used the computational procedure is straightforward. With an implicit function, a non-linear problem should be solved and an iterative process is needed, and ii) If z_{om} function is replaced in any wind profile expression, an essential modification is introduced. For this case, x, u_{10} and wave-age parameters dependence, do not explicitly appear anymore.

The wind profile based on the logarithmic law involving atmospheric stability becomes,

$$u_z = \frac{\bar{u}_{10}\sqrt{C_{d10}\xi_{u_{10}}}}{\kappa}\left(\begin{array}{l} \ln\left(\dfrac{(z-d_{om})x^{BD}}{\bar{u}_{10}^{2(1+BD)}F(u_{10})}\right) - \Psi_m\left(\dfrac{z-d_{om}}{L}\right) \\ +\Psi_m\left(\dfrac{\bar{u}_{10}^{2(1+BD)}F(u_{10})}{x^{BD}L}\right) \end{array}\right) \tag{2.20}$$

where d_{om} is the displacement height. Consequently, the logarithmic law as a three-layer model can be improved. The corresponding wind profile for stable atmospheric condition (L > 0) and using the explicit function is,

$$u_z = \frac{\bar{u}_{10}\sqrt{C_{d10}\xi_{u_{10}}}}{\kappa}\left[\begin{array}{l} \ln\left(\dfrac{(z-d_{om})x^{BD}}{\bar{u}_{10}^{2(1+BD)}F(u_{10})}\right) + \\ b\dfrac{z}{L}\left(1-\dfrac{z-d_{om}}{2z_i}\right) + \dfrac{z-d_{om}}{\ell_{MBL}} - \dfrac{z-d_{om}}{z_i}\dfrac{z-d_{om}}{2\ell_{MBL}} \end{array}\right] \tag{2.21}$$

where,

$$\ell_{MBL} = \frac{\bar{u}_{10}\sqrt{C_{d10}\xi_{u_{10}}}}{f_c}\frac{1}{55-2\ln\left(\dfrac{\sqrt{C_{d10}\xi_{u_{10}}}}{f_c}\dfrac{x^{BD}}{\bar{u}_{10}^{(1+BD)}F(u_{10})}\right)} \tag{2.22}$$

For engineering purposes, taking into account that even z_i can be approached to a specific value [Gryning *et al.* 2007], wind profile models are functions of u_{10} and x only. Therefore, the aerodynamic roughness length results on a missed variable.

2.3.4 Per-Blade and Body-Section Wind Speed

Once the wind speed u_z is calculated, it is seen as applied to a blade body-section and including wind shear and tower transference effects. The height of any blade body-section varies as it moves within the rotor disk area. Following the proposal in [Sørensen *et al.* 2002] and given in (2.2), a more detailed approach can be written as,

$$u_{d,bs}(r_{bs},\theta_{bs}) = u_z[C_{ws,bs}(r_{bs},\theta_{bs}) + C_{tt,bs}(r_{bs},\theta_{bs})] \tag{2.23}$$

where C_{ws} and C_{tt} are the wind shear and tower shadow coefficients, and *bs* means body section height. The angle θ_{bs} gets the influence of the gravitational, inertial and aerodynamic bending moments in the blade ± *y*-axis for the case of wind shear and in the blade ± *z*-axis for the case of tower transference phenomena.

This enhanced detailed modelling is a powerful concept to evaluate change in the kinetic energy flux (power input) for large wind turbine blades. The wind shear introduces cycling variation and tower transference sharped pulsations, acting both on the wind flow with the azimuth position of the rotor. It results in a reduced ability to extract the available wind power [Rozen *et al.* 2010].

2.3.5 Wind Shear involving Blade Pre-bent and Mechanical Loading

To include the wind shear effect in C_{ws}, two tasks are proposed:

i) Carefully define a $\Delta z(\theta_{bs})$ distance described by a point in a blade body-section. It rotates around the hub height, including rotor shaft tilt angle (RSTA) and structural overhang distance. The computational proposal in [Dolan and Lehn 2006] is followed,

ii) Make a Taylor's series expansion of an extended C_{ws} coefficient, containing atmospheric stability terms and where z_{om} is a functional model for sea applications.

Taking into account the wind profile adjustments in Section 2.3.3, any of them can be rewritten as,

$$u_z = u_{10} C_{ws}(z_{om}, L) \tag{2.24}$$

where the wind shear coefficient C_{ws} is discriminately defined as,

$$C_{ws\psi} = \sqrt{C_{d10}}\,\kappa^{-1} Z_{\psi} \tag{2.25}$$

or,

$$C_{wsG} = \sqrt{C_{d10}}\,\boldsymbol{\kappa}^{-1} G(z_{om}, L, \ell_{MBL}, z_i) \tag{2.26}$$

where *G* means Gryning wind profile in [Gryning *et al.* 2007].

The first task *defines the Δz value*, and a geometrical point of view of the wind generator is presented in Figure 2.3, as seen from the front and the corresponding right side. RSTA γ and overhang length O_{vh} (distance between hub apex and tower axes), are included.

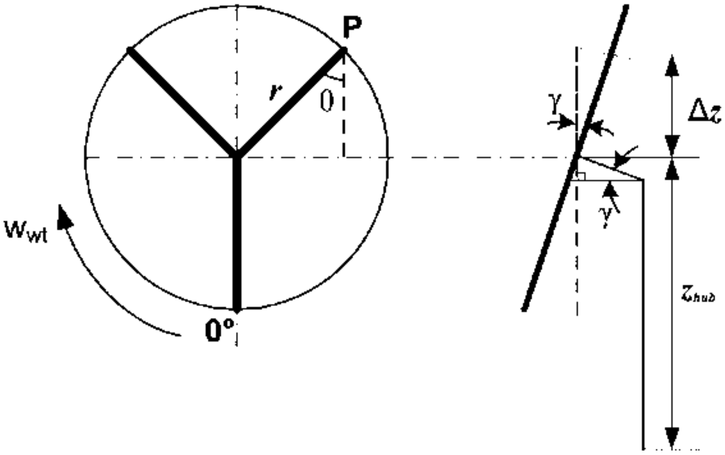

Figure 2.3 Front and right side view of the blade-tower related geometry

Triangle relationships in Figure 2.3 yields a per-blade height increment *Δz* given by,

$$\Delta z_b = -r_b \cos\theta_b \cos\gamma - O_{vh} \sin\gamma \tag{2.27}$$

where the minus sign means that the azimuthal reference angle $\theta = 0$ degrees is taken in this research when blade ‘1’ is at the bottommost of the disk area and in front of the tower.

Modelling the height increment as in (2.27), agrees and improves previous research, to include the RSTA γ [Carvalho 2003], [Dolan and Lehn 2006], [Das *et al.* 2011] and the overhang effect [Madsen *et al.* 1984]. When $\gamma = 0$, it is evident that z is equal to the hub height. These features contributes to make (2.27) a more exact Δz model.

For computational purposes and using Taylor’s series expansion, the wind shear effect has already been synthetized for the power law based wind profile in [Dolan and Lehn 2006], and for the logarithmic law in [Madsen *et al.* 1984]. The present research extends the wind shear mathematical expansion for the logarithmic law including atmospheric stability and three-layer methods, as presented in Section 2.2.1.

The second task for sea applications, defines a Taylor’s series expansion of the wind shear coefficient, as given in (2.25) or (2.26).

For the case of the logarithmic law, given the explicit roughness length function and stable condition (L > 0) it is,

$$C_{ws\psi S}=\sqrt{C_{d10}}\kappa^{-1}\left(\begin{array}{l} Z_{\psi o}+\\ [(z-d_{om})^{-1}-aL^{-1}]\Delta z-\\ (z-d_{om})^{-2}\dfrac{\Delta z^{2}}{2}+\\ (z-d_{om})^{-3}\dfrac{\Delta z^{3}}{3}\\ -(z-d_{om})^{-4}\dfrac{\Delta z^{4}}{4}+\\ (z-d_{om})^{-5}\dfrac{\Delta z^{5}}{5}\\ -(z-d_{om})^{-6}\dfrac{\Delta z^{6}}{6}+\ldots \end{array}\right) \tag{2.28}$$

Given now explicit roughness length function and unstable conditions (L < 0), the wind shear coefficient results to be,

$$C_{ws\psi U}=\sqrt{C_{d10}}\kappa^{-1}\left(\begin{array}{l} Z_{\psi o}+[(z-d_{om})^{-1}+C_{1U}]\Delta z+\\ [-(z-d_{om})^{-2}+C_{2U}]\dfrac{\Delta z^{2}}{2}+\\ [2(z-d_{om})^{-3}+C_{3U}]\dfrac{\Delta z^{3}}{6}+\\ [-6(z-d_{om})^{-4}+C_{4U}]\dfrac{\Delta z^{4}}{24}+\\ [24(z-d_{om})^{-5}+C_{5U}]\dfrac{\Delta z^{5}}{120}+\\ [-120(z-d_{om})^{-6}+C_{6U}]\dfrac{\Delta z^{6}}{720}+\ldots \end{array}\right) \tag{2.29}$$

Special care should be taken if using implicit functions in the case of sea application, where a nonlinear function appears involving the derivatives.

For the case of the power law based wind profile, the Taylor's series expansion of the wind shear coefficient around hub height produces $C_{ws\alpha}$ as,

$$C_{ws\alpha} = \frac{1}{H_o^{\alpha}} \begin{pmatrix} z_{hub}^{\alpha} + K_1\Delta z + K_2\Delta z^2 + K_3\Delta z^3 + K_4\Delta z^4 + K_5\Delta z^5 \\ +K_6\Delta z^6 + \ldots \end{pmatrix} \tag{2.30}$$

It is also possible to define the wind shear coefficient C_{wsG} term from (2.26) for stable conditions (L > 0) as,

$$C_{wsSG} = \sqrt{C_{d10}}\boldsymbol{\kappa}^{-1} \begin{bmatrix} \ln\left(\frac{z-d_{om}}{z_{om}}\right) + b\frac{z}{L}\left(1-\frac{z-d_{om}}{2z_i}\right) \\ +\frac{z-d_{om}}{\ell_{MBL}} \\ -\frac{z-d_{om}}{z_i}\frac{z-d_{om}}{2\ell_{MBL}} \end{bmatrix} \tag{2.31}$$

and for unstable conditions (L < 0) as,

$$C_{wsUG} = \sqrt{C_{d10}}\boldsymbol{\kappa}^{-1} \begin{bmatrix} \ln\left(\frac{z-d_{om}}{z_{om}}\right) - \Psi_{mG}\left(\frac{z-d_{om}}{L}\right) + \\ \Psi_{mG}\left(\frac{z_{om}}{L}\right) + \\ \frac{z-d_{om}}{\ell_{MBL}} - \frac{z-d_{om}}{z_i}\frac{z-d_{om}}{2\ell_{MBL}} \end{bmatrix} \tag{2.32}$$

The expansion of (2.31) using Taylor's series for stable conditions leaves,

$$C_{ws\psi S} = \sqrt{C_{d10}}\kappa^{-1} \begin{pmatrix} Z_{\psi o} + [(z-d_{om})^{-1} - aL^{-1} + \frac{b}{L}\left(1+\frac{d_{om}}{2z_i}\right) - \\ \frac{b}{z_i L}z + \ell_{MBL}^{-1} + (z-d_{om})(z_i\ell_{MBL})^{-1}]\Delta z \\ -\frac{(z-d_{om})^{-2} - b/(Lz_i)^{-1} + (z_i\ell_{MBL})^{-1}}{2}\Delta z^2 \\ +\frac{(z-d_{om})^{-3}}{3}\Delta z^3 - \frac{(z-d_{om})^{-4}}{4}\Delta z^4 \\ +\frac{(z-d_{om})^{-5}}{5}\Delta z^5 - \frac{(z-d_{om})^{-6}}{6}\Delta z^6 + \ldots \end{pmatrix} \tag{2.33}$$

and the expansion of (2.32) for unstable conditions yields,

$$C_{ws\psi U} = \sqrt{C_{d10}}\,\kappa^{-1} \begin{pmatrix} Z_{\psi o} + [(z-d_{om})^{-1} + C'_{wsU} + \ell_{MBL}^{-1} + \dfrac{z-d_{om}}{z_i \ell_{MBL}}]\Delta z \\ + \dfrac{-(z-d_{om})^{-2} + C''_{wsU} + (z_i \ell_{MBL})^{-1}}{2}\Delta z^2 \\ + \dfrac{2(z-d_{om})^{-3} + C'''_{wsU}}{6}\Delta z^3 + \ldots \end{pmatrix} \tag{2.34}$$

Constants associated to (2.28) – (2.34) are reported in the Appendix A.

2.3.6 Tower Transference involving Blade Pre-bent and Mechanical Loading

To include the tower transference effect *Ctt*, taking into account the tower geometry shown in Figures 2.4 and 2.5, a four step procedure to build clearance distance and tower radius parameters as variable values, is proposed in this research: i) to estimate a mathematical model to fit the design of pre-bending large-blades, ii) to evaluate the geometrical conditions just when the blade is in front of the tower, iii) to do the respective estimation for the after tilting conditions, and iv) to include the blade vibration coming from the blade structural loading.

The C_{tt} coefficient is taken from [Sørensen *et al.* 2002]; [Dolan and Lehn 2006], and it is conveniently modified for this research purposes. In a blade body-section context it is,

$$C_{tt,b}(r_b,\theta_b) = a_B^2 \frac{r_b^2 \sin^2\theta_b - x_b^2}{(r_b^2 \sin^2\theta_b + x_b^2)^2} \tag{2.35}$$

where a_B represents the tower radius at the bottommost blade-tip position including the changing blade-tip deflection; θ_b is the angle between every couple of blades including the deformation angle component from the blade structural loading; x_b is the clearance distance between blade and tower at the bottommost blade-tip, as affected by the blade dynamic forces respectively; r_b is the distance from the blade-root to the blade-body-section along the blade.

Pre-bent and not pre-bent blades, passing in front of the tower are analysed.

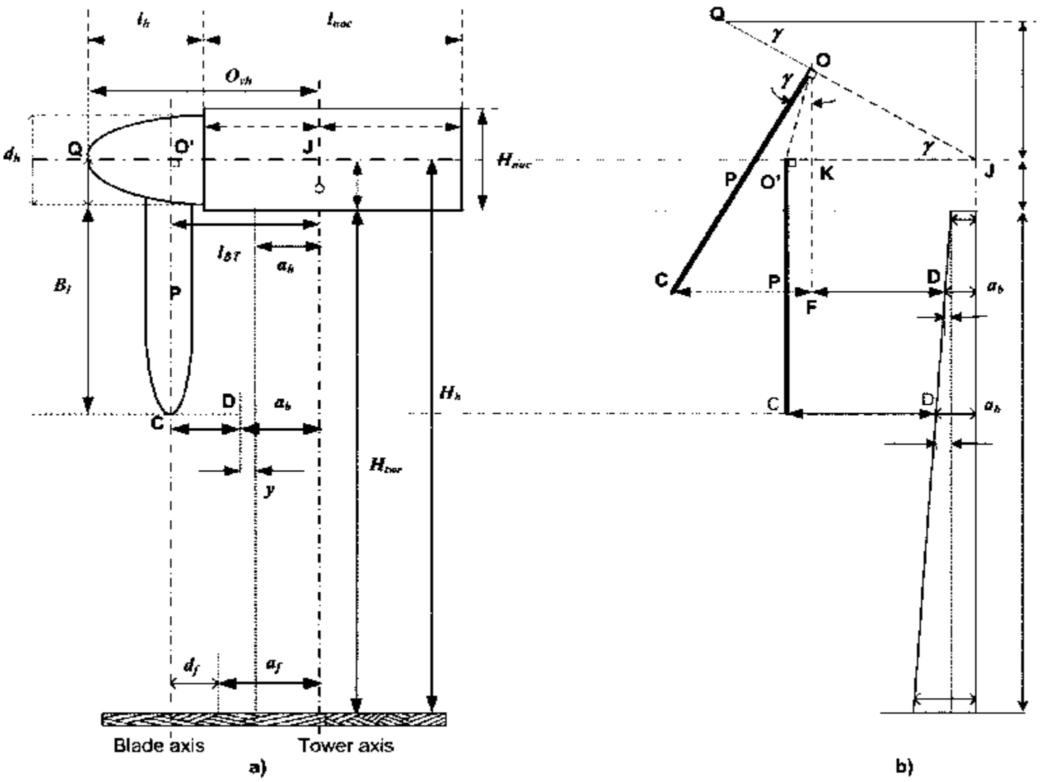

Figure 2.4 Not pre-bent blade at the tower: a) formal view, and b) geometric view

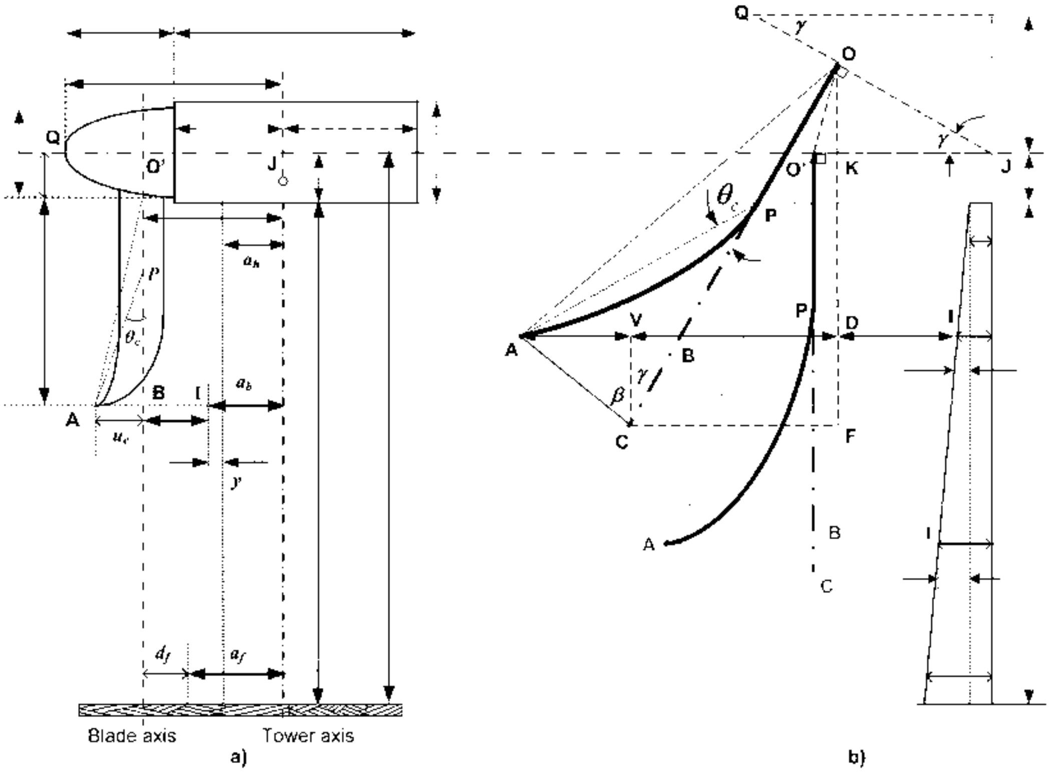

Figure 2.5 Pre-bent blade at the tower: a) formal view, and b) geometric view

The purpose is to represent the effects of wind shear and mechanical blade loading on a_b, θ_b, and x_b. As a first step, a draw approach to the blade-tower geometry is presented. Figure 2.4 represents the case of not pre-bent blade and Figure 2.5 the case of pre-bent blade. All distances in Figure 2.4 are referenced to VESTAS wind turbine blades for 2MW and 3 MW [VESTAS wind systems 2013]. In what follows the case 1 for not pre-bent blade and the case 2 for pre-bent blades are in detail developed.

2.3.6.1 Clearance Distance and Tower Radius Computation When Blades Are Not Pre-bent

Related to the nomenclature in Figure 2.4(a) and 2.4(b), it is seen that,

$$CO' = CO = R_{disk} = B_l + d_h / 2 \tag{2.36}$$

is the radius of the disk area. Despite of the fact of null pre-bent, it is expected the existence of a P point, where the inherent flexibility begins and then,

$$O'P = OP = B_l + d_h / 2 \tag{2.37}$$

where the blade length B_l in pu is measured from the blade root. Knowing the nacelle height H_{nac} and the tower height H_{twr}, the hub height in the Figure 2.4(b) is,

$$H_h = H_{twr} + \frac{H_{nac}}{2} + O_{vh} \sin\gamma \tag{2.38}$$

When γ is zero, the hub height in Figure 2.4(a) is recovered. Relating geometry and nomenclature in Figure 2.4(a) and 2.4(b), for similar triangles it can be written,

$$\frac{a_f - a_h}{y} = \frac{H_{twr}}{OF - OK - H_{nac} / 2} \tag{2.39}$$

and thus, the distance y on the tower at the bottommost blade-tip is determined as,

$$y = \frac{(OC\cos\gamma - OJ\sin\gamma - H_{nac} / 2)a_f - a_h}{H_{twr}} \tag{2.40}$$

With this, the clearance distance x_b between the blade-tip and the tower border is,

$$x_b = CF + FD \tag{2.41}$$

After replacing the corresponding parameters the clearance distance x_b is obtained as,

$$x_b = OC\sin\gamma + OJ\cos\gamma - a_h - y + \delta_z \tag{2.42}$$

where δ_z is the blade deflection effect due to the blade mechanical loading (BML), and which computation appears in Appendix A. The tower radius a_B results to be,

$$a_B = a_h + y \tag{2.43}$$

2.3.6.2 Clearance Distance and Tower Radius Computation When Blades Are Pre-bent

In Figure 2.5 it is observed that the blade pre-bent section starts at the point P. The distance AP is chosen in agreement with USA patent [Olesen *et al.* 2012] with a value of the order of 60% of the blade length. From the blade-root to the point *P*, larger torsional stiffness value is assumed. In the absence of other information, an exponential function has been assumed for the pre-bent section. As related to Figure 2.5(b), it is suitably obtained,

$$AC = PC\exp\left(\ln\left(-2\sin\left(\tfrac{\theta_c}{2}\right)\right)\right) \tag{2.44}$$

Also,

$$CO' = CO = B_l + d_h / 2 \tag{2.45}$$

Relating geometry and nomenclature in Figure 2.5(a), by similar triangles,

$$\frac{a_f - a_h}{y} = \frac{H_{twr}}{OC\cos\gamma - OJ\sin\gamma - H_{nac}/2 - AC\sin\gamma} \tag{2.46}$$

and thus, the distance y on the tower at the bottommost blade-tip position is determined as,

$$y = \frac{(OC\cos\gamma - OJ\sin\gamma - H_{nc}/2 - AC\sin\gamma)(a_f - a_h)}{H_{twr}} \tag{2.47}$$

It is seen that the clearance distance x_b can be expressed by,

$$x_b = AV + VD + DI \tag{2.48}$$

But $\beta + \gamma = \pi/2$ in Figure 2.6(b) is only a particular case. In order to generalize the β angle value, θ_c and $\beta + \gamma$ angles are related in triangle APC for AP segment using the cosine law resulting,

$$\beta = \operatorname{acos}\left(\frac{PC - AP\cos\theta_c}{AC}\right) - \gamma \tag{2.49}$$

After replacing the corresponding parameters, the clearance distance x_b is,

$$x_b = AC\sin\beta + OC\sin\gamma + OJ\cos\gamma - a_{hub} - y + \delta_z \tag{2.50}$$

where δ_z is the blade deflection effect due to BML. The tower radius a_B results to be,

$$a_B = a_h + y \tag{2.51}$$

Additionally, the radius of the disk area is measured by,

$$AO = \sqrt{AP^2 + PO^2 + 2AP(PO)\cos\theta_c} \tag{2.52}$$

where a positive AP value, as associated to triangle APC results from the solution of,

$$AP^2 - 2AP(PC)\cos\theta_c - (AC^2 - PC^2) = 0 \tag{2.53}$$

2.3.7 Per-Blade Equivalent Wind Speed Involving Wind Shear and Tower Transference

A weighted wind speed u_ψ at one blade can be defined as in [Sørensen *et al*. 2002], [Carvalho 2003] as,

$$u_\psi(r,\theta_b) = \frac{\int_{r_o}^{R} \psi(r)u(t,r,\theta_b)dr}{\int_{r_o}^{R} \psi(r)dr} \tag{2.54}$$

About u_ψ Sorensen remarks that it is ".. (a) weighting of all the wind speeds which are instantaneously seen for the wind turbine along one blade". Furthermore in [Carvalho 2003] it is emphasized that (2.54) corresponds to one-blade effect.

According to [Carvalho 2003] it is assumed that: i) u_ψ corresponds to an *equivalent per-blade value* as the contribution of the accumulated effect of all blade-body-sections, as calculated in Section 2.2.4. This is consistent with the computational process in [Sørensen *et al*. 2002], [Carvalho 2003] for the real part, and ii) being u in (2.54) the total wind speed according to (2.1), it can be suitably approximated to (2.23) which is redefined for the full length blade as,

$$u \approx u_{d,b}(r_b, \theta_b) = u_z[C_{ws,b}(r_b, \theta_b) + C_{tt,b}(r_b, \theta_b)] \tag{2.55}$$

for any z height. The sub-indexes *ws* and *tt* mean wind shear and tower transference, respectively. The expression (2.55) allows reinterpreting (2.54) for this research symbology as,

$$u_{d,eq,b} = \frac{\int_{r_o}^{R} \psi_b u_{d,b} dr}{\int_{r_o}^{R} \psi_b dr} \tag{2.56}$$

where the assumed linear function $\psi_b(r) = k_b r$ [Sørensen *et al*. 2002] is an aerodynamic coefficient showing the influence of the aero-load on the blade-root moment at r_b radius, with k_b being a constant value [Carvalho 2003], [Dolan and Lehn 2006]. Replacing this $\psi(r)$ function, (2.56) is rewritten as,

$$u_{d,eq,b} = \frac{2}{R^2 - r_o^2} \int_{r_o}^{R} r_b u_{d,b} dr \tag{2.57}$$

and replacing now (2.55) in (2.57), this can be expressed by,

$$u_{d,eq,b} = \frac{2u_z}{R^2 - r_o^2} \int_{r_o}^{R} r_b [C_{ws,b} + C_{tt,b}] dr \tag{2.58}$$

where C_{ws} and C_{tt} were previously defined. Or in abbreviate form as,

$$u_{d,eq,b} = u_{ws,eq,b} + u_{tt,eq,b} \tag{2.59}$$

After replacing wind shear coefficient expansion and tower transference models in (2.58), integrations are discriminated in order to obtain the components in (2.59) as follows. Using the power law [Masters 2004], $C_{ws,b}$ corresponds to (2.50) and $C_{tt,b}$ to (2.51). The new form of (2.58) is,

$$u_{d,eq,b} = \frac{2u_z}{R^2 - r_o^2} \int_{r_o}^{R} r_b \left(\begin{array}{l} \dfrac{1}{H_o^\alpha} \left(\begin{array}{l} h^\alpha + K_1 \Delta z + K_2 \Delta z^2 + K_3 \Delta z^3 + K_4 \Delta z^4 \\ + K_5 \Delta z^5 + K_6 \Delta z^6 + \ldots \end{array} \right) \\ + a_B^2 \dfrac{r_b^2 \sin^2 \theta_b - x_b^2}{(r_b^2 \sin^2 \theta_b + x_b^2)^2} \end{array} \right) dr \tag{2.60}$$

Solving for the integral, the components corresponding to (2.59) result to be,

$$u_{ws,eq,b} = \frac{2u_{z,b}}{H_o^\alpha (R_b^2 - r_{ob}^2)} \sum_{j=2}^{8} \frac{R_b^j - r_{ob}^j}{j} C_{Pj-2} \cos^{j-2}(\gamma) \cos^{j-2}(\theta_b) \tag{2.61}$$

$$u_{tt,eq,b} = \frac{2u_z}{R_b^2 - r_{ob}^2} \left(\begin{array}{l} \dfrac{a_B^2}{2\sin^2\theta_b} \left(\begin{array}{l} \log \dfrac{(R_b^2 \sin^2 \theta_b + x_{bv}^2)}{(r_{ob}^2 \sin^2 \theta_b + x_{bv}^2)} + \dfrac{x_{bv}^2}{(R_b^2 \sin^2 \theta_b + x_{bv}^2)} \\ - \dfrac{x_{bv}^2}{(r_{ob}^2 \sin^2 \theta_b + x_{bv}^2)} \end{array} \right) \\ + \dfrac{a_B^2 x_{bv}^2}{2\sin^2\theta_b} \left(\dfrac{1}{(R_b^2 \sin^2 \theta_b + x_{bv}^2)} - \dfrac{1}{(r_{ob}^2 \sin^2 \theta_b + x_{bv}^2)} \right) \end{array} \right) \tag{2.62}$$

Now, using the logarithmic law for sea application, explicit aerodynamic roughness length (z_{om}) function and the displacement height d_{om}, the new form of (2.58) for the stable case (L > 0) is,

$$u_{d,eq,b} = \frac{2u_{10}\sqrt{C_{d10}}\kappa^{-1}}{R^2 - r_o^2}\int_{r_o}^{R} r_b \begin{pmatrix} Z_{\psi o} + [(z-d_{om})^{-1} - aL^{-1}]\Delta z \\ -\frac{(z-d_{om})^{-2}}{2}\Delta z^2 + \frac{(z-d_{om})^{-3}}{3}\Delta z^3 \\ -\frac{(z-d_{om})^{-4}}{4}\Delta z^4 + \frac{(z-d_{om})^{-5}}{5}\Delta z^5 \\ -\frac{(z-d_{om})^{-6}}{6}\Delta z^6 + \ldots \\ +a_B^2 \frac{r_b^2 \sin^2\theta_b - x_b^2}{(r_b^2 \sin^2\theta_b + x_b^2)^2} \end{pmatrix} dr \qquad (2.63)$$

Notice that because of its definition in (2.51), the tower transference effect term remains unalterable in (2.62). Remind that the γ and the overhang distance O_{vh} are already included in a_B and x_b. Solving for the integral in (2.63), the wind shear component corresponding to (2.59) results to be,

$$u_{ws,eq,b} = \frac{2u_{10}\sqrt{C_d}\kappa^{-1}}{R^2 - r_o^2}\sum_{j=2}^{8}\frac{R_b^j - r_{ob}^j}{j} C_{S_{j-2}} \cos^{j-2}(\gamma)\cos^{j-2}(\theta_b) \qquad (2.64)$$

And the new form for the unstable case (L < 0) is,

$$u_{d,eq,b} = \frac{2u_{10}\sqrt{C_d}\kappa^{-1}}{R^2 - r_o^2}\int_{r_o}^{R} r_b \begin{pmatrix} Z_{\psi o} + [(z-d_{om})^{-1} + C'_{wsU}]\Delta z \\ +\frac{-(z-d_{om})^{-2} + C''_{wsU}}{2}\Delta z^2 \\ +\frac{2(z-d_{om})^{-3} + C'''_{'wsU}}{6}\Delta z^3 + \ldots \\ +a_B'^2 \frac{r_b^2 \sin^2\theta_b - x_b'^2}{(r_b^2 \sin^2\theta_b + x_b'^2)^2} \end{pmatrix} dr \qquad (2.65)$$

Solving for the integral, the wind shear component is,

$$u_{ws,eq,b} = \frac{2u_{10}\sqrt{C_d}\kappa^{-1}}{R^2 - r_o^2}\sum_{j=2}^{8}\frac{R_b^j - r_{ob}^j}{j} C_{U_{j-2}} \cos^{j-2}(\gamma)\cos^{j-2}(\theta_b) \qquad (2.66)$$

Using the three-layer modelling, explicit aerodynamic roughness length (z_{om}) function, the new form for the stable case of (2.58) is,

$$u_{d,eq,b} = \frac{2u_{10}\sqrt{C_d}\kappa^{-1}}{R^2 - r_o^2}\int_{r_o}^{R} r_b \begin{pmatrix} Z_{\psi o} + [(z-d_{om})^{-1} - aL^{-1} + \frac{b}{L}\left(1+\frac{d_{om}}{2z_i}\right) \\ -\frac{b}{z_i L}z + \ell_{MBL}^{-1} + (z-d_{om})(z_i\ell_{MBL})^{-1}]\Delta z \\ -\frac{(z-d_{om})^{-2} - b/(Lz_i)^{-1} + (z_i\ell_{MBL})^{-1}}{2}\Delta z^2 \\ +\frac{(z-d_{om})^{-3}}{3}\Delta z^3 - \frac{(z-d_{om})^{-4}}{4}\Delta z^4 \\ +\frac{(z-d_{om})^{-5}}{5}\Delta z^5 - \frac{(z-d_{om})^{-6}}{6}\Delta z^6 + \dots \\ +a_B'^2 \frac{r_b^2\sin^2\theta_b - x_b'^2}{(r_b^2\sin^2\theta_b + x_b'^2)^2} \end{pmatrix} dr \tag{2.67}$$

Solving for the integral in (2.67), the components corresponding to (2.59) are,

$$u_{ws,eq,b} = \frac{2u_{10}\sqrt{C_d}\kappa^{-1}}{R^2 - r_o^2}\sum_{j=2}^{8}\frac{R_b^j - r_{ob}^j}{j}C_{GS_{j-2}}\cos^{j-2}(\gamma)\cos^{j-2}(\theta_b) \tag{2.68}$$

The new form for the unstable case of (2.58) is,

$$u_{d,eq,b} = \frac{2u_{10}\sqrt{C_d}\kappa^{-1}}{R^2 - r_o^2}\int_{r_o}^{R} r_b \begin{pmatrix} Z_{\psi o} + [(z-d_{om})^{-1} + C'_{wsU} + \ell_{MBL}^{-1} + \frac{z-d_{om}}{z_i\ell_{MBL}}]\Delta z \\ +\frac{-(z-d_{om})^{-2} + C''_{wsU} + (z_i\ell_{MBL})^{-1}}{2}\Delta z^2 \\ +\frac{2(z-d_{om})^{-3} + C'''_{wsU}}{6}\Delta z^3 + \dots \\ +a_B'^2 \frac{r_b^2\sin^2\theta_b - x_b'^2}{(r_b^2\sin^2\theta_b + x_b'^2)^2} \end{pmatrix} dr \tag{2.69}$$

Solving for the integral in (2.67), the components corresponding to (2.59) is,

$$C_{wsGU} = \sum_{j=2}^{8}\frac{R_b^j - r_{ob}^j}{j}C_{GU_{j-2}}\cos^{j-2}(\gamma)\cos^{j-2}(\theta_b) \tag{2.70}$$

Constants of the type *K* in (2.60) and *C* in (2.61), (2.64)-(2.66), (2.68) and (2.70) are presented in the Appendix A.

2.3.8 Equivalent Wind Speed at Hub Height

Once the per-blade equivalent wind speed is obtained, the next step following the inflow theory [Sørensen *et al*. 2002], [Carvalho 2003], is to compose a hub height value, as the *mean value of the three blades contribution,* and expressed according to (2.56) by,

$$u_{d,eq} = \frac{1}{3}\sum_{b=1}^{3} u_{\psi b} = \frac{1}{3}\sum_{b=1}^{3} u_{d,eq,b} \tag{2.71}$$

In this research it is calculated as a logic referent, in order to compare to the improved per-blade wind speed models.

2.4 Simulation and Analysis

An offshore application is suitably selected, with a wind turbine operating at 25 Km from the shore. For a 2 MW wind turbine, it is assumed that the blade is not-pre-bent and has 44 m length [VESTAS wind systems 2013]. The wind speed at shore is assumed to be u_{10} = 7.4 m/s, and a maximum wind speed deviation of 2.8 m/s along 150 Km inside the ocean configure a $u_{10} = f(x)$ function according to [Hasager *et al*. 2008]. To extend the analysis for a 3 MW wind turbine, the blade is pre-bent and has 54.6 m length [VESTAS wind systems 2013]. For this case, the wind speed at shore is assumed to be u_{10} = 5.8 m/s in order to operate the wind turbine at 2 MW according to its power curve. Other conditions are similar.

Effects from wind shear, tower transference, mechanical blade loading, RSTA and pre-bent are involved. In Appendix A, a brief summary describing the mechanical blade loading used in this research [Hansen 2008] is presented.

The aerodynamic roughness function is presented in Figure 2.6. In Figure 2.6(a) z_{om} corresponds to a normalized value, relative to the traditional 0.2 mm value as used in WAsP program [Lange and Højstrup 2002]. Johnson, Taylor, Lange and Nordeng methods correspond to [Johnson *et al*. 1998], [Taylor and Yelland 2001], [Lange and Højstrup 2000] and [Saint-Drenan 2009] methods, respectively. They are taken as reliable references.

Then, minimal and maximal values for z_{om} function are chosen. It allows drawing Figure 2.6(b) in order to synthetize the effect of the height over sea on the terms of dimensionless Z_ψ factor in (2.3). While Figure 2.6(c) presents for two fetches and minimal and maximum z_{om} values, the wind profile based on logarithmic law, including atmospheric stability as used in this thesis.

As it is seen, the proposed z_{om} function calculated using $\bar{u}_{10}$ results closed to Johnson's function for both, 10 Km and 110 Km fetch. Note that Taylor's function for both fetches look for the base z_{om} value in a fetch independent way, as it really is.

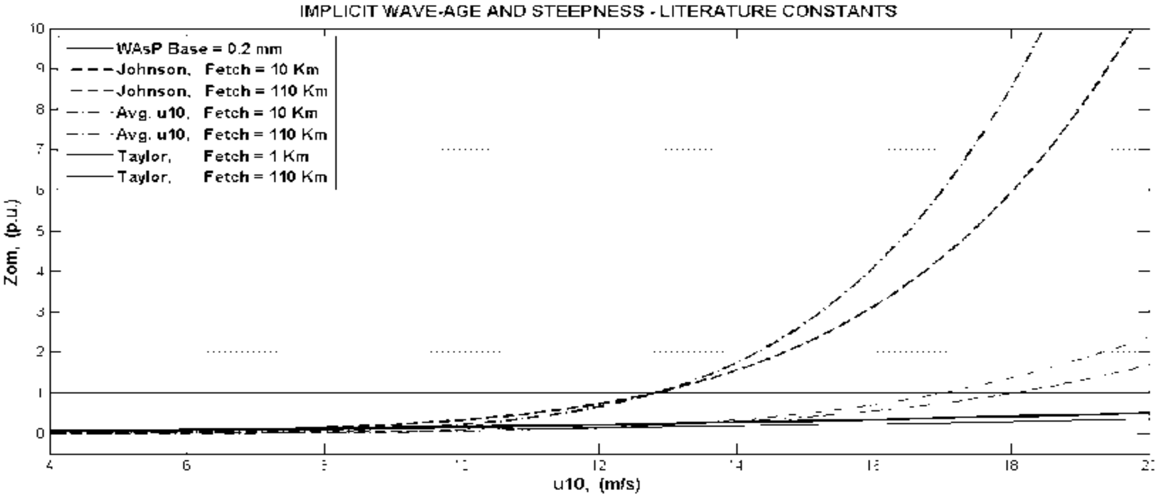

a)

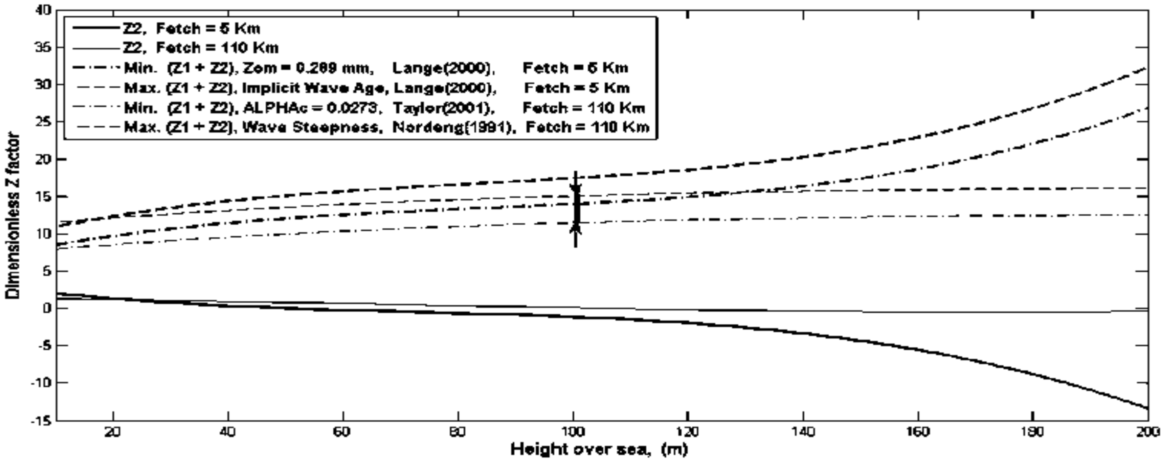

b)

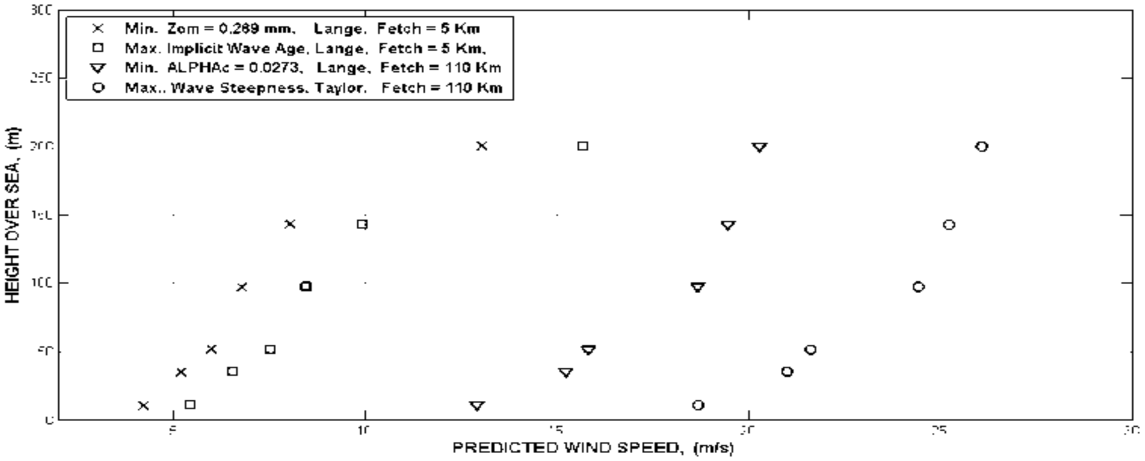

c)

Figure 2.6 Aerodynamic roughness length: a) Comparing the deviation of explicit and implicit z_{om} functions versus u_{10} using Literature constants with a z_{om} base = 0.2 mm., which represents the 1.0 p.u. value b) Wind Shear dimensionless Z factor behaviour including atmospheric stability effects, for a fetch varying between 5 and 110 Km, and c) Wind profile made with explicit and implicit fetch dependent aerodynamic roughness length functions.

As the fetch increases, all roughness functions including the by this thesis proposed, appear more closed to the Taylor's function. Results based on Figure 2.6 remarks that:

- The proposed formulation based on $\bar{u}_{10}$ to estimate the aerodynamic sea roughness length is coherent and mathematically consistent with those made from standard wave-age and wave-steepness methods, which are based on friction velocity u_{o*}, as observed in Figure 2.6(a).
- Given the computation for the Z_2 term, Figure 2.6(b) shows that, the primary effect of the aerodynamic roughness length function z_{om} on the wind profile is through the Z_1 term and the z/L based atmospheric stability Z_2 term. For small heights, the $Z_1 + Z_2$ characteristic trend to be almost fetch independent. As the height increases, there is a deviation of the characteristics at a height less than 80 m, and for a small fetch of the order of 5 Km. From there and after, this deviation is dominated by the Z_2 term effect. Although the first wind turbine would be usually found at a distance greater than 10 Km from the shore, the 5 Km fetch here selected was in order to emphasize this Z_2 effect. The Z_3 term results negligible.
- Something to highlight and graphically emphasized is the $Z_1 + Z_2$ characteristic for large fetches. It results practically constant, and comparing Taylor and Nordeng's

computational methods, it results of the order of an average value close to around 15.0. Between both methods, there is practically a constant difference of the order of 4.0. It seems to suggest that as the wind turbine size increases with mast height and blade length, the wind speed might be computed using a $Z_1 + Z_2$ constant value. It is in a range between $12.5 < Z_\psi < 16$.

- As a consequence of the Z_2 effect, in Figure 2.6(c), there is also a deviation of the wind profile at around 150 m height, and only observable for small fetches. This result is consistent with previous reported research, using constant z_{om} values in [Large and Pound 1981], [Taylor and Yelland 2001], [Peña and Gryning 2008]. Furthermore, in Figure 2.6(c), as the fetch increases the predicted wind speed also increases and the deviation at around 150 m height has practically disappeared. In this case, satellite observations as in [Hasager *et al*. 2008], allow building a logical mean wind speed u_{10} as fetch dependent, fitted as an exponential or linear formula. Although Hasager's report was made for the Baltic sea, it is used here as an engineering guide. Regional or local observations will give the real conditions.

To answer the question *how is the behaviour of the clearance distance between blade and tower if, RSTA, pre-bent angles and mechanical blade loading effects are included?*, some computational results are presented in Figure 2.7. For rigid 44 m. blade length they are in Figures 2.7(a) and 2.7(d).. The constant response (dashed gray line) in Figure 2.7(a) represents the clearance distance response x_b from the 44 m blade length, flying without any effect. Similar response is observed in Figure 2.7(b) from the flexible 54.6 m blade length.

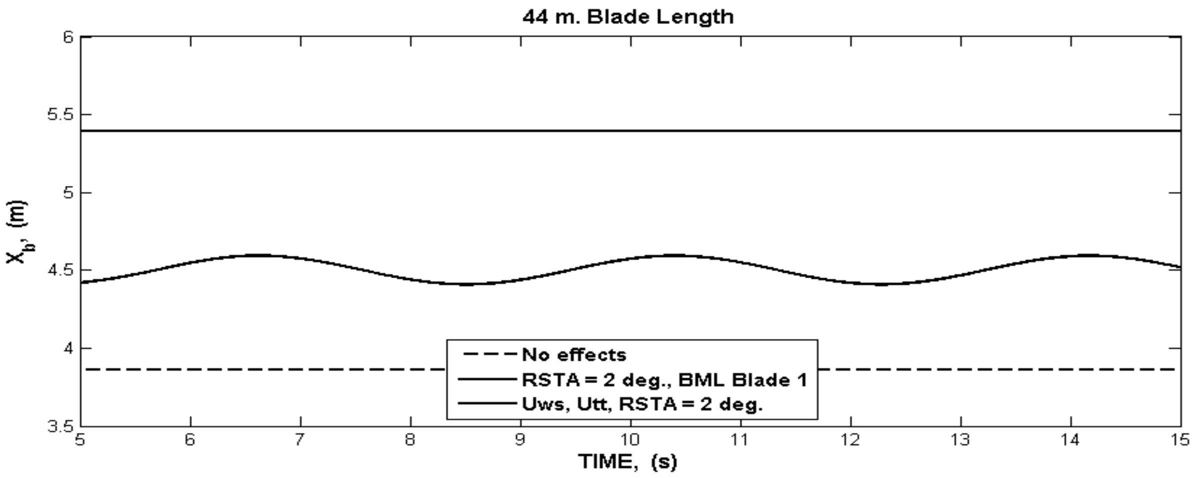

a)

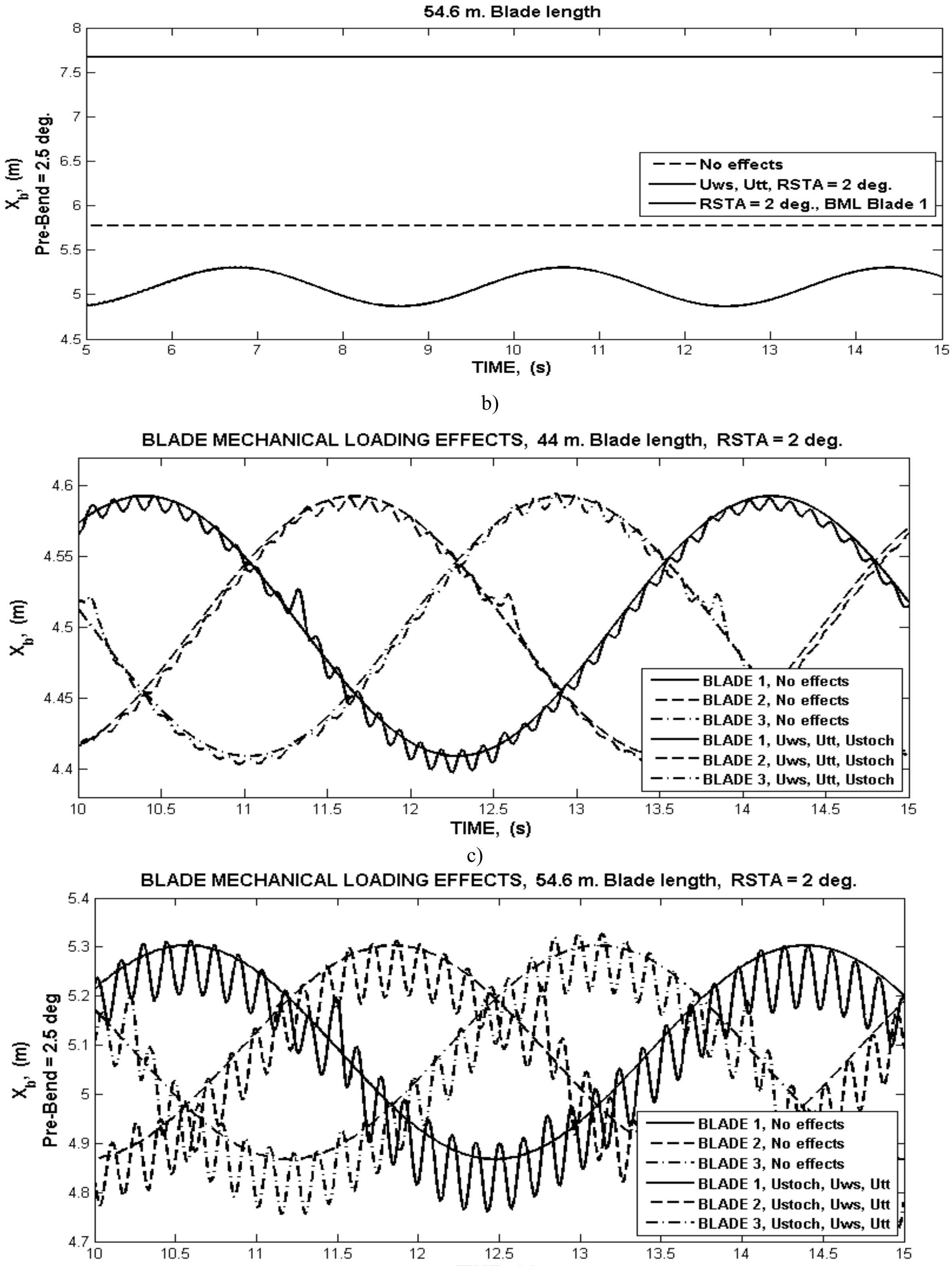

b)

c)

d)

Figure 2.7 Behaviour of the clearance distance x_b, for two different blades a) and c) responses without the BML effect, b) and d) responses with the BML effect.

If in this condition RSTA increases, despite wind shear and tower transfer effects, the clearance distance response x_b also increases and remains constant (continuous gray line).

But if BML is included, the clearance distance oscillates (black line). It appears closer to the tower if pre-bend characteristics are present, other words, if the blade is more flexible. The sinusoidal oscillation is mostly due to gravitational loading and the wind shear. This oscillation has of the order of 20 cm peak to peak, when the blade has 44 m in Figure 2.7(d) and approximately 40 cm when the blade has 54.6 m in Figure 2.7(e). The whole BML effect with the addition of the inertial and dynamic loads is better seen for the three blades in Figure 2.7 (d) for 44 m and in Figure 2.7(e) for 54.6 m, blade lengths. They are shown for a smaller time window in order to highlight the waving characteristics in *z* axis, representing a moveable blade-tip and the effect of the stochastic wind component. This effect deviates slightly out the waving axis around the sinusoidal waveform. There is a kind of feedback due to the tower transference effect over the x_b distance. It is noted as a sudden waving increase moving the blade away from the tower, and present for both blade lengths. As the blade length and flexibility increases, this waving increment is more noticeable. Therefore, when the blade-tip passes in front of the tower and BML is considered, the clearance distance x_b, as producing the tower transference phenomenon, receives also a feedback effect of it. This feedback is of the order of 3cm in rigid 44 m blade and 18 cm in flexible 54.6 m, blade lengths.

The effect of the *per-blade equivalent wind speed* is explored in Figures 2.8(a) to 2.8(f), for both, hub-height responses and those at 75 % of the blade 1, as measured from the blade-root.

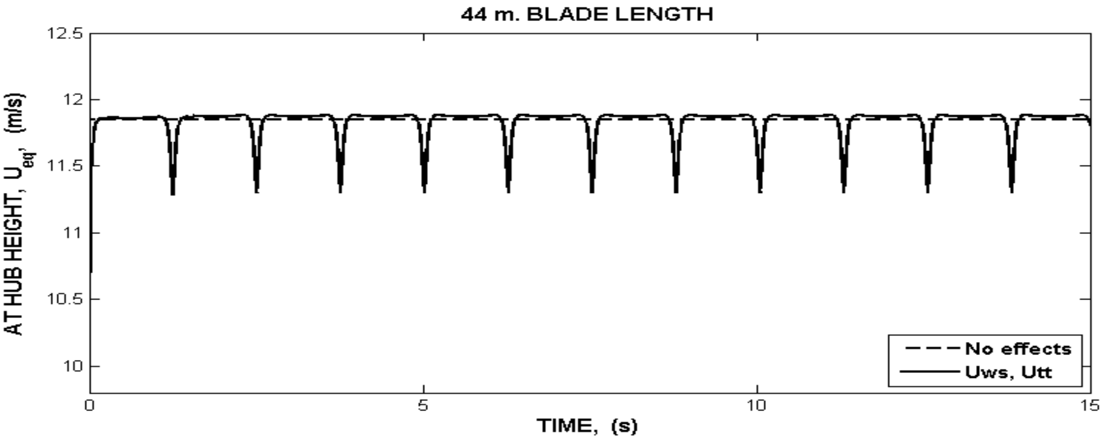

a)

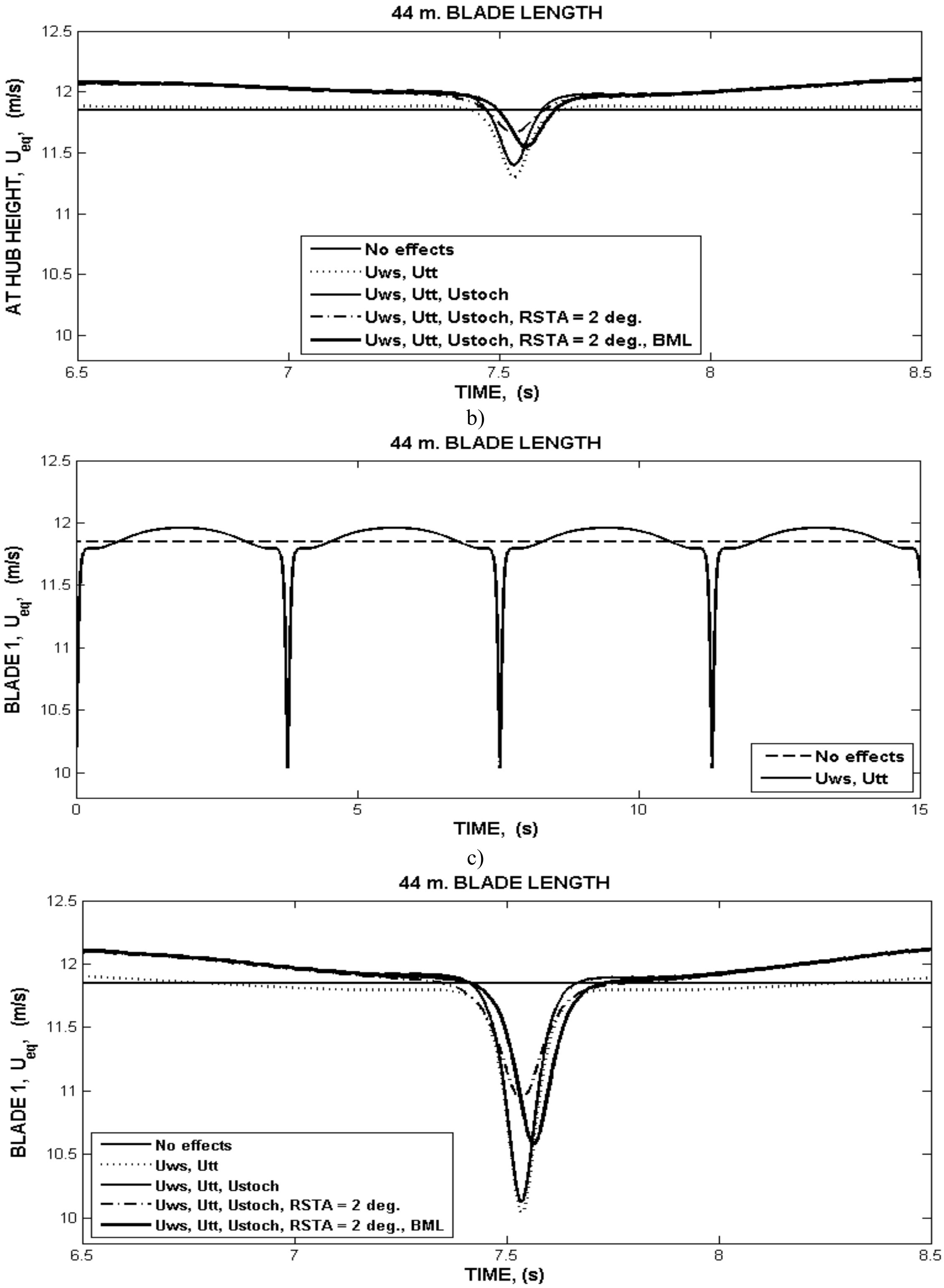

b)

c)

d)

Figure 2.8 Per-blade equivalent wind speed, for 44 m blade length: a) combined at hub height with the effect of u_{ws} and u_{tt}, b) zoom of the combination at hub height of one u_{tt} pulse at around 7.5 s, adding the effects of stochastic component, RSTA and BML, c) assessed at 75 % of the blade 1 including u_{ws} and u_{tt}, and d) zoom of one u_{tt} pulse at around 7.5 s. with the effects of stochastic component, RSTA and BML, and assessed at 75 % of the blade 1

The 11.85 m/s constant response (gray line) in all Figures corresponds to the wind without effects as computed using the logarithmic law including atmospheric stability. A one by one comparison makes evident that:

i) Response in Figure 2.8(a), combining the per-blade responses at the hub height, matches the response in [Carvalho 2003], and thus, the added effects in Figure 2.8(b), improves it. The u_{tt} pulses produced (~ 0.4 m/s) are of the order of 28 % of those in the case of its evaluation at 75 % of the blade length in Figures 2.8(c) and 2.8(d). Between pulses there is an almost plane response given by the wind shear effect. The effects of stochastic component trends to decrease the w_{tt} pulse, and RSTA decreases it even more. While the BML effect is counteracting them and to delay the wind speed response.

ii) At the per-blade responses in Figures 2.8(c) and 2.8(d), the u_{tt} pulses produced (~ 2 m/s), looks significantly larger than the evaluated at the hub-height.

iii) The frequency associated to hub-based w_{tt} pulses in Figure 2.8(a) is three times the frequency associated to blade based u_{tt} pulses in Figure 2.8(c). It means that as expected, pulses due to each blade at the hub height are seen three times each rotor lap, while inherent to the specific blade, they are seen only one time each rotor lap.

From the observations above, the hub-based wind speed responses hide very significant mechanical dynamics.

For a rotor with 54.6 m pre-bent blades, the wind speed results are presented at Figures 2.9 (a) to 2.9(d). For comparison purposes, the *u10* wind speed is modified, in order to match this new blade with the 2 MW induction generator.

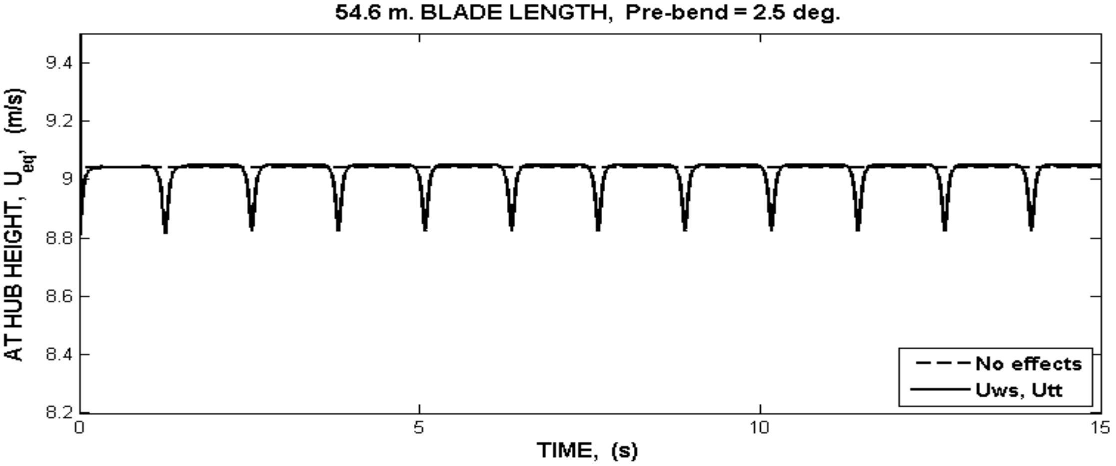

a)

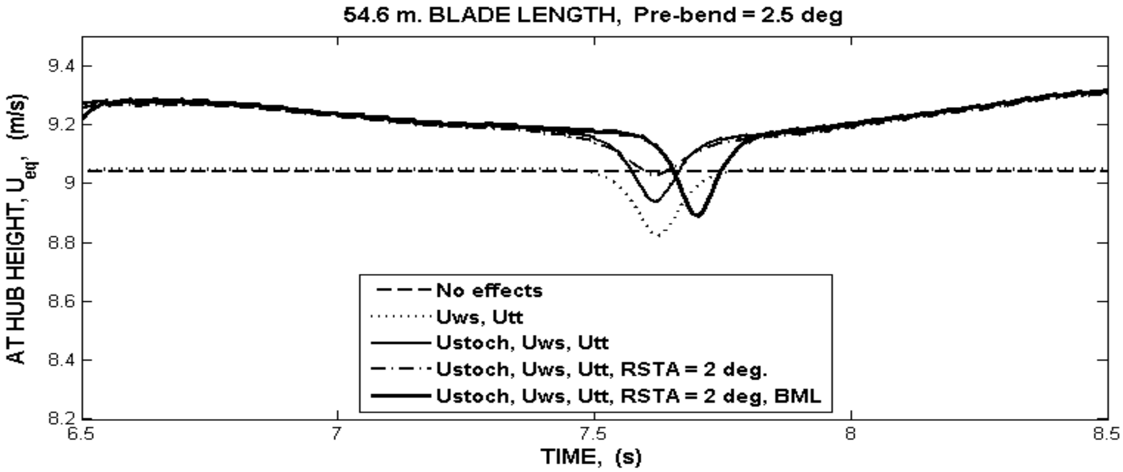

b)

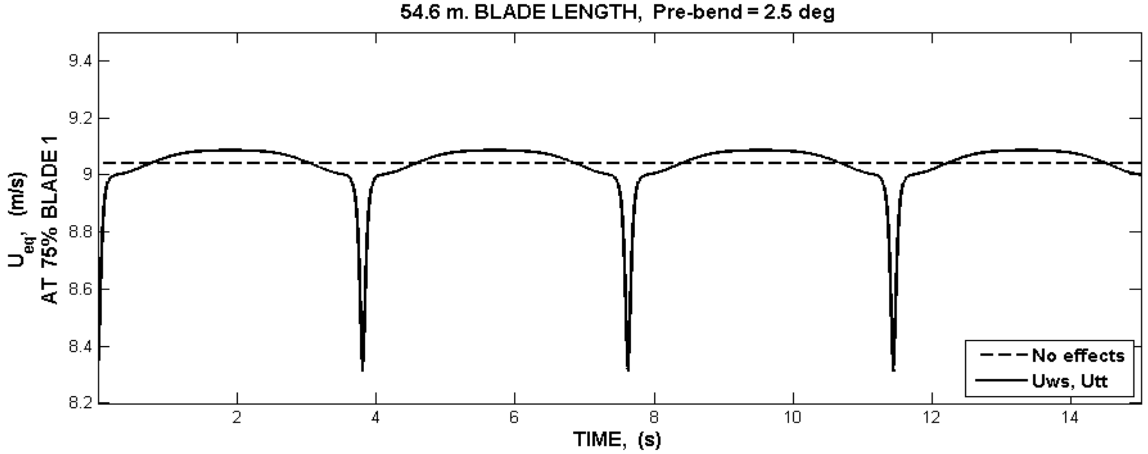

c)

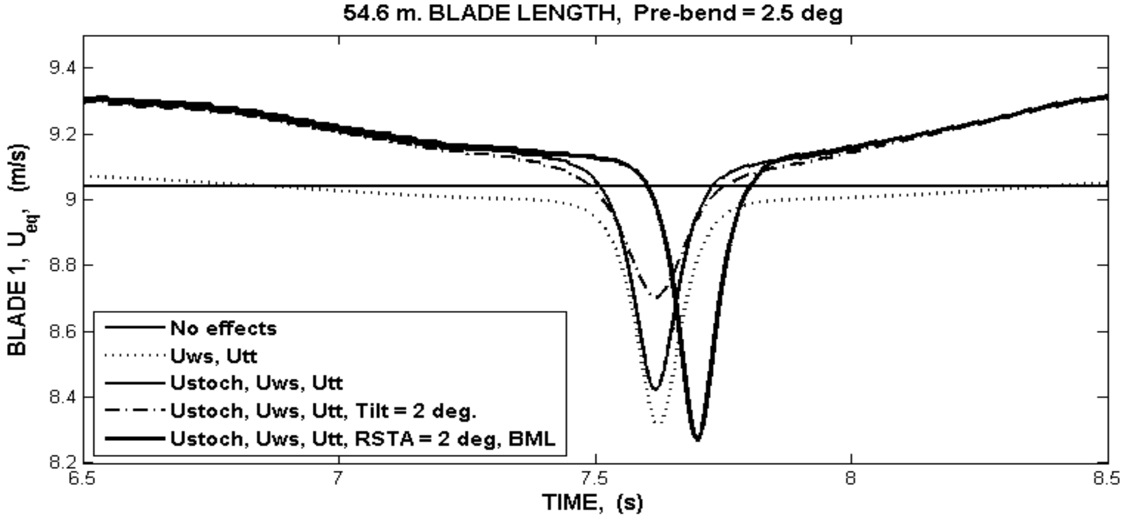

d)

Figure 2.9 Per-blade equivalent wind speed, for 54.6 m blade length: a) combined at hub height with the effect of u_{ws} and u_{tt}, b) zoom of the combination at hub height of one u_{tt} pulse at around 7.5 s, adding the effects of stochastic component, RSTA and BML, c) assessed at 75 % of the blade 1 including u_{ws} and u_{tt}, and d) zoom of one u_{tt} pulse at around 7.5 s. with the effects of stochastic component, RSTA and BML, and assessed at 75 % of the blade 1

The wind speed responses are relatively analogue to those obtained from the rigid blade with 44 m length.

The wind speed reference for the response with any effect, as a blade combination at the hub height, is now 9.05 m/s. It changes due to the technical compromise of the new wind turbine rotor with flexible 54.6 m blades and the retained 2 MW induction generator.

The hub height combined response in Figure 2.9(a) and 2.9(b) presents now u_{tt} pulses of the order of 0.2 m/s. They are the 50 % of those when the rigid blade has 44 m, and of the order of 55 % of those in the case of its evaluation at 75 % of the blade length in Figures 2.9(c) and 2.9(d). The wind shear effect is also analogue by comparing Figures 2.8(c) and 2.9(c), producing with both blades a no-symmetric sinusoidal type waveform. The effects of the stochastic component of the wind speed and RSTA operate in the same direction of those on the rigid 44 m blade length.

However the BML increases now the per-blade evaluated wind speed pulse response, as shown in Figure 2.9(d). It is assumed as the direct consequence of the increment in the blade mechanical flexibility. Note that it is not observed at the hub height combined response in Figure 2.9(b). It is concluded that, as the blade length and its flexibility increases, the BML effect turns to be determinant, more than other effects, because the waving of the blade-tip makes it passes closer to the tower, even if the RSTA is different of zero.

2.5 Conclusion

In this Chapter a *per-blade equivalent wind speed* model is constructed. Instead of the friction velocity, an averaged mean wind speed at 10 m height, as seed wind speed, is proposed. This engineering concept is consistent with local measures even into the ocean, and then a sea aerodynamic roughness length function, as additionally fetch dependent, is constructed for the computation of wind shear effect including atmospheric stability.

The sea aerodynamic roughness length function, as $\bar{u}_{10}$ dependent, appears consistent with previous reported results based on friction velocity. It makes the proposed $\bar{u}_{10}$ concept, very promising for wind power planning purposes. The wind shear effect is now a more reliable model, which integrates the dependencies on $\bar{u}_{10}$, fetch and atmospheric stability. It consistently reproduces wind profiles, as obtained from meteorological studies.

The clearance distance, for tower transference effect computation, results no constant anymore, and highly influenced by the blade mechanical loading, which produces blade-tip oscillation. These are more noticeable as the blade flexibility increases.

In addition, both wind shear and tower transference are influenced by blade angle deformation and deflections coming from the blade mechanical loading.

The analysis demonstrates that the wind speed at each blade presents larger magnitude than the rotor wind speed, independent of the blade length. As expected, if the RSTA increases, the clearance distance will increase, and then, the tower transference pulse decreases. The BML effects delay the tower transference pulse. These results are in agreement with previously reported ones. In this way a robust deterministic per-blade wind speed model is proposed.

* * *

THIS PAGE IS INTENTIONALLY LEFT BLANK

3

Two-mass Drive-Train Model Based on Large Blade Mechanical Properties

3.1 Introduction

Without doubt, the standard 2-mass drive-train model (S2m) has gained to date a satisfactory technological position, to represent wind turbine rotors with rigid blades. The model establishes the wind turbine drive-train representation, based on two masses: the wind turbine rotor mass and the generator mass, to highlight the relevant masses. Its credit is instituted since the year 2003 [Akhmatov 2003], and: i) it sinks its reliability in the registered induction generator rotor oscillation, as reported in a wind farm islanding experiment in the year 2000 and described in [Pedersen *et al*. 2000] and [Pedersen *et al*. 2003]. The period of that oscillation determine the low-speed shaft mode frequency, as seen from the electrical generator rotor side, and allows computing a corresponding typical value of the low-speed shaft mechanical stiffness, ii) it uses manufacturer information for the two equivalent inertia constants. Actually, this information originally applied to a wind turbine with 44 m rigid blade length, is usually reported as a range of typical data [Ackermann 2005].

When trying to generalize the S2m model to include large blades, it is expected that as the blade length increases its moment of inertia increases too, and then, the three-blades moment of inertia increments the respective moment of inertia of the whole wind turbine. If this new wind turbine value is delivered by the manufacturer as a blade length function, the problem is solved. If not, a guess should be done, which is not a reliable practice.

To be consistent with the blade technology advances, this research proposes the construction of an innovative blade based 2-mass (BB2m) drive-train model, to include blade mechanical properties, as its length, mass density and pre-bending features. Carefully segmenting the blade length in blade-body segments, the beam theory can be applied. The one-blade moment of inertia results referred to the rotor axis, and by extension, the whole wind turbine including hub and low-speed shaft, moments of inertia, can also be computed. Additionally, time-varying blade angle deformation and deflection due to the blade mechanical loading (BML) effect can be added, and as a consequence, the wind turbine moment of inertia and also the low-speed shaft stiffness, result also time-varying. The BB2m model is able to include flexible and rigid blades, and also hub and gear box moments of inertia. All these features make the BB2m a more robust drive-train model.

3.2 Standard Two-mass (S2m) Model

In [Akhmatov 2003] a physically based 2-mass drive-train model to represent the wind turbine drive-train was proposed. A schematic interpretation is presented in Figure 3.1, where a body with non-canonical regular form and assumed uniformly distributed mass m_1, configures the wind turbine rotor.

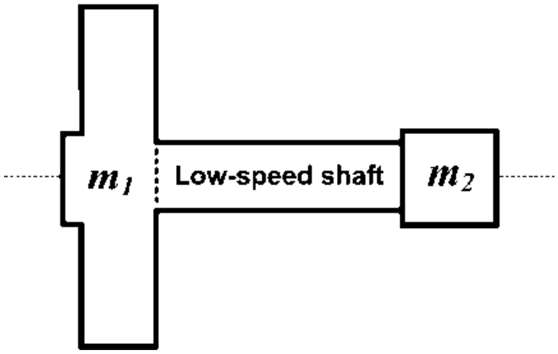

Figure 3.1. Reduced scheme of a standard 2-mass model

It rotates with a low wind turbine rotor speed in a range between 14 and 20 revolutions per minute (rpm) [VESTAS wind systems 2013]. The main components are three identical blade masses, the hub mass where blades are connected, the break wheel and the low-speed shaft. These six bodies constitute one single rotatory rigid mass, which total static moment of inertia J_{m1} is given by the manufacturer. Blades make the larger mass contribution and the low-speed shaft mass is intuitively integrated.

The other assumed uniformly distributed mass m_2 in Figure 3.1 rotates at several tens of times the wind turbine rotor speed, and its components are the gear-box, the high-speed shaft and the electrical generator rotor. For an induction generator, standard rotational speeds are between 1500 and 3000 rpm for 2 and 4 pole pairs and 50 or 60 Hz, respectively. Its respective static moment of inertia J_{m2} is smaller than J_{m1}. Given the speed ranges for the masses m_1 and m_2, the expected speed ratio in the gear-box is large. As an engineering practice, it is also usual that in J_{m2}, both the gear-box (GB) and the high-speed shaft masses are neglected.

Typical J data like the found in [Ackermann 2005], where J_{m1} is into a range between 2 y 6 p.u and J_{m2} between 0.4 y 0.8 p.u., demonstrates that J_{m2} is always very small as compared to J_{m1}. This characteristic together to small low-speed shaft stiffness, configure a very soft two-mass turbine-generator system, as compared to conventional power plants [Hinrichsen and Nolan 1982]. Figure 3.2 is a sketch of a mass network for a S2m model, where the masses are specified to produce J_{wt} representing J_{m1}, and J_g representing J_{m2}.

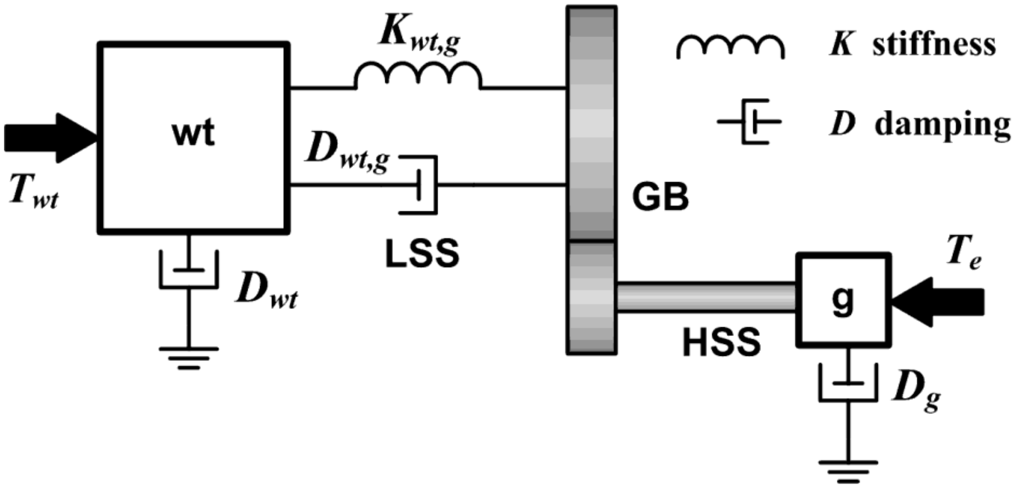

Figure 3.2 Mass network of a standard 2-mass drive-train model

According to Figure 3.2 and taking into account [Rao 2006], [Akhmatov 2003], , a S2m model formulation referred to the low-speed shaft is,

$$\begin{aligned}
&p\omega'_g = [D_{wt,g}(\omega_{wt} - \omega'_g) + K_{wt,g}(\theta_{wt} - \theta'_g) + T_e - D'_g\omega_g]/(J_{GB} + J'_g) \\
&p\omega_{wt} = [D_{wt,g}(\omega_g - \omega_{wt}) + K_{wt,g}(\theta_g - \theta_{wt}) - T_{wt} - D_{wt}\omega_{wt}]/J_{wt} \\
&p\theta_g = w_g \\
&p\theta_{wt} = \omega_{wt}
\end{aligned} \tag{3.1}$$

where ω_i and θ_i are the rotational speed and twist angle at the mass '*i*' respectively. Mechanical wind turbine torque T_{wt} and electromagnetic torque T_e are the input mechanical sources. Symbol (') takes into account the gear-box effect to see mechanical variables at the low-speed side. The low-speed shaft stiffness $K_{wt,g}$, is based on the shaft torsional mode, as extracted from a wind farm islanding experiment [Pedersen *et al*. 2000], [Pedersen *et al*. 2003], at Rejsby Hede wind farm, with 40x600 kW squirrel-cage induction generator and fixed-speed wind turbines. Using information from this experiment, the low-speed shaft stiffness $K_{wt,g}$ parameter is reported to be 0.3 p.u. for a 2 MW wind turbine [Akhmatov 2003]. This value was used to analyse voltage stability in a 80x2 MW Hørns-Rev wind farm, with double-fed induction generator and variable-speed wind turbines, according to [Wesstlake *et al*. 1996]. The wind turbine blade in this case had 44 m length.

3.3 Proposed Blade Based Two-mass (BB2m) Model

From the above Section two aspects deserve to be highlighted: i) Since the masses m_1 and m_2 are manufactured related, the S2m model focuses its attention on the low-speed shaft, ii) The mechanical properties of both m_1 and m_2 mass components are neglected. This affirmation is particularly meaningful when the large blade technology is considered. As a fact, it is known to be continuously increasing, as the power of wind energy conversion systems increase.

Given these technology matters, the model here proposed focuses on mass m_1 to include blade length, mass density and BML. It is assumed that there is a historical technological limit, below which a wind turbine blade presents much more rigid mechanical structure than above it. In this last case the technology progressively goes to higher structural flexibility, involving different materials for blade transversal and longitudinal structure [Chortis 2012]. The corresponding BB2m mathematical model is similar to (3.1), but new turbine moment of inertia J_{*wt} and low-speed shaft stiffness $K_{*wt,g}$ parameters are going to appear as,

$$J_{*wt} = f(B_l, m, J_h, J_{LSs}, \delta_y(t), \delta_z(t)) \tag{3.2}$$

$$K_{*wt,g} = f(f_{ff}, J_{*wt}) \tag{3.3}$$

where, B_l is the blade length, m is the blade mass density, J_h is the hub moment of inertia, J_{LSs} is the low-speed shaft moment of inertia, $\delta(t)$ is the time-varying blade deflection as due to BML at axis y and z respectively, and f_{ff} is the free-free rotor oscillation frequency. Since the configuration of mass m_2 is out of this study subject, it is assumed given by the manufacturer, as in the S2m model. In this research the blade mechanical properties are referred to a baseline 5 MW wind turbine with 61.5 m blade length [Jonkman *et al*. 2009]. Therefore, neither J_{wt} nor $K_{wt,g}$ are not going to be input values anymore.

3.3.1 Blade Mass Density Function

This longitudinally distributed blade mechanical property in kg/m, inherently involves the blade structural mechanics along the blade. In [Jonkman *et al*. 2009] blade mass density is measured at each blade-body section, and the corresponding blade length 61.5 m is taken as the reference length in this research. The data list is synthetized as a Gaussian function [Guo 2011] using the `cftool` command in Matlab, resulting,

$$m = \sum_{k=1}^{8} a_k \exp\left(-\frac{l - b_k}{c_k}\right)^2 \tag{3.4}$$

where l represents the length of the blade-body segment in pu values. The fitting parameters a, b and c are given in Table 3.1 for $k = 1,\ldots,8$.

Table 3.1 Parameters associated to the Mass Density Function (Kg/m)

k	1	2	3	4	5	6	7	8
a_k	546.0	128.1	10.01	42.25	98.34	0.0	336.0	31.29
b_k	0.005768	0.05562	0.1646	0.1079	0.1726	10.23	0.2765	0.8245
c_k	0.06991	0.01659	0.005838	0.01467	0.05142	0.00166	0.4607	0.1456

This function is drawn in Figure 3.3, where the blade length is in pu values, thus enabling the results to be suitably used with larger or shorter blades, assuming similar mechanical properties. For the BB2m modelling purposes, it is not crucial the unmatched points at the blade-tip.

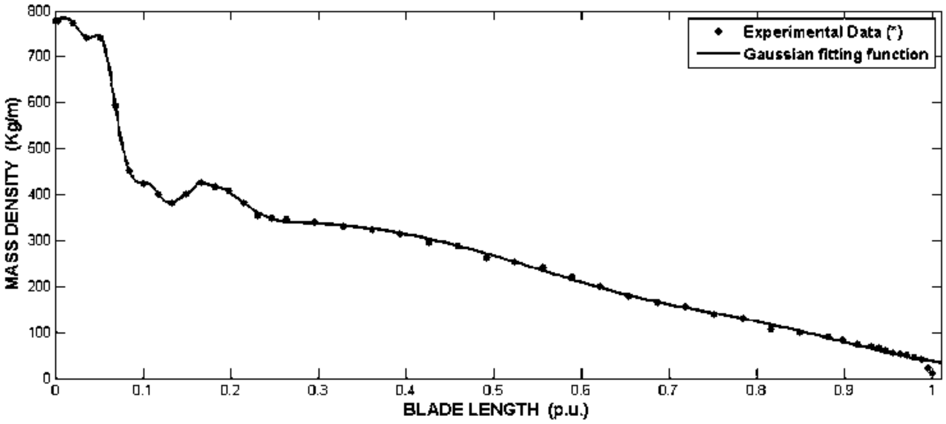

Figure 3.3 Mass density function. Experimental data (*) corresponds to [Jonkman *et al.* 2009]

3.3.2 One-Blade Moment of Inertia

The one blade moment of inertia J_b is computed by segmenting the blade in as many as necessary blade-body segments. As shown in Figure 3.4, the point P_{pb} where the pre-bending characteristic starts, defines two zones. The zone 1 is measured from the blade-root to P_{pb} and it corresponds to a straightforward length, where all the blade segments are lined-up. The zone 2 from the P_{pb} point to the blade-tip involves the pre-bent length, with blade segments not lined-up with the blade axis and progressively moving way from it, as detailed in Figure 3.4(b). At the blade tip, the point B moves to the point A producing an angle γ with the blade axis.

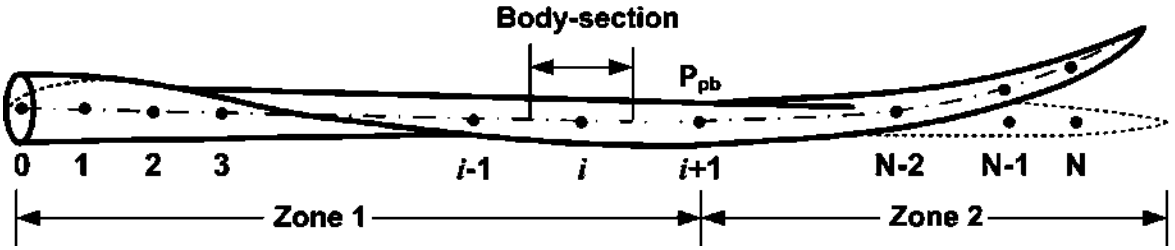

Figure 3.4 Blade segmentation in N blade-body parts, as numbered from the blade-root to the blade-tip.

In zone 2, as shown in Figure 3.5, any blade-body segment is displaced from the blade axis. That displacement results from combining geometry and blade mechanical loading effects.

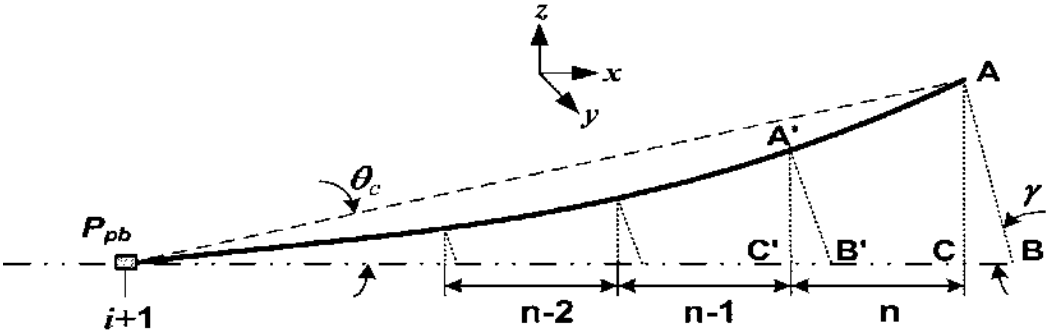

Figure 3.5 Schematic description of the blade pre-bend zone

The distance AC in Figure 3.5 corresponds to the blade-tip displacement from the blade axis and due to the pre-cone angle θ_c. For a spatial displacement due to BML and over the blade framework, axis y is assumed positive in the same direction the blade moves, axis z is assumed positive going out of the disk area and in opposition to the upstream wind, and axis x is along the blade from the blade root to the blade-tip. In the wind model of Chapter 2, the blade mechanical loading function allows the determination of time-varying blade deflections $\delta_y(t)$ and $\delta_z(t)$ at any blade-body section. It involves changes due to the wind speed, rotational speed and sudden acceleration. Thus, the original position of the triangle ABC in the z-x plane, as seen in Figure 3.5, is displaced back by $\delta_y(t)$ and then up by $\delta_z(t)$.

Note that moving the observation in Figure 3.4(b) at the end of any body-section (n-1, n-2,…), the rectangle triangles A'B'C', A"B"C",… result similar to the rectangle triangle ABC. The distance AC also progressively decreases from the blade-tip to the P_{pb} point, configuring a bend, whose characteristic is expected to be obtained from physical measurements. In this research and related to Figure 3.4, under the absence of physical information, a cubic polynomial curve fitting assumed blade-bending distances AC, A'C', A"C",…, is given by,

$$z = -0.34x^3 + 1.23x^2 + 0.1125x - 0.0034 \tag{3.5}$$

where, z represents fractional distances of the AC type in the position of the blade-body sections from n to i+1, and x represents the fractional distances from the segment i+1 to the position of the corresponding actual blade-body segment. Taking into account the BML effects, a more realistic Z displacement of the AC type at any body-section, can be assessed as,

$$Z_{AC}(t) = z + \delta_z(t) \tag{3.6}$$

the combined displacement at any body-section relative to the blade axis results to be,

$$Z_{BD_1}(t) = \sqrt{[z + \delta_z(t)]^2 + \delta_y^2(t)} \tag{3.7}$$

Taking account these statements and changing the point of view according to the beam theory [Beer and Johnson 2009], the one blade moment of inertia J_b as seen at the blade root can be computed as,

$$J_b = \sum_{k=n}^{i+1} m_k x_k^2 + \sum_{k=i}^{1} m_k x_k^2 \tag{3.8}$$

where the first term at the right of the (3.8) takes into account the contributions of the blade segments in zone 2 and the second, the contributions of those in zone 1. The x_k value is measured from the blade-root to the blade segment. In zone 1, x_k is a straightforward parameter because the blade-body sections are lined-up, but in zone 2 it is a spatial combination. Something to highlight about (3.8), is its blade positional dependence according to (3.6) and (3.7), which produces a no constant value.

3.3.3 Three-Blades Moment of Inertia

For a symmetrical location of the P_{pb} point at each blade, the three-blades moment of inertia J_{3b} is equal to three times the one blade moment J_b. The mechanical fatigue along a period of time, may displace this P_{pb} point. Then, in order to take into account this fact, it is proposed to evaluate (3.8) for each blade, resulting in an appropriate model for asymmetrical conditions. Thus, it is proposed,

$$J_{3b} = \sum_{b=1}^{3} J_b \tag{3.9}$$

which due to BML and in agreement with (3.6) and (3.7) results to be blade positional dependent.

3.3.4 Hub Moment of Inertia

Concerning to private manufacturers information are the hub and low-speed shaft moments of inertia. Because they are not usually published, some researchers assume the hub moment of inertia J_h, as a value of the order of e.g. 11 % of the wind turbine rotor J_{3b}, for 3 MW wind turbine [Salman and Teo 2002], [Li and Chen 2008]. In the absence of further information, it is assumed that J_h should be slightly below that percent value for 2 MW, and for large blades, it is expected to increase, as the blade-root diameter increases. In this way assuming k_h as a pu value, it can be written as,

$$J_h = k_h J_{3b} \tag{3.10}$$

3.3.5 Wind Turbine Moment of Inertia

Taking into account (3.9), the wind turbine moment of inertia J_{wt} for the combined mechanical structure of three-blades, hub and low-speed shaft masses results to be,

$$J_{wt} = (1 + k_h)\sum_{i=1}^{3} J_{bi} \tag{3.11}$$

or if J_h is based in J_{wt} instead on J_{3b},

$$J_{wt} = \frac{1}{1 - k_h}\sum_{i=1}^{3} J_{b_i} \tag{3.12}$$

which is also blade positional dependent in agreement to (3.6) and (3.7), if blade mechanical loading effect is involved. According to (3.2), (3.11) or (3.12) corresponds to J_{*wt}.

3.3.6 Low-Speed Shaft Stiffness

In [Akhmatov 2003] and based on (3.1), a low-speed shaft torsional stiffness $K_{wt,g}$ model is proposed. This model is based on a wind farm islanding experiment reported in [Pedersen *et al.* 2000], [Pedersen *et al.* 2003], for the Rejsby Hede wind farm (Denmark), with 40x600 kW squirrel-cage induction generator and fixed-speed wind turbines, 10 m/s wind speed and 80% of reactive power compensation. It was tripped from the network during around 1 second. What the S2m model concerns in that experiment, the frequency oscillation at the wind turbine side was registered before it collapses. This frequency oscillation was adapted to a generator rotor oscillation, and it was computationally synthetized [Pedersen *et al.* 2003]. In [Akhmatov 2003], the period T of that oscillation was read to be 0.6 s, and interpreted to represent the shaft torsional mode frequency $f_{ff} = 1/T = 1.6667$ Hz, as seen from the generator rotor side. This concept was used to identify the low-speed shaft stiffness $K_{wt,g}$ [Akhmatov 2003], which results to be equal to 0.29088 p.u/el.rad, and reported equal to 0.3, as a typical value. To obtain this value the gear-box moment of inertia was neglected. Despite the original power in the experiment, it was also assumed for a 2 MW wind turbine [Akhmatov 2003] with three rigid blades with 44 m blade length, wind turbine inertia constant H_{wt} = 2.5 s. and generator inertia constant H_g = 0.5 s, as typical values from the manufacturer. For different operating conditions, other researchers i.e. [Muyeen *et al*. 2007], have found that f_{ff} is in the range,

$$1Hz < f_{ff} < 3Hz \tag{3.13}$$

Also in [Ackermann 2005] the $K_{wt,g}$ parameters are in the range between 0.35 and 0.7 pu, which are beyond the 0.3 pu proposal in [Akhmatov 2003].

However, a more careful reading in the frequency versus time reported in [Pedersen *et al*. 2000] allows identifying that T is closer to 0.5667 s than to 0.6 s. Although it seems insignificant, the period error is 5.6 % and it propagates to the mechanical variables in the simulation. A no less determinant consequence is the combination of this discussion with (3.11). It produces a time-varying $K_{wt,g}$(t) model, given by,

$$K_{wt,g}(t) = \frac{4\pi\left(1/T\right)^2}{f}\frac{H_{wt}(t)H_g}{H_{wt}(t)+H_g} \tag{3.14}$$

where f is the network frequency. These results are very important for comparison purposes between S2m and BB2m models.

Using the S2m model, the f_{ff} frequency is typically assumed in the absence of specific wind turbine/farm test or manufacturer information. Consequently, the wind turbine stress is a unique value along the simulation time. While with the BB2m model, the $K_{wt,g}$ parameter is computed and time dependent. Thus, any mechanical or electrical perturbation is going to produce different torsional response. According to (3.3), (3.14) corresponds to $K_{*wt,g}$.

3.4 Generator Rotor Frequency in the S2m model

A simulation is conducted to reproduce the original condition in [Akhmatov 2003] and to explore a methodology to use this S2m model to take into account the increase of blade length. To achieve it, the following steps are proposed:

i) Compute H_g value if unknown. In the present research, the generator rotor moment of inertia J_g value for the induction generator rotor is known and equal to 90 kg-m2. Unknowing the high-speed shaft moment of inertia $J_{HSshaft}$, it is assumed integrated to J_g. In order to add the gear-box effect, it is taken into account that gear-box inertia constant H_{GB} is reported to be equal to 0.0806 pu for a 350 kW wind turbine [Muyeen *et al*. 2007]. This value is around of 57 % of H_g. Expecting a no linear increase of the corresponding J_{GB} when the wind turbine size increases, it can be inferred that J_{GB} can be varied from 0 % to at least 60 % of J_g.

ii) Select an H_{wt} = 2.5 s to represent the whole wind turbine rotor including three blades, hub and low-speed shaft. The blade length in the S2m model is not part of the input data but it is only secondary information. Unknowing the relationship between blade length and the corresponding H_{wt} increment, this value is varied from 2 s. to 6 s [Ackermann 2005], in order to prevent larger than 44 m blade length,

iii) Instead of using the proposed $K_{wt,g}$ = 0.3 pu in [Akhmatov 2003], and taken into account the range in (3.13), the constant $K_{wt,g}$ value is estimated. It is explored using (3.14), as related to the influence of H_{GB} if this value is included in H_g and with T = 0.6 s. $K_{wt,g}$ is computed, as the H_{GB} increases, for several H_{wt} values. This tries to integrate in H_{wt}, the blade increase, being the only possible way in the S2m model. The results are presented in Table 3.2, where a specific column for H_{wt} = 2.5 is built in it and the row for H_{GB} = 0 is highlighted.

For comparison purposes, this methodology is reproduced in Table 3.3 for T = 0.5667 s, which is estimated to be a more exact value. In both Tables by convenience with (3.14), J values are converted to H values. In Table 3.2 the row corresponding to H_{GB}

= 0.0 appears highlighted in order to regard it corresponds to the condition in [Akhmatov 2003].

Tables 2 and 3, are the base for computational look-up tables. In this way they constitute a tool to identify the most convenient $K_{wt,g}$ parameter, to include both the effect of H_{GB} and the increment in H_{wt} due to blade increase, in the S2m model.

Table 3.2 $K_{wt,g}$ (pu/el.rad.) values for T =0.6 s

		H_{wt}(s)					
H_{GB}(%)	H_g(s)	2	2.5	3	4	5	6
0.0	**0.5552**	**0.3034**	**0.3172**	**0.3271**	**0.3403**	**0.3488**	**0.3548**
0.05	0.5554	0.3035	0.3173	0.3272	0.3405	0.3490	0.3549
0.1	0.5557	0.3036	0.3174	0.3273	0.3406	0.3492	0.3551
0.5	0.5579	0.3046	0.3184	0.3284	0.3418	0.3504	0.3564
1	0.5607	0.3057	0.3197	0.3298	0.3433	0.3520	0.3580
10	0.6107	0.3266	0.3426	0.3542	0.3699	0.3799	0.3870
20	0.6662	0.3489	0.3672	0.3806	0.3987	0.4104	0.4186
30	0.7217	0.3702	0.3910	0.4061	0.4268	0.4403	0.4498
40	0.7772	0.3908	0.4139	0.4310	0.4543	0.4696	0.4804
50	0.8327	0.4105	0.4361	0.4551	0.4812	0.4984	0.5105
60	0.8883	0.4294	0.4576	0.4785	0.5074	0.5266	0.5402

Table 3.3 $K_{wt,g}$ (pu/el.rad) values for T = 0.5667 s

		H_{wt}(s)					
H_{GB}(%)	H_g(s)	2	2.5	3	4	5	6
0.0	**0.5552**	**0.3401**	**0.3555**	**0.3666**	**0.3815**	**0.3910**	**0.3977**
0.05	0.5554	0.3402	0.3557	0.3668	0.3817	0.3912	0.3979
0.1	0.5557	03403	0.3558	0.3669	0.3818	0.3914	0.3980
0.5	0.5579	0.3414	0.3570	0.3682	0.3832	0.3928	0.3995
1	**0.5607**	**0.3427**	**0.3584**	**0.3697**	**0.3849**	**0.3946**	**0.4013**
10	**0.6107**	**0.3661**	**0.3841**	**0.3971**	**0.4146**	**0.4259**	**0.4338**
20	**0.6662**	**0.3911**	**0.4117**	**0.4266**	**0.4469**	**0.4601**	**0.4693**
30	**0.7217**	**0.4150**	**0.4383**	**0.4553**	**0.4785**	**0.4936**	**0.5042**
40	0.7772	0.4380	0.4640	0.4831	0.5093	0.5264	0.5385
50	0.8327	0.4601	0.4889	0.5101	0.5394	0.5587	0.5723
60	0.8883	0.4814	0.5129	0.5363	0.5688	0.5903	0.6055

In both tables it is observed that even when H_{GB} = 0.0, this is when gear-box effect is neglected, $K_{wt,g}$ values are greater than 0.3 pu. Also, as the H_{GB} increases $K_{wt,g}$ increases too, for any H_{wt} value. It deserves to be highlighted that this increase is non-linear.

Note that for a specific case in Table 3.2, if H_{wt} = 2.5 s and H_{GB} = 0.0, $K_{wt,g}$ results to be equal to 0.3172 pu. If this value is compared to the reference 0.3 value, it presents a deviation of 5.7 %. While the respective value in Table 3.3 present a deviation of 18.5 %. This is equivalent to say that if T in Table 3.3 deviates 5.6 % below the T value in Table 3.2, the resulting $K_{wt,g}$ value deviates 12.8 % above the reference value. The increment in $K_{wt,g}$ value is going to hide some torsional dynamics in the low-speed shaft, and consequently in the drive-train as a whole. This fact remarks the importance to use a very good engineering criterion for a specific wind turbine, in the selection of the K parameter, for the S2m model.

In Figure 3.6, the original conditions in [Akhmatov 2003], [Pedersen *et al*. 2000], [Pedersen *et al*. 2003] with $K_{wt,g}$ = 0.3, and H_{GB} = 0, are computationally reproduced. They are compared to the $K_{wt,g}$ values obtained using Tables 3.2 and 3.3. Figure 3.6(a) shows the generator rotor frequency responses comparison for these three values of $K_{wt,g}$, and Figure 3.6(b) presents a variation of J_{GB} from 0 to 30% of J_g. This change of parameter from H to J does not introduce any effect, and is conveniently made for this research. The 1-mass standard model response, is found to be of the type of an average response, and thus it is used in analogue way to the proposed in [Akhmatov 2003].

As it is observed in Figure 3.6(a), the effect to increase $K_{wt,g}$ put forward the corresponding response. Despite to start all responses together at 6 s, the resulting in advance feature, increases from the tripping instant, being larger at the second maximum. The worst case reproducing the period condition is when using the suggested typical value $K_{wt,g}$ = 0.3 pu/el.rad, with a period error equal to 2.67 %. Note that using $K_{wt,g}$ = 0.3172 from Table 3.2, the match is approximately perfect, with a very low period error of 0.33%. The successful case is when $K_{wt,g}$ = 0.3555 pu/el.rad, as computed in this work in Table 3, with a period error equal to zero. It evidences the well choice in this work for T = 0.5667 instead of T = 0.6. The frequency change between the end of the islanding time (7 s) and the tripping instant (6 s), as measured on the 1-mass model response, corresponds to 0.16 pu in the base of 50 Hz. As compared to 0.1 pu in [Akhmatov 2003], the frequency change error is of the order of 6 %. Figure 3.6(b) shows that leaving constant H_{wt} = 2.5 s and T = 0.5667 s in Table 3.3, when H_{GB} increases from 0 to 30 % of H_g, a progressive decrease of the oscillation amplitude is produced, followed by a shorter T.

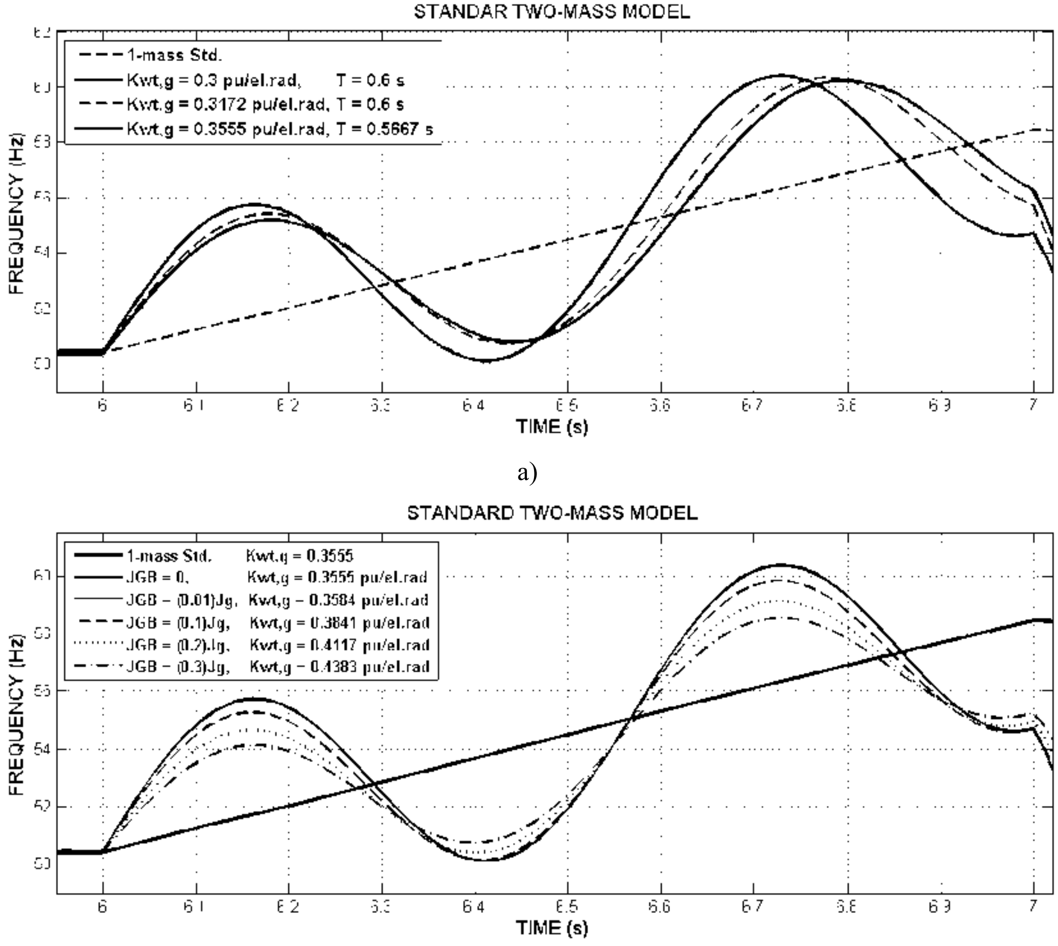

a)

b)

Figure 3.6 Induction generator rotor frequency response for a wind turbine with 44 m blade length through the S2m model: a) when H_{GB} = 0.0, H_g = 90 kg-m^2, H_{wt} = 2.5 s., $K_{wt,g}$ as in Table 3.2, and b) for several values of J_{GB}: 0, 1, 10, 20 and 30 % of J_g

It appears to demonstrate that if pairs J_{GB}, $K_{wt,g}$ are consequent to T, when J_{GB} increases the oscillation amplitude decreases, and it evolves to be virtually closer to the one-mass response. It is expected that, the consequent effects on the wind turbine dynamics, also evolves in the same direction.

In Figure 3.7, J_{GB} is left constant and $K_{wt,g}$ is chosen according to the corresponding values in Table 3.3. In this condition the H_{wt} value is varied, trying to simulate an arbitrary blade length increase, which necessarily should be reflected in H_{wt}. This is done due to the fact that in the S2m model there is no another option to directly include the blade length increase.

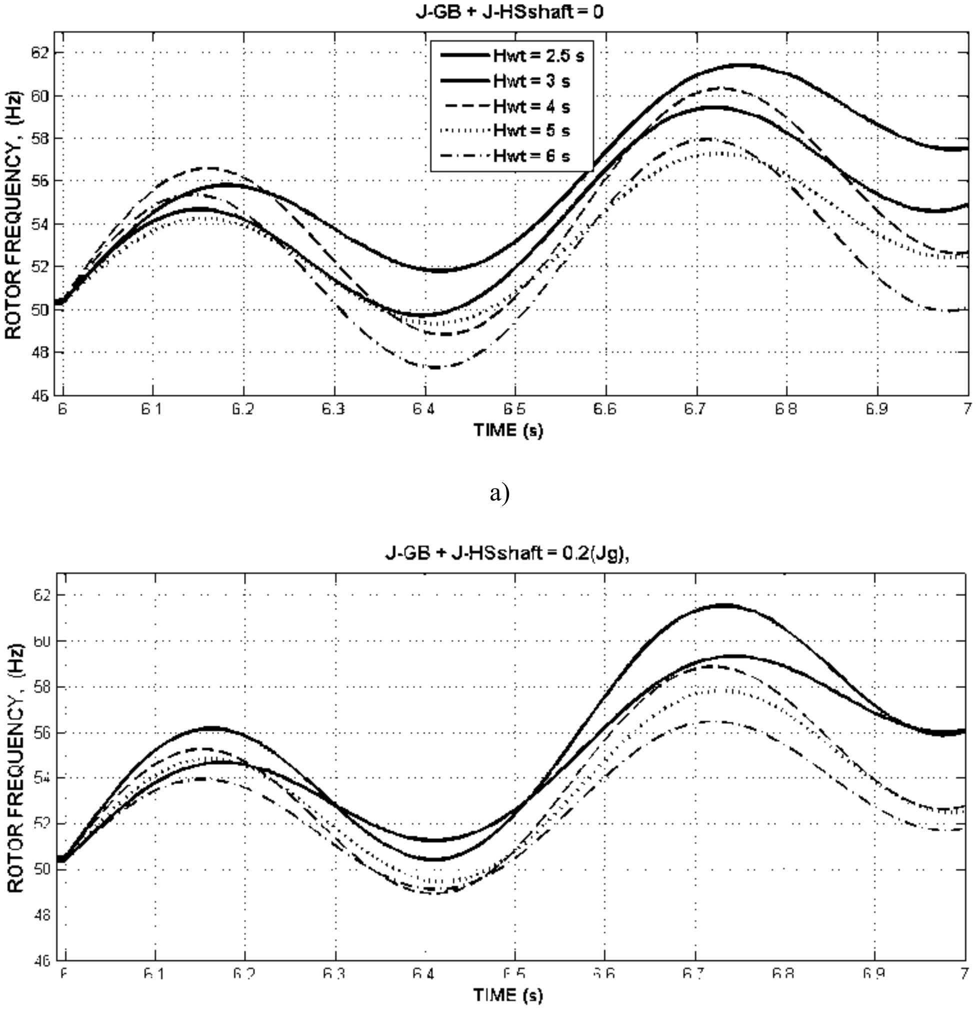

a)

b)

Figure 3.7 Induction generator rotor frequency response for a wind turbine with 44 m blade length through the S2m model, for several values of H_{wt} and $K_{wt,g}$, both as in Table 3.3: a) when $J_{GB} + J_{HSshaft}$ = 0.0, and b) when $J_{GB} + J_{LSshaft} = 1.2(J_g)$

In Figure 3.7(a), the rotor frequency responses present a trend to descend in relative position to H_{wt} = 2.5 s, as H_{wt} increases. If compared to the responses in Figure 3.7(b), this descending feature is larger. This makes evident that: i) if the blade length increases, its corresponding increment of moment of inertia produces a descending feature of the oscillation, and ii) this descending feature is smaller if gear-box and high-speed shaft are taken into account.

These results emphasize the need to correctly use the S2m model in the selection of f_{ff}, and its inherent difficulty to reliably include the incremental wind turbine moment of inertia, as the blade increases. It is relevant the relative importance of including the gear-box and high-speed moments of inertia.

3.5 Generator Rotor Frequency in the BB2m model

In this section is demonstrated that changing the modelling paradigm, the 2-mass model can gain in robustness. It is evident from the Section 3.4 that the S2m model is disable to represent blade length and pre-bend features. Then, this section illustrates the ability of the BB2m model to represent both, rigid and flexible blades with pre-bend features.

Four variables representing physical characteristics, support variations in the BB2M model. Related to the mass m_1, the point P_{pb} where the pre-bend characteristics begin and its related angle θ_c of the pre-bend itself. While related to the mass m_2 the hub J_h and the gear-box J_{GB}, moments of inertia.

Figure 3.8 illustrates the behaviour of the proposed BB2m model, using a 61.5 m blade length with θ_c = 2.5 degrees, as the tested in [Jonkman *et al.* 2009]. The period T = 0.5667 s is selected and the component J_{wt} is computed by (3.11). In Figure 3.8(a), if the value of the pre-bend point P_{pb} is incremented by 20 % reducing the pre-bent zone and thus increasing the rigid zone, the waveform progressively displaces above. It highlights the fact that if blade characteristics move to be more rigid, BB2m and S2m waveforms move to match each other. Although not shown, this statement is also true in the opposite direction. As it is seen, the effect of incrementing the contribution of J_h and J_{GB} to J_{wt} and to J_g, respectively in the BB2m model, is to decrease the maximum amplitudes of the rotor frequency oscillation response. It makes that, the maximum frequency deviation moves to, which is not possible to observe through the S2m model. In this way, the BB2m model remarks wind turbine rotor design features. In Figure 3.8(b), both S2m and BB2m rotor frequency responses are compared. The responses from the BB2m model are both for the same technical conditions, except the point where pre-bend begins. The responses from the S2m model correspond to a guess of technical conditions in order to reproduce the BB2m model response when the P_{pb} point is at 60% and 80 % of the blade length, as measured from the blade-root. If the P_{pb}

point location goes far from the blade-root, the rigid zone increases and the waveform is comparable to be closed to of the S2m model. While if the P_{pb} point location goes near to the blade-root, the pre-bend zone increases and thus, the S2m model is less comparable to the BB2m model response. Once the wind turbine system is reinserted to the power system, the restoration process also exhibits dynamic recovery as P_{pb} location dependent.

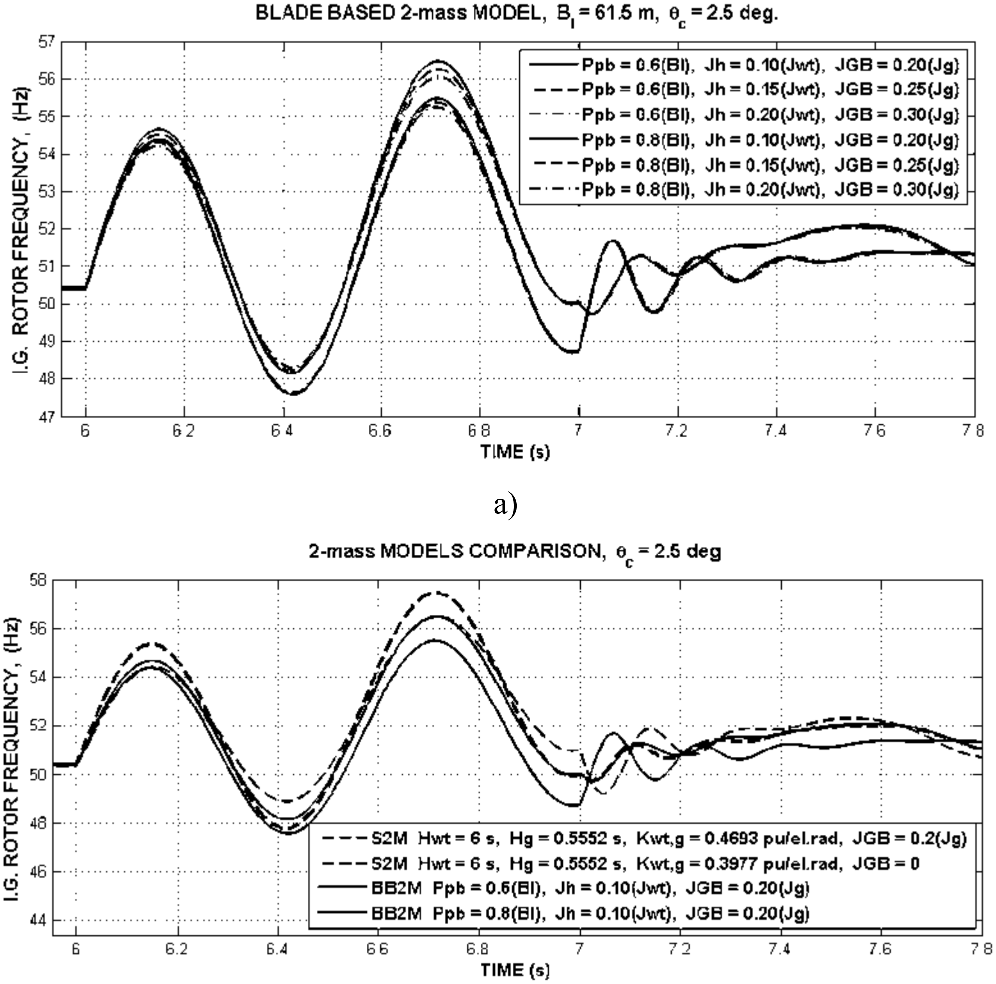

a)

b)

Figure 3.8 Induction generator frequency response for a wind turbine with 44 m blade long, which mechanical structure is assumed similar to the one in [Jonkman *et al.* 2009].

3.6 Wind Turbine Mechanical Torque

Figure 3.9 presents the wind turbine mechanical torque. It is conditioned to an original blade-tip deflexion of 2 m, the P_{pb} point is at 60 % of the blade length, the gear box effect is neglected, RSTA = 0 deg, and the wind speed corresponds to the model response in Chapter

2. Figure 3.9(a) shows the torque as seen at each blade through the BB2m drive-train model. While Figure 3.9(b) is a comparison of the traditionally computed torque as seen at the rotor axis through the S2m model and the blade composed torque, as seen through the BB2m model in this research, at the rotor axis too. As it is evident, Figure 3.9(a) shows a result that can be obtained at each blade-body section, allowing the evaluation of individual blade-body contributions. A particular interest can be on the blade pre-bent zone contributions, where different mechanical characteristics can be of design importance. In both Figures, if BML is

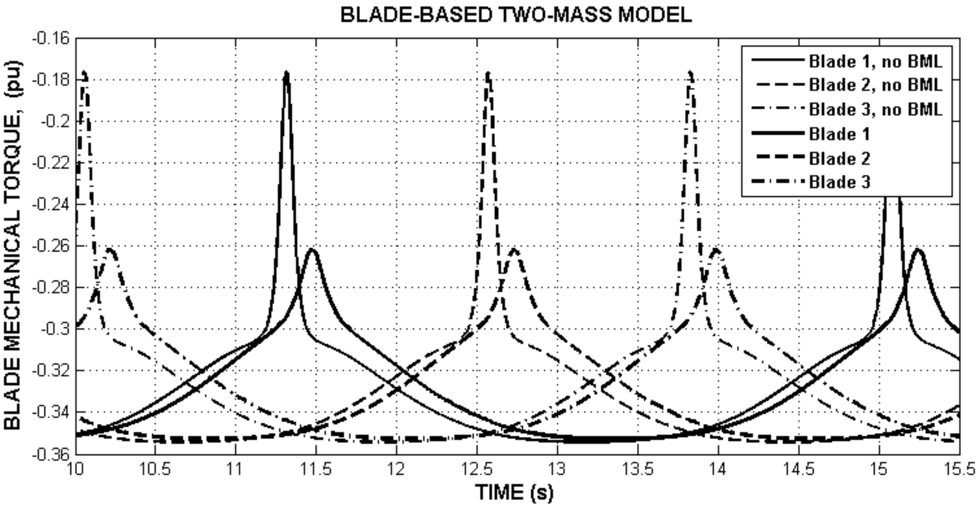

a)

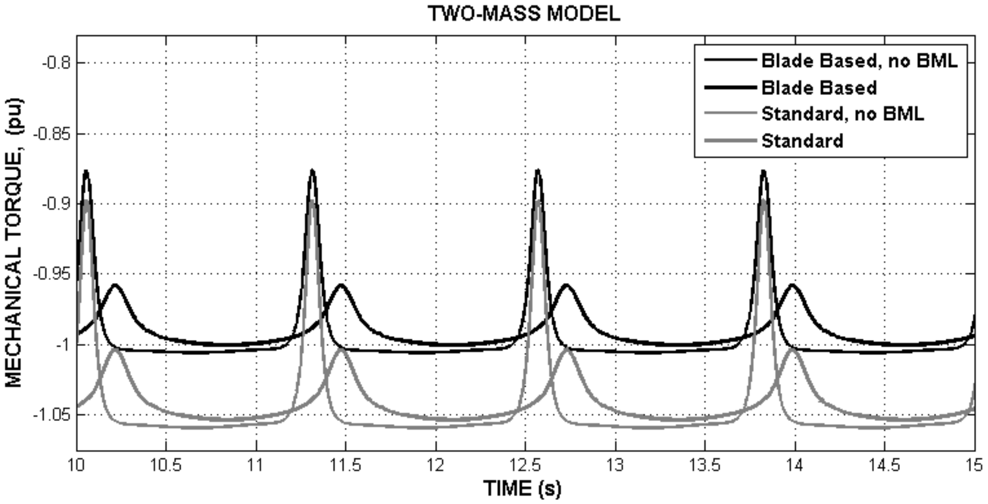

b)

Figure 3.9 The wind turbine mechanical torque: a) blade components through the BB2m model, and b) comparison between the BB2m and S2m drive-train model responses, and integrating the effects of the per-blade equivalent wind speed model

neglected the tower transference pulsation is noticeable sharper than if it is not. Furthermore the response with BML is delayed. In Figure 3.9(b), in the base of the response if tower transference effect were neglected, S2m torque response exceeds BB2m response by of the order of 5 %. At the time the tower transference pulse happens, if BML is neglected the S2m torque response exceeds the BB2m response by of the order of 5.3 %, and if BML is included the pulse difference is of the order of 4 %.

3.7 Conclusion

In this chapter a new strategy to construct the wind turbine rotor moment of inertia, significantly improves the S2m model. Carefully segmenting the blade, the beam theory is applied to define a one-blade contribution to the moment of inertia, and by extension, to the whole wind turbine rotor moment of inertia. If besides the time-varying blade angle deformation and deflections from the blade mechanical loading are added, the wind turbine rotor moment of inertia and low-speed shaft stiffness parameters, result to be time varying and operational conditions dependent. The proposed BB2m model allows varying mechanical blade features such as the blade length, pre-bent length and mass density, which cannot be directly included in the S2m model.

As expected, the induction generator rotor frequency oscillations, starting from identical paradigm considering a given period *T*, have similar characteristics, as produced by both BB2m and S2m models. However, the proposed BB2m model presents smaller frequency deviation than the observed with the S2m model, and more reliably represents pre-bent blades. It has been demonstrated that the allocation of the *Ppb* point determines the degree of similarity between BB2m and S2m modelling. The shorter the rigid zone the more dissimilar results from both models, and vice versa. The mechanical torque, as evaluated through the BB2m model with per-blade wind speed, allows observing torque values at each blade-body section if needed, and at the rotor axis, results from BB2m model are about 5% smaller than the traditionally computed and processed through the S2m model. In both cases, BML effect delays the torque response. Notice that the traditional torque computation has been enabled to include per-blade equivalent wind speed produced, as seen at the hub height.

4

Phase-Coordinates (*abc*) Induction Generator: Basics and Strategy

4.1 Introduction

The knowledge paradigm around electric machinery has been built under the Maxwell's principles [Krause *et al*. 2002]. According to it, the electromagnetic behaviour of any electrical element (resistive, inductive and capacitive) is seen through their associated voltages, currents and magnetic fluxes. In this way, it is a fact that *n*-phase physical arrangement ($n = 2, 3, 6$) of any electrical element can be seen through *n* variables. Despite of this, the *abc* framework is selected only as the starting point to define an orthogonal reference frame *d-q* with two-variables. Around this paradigm has been also established a whole two-transformation *abc*↔*dq* methodology through transformation matrices [Park 1929], [Krause *et al*. 2002], under the assumption of constant electric parameters, in order to: i) avoid high-order modelling and the consequent increase in complex computation, although it is not true anymore with actual computational technology, and ii) be used for cost-effective computational purposes in control theory, where e.g. the voltage variable is taken in the *abc* framework, processed in *dq* frame and supplied in *abc* again.

But an essential aspect around this frame transformation methodology is that it is valid, if only if, electric machines are symmetric structures and they perform in symmetric and balanced operation. The first is a manufacturer matter to fulfil international regulation and standards. The second, associated to voltage quality, has two inputs: i) the occurrence probability of asymmetrical faults, which increases with the outdoor characteristics of the also increasing power system. They invariably produce asymmetrical reaction in the electrical equipment, and ii) the today common power electronic interface, which no matter the architecture produces harmonic content. Both inputs modify the otherwise ideal sinusoidal supply. The analysis of a disturbed symmetrical induction machine, is usually reported using balanced three-phase fault and sudden load mechanical changes, with the machine operating in motor mode. This traditional approach can be valid under certain circumstances. but it is certainly doubtful in grid-connected outdoor wind power plants. For the case of modern wind power plants, the low-voltage fault ride-through has been supplemented to include asymmetrical faults in grid codes [Iov *et al*. 2007], [Tsili and Papathanassiou 2009]. Also in order to fill some weak fault mapping for power quality, several non-standard asymmetrical faults has been added to the traditional list, to include voltage sags [Bollen 2000].

This doctoral research contributes to provide an option to credit a detailed *abc* induction generator model, to: i) skip the computational restrictions using the actual computers technology with multi-process and great storage, and ii) emphasize its use for asymmetrical conditions, which comes from the voltage supply and operating conditions compromising the physical machine characteristics.

4.2 Induction Machine Model with Constant Parameters and Fluxes as state variables

An ABC model to sink this doctoral research is based in the following assumptions [Kraus *et al*. 2002]:

- Using fluxes as state variables is a six-order dimension model and does not involve great computational effort.
- The flux-current function is assumed linear for mathematical formulation.
- Air-gap flux is assumed sinusoidal varying, idealizing physical core properties.
- Constant stator and rotor parameters comes from standard no-load and blocked-rotor tests [IEEE Std-112 2004], [Arshad *et al*. 2008a], and rotor parameters are referred to the stator side. Along this research some proposals are made to emphasize the need of phase measuring in the standard tests, and the use of renewed measuring technologies.

- In the case of a wind turbine driven induction generator, both mechanical rotor speed w_{rm} and angular position θ_{rm} variables, come from the drive-train model. In this research it is presented in Chapter 3.

- Ordinary non-linear differential equations represent the voltage-current interaction, and they can be represented in the general state-space form,

$$\boldsymbol{px} = \boldsymbol{Ax} + \boldsymbol{Bu} \tag{4.1}$$

where p is the operator $d(.)/dt$, $\boldsymbol{x}$ is the state vector, $\boldsymbol{u}$ is the input vector, $\boldsymbol{A}$ and $\boldsymbol{B}$ are the state and control matrices, respectively.

4.2.1 Comparison Between *qd0* and *abc* Induction Generator Models with Constant Parameters.

From both the previous analysis and in order to build a base principle to adjust the known *abc* induction machine modelling, a dynamic comparison between *abc* and *dq* modelling was presented to the ICEMS'09 IEEE International Conference [Fajardo *et al.* 2009].

Some *special dynamic parameters* are defined for the *qd* model in [Novotny and Woterse 1976], based in no-load and load standard test stator and rotor parameters. Following the Novotny's idea these parameters such as, leakage saturation factor σ, normalized ratio of transient stator/rotor decrement factors α, rotor transient time constant τ'_r (s), rotor slip at the operation point S_o, grid synchronous frequency w_{grid}, normalized grid frequency w_o, normalized slip frequency w_{so}, are conveniently redefined for *abc* modelling. Then, through simple parameter variations produced by symmetric and asymmetric disturbed voltage, these parameters are computationally registered. Thus, the abc formulation for open and closed loop eigenvalues shows a non-linear move, predominantly due to rotor resistance, moderately by rotor leakage inductance and slighter by magnetizing inductance variations. Given the determinant roll of rotor time constant in large machines, results suggest that phenomena affecting rotor resistance are more dominant than the phenomena affecting stator and rotor leakage inductances. Phenomena affecting magnetizing inductance appear to be less significant.

Additional time domain simulations including voltage unbalance and harmonics have shown that the *special dynamic parameters* significantly influence the electromagnetic torque and rotor speed, and no similar responses can be expected from *abc* and *dq* models. Special attention was given on the overall-loop transfer function gain. It appeared to have sinusoidal variations instead of constant value, as originally proposed.

These results allow inferring the need to formulate a reliable induction generator model, to efficiently represent the power electronic coupling interface and the power grid performance. A research hypothesis is established for large induction machines as: *If time-domain magnetic saturation, iron-losses and deep-bar effects, acting individually or together produce time-varying parameters, it is expected that operational variables will have a more realistic operational behaviour.* As a consequence, in a wind turbine driven induction generator, the electrical and electro-mechanical variables are expected to be significantly qualified.

4.3 Phase Coordinates *abc* Induction Machine with Time-Varying Parameters

This doctoral research proposes and develops time-varying magnetic inductance, iron loss resistance, rotor resistance and rotor leakage inductance, to suitably represent magnetic saturation, iron losses and deep-bar effects. These effects are recognized to be significant in large size squirrel-cage induction machines [Akbaba and Fakro 1992], [Seyoum *et al.* 2003], [Ranta *et al.* 2009].

Time-varying parameters, as a real fact in induction machines, is extensively reported e.g. in [Seman *et al.* 2003], [Babau *et al.* 2007], [Tu *et al.* 2008], [Ranta *et al.* 2009], using advanced instrumentation technology and measuring strategies to suitably supplement the standard test. In addition, it is known that the electromagnetic behaviour due to inherent characteristics in small commercial machines works out in a different way in large machines [Akbaba and Fakro 1992]. These machines are usually special designs particularly for generation purposes. For the case of this research, the induction machine has double delta-connected stator windings and an X_1/X_2 ratio out the range of the standard recommendation [IEEE Std-112 2004], among other features. This makes doubtful the modelling validation based on small laboratory machines and evidences the crucial need for reliable phase based standard test.

Furthermore, knowing that the power electronic technology efficiency increases using full-power coupling interface, squirrel-cage instead of wound rotor machine is favoured. In fact, there is a trend to use a technological combination of squirrel cage induction machine, which is voltage controlled by STATCOM [Babau *et al*. 2007]. This empowers the need of a more reliable induction generator model. This whole paradigm was also identified, as a promising research focus during the nine months research staying of the author, at the Department of Energy Technology at Aalborg University in Denmark, from 2006 to 2007.

The selected modelling strategy to include this research proposal is presented in Figure 1. It shows interconnected feedback blocks to supplement the basic *abc* induction generator model with constant parameters. The core-losses block creates a time-varying non-linear core-loss resistance, as slip, voltage and stator fluxes dependent. It also includes the effect of the power converter to involve non-sinusoidal voltage supply.

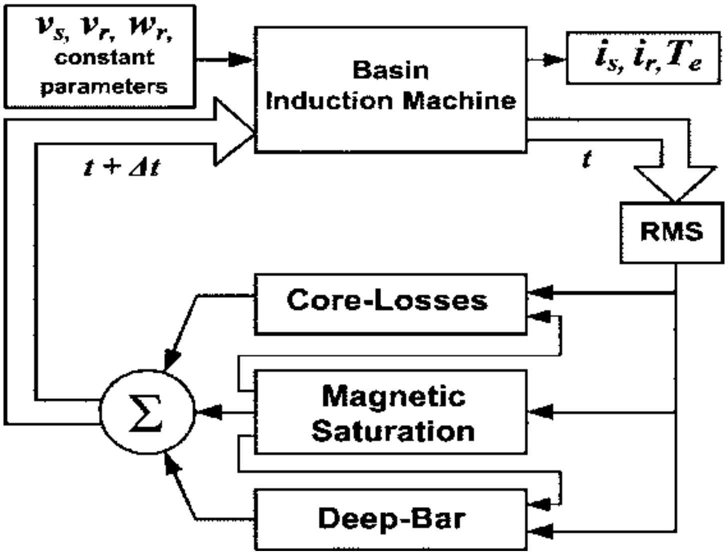

Figure 4.1 Computational flow diagram, to integrate time-varying parameters in a detailed *abc* induction machine model

At time $t+\Delta t$, parameters are updated relative to the existing at time t, due to terminal voltage, internal fluxes or stator/rotor current variations. Three sources can produce these variations for large machines, and thus, three functions are proposed for them:

i) A test based one saturation function of the type L_{ms} vs V to produce ABC time-varying magnetizing inductance parameters and to model the main path magnetic saturation. Three saturation functions representing per-phase saturation function try to distinguish phase contributions to the main flux. This block produces time-varying and voltage dependent *abc* magnetizing inductance parameters.

ii) A test based iron-losses function to produce ABC time-varying non-linear iron-losses resistances, for modelling the stator and rotor iron losses, including the effect of the electronic power converter interface.

iii) A test based deep-bar function to produce ABC time-varying and slip dependent non-linear rotor resistances and leakage reactance.

The RMS block, is a secondary by necessary function to compute the RMS stator voltage and flux values or their corresponding spatial vectors.

4.4 Conclusion

Given a well-recognized ABC constant parameters induction machine model, a strategy is adopted to build a modular computational solution, to produce time-varying parameters. Three sources of electromagnetic effects are considered: i) A no-load test based main path magnetic saturation function of magnetizing inductance as voltage dependent. It can be expanded to three saturation functions in order to enable per-phase contribution, which produces ABC magnetizing inductance parameters, ii) A no-load test based iron-losses function which includes the effect of the power converter interface. It produces ABC iron-losses resistances parameters, and iii) A blocked-rotor and load test based deep-bar function, which produces *abc* rotor resistance and leakage reactance parameters. A common characteristic for all these parameters is they are time-varying and then, they improve the induction generator responsiveness during the transient state.

* * *

5

Time-Varying and Voltage Dependent Magnetizing Inductance based *abc* Saturation Function

5.1 Introduction

From the no-load standard test at a speed very close to the synchronous speed, the rotor circuit is by far an open circuit, due to the fact that the resultant slip is very low. Under these operating conditions, the voltage-current pair determines at each measuring the respective total impedance. It includes a series connection of stator and magnetizing branches only, in the equivalent circuit [IEEE Std-112 2004]. Under the knowledge of stator parameters, the assessment of this series connection leaves the magnetizing inductance, because the magnetizing branch is usually assumed mainly inductive.

If in the no-load test, phase voltages and currents are averaged [IEEE Std-112 2004], one voltage to magnetizing inductance L_m-V saturation function is obtained. It is similar to the algorithm in [Marquardt 1963] which relates magnetizing inductance to magnetizing current. The L_m-V function originally found in [Donescu *et al*. 1999], [Seyoum *et al*. 2003], is proposed in an *ABC* phase perspective in connection to the strategy in Chapter 4 and Appendix B, to be directly obtained from the no-load test. In opposition, the traditional saturation function, relating flux density to magnetic field, usually is an indirect function obtained from additional computation on no-load data. Moreover and as an advantage, the L_m-V function is data-sheet based and does not require additional information from the core geometry.

If instead of averaging the no-load data, they are per-phase processed, three saturation functions relating each phase voltage with a per-phase magnetizing inductance are obtained. These three functions can be equidistant or not, as machine physical properties dependent.

To simulate voltage variations, asymmetric line-to-ground fault and symmetric three-phase fault are applied at the point of common coupling (PCC) of the wind turbine. The power system setup including the 2 MW induction machine and the corresponding voltage drops, are identified in the Appendix B.

5.2 One Magnetic Saturation Function

It is known that the stator flux mainly determines the behaviour of the magnetization inductance [Klaes 1993], and that this dependence can be extended to the stator mutual inductances [Donescu *et al*. 1999]. In association, the magnetization inductance is characterized as voltage dependent, based on no-load standard test at constant synchronous speed [Seyum *et al*. 2001]. In this way, processing no-load data to compute the magnetizing inductance for each no-load voltage – current pair, a magnetizing inductance function, as stator phase voltage dependent, can be created. It is usually presented as an average value of the *ABC* stator phase voltages. The following methodology justifies the approach.

Neglecting stator resistance and for rotor speed very close to the rated value [Klaes 1993], [Seyoum 2000], [Seyoum *et al*. 2003], the *ABC* stator phase voltages are proportional to the derivate of the *ABC* phase fluxes [Donescu *et al*. 1999]. As a consequence, the RMS phase voltage magnitude is proportional to the RMS phase flux magnitude, i.e.

$$E_{rms,ABC} \propto \Psi_{rms,ABC} \tag{5.1}$$

where $E_{rms,ABC}$ and $\Psi_{\mathrm{rms},ABC}$ mean the magnitude of RMS generated stator voltage and stator flux, respectively. In the transient state, these RMS values are intended to be time-varying when the machine is disturbed, e.g. by symmetrical and asymmetrical short circuit faults. The magnetizing inductance L_{ms} dependence on flux is identically proportional to its dependence on voltage, i.e.,

$$L_{ms,ABC} \propto E_{rms,ABC} \tag{5.2}$$

Simple algebra allows processing the no-load data using the Matlab **cftool** for curve fitting functions. For the case of one saturation function a Gaussian function matches test data, resulting,

$$L_{ms,ABC}(x) = \sum_{i=1}^{5} a_i \exp(-((x - b_i)/c_i)^2) \tag{5.3}$$

where *x* represents the instantaneous RMS voltage in per unit values, as based on the rated voltage value, and the string *exp* represents by text convenience the exponential function *e*. Figure 5.1(a) shows the magnetizing inductance function based on one-curve for the machine used in this research, according to the Appendix B. It, given the no-load test symmetrical origin, represents the idea that the main magnetic path gets equal symmetric phase contribution for symmetric operation. Constants a_i, b_i, c_i for (5.3) are compiled in Table 5.1.

5.3 Three *ABC* Magnetic Saturation Functions

Expanding and individualizing the *ABC* perspective, three L_m-V saturation functions highlights the individual capability of phase windings to detect A, B, C phase voltages and to produce individual currents, then individual fluxes and thus individual magnetizing inductances L_{msA}, L_{msB}, L_{msC} values. The L_{msA}-$E_{rms,A}$ function corresponds to real experimental data. For phases B and C, suitable not real data but closed to the phase A data, is assumed. It allows computing L_{msB}-$E_{rms,B}$ and L_{msC}-$E_{rms,C}$, saturation functions, to simulate what is expected from tests, if phase data are processed. In opposition to one saturation function, this three saturation function proposal allows assuming that each phase magnetizing flux contributes with a component of the total linking flux on the main path. This is crucial when asymmetric faults are present.

Two ways to interpret the grouping of A, B and C phases are proposed:

A first grouping method assumes arbitrary data to build **three equidistant saturation functions**, as shown in Figure 5.1(b). In the absence of appropriate information, this thesis assumes that phase B saturation function is below phase A and phase C saturation function above phase A. The second grouping method builds **three non-equidistant saturation functions**, as displayed in Figure 5.1(c). In the absence of appropriate information, their relative position is subjectively assumed at different regions.

The three equidistant saturation functions in Figure 5.1(b) are built with identical Gaussian functions, and data in the neighbourhood of phase A. For the three non-equidistant saturation functions in Figure 5.1(c), data is well matched by a polynomial function for phases B and C as,

$$L_{ms,ABC}(x) = \sum_{i=1}^{10} p_i x^{10-i} \tag{5.4}$$

Constants p_i for (5.4) are compiled in Table 5.1.

5.4 Saturation Models

With the strategy exposed above, three L_{ms} values can be derived giving place to three possible saturation models.

First, the ***L*$_{mean}$ Saturation Model** is consistent with the traditional symmetry paradigm [Krause *et al*. 2002]. Consequently, an only one average magnetizing self-inductance L_{ms} value is composed as,

$$L_{ms,ABC} = L_{mean,ABC} = \frac{1}{3}(L_{msA} + L_{msB} + L_{msC}) \tag{5.5}$$

where $L_{A,B,C}$ is the magnetizing inductance associated to *ABC* phase voltages, according to Figure 5.1(a), with all phases matching phase A. This model equally modifies the main diagonal elements of the inductance matrix.

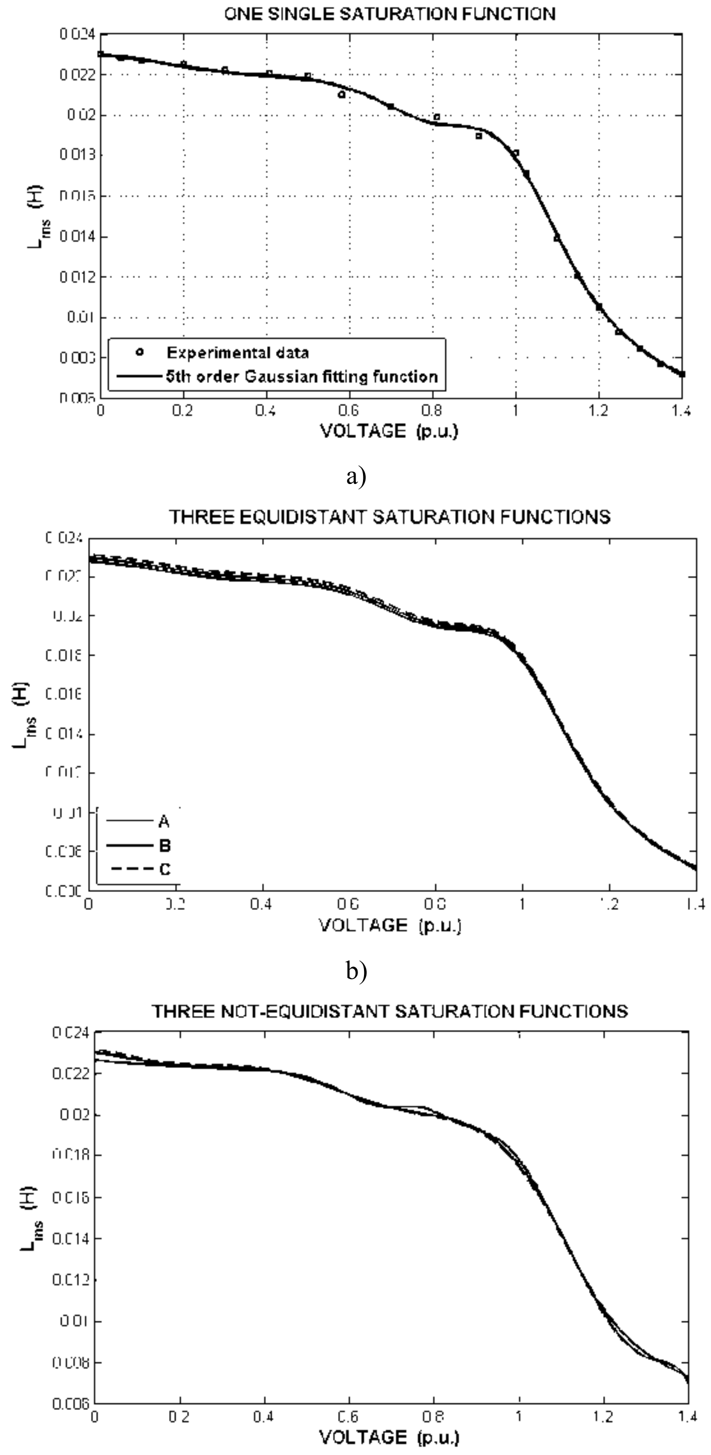
ONE SINGLE SATURATION FUNCTION

a)

THREE EQUIDISTANT SATURATION FUNCTIONS

b)

THREE NOT-EQUIDISTANT SATURATION FUNCTIONS

c)

Figure 5.1 Saturation Function based on *Magnetizing inductance* as a function of individual A, B, C phase voltages: a) one saturation function, b) three equidistant ABC saturation functions, and c) three non-equidistant ABC saturation functions

Table 5.1 Constants to be used with saturation functions

PHASE	**ONE AND THREE EQUIDISTANT SATURATION FUNCTIONS**														
	a_1	b_1	c_1	a_2	b_2	c_2	a_3	b_3	c_3	a_4	b_4	c_4	a_5	b_5	c_5
A,B,C~	-0.0029	-0.5715	0.3076	0	0.5619	0.0006	0.0039	0.6890	0.3402	0.0041	0.9805	0.1630	0.0232	-0.1454	1.4170
	THREE NOT-EQUIDISTANT SATURATION FUNCTIONS														
B	0.0015	0.6079	0.2128	0.006	0.4752	0.4952	0.0014	0.7704	0.0960	0.0059	0.974	0.1886	0.0453	-2.702	3.013
	p_1	p_2	p_3	p_4	p_5	p_6	p_7	p_8	p_9	p_{10}					
C	-0.8373	4.492	-9.581	10.3	-5.805	1.583	-0.1548	0.0011	-0.0038	0.0232					

Second, the ***L***$\boldsymbol{L_{abc}}$ **Saturation Model** distinguishes three L_{ms} values as derived for each phase voltage, according to (5.4). It allows qualifying the phase voltage influence on the diagonal elements of the inductance matrix. This model, unequally modifies the main diagonal elements of the inductance matrix and is determinant in the simulation of asymmetric faults.

Third, the $\boldsymbol{L_h}$ **Saturation Model** is consistent with and improves the proposal in [Donescu *et al*. 1999]. For a Δ-connected relatively small induction motor with 15 HP, 208 V, 2-pole pairs, it was experimentally found that 5th harmonic results of the order of 4.17 % of the fundamental line current at rated voltage, 5.7 % at 120 % rated voltage and 11.25 % at 130 % rated voltage. He also concludes that although measured 3rd harmonic results more aggressive, it is cancelled in the delta winding connection. Donescu's methodology proposes a step by step computational process to approach a measured 5th harmonic line current, based on two parameters: i) a first factor $\gamma < 1.0$ takes into account that the magnetic paths related to stator mutual inductances are different to those of stator self-inductance of the winding in each phase, and ii) a second factor ξ includes the teeth saturation effect on stator mutual inductances. Donescu established that the line current 5th harmonic is the most important, flowing to the induction machine at the load standard test.

In this research, under the absence of line current 5th harmonic datum, the Donescu's parameters γ and ξ are assumed per-phase input parameters, which can be varied to appropriately simulate special mutual paths conditions and teeth effects. In addition, the magnetizing inductances are per-phase evaluated instead of constant values.

In agreement with Donescu, the traditional computational element $L_{ms}/2$ into the mutual stator inductances, as in [Krause *et al*. 2002], is transformed. Instead of normalizing the stator fluxes for vector control purposes [Donescu *et al*. 1999], it is proposed the use of instantaneously induced *ABC* voltages according to (5.3) or (5.4). In addition, the angular position of the phase stator flux vector θ_f [Donescu *et al*. 1999], is proposed as a reference for the angular position of the phase stator voltages.

Taking into account the nomenclature in the Appendix B, the stator mutual inductances can be expressed as,

$$L_{AB} = L_{BA} = -\frac{L_{msA}(\gamma_A E_{rms,A})}{2}\left[1 - \xi_A k_{satA} \sin^2(\theta_f + \pi/6)\right]$$

$$L_{BC} = L_{CB} = -\frac{L_{ms,B}(\gamma_B E_{rms,B})}{2}\left[1 - \xi_B k_{satB} \sin^2(\theta_f - 3\pi/6)\right] \tag{5.7}$$

$$L_{CA} = L_{AC} = -\frac{L_{msC}(\gamma_C E_{rms,C})}{2}\left[1 - \xi_C k_{satC} \sin^2(\theta_f + 5\pi/6)\right]$$

where γ_{ABC} and ξ_{ABC} are the Donescu's parameters in *ABC* coordinates, to identify individual internal iron and teeth associated asymmetrical conditions. The also Donescu's saturation factor $k_{sat,ABC}$ is calculated for each phase from Figure 5.7 as,

$$k_{sat,ABC} = \frac{L_{m0} - L_{ms,ABC}}{L_{m0}} \tag{5.8}$$

where L_{m0} is assumed at V ≈ 0 pu in Figure 5.1, as suggested in [Donescu *et al.* 1999].

5.5 Simulation and Analysis

5.5.1 Magnetizing Inductance Parameter Based On One Saturation Function (OSF)

The goal of this Section is to explore how the time-varying magnetizing inductance response changes, as related to one or three *abc* saturation functions.

The followed analysis methodology considers a first step, where the constant L_{ms} parameter response is taken as a reference. Its numerical value corresponds to the magnetizing reactance at the test frequency, as an input obtained from the data sheet. As a second step and under fault conditions, observations are made comparing magnetizing inductance responses in relation to the reference, in order to explore how much the magnetizing inductance deviates, as produced from each saturation model. As a third step, general inferences are made.

5.5.1.1 Combining OSF with the L_{mean} Saturation Model

Figure 5.2 shows the time-varying magnetizing inductance response from OSF, when LG in Figure 5.2(a) and LLL in Figure 5.2(b) faults, are applied at PCC according to the wind turbine setup in Appendix B. Waveforms are obtained for the three saturation models.

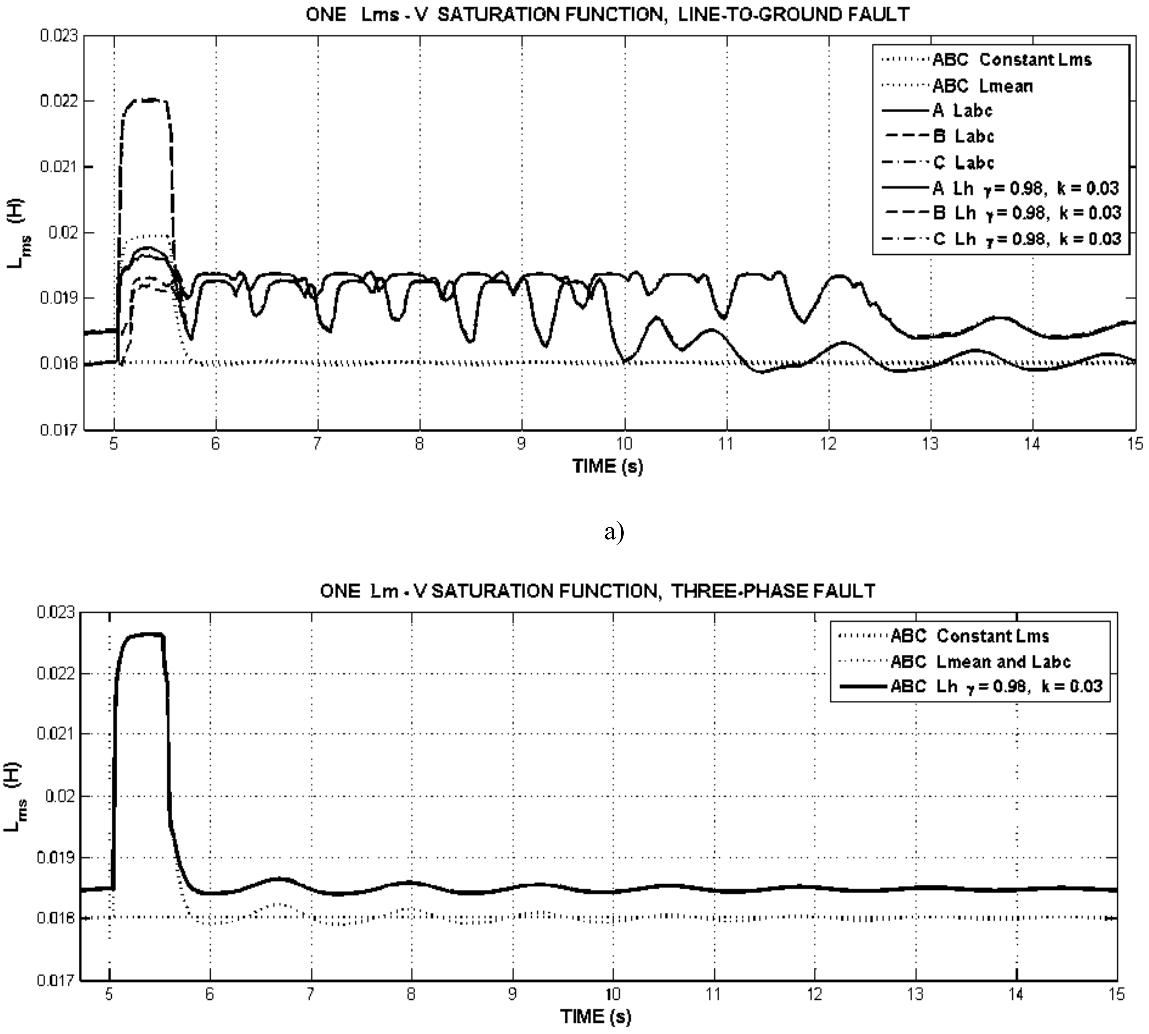

a)

b)

Figure 5.2 Time-varying magnetizing Inductance behaviour, a) when an asymmetric LG fault is applied at the PCC, and b) when a symmetric LLL fault is applied at the PCC

What this section concerns, the L_{mean} saturation model (dotted black line) waveform response, appears matching the reference response (dotted gray line), except during the fault duration interval, and after it oscillates going to the steady-state. These of the order of 0.8 Hz oscillations are more significant when they are produced from the LLL fault. The peak amplitude during the fault interval is of the order of 11.11 % above the reference value for LG fault and of the order of 25.67 % above it for LLL fault.

The time-varying L_{ms} parameter in this way produced, will equally modify the diagonal elements of the stator and rotor inductance sub-matrices, related to (B.1) in the Appendix B, preserving the machine symmetry.

It is inferred that this model faithfully reproduces the reference magnetizing inductance value and in addition introduces transient variations otherwise hidden by the constant parameter reference value. The transient magnetizing inductance peak, as related to the fault impedance producing specific RMS voltage drops, is significant and larger than 10 % of the reference value. This model is unable to reproduce phase contributions due to asymmetrical faults.

5.5.1.2 Combining OSF with the L_{abc} Saturation Model

As related to Figure 5.2, unlike the L_{mean} saturation model, the L_{abc} saturation model is able to reproduce asymmetrical conditions during the fault interval only, as seen in Figure 5.2(a) for LG fault. Responses for phases A and B appear smaller than the phase C, which exhibits in this case the largest response, of the order of 22.22 % above the reference value. As compared to L_{mean} model response, the phase C response is of the order of 10 % larger than it. As compared to the LLL fault in Figure 5.2(b), the phase C presents a peak value 2.82 % above it. This allows inferring that, given certain fault conditions like the ones in this case, some phase response can be even larger than the L_{mean} model response and that from the LLL fault response. Furthermore, the L_{abc} saturation model in Figure 5.2(b), also faithfully reproduces the reference magnetizing inductance value and matches the L_{mean} saturation model response.

Phase responses after the LG fault is cleared, are not individually distinguished, as shown in Figure 5.2(a), but also unlike the L_{mean} saturation model responses, they show very significant oscillations going to the steady state. It is probably due to phase unbalanced fluxes amplitude. This condition makes they strongly tie up the fault conditions enlarging their effects beyond the fault interval. In this case that effect is noted for about 4.5 seconds after the fault is cleared. Note that in the case of LLL post-fault interval in Figure 5.2(b), given the symmetrical fluxes condition, they immediately relax, and the magnetizing inductance responses softly go to the steady-state.

It is inferred that, i) the L_{abc} saturation model is more reliable that the L_{mean} saturation model to represent asymmetrical conditions, and comparable to it for symmetrical conditions, ii) special fluxes conditions appear after the fault is released due to asymmetrical fault, that tie up the fault conditions enlarging their effects beyond the fault interval, and producing significant oscillations going to the steady state, and iii) it is possible to expect some L_{abc} saturation model phase response even larger than those from the L_{mean} model response and the LLL fault response.

5.5.1.3 Combining OSF with the L_h Saturation Model

As related to Figure 5.2, this model includes additional effects to the L_{abc} saturation model, as teeth saturation harmonics effect and the consequent reduction on phase magnetic fluxes. Parameters $\gamma = 0.98$ and $k = 0.03$ are *arbitrary* selected by simulation to be representative for the 2 MW induction machine in this thesis, in order to reproduce stable responses. Despite of that, the steady-state magnetizing inductance L_h responses in Figure 5.2 appears 2.83 % above the reference value, and given an asymmetrical LG fault as in Figure 5.2(a), although with smaller post-fault oscillations, they last more time than with the L_{abc} saturation model, up to 7.5 s. It was found that k values larger than 0.05 produce even more critical post-fault responses. The model works well, supporting larger k values and producing steady-state stator line current waveforms with harmonic content. The post fault oscillations, besides to hide individual phase effects, they can cause a stopping and starting oscillatory process in the electromagnetic torque, with oscillatory acceleration of the induction generator. The symmetrical LLL fault as shown in Figure 5.2(b) does not present this behaviour and produces a cleaner waveform, with the same parameter set.

It allows inferring that: i) the combined effect of γ and k parameters is to increase the magnetizing inductance, relative to the reference value, and, ii) the inclusion of teeth saturation by mean of the L_h saturation model increments in certain way, a dramatic oscillatory behaviour in the magnetizing inductance. In addition to instability of the induction machine, it probably accuses temperature rising, and iii) if some asymmetrical faults condition can cause these instability effects, it is reasonable to evolve asymmetrical events in the wind turbine dynamic studies, despite the fact of the power system paradigm where only symmetric faults are involved.

5.5.2 Magnetizing Inductance Parameter Based On Three Saturation Functions (TSF)

In this Section and for LG and LLL fault types, the magnetizing inductance response, from three equidistant (TESF) and non-equidistant (TnESF) *abc* saturation methods are presented. Shorter names are used for resultant saturation models, as follows:

a) The L_{3abc} saturation model combines the L_{abc} saturation model and TESF

b) The L_{abc3} saturation model combines the L_{abc} saturation model and TnESF

c) The L_{3h} saturation model combines the L_h saturation model and TESF. Parameters γ = 0.98 and k = 0.03 are selected.

d) The L_{h3} saturation model combines the L_h saturation model and TnESF. Parameters γ = 0.98 and k = 0.03 are selected.

Figures 5.3 and 5.4 present these results, where the constant L_{ms} input value is the reference.

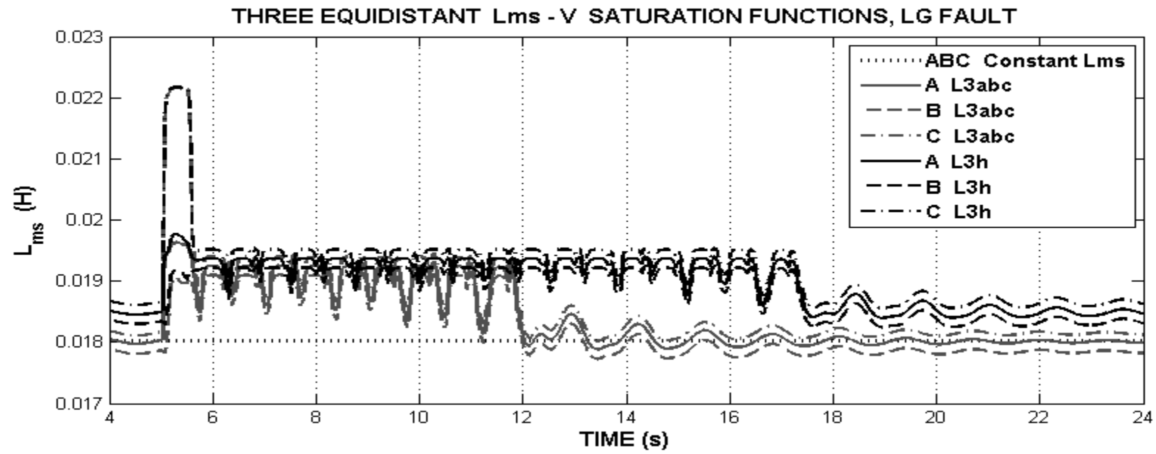

a)

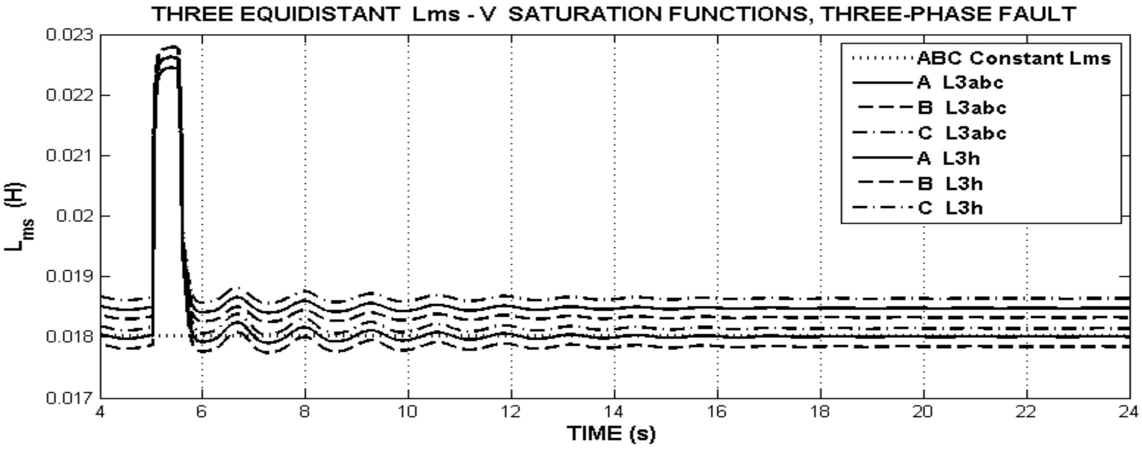

b)

Figure 5.3 Time-varying magnetizing inductance behaviour from TESF when, a) asymmetric LG fault, b) symmetric LLL fault, are applied at PCC

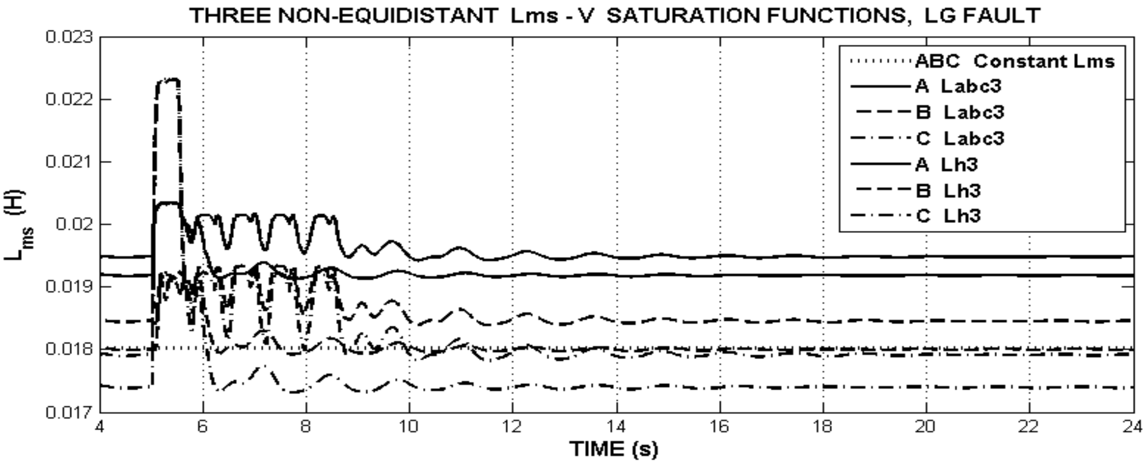

a)

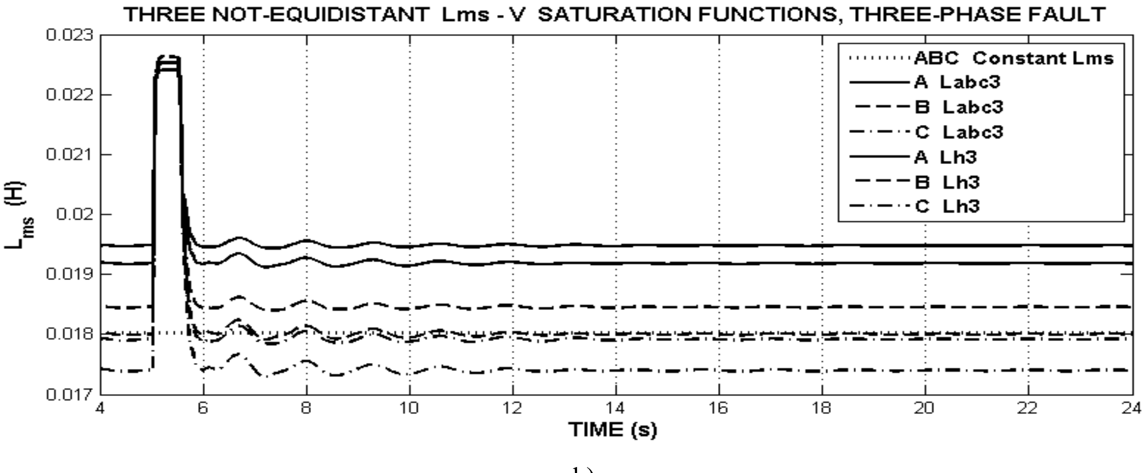

b)

Figure 5.4 Time-varying magnetizing inductance behaviour from TnESF when, a) asymmetric LG fault, b) symmetric LLL fault, are applied at PCC

It is reasonable to expect that the diagonal terms of the inductance matrix will be affected by different L_{ms} parameters at each phase, due to the double effect of both, voltage *ABC* variations and equidistance properties.

Because of the results in Figures 5.3 and 5.4 are related to the characteristics of saturation functions in Figures 5.1(b) and 5.1(c), they are suitably redrawn in Figure 5.5 with a zoom in the compromised voltage zone, according to Figure B.3 for asymmetric LG fault. Note that the vertical scale in Figure 5.5 matches the corresponding one in Figures 5.3 and 5.4.

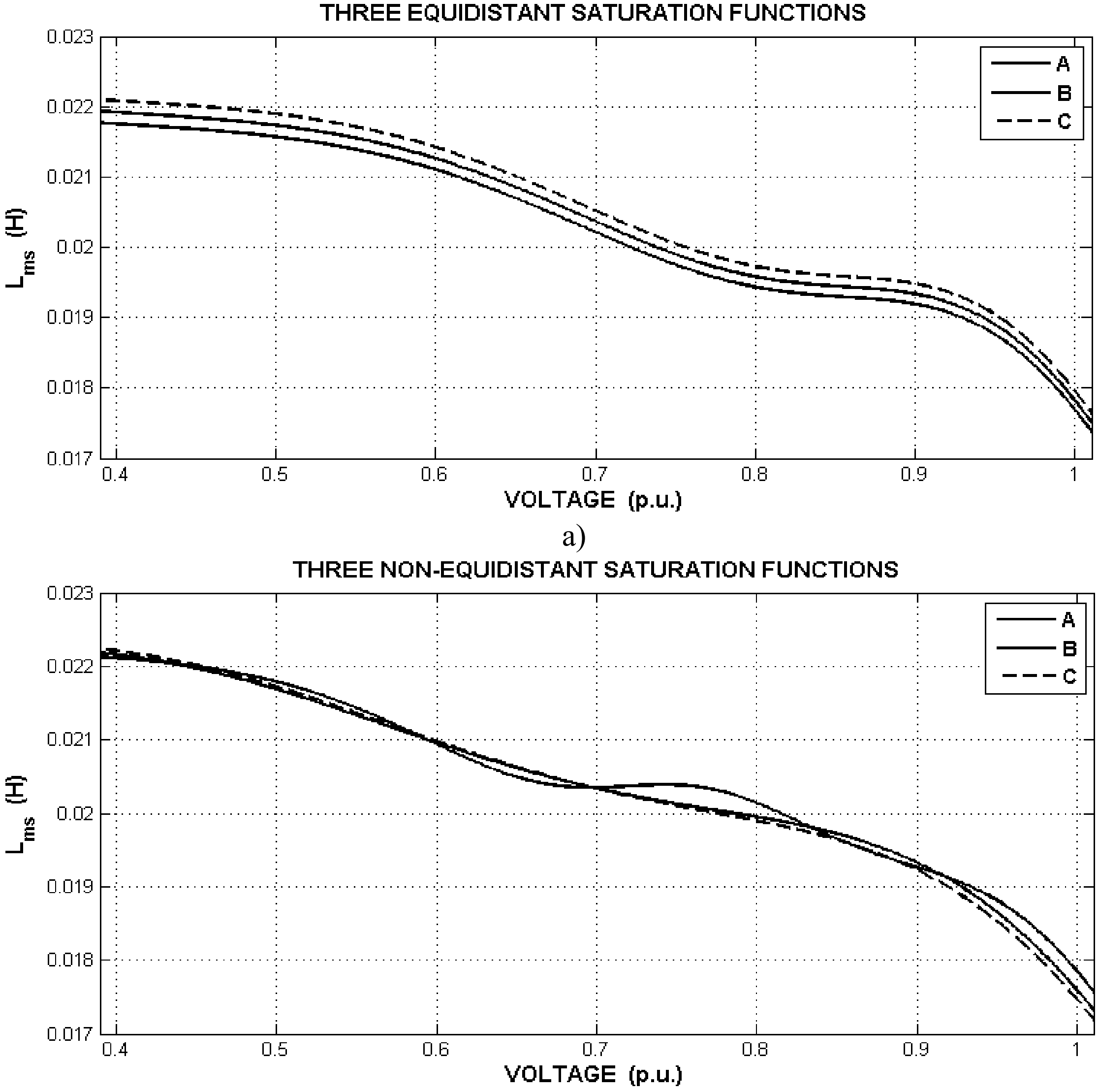

a)

b)

Figure 5.5 Zoom in Figure 5.1, to highlight the compromised voltage zone: a) for TESF, and b) for TnESF

The individual waveforms associated to TnESF in Figure 5.5(b) looks relatively very close each other than in the case of the TESF in Figure 5.5(a). Given a voltage value in this Figure, there is uniform significant data deviation between 0.019 and 0.022 Henry, despite they are inside the 2 % relative to phase A. Relative to phases A and C, the phase B in Figure 5.5(b) also presents meaningful, although non-uniform, data deviation for L_{ms} values between 0.019 and 0.022 Henry. The slope of each phase characteristic in its operational point is also slightly different being a factor to be taken into account in the following analysis.

If TESF method is used, as shown in Figure 5.5(a): i) combined to three symmetric time-varying *abc* voltages, they produce three equidistant and with identical phase order magnetizing inductance values, and ii) combined to three asymmetric time-varying *abc* voltages, the three different magnetizing inductance values will be in correspondence to the phase asymmetry.

If TnESF method is used, as shown in Figure 5.5(b), the resultant three *abc* magnetizing inductance values entirely depend on the non-equidistant conditions all along the voltage span where the variations occur, and particularly at the operating point, around which voltages recover.

5.5.2.1 Combining Saturation Methods with Saturation Models

Figure 5.3(a) and 5.3(b) presents the combination of TESF method with L_{3abc} and L_{3h} saturation models. Due to logical similarities between Figure 5.3 and Figure 5.2, the analysis in this Section is based on their comparison.

The combination of TESF method with L_{3abc}, as shown in figure 5.3 allows noticing that, when magnetizing inductance responses come from an asymmetric LG fault, i) they are individually valued now, with a specific value at each phase and slightly apart each other, and have similar waveform of that presented in Figure 5.2(a), ii) during the fault interval their waveforms do not differ of their equivalent in Figure 5.2(a) with larger phase C peak, and iii) at the post-fault interval, from a total of 9 oscillations with a period of the order of 0.704 s, individual phase A oscillation is between 0.0184 and 0.01924 Henry, phase B oscillation is between 0.0183 and 0.01908 Henry and phase C oscillation is between 0.01854 and 0.01939 Henry. These oscillations go 2 seconds beyond the corresponding in Figure 5.2(a), and relative to Figure 5.5(a) they develop in a zone where the respective phase saturation functions are relatively closer each other. While, if magnetizing inductance responses are derived from a symmetric LLL fault, as shown in figure 5.3(b), besides to be individually characterized they are a practical phase replica of that in Figure 5.2(b). At the fault interval individual phase responses appear.

The combination of TESF with L_{3h} allows , as shown in figure 5.3 observing that, when magnetizing inductance responses come from an asymmetric LG fault, i) they are individual too, ii) during the fault interval, they follow the corresponding waveforms in Figure 5.2(a), and iii) from a total of 8 oscillations with a period of the order of 1.4 s, individual phase A oscillation is between 0.01883 and 0.01937 Henry, phase B oscillation is between 0.01868 and 0.01922 Henry and phase C oscillation is between 0.01882 and 0.01952 Henry. There is 8 oscillations. Meanwhile, when magnetizing inductance responses are derived from a symmetric LLL fault, they are a practical phase replica of those in Figure 5.2(b), and also individual phase responses appear during the fault interval.

As an inference for asymmetric LG fault, the TESF method and L_{3abc} and L_{3h} saturation function combination leaves individual phase *abc* magnetizing inductance responses similar to the single response from OSF method and L_{abc} and L_h, respectively. The number of oscillations increases and they are also individual for each phase now. Thus, it forces individual oscillations limits. These limits correspond to a saturation function zone where uniformly separated individual phase saturation characteristics are relatively closer each other. It is assumed that, given the relative slower phase voltage recovery in Figure B.3 of the Appendix B together to the asymmetric inductance matrix instantaneous state, the oscillations last more than in the case of OSF method.

From the symmetric LLL fault, despite of the relative slower voltage recovery in Figure B.3 of the Appendix B, as equal for the three phases, and together to the symmetric inductance matrix instantaneous state, the magnetizing inductance responses go quickly back after the fault is cleared, without the oscillations observed in the case of asymmetric LG fault.

From other point of view, Figure 5.4(a) and 5.4(b) display the combination of TnESF method with L_{abc3} and L_{h3} saturation models. Due to logical similarities between Figure 5.4 and Figure 5.2, the analysis in this Section is also based on their comparison.

The combination of TnESF method with L_{abc3}, as shown in Figure 5.4 allows noting that, when magnetizing inductance responses come from an asymmetric LG fault, i) they are individually valued as from TESF method, ii) the maximum during the fault interval reach phase values larger than in the case of OSF and TESF methods, and iii) oscillations are practically zero and the recovery process develop in a zone where the phase saturation characteristics are relatively apart each other, as comparing Figure 5.4(a) and 5.5(b). While, if magnetizing inductance responses are derived from a symmetric LLL fault, although they keep on being a practical phase replica of those in Figure 5.2(b), they are now too much apart than in the case of TESF method.

The combination of TnESF method with L_{h3}, as shown in figure 5.4 allows noting that, when magnetizing inductance responses come from an asymmetric LG fault, i) they are individually valued as from TESF method, ii) post-fault oscillations are now as meaningful as in the case of TESF method but, firstly they are too much apart, and secondly they are only fewer than those, with a consequent shorter duration time.

5.5.2.2 Average Magnetizing Inductance L_{mean} from TSF type methods

Figure 5.6 displays averaged magnetizing inductance parameter responses L_{mean}, as produced from TESF and TnESF methods, when an asymmetric LG fault is applied at PCC. It allows comparing these results to L_{mean} from OSF in Figure 5.2(a).

For comparison purposes, the L_{mean} response produced from OSF method is used as a reference.

From TESF method, i) L_{3abc} and L_{3h} saturation models responses run significantly apart of the reference, ii) the peak value during the fault interval is around 1.65 % above the peak reference from both the) L_{3abc} and L_{3h} saturation models, and iii) after the fault is cleared, the L_{3abc} model response although oscillatory quickly converges to the reference and faster than the L_{3h} model response, which goes beyond the L_{3abc} model response.

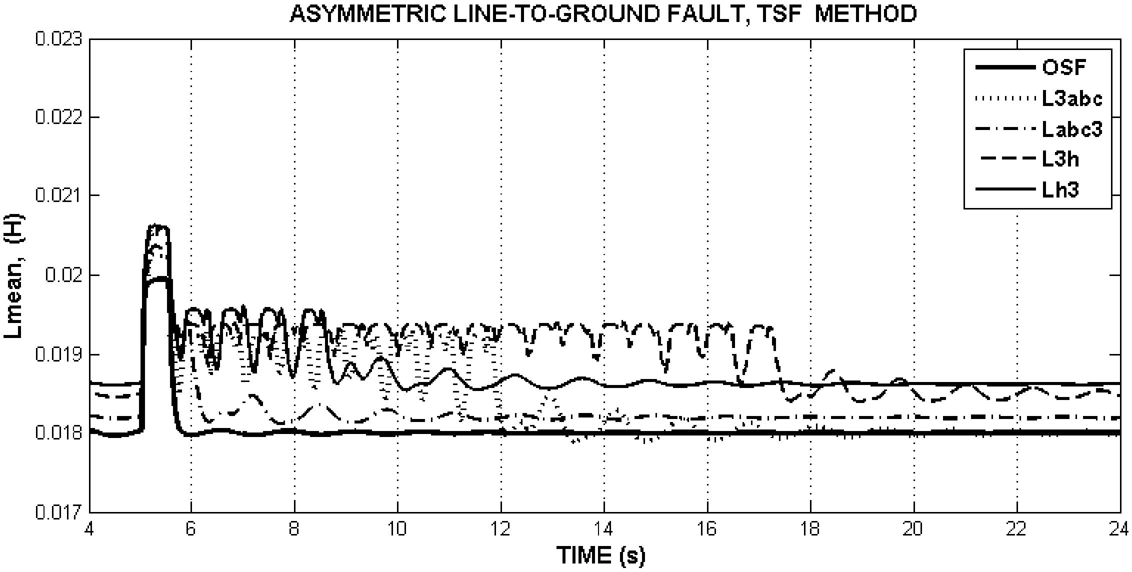

Figure 5.6 Average magnetizing inductance from TSF type methods, as compared to that from OSF method

From TnESF method, i) The L_{abc3} and L_{h3} saturation models responses run closer to the reference than those from TESF method, ii) the peak value during the fault interval is around 3 % above the peak reference from the L_{abc3} model response. The same comparison leaves 3.26 % from the h3 method, iii) after the fault is cleared, the L_{abc3} model response appears as the most damped and running closer to the reference than L_{h3} model response. However both of them are more damped than the responses produced from TESF method.

These results allow inferring that: i) The TnESF method produce responses closer to the reference and more damped than those from the TESF method, ii) the TESF methods produce less peak difference during the fault interval than the TnESF method, as compared to the reference, iii) in opposition to the peak responses, the TnESF methods produce less oscillatory responses than the TESF method, as compared to the reference, and iv) as expected from the results in Figure 5.2, both TESF and TnESF methods produce responses which go to an of the order of 3 % larger steady-state than the reference response.

5.6 Saturation Modelling Effect on Electromagnetic Torque

It is usual to find research reports about saturation in induction machines, illustrating its effect on the stator current magnitude, [Therrien *et al.* 2012], [Arshad *et al.* 2010], [Bolik

2003]. This is probably due to the fact of most of them are focused on the machine, as working in motor operation mode. Considering the machine in generator operation mode and the fact that stator and rotor currents contribute to produce the electromagnetic torque, a change is made here selecting this variable to illustrate the saturation modelling effects. This assumption takes into account that it is a meaningful control variable for wind turbine applications. Three aspects are observed:

a) The shape of the starting oscillations, and the resultant steady-state
b) The time when the maximum torque is reached and its corresponding magnitude,
c) The damping when waveforms converge to the steady-state

For comparison purposes and to conveniently identify two L_h modelling alternatives, they are named L_{h_A} when $\gamma = 0.98$ and $k = 0.03$, and L_{h_B} when $\gamma = 0.97$ and $k = 0.16$.

5.6.1 Electromagnetic Torque Responses from OSF method

Figure 5.7 presents the time-varying electromagnetic torque start-up process responses, computed from one saturation function as combined with L_{mean}, L_{abc} and L_h saturation models. The shape at the starting is as expected [Krause *et al.* 2002], independent on the saturation model, as shown in Figure 5.7(a).

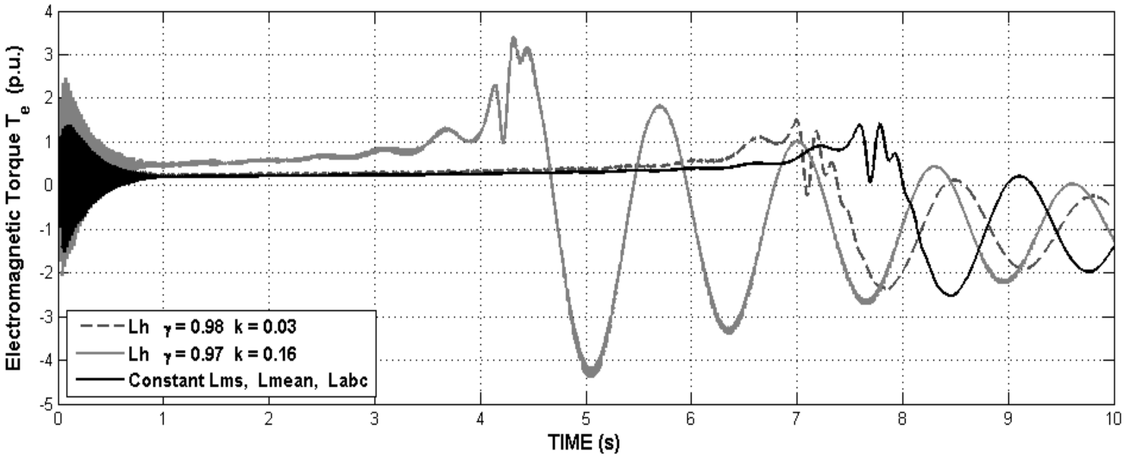

a)

The L_{ms}, L_{mean} and L_{abc} responses result identical, and it is assumed as the reference response. The breakdown torque, if saturation is neglected is 1.381 pu at7.592 s, in motor

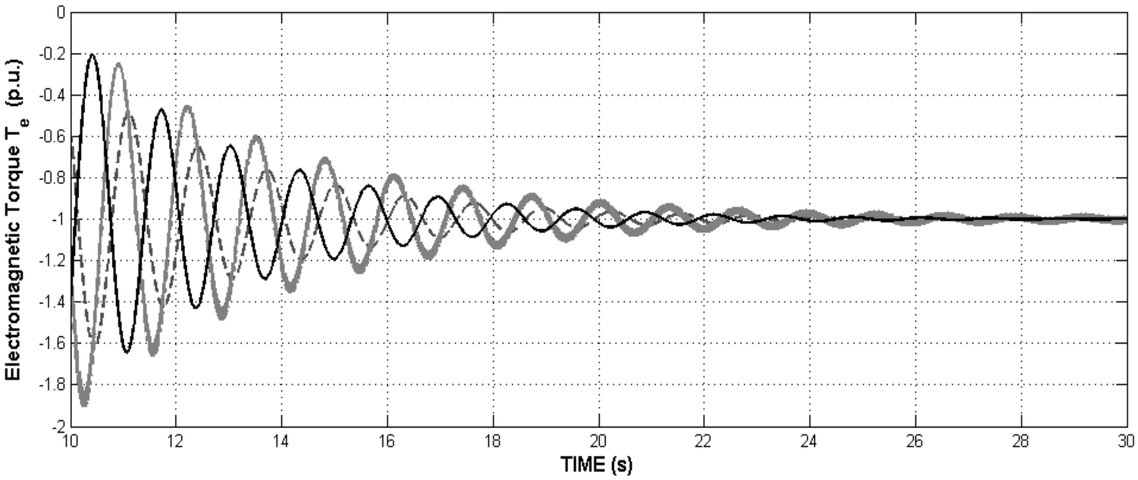

b)

Figure 5.7 Electromagnetic torque response, as affected by saturation models based in OSF, a) start-up process, b) convergence process to the steady-state.

mode and from the reference response The L_{h_A} saturation model response at the breakdown torque, deviates from it +8.8 % at 6.995 s, and the L_{h_B} saturation model deviates from it +148.1 % at 4.315 s. Given the k parameter variation in L_{h_B} relative to L_{h_A}, it suggests that the teeth harmonics effect through the k parameter is the responsible of these deviations.

The three responses in Figure 5.7 are almost ‘pure’ responses with very small and negligible high frequency oscillations.

Once the electromagnetic torque response from any model crosses the zero value going to the generator mode, it makes it with a low frequency damped oscillation. It is seen that the L_{h_B} alternative produces the largest low frequency oscillation, this is, teeth harmonics effect with larger k parameter values can put in advance the torque response and cause large torque damped low frequency oscillations, as shown in Figure 5.7(a). In Figure 5.7(b) this damping process keeps on smaller from the L_{h_B} saturation model than L_{h_A} saturation model.

As an inference, the effect of teeth saturation through the parameter k is advancing the torque response and producing a damped low frequency oscillatory process, once the breakdown torque is reached. The largest k parameter, the largest low frequency oscillations produced.

5.6.2 Electromagnetic Torque Responses from TSF type methods

Figure 5.8 shows this responses set from L_{abc} and L_h type saturation models.

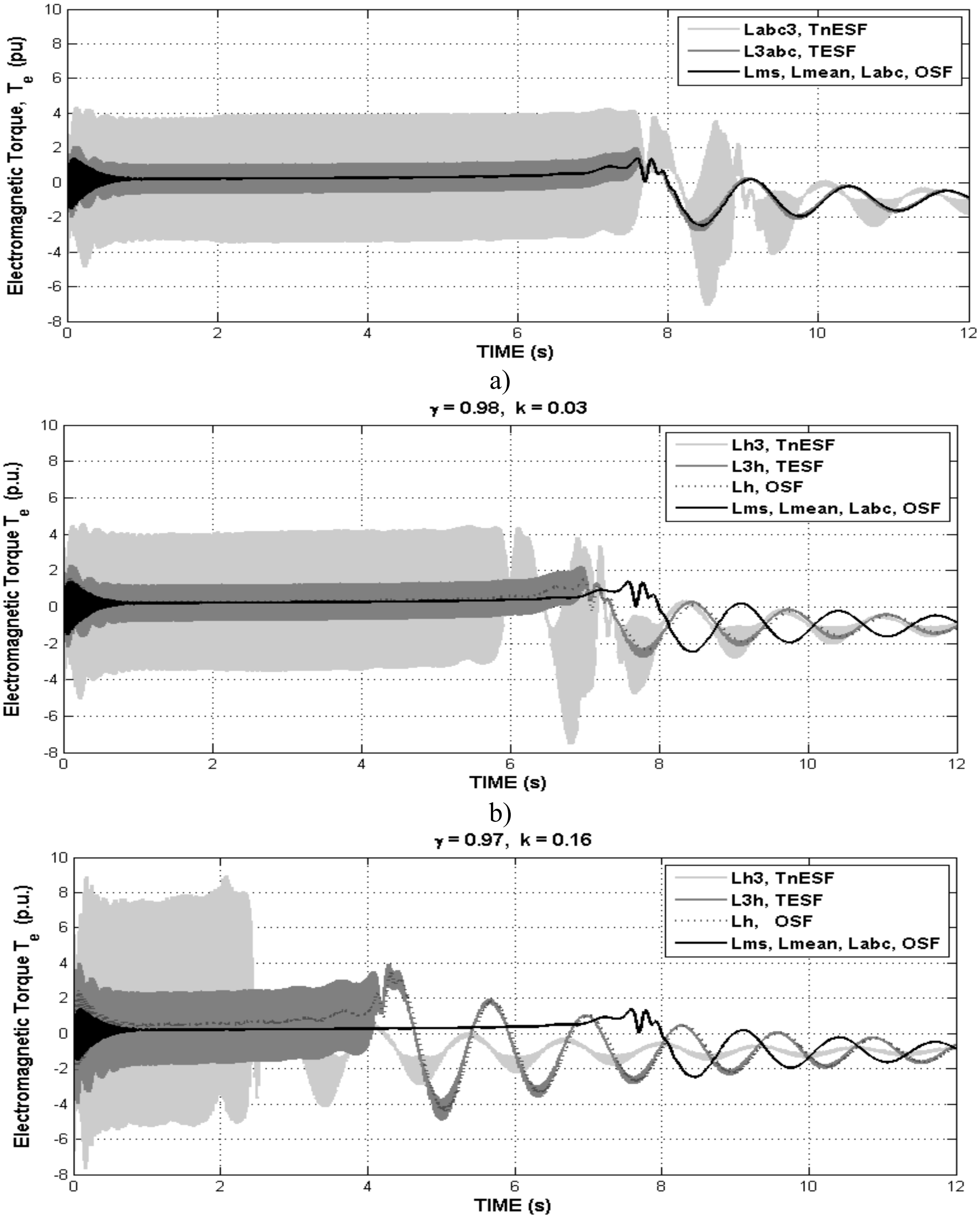

a)

b)

c)

Figure 5.8 Electromagnetic start-up torque response from TSF type methods, as affected by: a) L_{abc} type saturation models, b) L_{h_A} saturation model, c) L_{h_B} saturation model

It is seen that the electromagnetic torque T_e, as produced using constant L_{ms} parameter, or L_{mean} or L_{abc} saturation methods, results the same. Then, this response produced from the OSF method, is used here as a reference.

In (5.7) it is evident that, if $\gamma = 1.0$ and $k = 0.0$ in the L_h type saturation models, the teeth harmonic effect is zeroed and the mutual inductance terms recover their traditional value $L_{ms}/2$. However, this condition together to TESF or TnESF methods, leaves still enabled the effect of individual phase modifications in the diagonal terms. It reproduces the L_{abc} saturation model. Also in (5.7) it is manifested that the expected effect of the γ parameter is to decrease the voltage value, due to the effect of teeth harmonics.

Figure 5.8(a) shows the combination of TSF type methods with L_{abc} type saturation models, where the teeth harmonics effect are neglected. Figure 5.8(b) shows the combination of TSF type methods with L_{h_A} type saturation models, where the teeth harmonics effect with the parameters γ and k according to this thesis selection, are included. Figure 5.8(c) shows the combination of TSF type methods with L_{h_B} type saturation models. This modeling includes the teeth harmonics effect with the parameter k in a critical way.

If teeth harmonic effect is neglected as shown in Figure 5.8(a), the electromagnetic torque response from TESF-L_{3abc} method appears less oscillatory amplitude than that from TnESF-L_{abc3} method, although both follow the reference response. The amplitude of the oscillations going to the breakdown torque are of the order of 0.8 pu in the response from TESF method and 3.6 pu in the response from TESF method.

In opposition, under the existence of teeth harmonics contribution, if k increases and the electromagnetic response goes in advance and oscillations dramatically increase, as shown in Figure 5.8(b) and 5.8(c). Note that this is independent on the TSF type method, and if OSF method is used, the non-oscillatory response (dotted line) runs together to the TESF-L_{3h} response, with both L_{h_A} and L_{h_B} computational options.

As an inference, high frequency oscillations are built from the combination of saturation functions in Figure 5.5 and the instantaneous phase modification of the inductance matrix in the diagonal terms. However, the teeth harmonic effect can magnify the amplitude of the oscillations, as seen in Figure 5.8(c). Furthermore and through the k parameter, it produces an advance in the response. Figure 5.8 demonstrates that, if a ‘pure’ T_e response as the reference in this thesis appears when teeth harmonics are neglected, any light inclusion of them combined with TSF type methods manifest creating oscillating start-up process. Even with OSF method, teeth harmonics destroy the uniformity given by the reference torque response, as shown in Figure 5.6 and Figure 5.8(b) and 5.8(c) by the L_h saturation model.

In order to determine if the oscillatory behaviour is at least partially due to numerical stability, other solvers and integration steps in Matlab/Simulink® were probed. Table 5.2 presents the tested alternatives, where Ode15s is the solver used in this thesis. The response produced by TnESF method (light gray) and particularly the corresponding to L_{h3} saturation model in Figure 5.8(b) and 5.8(c), being in addition susceptible to the k parameter influence, is taken for the test.

Table 5.2 Computational characteristics for solver test comparison, using Matlab/Simulink®

SOLVER	TYPE - STEP	First Range/Step Size	Second Range/Step Size
Ode15s (Stiff/NDS)	VARIABLE	1-100 μs	0.5-50μs
Ode23t (Mod.Stiff/Trapezoidal)	VARIABLE	1-100 μs	0.5-50μs
Ode4 (Runge-Kutta)	FIXED	20 μs	10
Ode1 (Euler)	FIXED	20 μs	10

With the first range/step size all methods produce identical response. A simulation time of 10 s was used, in order to reproduce the start-up process. If this range or simulation time is reduced or amplified, as e,g, the second range/step size in Table 5.2, responses remains oscillatory. The amplitude of the oscillations does not change in any of the test alternatives. Also changes were done in γ and k parameters and oscillations remain meaningful. This computation test demonstrates that the torque large amplitude and high frequency oscillations in Figure 5.8 are mainly due to the combination of three saturation functions in Figure 5.5, and the instantaneous phase modification of the inductance matrix in the diagonal terms. Teeth harmonics support but they are not the cause of the noted high frequency oscillations

5.7 Conclusion

Given the no-load standard test data, a L_m-V saturation function is constructed, where voltages are assumed to be the average value of the three phases. Given the standard test characteristics and for *abc* modelling, the single phase processed data is assumed to represent the phase A only. Starting from this one saturation function, an *abc* main path magnetic saturation model with three saturation functions, is proposed. Saturation functions for phases B and C are assumed identical to phase A in the neighbourhood of it and with equidistant or non-equidistant characteristics.

This reasoning remarks the individual capability of phase windings to detect A, B, C phase voltages and produce individual currents, then individual fluxes and thus individual magnetizing inductances L_{mA}, L_{mB}, L_{mC} values. Consequently, each phase magnetizing flux contributes with a component of the total linking flux on the main path.

Furthermore, three saturation models are proposed. The first saturation model produces an average magnetizing inductance value. The second saturation model produces a phase distinguished magnetizing inductance. The third saturation model extends the second model to include teeth harmonics effect.

In this way, the specific aim proposed in the Introduction is fulfilled, and an *abc* time-varying magnetizing inductance results as time-varying stator voltage dependent.

Results show that the magnetizing inductance parameter variation is consistent with the saturation function models, i.e. when voltage drops the magnetizing inductance increases and vice versa. The voltage drops are illustrated by symmetric and asymmetric faults applied at the PCC, according to Appendix B. It is also demonstrated that the average value of the magnetizing inductance is less meaningful than other two models, which emphasize the phase contribution.

The magnetizing inductance differences point to point in the phase based saturation functions, including the respective slope between them, produce magnetizing inductance responses separation at each phase and consequently, wide oscillations in the electromagnetic torque. It is more visible in the start-up process, which is illustrated in this thesis. This fact remarks the need to use well calibrated and very exact instrumentation in the no-load test, as a basic measure to be taken into account.

* * *

6

Time-Varying and Voltage-Flux Dependent Non-linear Iron-Losses Resistance *abc* Function, for Sinusoidal and No-Sinusoidal Voltage Supply

6.1 Introduction

As an engineering effort to represent the iron-losses for large induction generators and to take into account aspects as,

i) The non-linear behaviour of resistance representing iron losses in the general arrangement of a non-linear saturable inductor [Chua 1971],

ii) Frequency and induction dependant iron losses, eddy-current loss and hysteresis-loss coefficients, having a sinusoidal supply [Boglietti *et al*. 2010],

iii) High frequency switching as produced in solid-state power electronic interface in grid-connected solutions, and their consequent increment of iron losses through: current waveform deformations, varying flux linkage, slip, and high frequency currents due to the magnetic materials used [Boglietti *et al*. 1996], [Benhaddadi *et al*. 1998], [Boglietti *et al*. 2007],

iv) The inclusion of hysteresis and magnetic saturation effects [Ranta *et al*. 2009],

v) The need to avoid possible adjustments in the control strategy design when iron losses are neglected,

vi) The usual strategy to model an iron-losses resistance, parallel-connected to the magnetizing branch in a coil model, a robust data-sheet and non-linear *ABC* resistance to model iron losses, is proposed in this research.

The model is based in its ability to reliably represent the desired transient and steady-state iron-loss profile. In the transient state, the hysteresis losses dynamic effect, acts based on voltage-flux variations and referred to the no-load iron-loss resistance value. In the steady-state, both eddy-current and hysteresis losses effects act together to the power converter effects, to reproduce an iron-loss resistance closed to the no-load value. Worldwide concepts like iron-losses and induction are adopted instead of local ones such as core-losses and flux density. Instead of neglecting stator current harmonics and saturation, as usual, a try is made to include them as coming from the power electronic interface, and also the consideration that the equivalent time constant of the iron-loss phenomena is much smaller than the stator time constant [Boglietti *et al*. 2007], [Shinnaka 1989]. Additionally, the iron-loss current is suitably added to the stator current, to include its effect [Ranta *et al*. 2009].

6.2 Iron-loss Components

In [Khalig *et al*. 2005], [Boglietti *et al*. 2007], [Popescu *et al*. 2010], it is established that for sinusoidal supply, iron losses P_h, eddy-current loss k_e and hysteresis-loss k_{hy} factors, are frequency f and induction B dependent. A general expression for the total iron losses P_h is the combination of eddy-current losses -subindex e, hysteresis losses -subindex hy,

$$P_h = k_e(f,B)f^2B^2 + k_{hy}(f,B)fB^x \qquad (6.1)$$

where x is the Steinmetz coefficient and every magnetic material has its respective k_e and k_{hy} constants [Boglietty *et al*. 2003]. In (6.1) a by excess losses term can be added, but it is excluded because it represents a few per cent value of the eddy-current losses and is not determinant for the modelling purposes.

6.2.1 Slip Dependent Eddy-Current Loss Resistance

Equation (6.1) can be written for stator (*S*) and rotor (*R*) iron-losses taking into account the slip based rotor frequency, and eddy-current component can be evaluated for near to and higher than the rated frequencies. Under these conditions, hysteresis losses can be neglected and the stator and rotor components result to be [Khalig *et al*. 2005],

$$P_{e,S} = \frac{f_s^2 B^2}{1/k_e} \tag{6.2}$$

$$P_{e,R} = \frac{(slip \times f_s)^2 B^2}{1/k_e} \tag{6.3}$$

where f_s is the stator frequency and the denominator $1/k_e$ has a resistance units. It is known that in [IEEE-Std.-112 2004] the eddy-current losses are represented by a resistance R_{Fe}. In (6.2) and (6.3), both stator and rotor eddy-current losses resistances are associated to $1/k_e$. Adding (6.2) and (6.3), and introducing an *abc* separation to evaluate the phase contribution, the total eddy-current losses resistance results to be,

$$R_{Fe,abc}^{S+R} = \frac{R_{Fe,abc}}{1+slip^2} \tag{6.4}$$

and $R_{Fe,abc}$ is calculated as the inverse value of the respective conductance $G_{Fe,abc}$ as,

$$G_{Fe,abc}(t) = \frac{P_{e,abc}(e_{abc})}{[e_{abc}(t)]^2}\left(1+\frac{X_{1,abc}}{X_{m,abc}}\right)^2 \tag{6.5}$$

where $P_{e,abc}$ is a time-varying iron-loss function, as dependent on the generated voltage e_{abc}, X_l is the stator reactance and X_m is the magnetizing reactance, both of them assumed per-phase values. As previously announced, instead of neglecting the magnetic saturation, it is included in X_m according to the modelling in Chapter 5.

A similar computational procedure to (6.1), associated to the stator and rotor hysteresis-loss components, can be evaluated for low frequencies. For this case the eddy-current loss component can be neglected, resulting in,

$$R_{hy,abc}^{S+R} = \frac{R_{hy,abc}}{1+slip} \tag{6.6}$$

In (6.6), it is assumed that the hysteresis resistance can be measured in the no-load test, as is the case of the eddy-current losses resistance R_{Fe}. However, it can be inferred through modelling, as explained in the next Section.

6.2.2 Non-Linear Iron-Loss Resistance

The iron-loss resistance is conveniently assumed as the parallel combination of two resistances, one representing the eddy-current losses and the other one, the hysteresis losses [Ranta *et al*. 2009]. The hysteresis resistance is classified as a first-order non-linear resistor in [Chua *et al*. 1970], [Chua *et al*. 1971], it inherently has dynamic behaviour, and by spatial vector approach it is defined in [Ranta *et al*. 2009] as,

$$R_{hy} = \frac{R_{Fe}\,|\,e\,|}{k\,|\,\psi\,|^{n-1}} \tag{6.7}$$

where |.| is understood as the magnitude of the voltage and flux spatial vectors respectively, n is defined as a constant between 1 and 2, and k is a tuning parameter. Three characteristics deserve the attention in (6.7):

a) By spatial vector definition, an only one hysteresis loss resistance is expected with identical *ABC* phase contribution, which protects the entirely symmetric machine paradigm. It means that for this research purpose, phase variables would be computed later by backward transformation. This is an indirect *ABC* computational process, in certain way similar to $abc \rightarrow qd \rightarrow abc$ transformation, what this thesis is avoiding. Furthermore it includes a spatial vector induction machine model, which is out of the scope of this thesis.

b) To be consistent with (6.1), the '*n*-1' exponent in [Ranta *et al*. 2009] can be related to the Steinmetz coefficient in [Boglietti *et al*. 2003] and replaced by N. In this way, only *k* would be tuned by simulation to fit in combination to eddy-current losses, a closed to no-load iron-loss resistance in the steady-state, and

c) If the denominator in (6.7) should have volt units, then if ψ is in weber (volt-second), *k* has the dimension of 1/s. It is expected a low value for *k* in order to proportionally affect the stator flux, and take into account the effect of other magnetic core characteristics, which are not explicitly represented in (6.7).

The Steinmetz coefficient is dependent on magnetic material, frequency and flux density. In [Akiror 2012] several Steinmetz coefficient ranges for several materials are reported, with sinusoidal supply only and for up to 1.7 T and 1000 Hz. According to these conditions, a synthesis for the classical Steinmetz coefficient is between 1.76 and 2.085. From a modified model [Akiror 2012], it is between 1.08 and 1.99. In [Boglietti *et al*. 2003] the range is between 1.74 and 2.12, as measured in different materials with different physical and magnetic properties, and switching frequency between 2 and 3 kHz.

Considering these comments, a modification of (6.7) to directly compute R_{hy} in phase coordinates is proposed as,

$$R_{hy,abc} = \frac{R_{Fe,abc} e_{abc}}{k_{abc} \psi_{abc}^{N}} \tag{6.8}$$

where the space vectors magnitudes have been replaced by per-phase stator voltage and flux RMS values. Moreover, *k* values are proposed to be tuned in each phase, which makes possible the introduction of individual phase magnetic asymmetries.. Combining (6.1) and (6.4), the per-phase *ABC* eddy-current losses can be defined as,

$$P_{Fe,ABC} = \frac{e_{ABC}^{2}}{R_{Fe,abc}}(1 + slip^{2}) \tag{6.9}$$

The two components in (6.9) constitute an adjusted eddy-current power of the form,

$$P_{Fe,ABC} = P_{e} + \Delta P_{e} \tag{6.10}$$

where, P_e is the eddy-losses in the steady-state, and

$$\Delta P_{e} = slip^{2} \times P_{e} \tag{6.11}$$

gets the squared value of the rotor frequency. Linking now (6.1), (6.6) and (6.8), it is possible to define per-phase *ABC* hysteresis losses as,

$$P_{hy,ABC} = \frac{(k_{abc}\psi_{abc}^{N})e_{abc}}{R_{Fe,abc}}(1 + slip) \tag{6.12}$$

Again the second component in (6.12) acts as a slip dependent correction summa term. With these powers, the total iron losses for sinusoidal supply can be expressed by,

$$P_{h,ABC} = P_{Fe,ABC} + P_{hy,ABC} \tag{6.13}$$

6.2.3 The Effect of Voltage Supply

Considering the implication of power converter interface [Boglietti *et al*. 2001], [Boglietti *et al*. 2003], [Ionel *et al*. 2008], and what this investigation concerns, it is established:

i) Given the computational paradigm change from spatial vectors magnitude in (6.7) to RMS phasor values in (6.8), it is tried a quality of precision to efficiently represent the rotational magnetization effects.

ii) The peak induction value is proportional to the average of the rectified supply voltage, which makes vary the hysteresis-losses [Boglietti *et al*. 2003], and

iii) The eddy-current losses as dependent of the rate of the induction (dB/dt), can be associated to the RMS voltage supply value.

As a consequence, the proposal in [Boglietti *et al*. 2003] is extended to phase coordinates A,B,C, to adjust (6.13) as,

$$P_{h,ABC} = \chi_{ABC}^{2} P_{Fe,ABC} + \eta^{x} P_{hy,ABC} \tag{6.14}$$

with,

$$\eta = \frac{U_{avg}}{U_{1,avg}} \tag{6.15}$$

$$\chi_{ABC} = \frac{U_{rms,ABC}}{U_{1,rms,ABC}} \tag{6.16}$$

where, U_{rms} in (6.12) the root mean square of the supply phase voltage, $U_{1,rms}$ is the respective similar value for the fundamental component, and U_{avg} in (6.13) is the average value of the rectified supply phase voltage and $U_{1,avg}$ is the similar value for the fundamental component. The parameter x is the Steinmetz coefficient for the magnetic lamination used.

Then, as proposed by the present research, the total iron-losses resistance results to be,

$$R_{h,ABC} = \frac{e_{rms}^{2}}{P_{h,ABC}} \tag{6.17}$$

6.2.4 Proposed Iron-Loss Non-Linear Resistance

If (6.14) is computationally processed according to (6.8), (6.9) and (6.10), a total iron-loss resistance, excluding iron-losses separation and 'partially' including switching effects, can be obtained. As an analogy with the non-linear resistance defined in [Ranta *et al*. 2009], using now RMS values instead of spatial vectors and including the slip effect, it results as,

$$R_h(e,\psi,slip)_{ABC} = \frac{R_{Fe,ABC}}{slip^2 + ((1+slip)k_{ABC}\psi_{ABC}^{N} / e_{ABC}) + 1} \tag{6.18}$$

or following the idea in [Ranta *et al*. 2009] according to (6.7), and using N instead of n-1,

$$R_h(|e_s|,|\psi_s|,slip)_{ABC} = \frac{R_{Fe,ABC}}{slip^2 + ((1+slip)k_{ABC}|\psi_s|^{N} / |e_s|) + 1} \tag{6.19}$$

If instead of this, iron-losses separation is included and full switching effects as in (6.14), a very significant improvement is achieved. Then R_h in ohms results to be,

$$R_h(e,\psi,\eta,\chi)_{ABC} = \frac{R_{Fe,ABC}}{\chi_{ABC}^{2}(1+slip^2) + \eta^{x}(1+slip)k_{ABC}\psi_{ABC}^{N} / e_{ABC}} \tag{6.20}$$

or following the idea in [Ranta *et al*. 2009] and according to (6.7),

$$R_h(|e_s|,|\psi_s|,\eta,\chi)_{ABC} = \frac{R_{Fe,ABC}}{\chi^2_{ABC}(1+slip^2)+\eta^x(1+slip)k_{ABC}|\psi_s|^N/|e_s|} \tag{6.21}$$

which, according to the ratios in (6.16) and (6.17), besides to include the features in (6.18) and (6.19) are useful for both, sinusoidal and not sinusoidal voltage supply.

It is to expect that a current $i_h(v)$ flows by the branch containing R_h. It is evaluated as a function of the applied voltage. The most accurate option is with the internal voltage e taking into account the voltage drop at the stator windings, and an approached option uses the applied voltage v at the machine terminals. It is,

$$i_{h,ABC} = \frac{e_{ABC}(t)}{R_{h,ABC}} \approx \frac{v_{ABC}(t)}{R_{h,ABC}} \tag{6.22}$$

In order to include it in the induction machine operation, this research algebraically adds it to the stator current, at each time step, as a correction function.

Additionally, the hysteresis current i_{hy} can be computed as,

$$i_{hy,ABC} = \frac{e_{ABC}(t)}{R_{hy,ABC}} \approx \frac{v_{ABC}(t)}{R_{hy,ABC}} \tag{6.23}$$

6.2.4.1 Tuning the N and *k* Parameters

Fixing the η and χ parameters to 1.0, the effect of the power converter is neglected in (6.19), and then N and the k parameters are tuned by couples to produce an induction machine iron-loss power value, closed to a reference power.

This reference is selected taking into account that: i) A no-load test measured power P_e representing the eddy-current losses, is available, ii) As a fact the “by excess losses” are not quantified in the no-load test and thus, a "global eddy-current losses" (GEC) paradigm is created to include them in the classical concept, iii) According to [Boglietti *et al*. 2003] for soft magnetic materials, these GEC are expected to increase of the order of 5 % at 50Hz due to load induction **B** increments. This is the maximum expected value. Identical assumption should be applied to hysteresis losses. In this research, once R_{Fe} in (6.5) is produced with the adjusted eddy-current power $1.05(P_e)$, it considers the effect of other computations, as in (6.9) and (6.12). Considering the data sheet for the induction machine used in this investigation, and using the adjustment criterion, it can be known that the eddy-current power is of the order of 1.05(11910) = 12505.5 Watts. Note besides that if N = 1 and k = 1 in (6.8) the non-linear effect they introduce is cancelled, although the R_{hy} values are not zeroed. In this way the total iron-losses power produced in these conditions, which involves eddy-current and hysteresis losses, is taken as the real reference power. It results of the order of P_h = 12972 Watts. This reference value can vary according to the per-cent quantity assumed to account for the load induction **B** increments, which is an input value.

The results in [Ranta *et al*. 2009] about the N and k tuning, were conducted by finite element analysis and experiments in a 45 kW, 400 V, 50 Hz cage induction machine. For this research purposes, several N-k couples were computationally tested for a 2 MW, 960 V, 50 Hz cage induction machine. They are summarized in Table 6.1 for a N range between 0.1 and 2.9.

Table 6.1 Computational tuning of N and k parameters for a 2 MW, 960 V, 50 Hz cage induction machine. The reference iron-loss power is 12972 Watt.

N	k	P_h (Watt)	Error (%)	R_{Fe} (ohm)
2.9	0.2	13005	0.25	213.6
2.5	0.4	13011	0.3	213.3
1.9	0.5	12978	0.05	213.8
1	1	12963	0.07	214
0.1	2.2	12954	0.14	214.3

Changing the *n-1* parameter in (6.7) [Ranta *et al*. 2009] by N in this investigation, has allowed to include the Steinmetz coefficient *x* range (1.74 – 2.12) for soft magnetic materials, into the N range. It is assumed that they are related, because they are conceived to apply for the same magnetic material.

6.2.4.2 Power Converter η-χ Parameters

From the η and χ definitions in (6.16) and (6.17), it is assumed [Mohan *et al*. 2003] they are near to 1.0. They can be assumed to vary due to operation and commutation frequencies, harmonic distortion rate of the power converter and 'true' measurements of average and RMS voltage values. They depend on power converter and induction machine operating conditions. In order to suitable select them, it is assumed that iron-losses increase in a large induction generator when it interacts with the sinusoidal voltage supply through a power converter [IEC 60034-2-1 2007], [Boglietti 2003].

To solve the uncertainty on η and χ parameters, a computational experiment was designed. Fixing to 1.0 one of the parameters, the other is varied in a widely range between 0.7 to 1.2, and the resulting R_h value in (6.19), is compared to the reference R_{Fe} = 224.4767 ohm, as computed from the data-sheet following the methodology in [IEEE Std-112 2004]. Steinmetz coefficient x = 1.9, N = 1.9 and k = 0.5 were also selected, according to Table 6.1. Table 6.2 shows this experiment results.

Table 6.2 Looking for the η or χ largest influence on the non-linear iron-loss resistance

η	χ	P_h	R_h
1	0.7	2128	434.6
1	1.2	6232.8	148.6
0.7	1	4137	214.36
1.2	1	4334	213.5

As it is observed, the largest R_h change comes from χ parameter variations. Relating this computational experiment with [IEC 60034-2-1 2007], [Boglietti *et al*. 2003], four assumed iron losses P_h increments of 3, 5, 10 and 15 % in (6.14) are explored. Then η - χ couples to match these values are selected. Results are shown in Figure 6.1

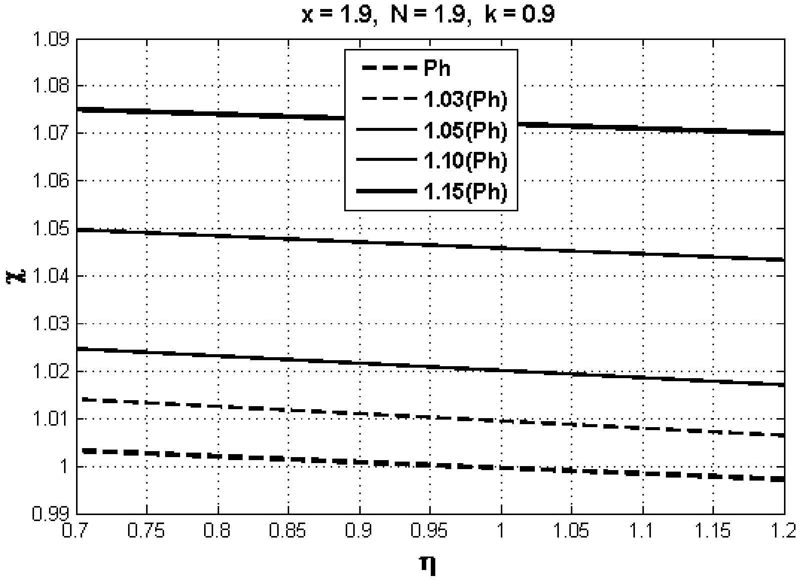

Figure 6.1. η and χ relationship, for 3, 5, 10 and 15 % of iron-losses power increment

Three aspects are highlighted about the power converter parameters, as synthetized in Figure 6.1. In it: i) there are n, k and Steinmetz coefficient *x* conditions to validate a reliable power converter operative zone for target iron-losses, ii) given a power losses target curve, χ decreases as η increases and vice versa, iii) once fixed an operative η value, the corresponding χ value increases as the iron-losses increase and vice versa. Laying on Figure 6.1, any power converter operating point can be selected and the resultant induction machine iron-losses can be computed.

6.2.4.3 Iron-Losses Modelling alternatives

Despite of the per-phase *ABC* contributions computation, it is assumed that each model produces an *ABC* average iron-loss resistance R_h and power P_h responses. It matches the entirely symmetric induction machine paradigm.

As a synthesis of the proposed modelling and for comparison purposes, three modelling alternatives are compared:

i) A **Slip** model, where ***eddy-current losses*** are affected by the rotor mechanical slip according to [Khalig *et al.* 2005]. In this case a time-varying R_h resistance value is computed as a function of the actual *ABC* terminal voltages.

ii) A non-linear **Flx1** model as in (6.18) is a modification of the proposed in [Ranta *et al*. 2009] to involve RMS values, representing both ***eddy-current*** and ***hysteresis losses*** involving both stator and rotor magnetic properties and also the rotor frequency through the mechanical slip. In this case the R_h resistance is dependent on stator phase voltage and stator and rotor fluxes, besides of the mechanical slip. Special N and k parameters are used to tune the hysteresis component. Several N-k couples well performing in the entire model are proposed in the Section 6.2.4.1. If Flx1 is associated to a spatial vector computation as in [Ranta *et al*. 2009], it is named **Flx1-SV**

iii) The **Flx2** model extends the non-linear **Flx1** model in (6.19) to represent in addition the effect of the power converter, for no sinusoidal supply. This model involves η and χ parameters as defined in (6.15) and (6.16), respectively. If Flx2 is associated to a spatial vector computation, it is named **Flx2-SV**

6.3 Time-varying Iron-Losses Resistance Parameter

The time-varying features of the iron-loss resistance R_h are explored for asymmetrical line-to-ground LG and symmetric three-phase LLL faults. The corresponding setup, fault characteristics and conditions are shown in Appendix B.

6.3.1 Voltage Supply Affected by Asymmetric Line-to-Ground Fault

Figure 6.2 shows the iron-loss resistance R_h responses, as *ABC* average in Figure 6.2(a) and per-phase contributions in Figure 6.2(b). Dashed lines correspond to no-fault responses. **Flx1** and **Flx2** iron-loss models have in common N = 1.9 and k = 0.5 parameters, taken from Table 6.1. **Flx2** iron-loss model has been simulated for two couples of η-χ power converter parameters, as taken from Figure 6.1.

The simpler **Slip** model appears as the top magnitude for the R_h response. It certainly hides hysteresis losses effects, but trustable reproduces eddy-current losses effects. This is the reason why out of the fault interval, all RMS based models appear dynamically equivalent. While the SV based models, i) are slightly down by around 0.47 % relative to the RMS based models, and ii) are very oscillatory, during the fault interval with an amplitude of the order of 2.27 %. The oscillation resembles a waveform of a complete wave rectification. It is also observed that the model responses computed by RMS voltage and fluxes values, act very close to the peak of the oscillations from the SV models. Once the fault is released, there is a very short low-frequency oscillation before reaching the steady-state. For each iron-loss RMS based model, the difference between the no-fault (slip model) response and the corresponding LG fault response is of the order of 2.6 %.

From other point of view, the response from **Flx1** model deviates decreasing around 0.9 ohms or 0.42 %, and as compared to the Slip model response. The **Flx2** model deviates decreasing 9 ohm (4.19 %) when $\eta = 0.95$, $\chi = 1.02$, which corresponds to a point closed to the 5 % increment of the reference iron-losses in Figure 6.1.

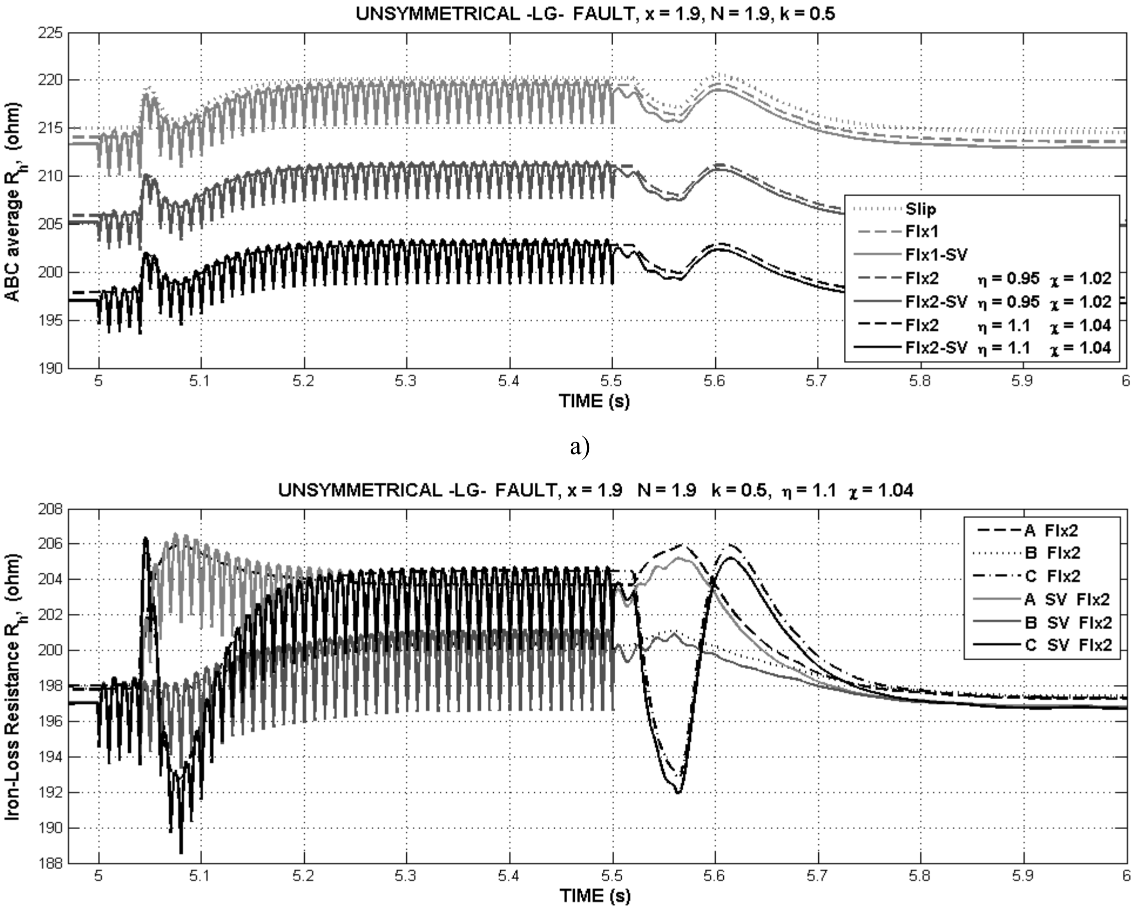

a)

b)

Figure 6.2 Iron-losses resistance responses when a LG fault is applied at PCC, a) for Slip, Flx1 and Flx2 iron-losses models, as an *ABC* average, and b) *ABC* phase contributions in the Flx2 model.

Meanwhile, the **Flx2** model deviates decreasing 17 ohm (7.9 %) when $\eta = 1.1$, $\chi = 1.04$, which corresponds to a point closed to the 10 % increment of the reference iron-losses in Figure 6.1. Other words, when the operating point of the power converter brings an increase of the iron-losses, the R_h decreases.

Figure 6.2(b) is an *ABC* phase R_h response, illustrated as an example for the **Flx2** and **Flx2-SV** models. With the emphasis of this research in individual phase contribution, it demonstrates that: i) the dominant effect on the response in Figure 6.2(a) is from the C phase contribution. Also the effect of the Fluxes in (6.8) is more determining than de drop of the voltages, ii) the *ABC* average response in Figure 6.2(a) misses specific phase contributions, which are larger in most of the cases. For example, R_h in phase C transiently presents peak contribution larger than those seen in Figure 6.2(a), iii) by simulation it is established without any doubt that, the other iron-losses models react with similar *ABC* phase responses, and related to their respective magnitudes in Figure 6.2(a).

As a summary: i) all iron-loss models responses waveforms, are identical to the **Slip** model waveform, ii) the effect of the non-linear model **Flx1** is to decrease the R_h value, as compared to the **Slip** model, and iii) the **Flx2** model, including the power converter and due to voltage quality variations through the η and χ parameters, adds even larger reductions to the R_h value, proportional to the iron losses increments they produce, iv) the phase distinguished R_h response has more meaningful information about the step-by-step phase contribution on the time-varying iron losses response.

From simulations can be inferred that, due to the hysteresis resistance is of the order of 2000 ohm, its parallel combination with the eddy-current resistance of the order of 200 ohm, produces again a resultant resistance of the order of 200 ohm too. Also the time-delay in the RMS based model responses, appearing immediately after the fault is inserted and released, is more a computational weakness in the RMS voltage computation than a physical feature.

6.3.2 Voltage Supply Affected by Symmetric Three-Phase Fault

Figure 6.3 shows this fault condition, and it is representative of both *ABC* average and phase distinguished iron-losses R_h responses, for each iron-loss model. All phase responses match each other and correspond in addition to the phase voltage drops.

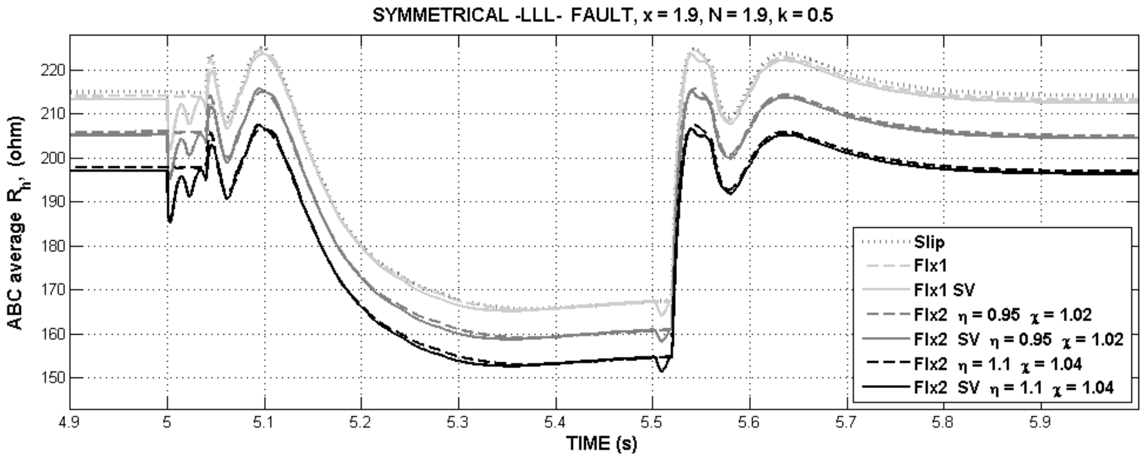

Figure 6.3 Iron-losses resistance responses when a LLL fault is applied at PCC, for Slip, Flx1 and Flx2 iron-losses models, and both *ABC* average and *ABC* phase contributions.

It is observed that: i) as in Section 6.3.1, all iron-losses model responses present identical time-varying waveforms to the **Slip** model, ii) at the beginning of the fault interval and also at the beginning of the post-fault, there are low-frequency oscillations as in the case of LG fault, iii) the **Flx1** model response looks closer to the **Slip** response than for the case of LG fault in the Section 6.3.1, iv) the R_h deep drop responses in the fault interval is now larger than in the LG fault case. Relative to their own no-fault characteristics (dashed lines), the **Slip** model presents a 23 % drop and it matches **Flx1.** The **Flx2** model has an average deep drop value of the order of 22.7 %, v) the effect of the power converter through the **Flx2** model is also to reduce the magnitude of the R_h response, and vi) the hysteresis losses effect is unrevealed.

6.4 Time-varying Iron-Losses Power

6.4.1 Voltage Supply Affected by Asymmetric Line-to-Ground Fault

Figure 6.4 shows the time-varying hysteresis losses. An ABC combination is presented in Figure 6.4(a) and the individual phase contributions in Figure 6.4(b). For the combination, each phase contribution is assumed to be 1/3 of the total power. In agreement to Section 6.2.4.3, this hysteresis power loss is not computed in the **Std** and **Slip** models.

Clearly, the hysteresis losses in Figure 6.4 are too small per cent values, in the base of the 2 MW machine power. **Flx1** and **Flx2** and also **Flx1-SV** and **Flx2-SV** iron-losses models produce responses matching each other, respectively, as shown in Figure 6.4(a).

The first pair, once the fault is inserted, softly deviate from the pre-fault value to a lower constant value, and when the fault is released, they recover to the pre-fault value again. With the second couple, once the fault is inserted, response oscillates with high frequency and the amplitude duplicating the pre-fault value.

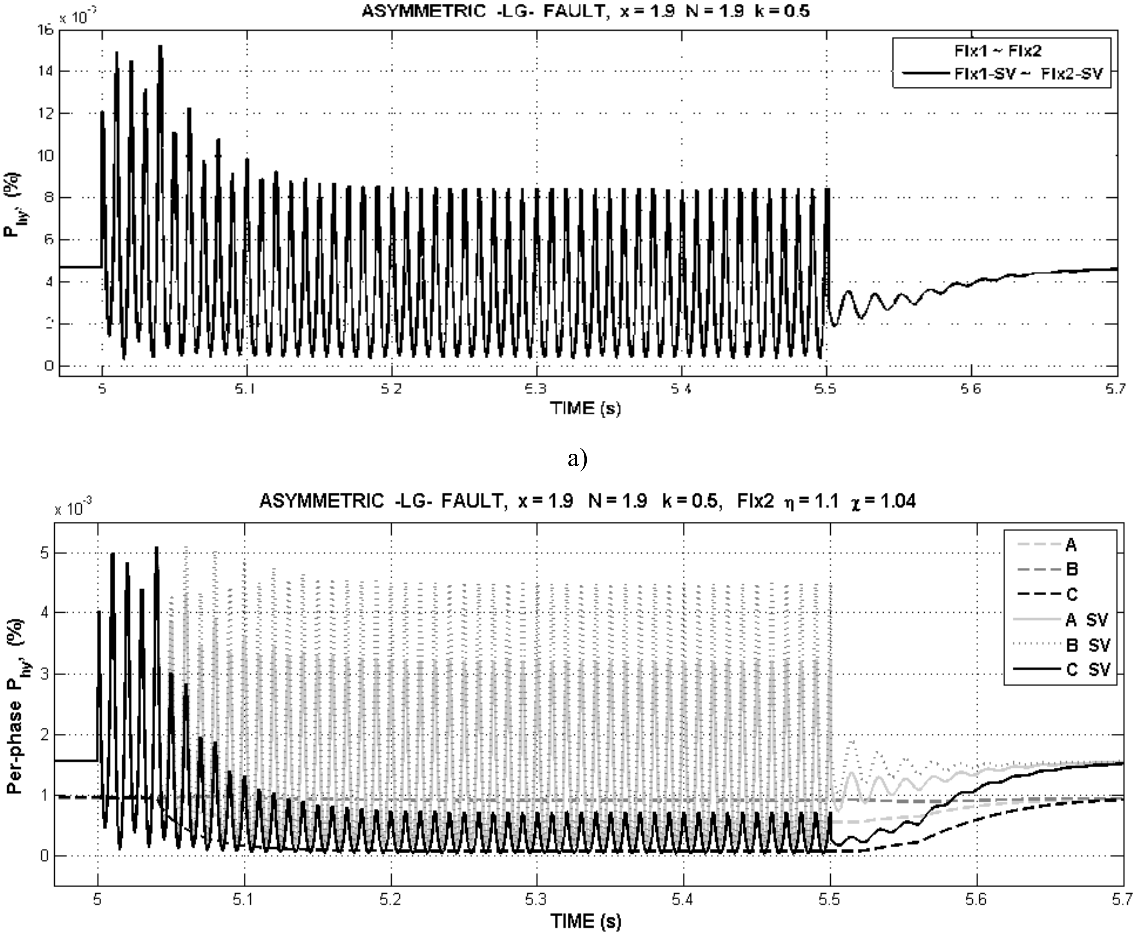

a)

b)

Figure 6.4 Hysteresis-losses power response when an asymmetrical LG fault is applied at PCC, a) *ABC* combination, b) individual *ABC* phase contributions

The per-phase responses in Figure 6.4(b) show that during the fault interval, the phase C contribution largely decreases as the fault duration increases. For a given time, each point in Figure 6.4(a) responses corresponds to the addition of the three corresponding points in Figure 6.4(b). In that addition, phase B contributes more than phase A and this more than phase C. In this transient process, being asymmetrical the phase contributions, it is not true that every phase equally contributes, as the commonly established knowledge.

As an example and with the RMS computational method here proposed, at 5.4 s can be read in Figure 6.4(b) that phase **C** contributes with $0.065\text{x}10^{-3}$ %, phase **A** with $0.545\text{x}10^{-3}$ and phase **B** with $0.905\text{x}10^{-3}$. The addition of these figures gets $1.515\text{x}10^{-3}$, as seen in Figure 6.4(a). This is interpreted here, as the magnetic load in the iron is asymmetrical, due to phase voltage and flux asymmetries and mechanical slip time-variations. This agrees with (6.8) and (6.12), where these variables are the responsible for hysteresis loss phase variations.

Due to the hysteresis phase power loss waveforms are similar to the phase voltage drops, it is inferred that the phase voltage effect is dominant. While in responses under the SV computational method, voltages and fluxes are proportionally responsible for the oscillation. Both of them oscillate when the fault is applied.

Figure 6.5 illustrates the total stator/rotor and eddy-current/hysteresis iron-losses. An *ABC* combination is presented in Figure 6.5(a) where each phase contribution is assumed to be 1/3 of the total power. The individual phase contribution in Figure 6.5(b), corresponds to an specific case of the **Flx2** model.

As it is evident, the waveform for the total losses has some similarities to the obtained for the hysteresis losses power P_{hy}, through the RMS approach.

During the fault interval in Figure 6.5(a), total iron-losses responses present a deep drop relative to their pre-fault values. These deep drops in per-cent values are of the order of 0.2521 for the **Slip** model, 0.2620 for the **Flx1** model, 0.2733 for the **Flx2** model when $\eta = 0.95$ and $\chi = 1.02$, and 0.2819 for the **Flx2** model when $\eta = 1.1$ and $\chi = 1.04$. The deviation of the iron-losses models relative to the **Slip** model response increases as the iron-losses includes more significant parameters. In the pre-fault time, this deviations are 0.0643 for the **Flx1** model, 0.0403 for the **Flx2** model when $\eta = 0.95$ and $\chi = 1.02$, and 0.077 for the **Flx2** model when $\eta = 1.1$ and $\chi = 1.04$.

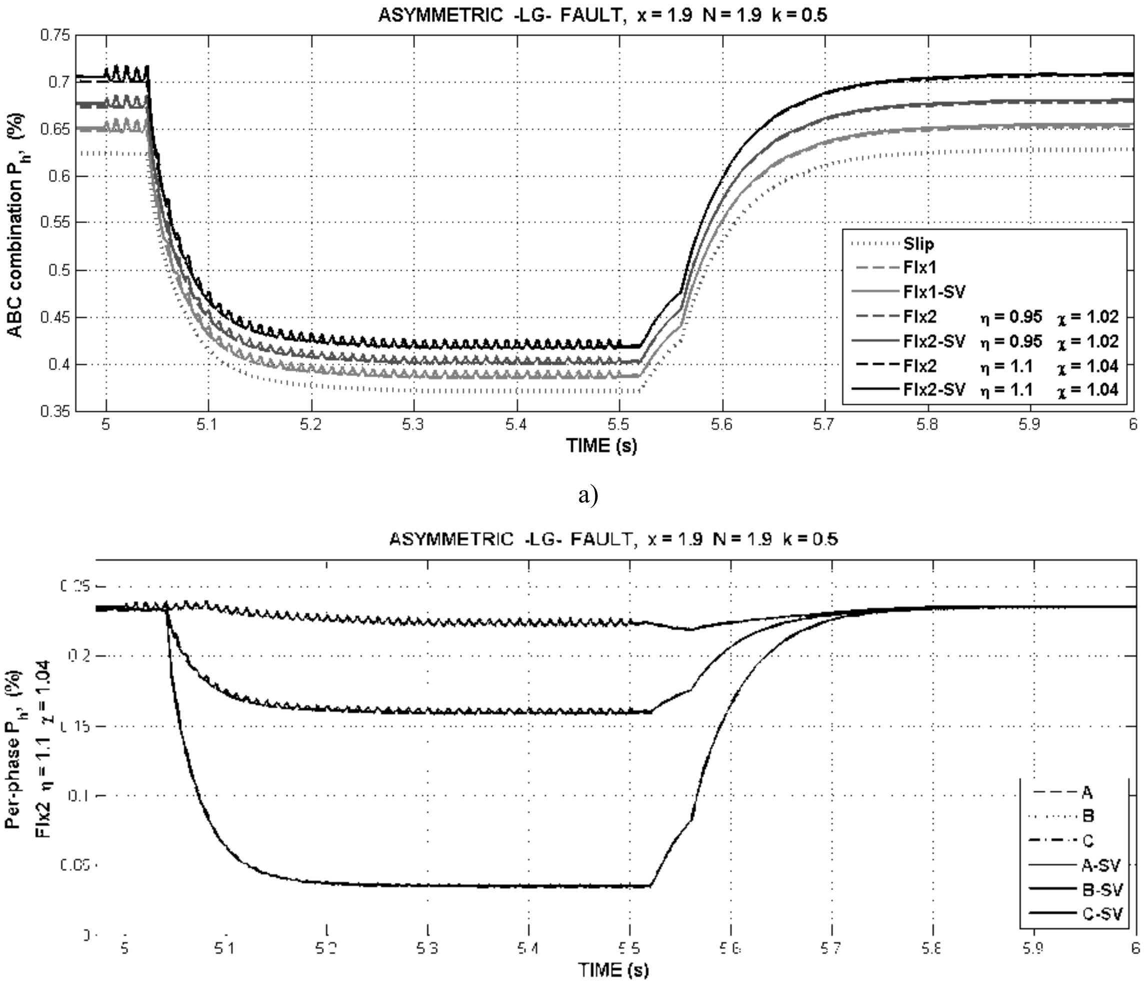

a)

b)

Figure 6.5 Total iron-losses power response when an asymmetrical LG fault is applied at PCC, a) *ABC* average, b) individual *ABC* phase contributions

It is inferred then, i) the deep drop increases as the iron-losses increases, and ii) deviations from the Slip model increase as the iron-losses increases at the steady-state, but during the fault interval they trend to decrease. As observed, the SV modelling introduces a small oscillation, which is related to the hysteresis resistance. The RMS modelling responses appear just as at the bottom of this oscillation, for each iron-loss model.

After the fault is released, the recovery process softly and uniformly takes the responses to their pre-fault values.

Figure 6.5(b) reveals that for the specific asymmetrical conditions in this investigation, the major contribution for the total iron-losses comes from the phase **B**, an intermediate contribution from the phase **A** and the smallest contribution from the phase **C**. Again it is interpreted as, given an asymmetrical condition, there is an asymmetric magnetic loading in the iron of the induction machine, where each phase has its own contribution.

6.4.2 Voltage Supply Affected by Symmetric Three-Phase Fault

In Figure 6.6(a) the *ABC* combined hysteresis iron-losses responses are presented when a symmetric three-phase LLL fault is applied at the PCC, and in Figure 6.6(b) the corresponding individual *ABC* phase contributions.

As a general statement, in Figure 6.7(a) the hysteresis loss waveform, from all iron-losses models, follows in the fault interval the RMS voltage drop waveform. This behaviour justifies the RMS computational method as proposed in this thesis, for symmetrical or almost symmetrical faults.

The **Slip** model is the top response and credibly representing the eddy current response. It is not far from the non-linear **Flx1** model, except at the start of the fault interval. However, the effect of the fluxes is enriched from the SV computational method, like an oscillatory drop just at the time when fault conditions change; this is at the beginning of the fault interval and at the end of it. Once the fault is released, the hysteresis losses response softly tends to the reference value.

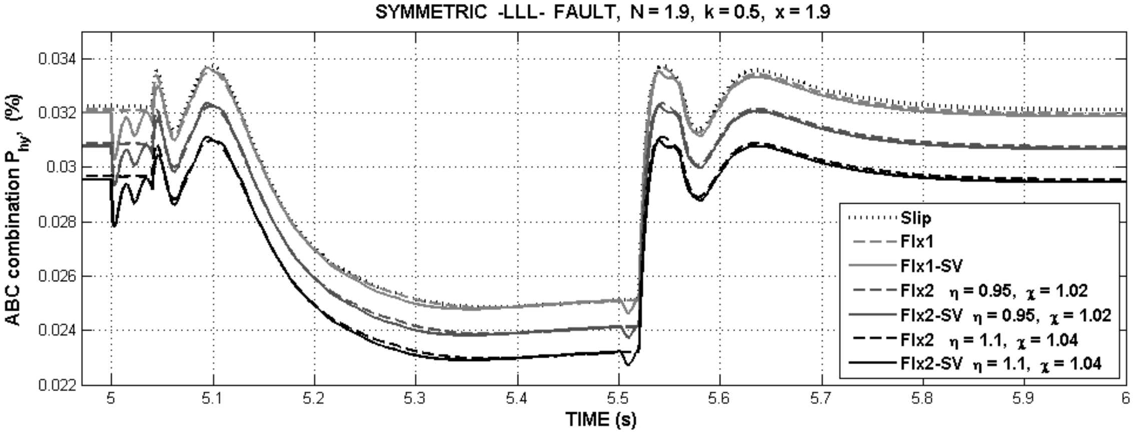

a)

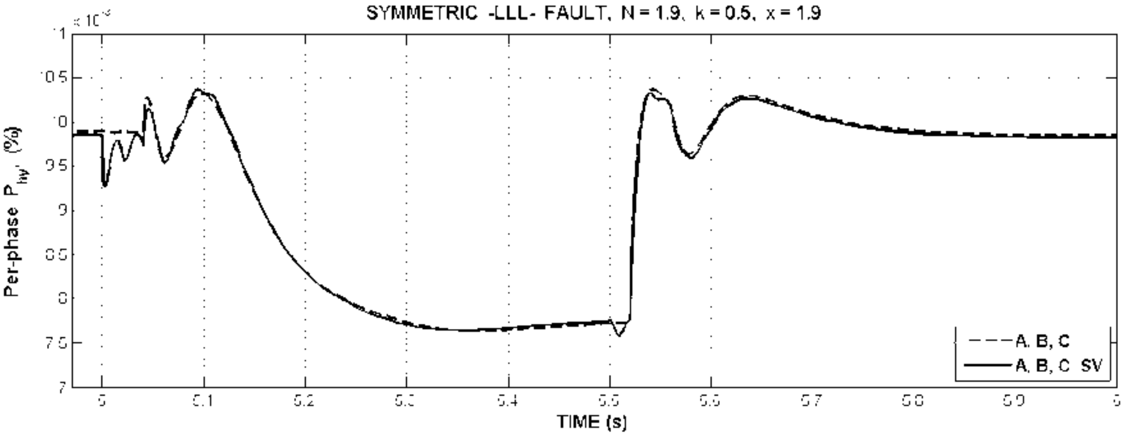

b)

Figure 6.6 Hysteresis-losses power response when a symmetrical LLL fault is applied at PCC, a) *ABC* average , b) individual *ABC* phase contribution

As it is seen, the iron-losses responses are now simpler than in the case of asymmetrical LG fault. The **Flx1** type models match each other. Similar property exhibits the **Flx2** type models as shown in Figure 6.6(a). Phase contributions in Figure 6.(b) are smaller and its waveform shows identical properties than those of Figure 6.6(a). As a consequence, the *ABC* combined response in Figure 6.6(a) is practically 3 times one phase.

In Figure 6.7 the total iron-losses response is presented. As before, an *ABC* combination is presented in Figure 6.7(a) and the individual phase contributions in Figure 6.7(b).

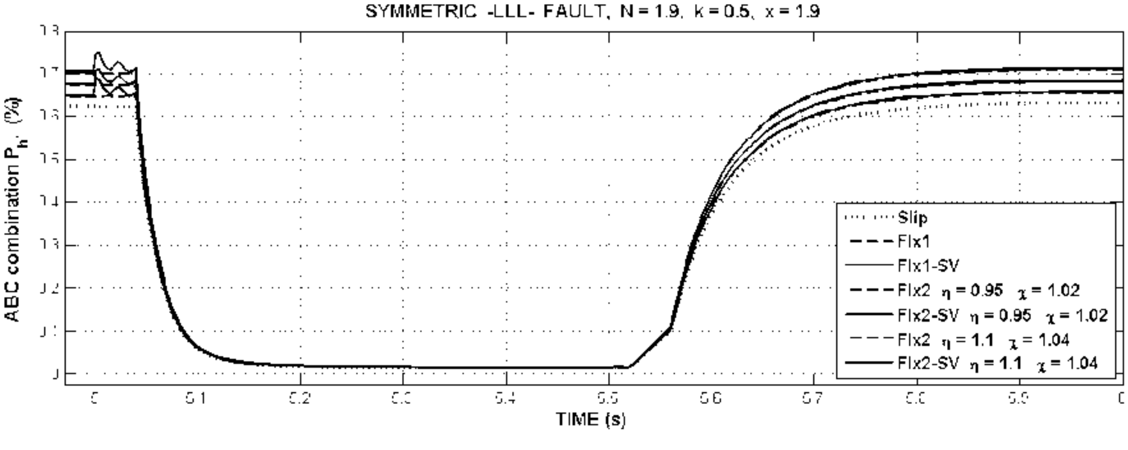

a)

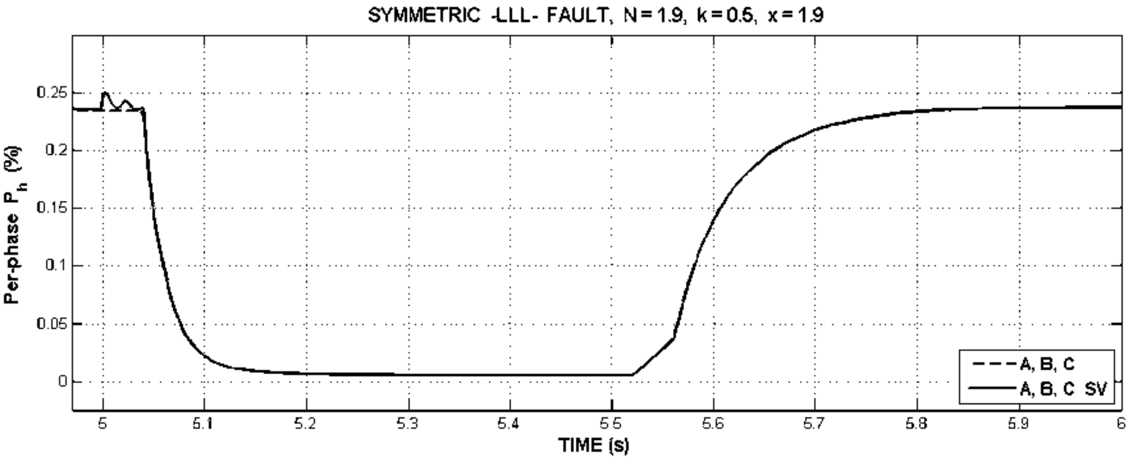

b)

Figure 6.7 Total iron-losses power response when a symmetrical LLL fault is applied at PCC, a) *ABC* average, b) individual *ABC* phase contribution

This response practically follows the RMS voltage drop waveform. This behaviour justifies the RMS computational method as proposed in this thesis, for symmetrical or almost symmetrical faults. During the fault interval, responses from all iron-loss models appear equal and slightly above than zero in both Figures 6.7(a) and 6.7(b), and there is no any *ABC* phase individual response in Figure 6.7(b). In this way, the fact that each phase contributes with 1/3 of the total iron losses is according to the traditionally established knowledge. Again, the effect of the power converter is to increase the iron-losses, which although clearly seen at the pre-fault and post-fault states, is not true during the fault interval, where all model responses match each other. If the Slip model represents in practice the one hundred per cent iron losses, all other iron-losses model responses appear above it, as expected, except in the fault interval.

6.5 Hysteresis and Total Iron-losses Currents

Following the methodology of applying symmetrical and asymmetrical perturbations at the PCC in order to obtain transient time-varying variables, Figure 6.8 illustrates the hysteresis iron-losses current i_{hy}, as flowing by the hysteresis resistance. Figure 6.8(a) corresponds to a short fault interval from a line-to-ground LG fault response, Figure 6.8(b) to a three-phase LLL fault response and Figure 6.8(c) to the steady-state response.

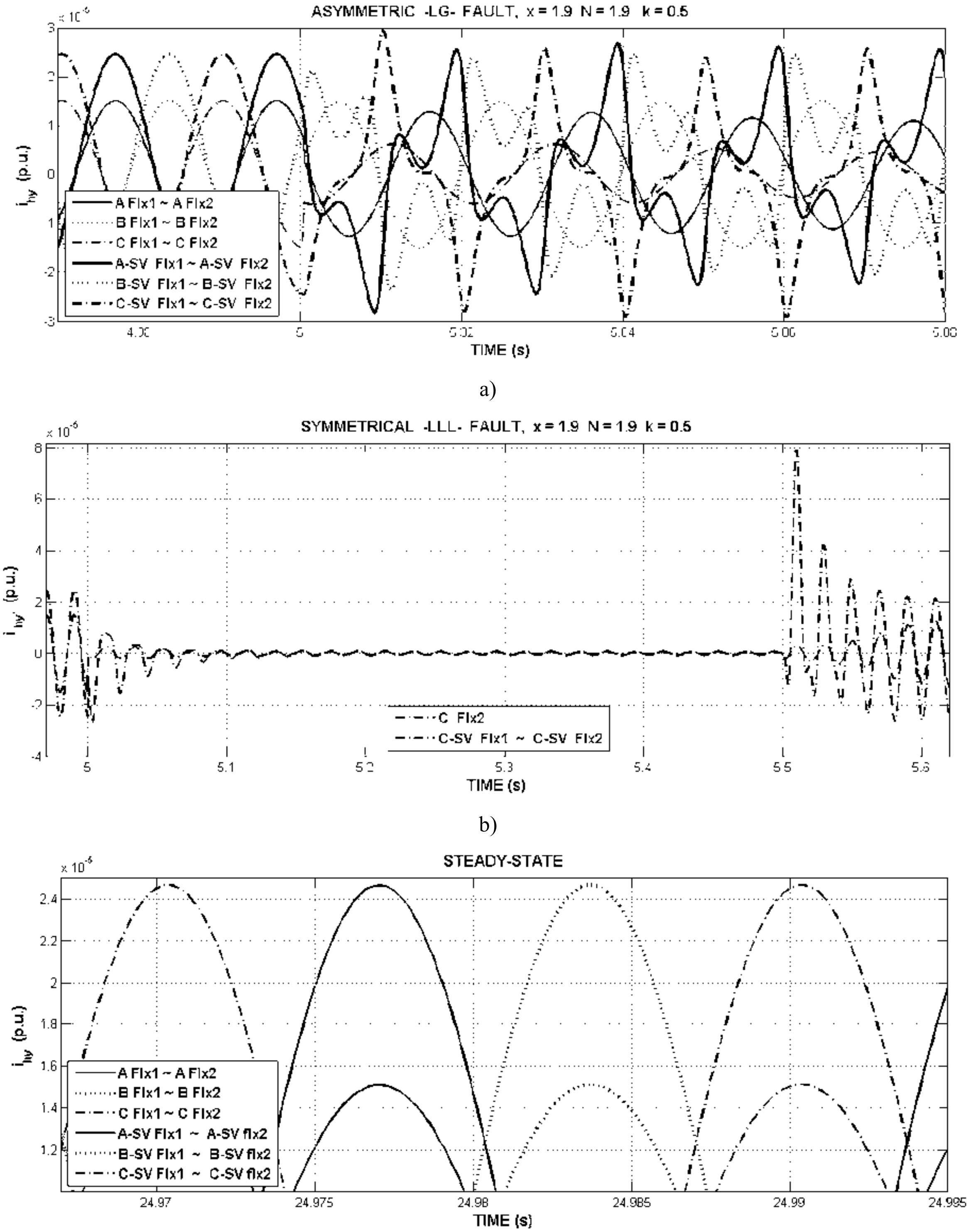

a)

b)

c)

Figure 6.8 Per-phase hysteresis current response, a) a short part of the fault interval showing the waveform change once the LG fault is inserted, b) similar time-window for the case of LLL fault, and c) is the steady-state response.

The *ABC* hysteresis current i_{hy} results very small due to the very large hysteresis resistance, through which it flows.

Due to LG fault in Figure 6.8(a), it is observed that: i) the hysteresis current i_{hy} as computed by SV formulation, is a periodic waveform with harmonic content, regarding the no-load condition of a power transformer, ii) although a very short fault interval is shown by drawing convenience, it is confirmed that this waveform has uniform amplitude during all of it, and also it softly reacts once the fault is released. In this case **SV Flx1** and **SV Flx2** iron-loss model responses match each other. iii) waveforms from the RMS formulation are sinusoidal, with smaller amplitude, and they also softly react once the fault is cleared. In this case **Flx1** and **Flx2** iron-loss model responses match each other. While, in Figure 6.8(b) for phase C and due to LLL fault: i) there is no current distortion during the fault interval, it rapidly decreases to a very small value, and once the fault is released, its first peak value is very large and then rapidly decreases to the steady-state, iii) RMS formulation produces smaller i_{hy} peak values than the observed from SV formulation and after the fault is released, they softly and progressively increases to the steady-state.

In the steady-state as shown in Figure 6.8(c), the **RMS** based **Flx1** and **Flx2** type models produce similar responses, and also the **SV** based **Flx1** and **Flx2** type models, match each other. It is clearly seen that amplitudes from the RMS formulation result smaller than those from the SV formulation.

From above observations it is inferred: i) the i_{hy} current distortion is due to hysteresis resistance, which introduces harmonic behaviour. It is observed during the fault interval only. As the non-linearity representation increase, this behaviour is more noticeable, ii) the SV formulation appears more reliable than the RMS formulation, to represent the hysteresis current. It besides enlarge its amplitude, iii) the asymmetrical conditions operation magnifies and qualifies the behaviour of the hysteresis losses effect.

Figure 6.9 presents the total iron-losses current i_h, as a combination of eddy-current and hysteresis, iron-losses currents. Figure 6.9(a) corresponds to a line-to-ground fault response, 6.9(b) to a three-phase fault response and 6.9(c) is the steady-state response.

This i_h current also presents very small amplitude. However, in opposition to the hysteresis current, the total iron-loss current i_h does not present currents with harmonic

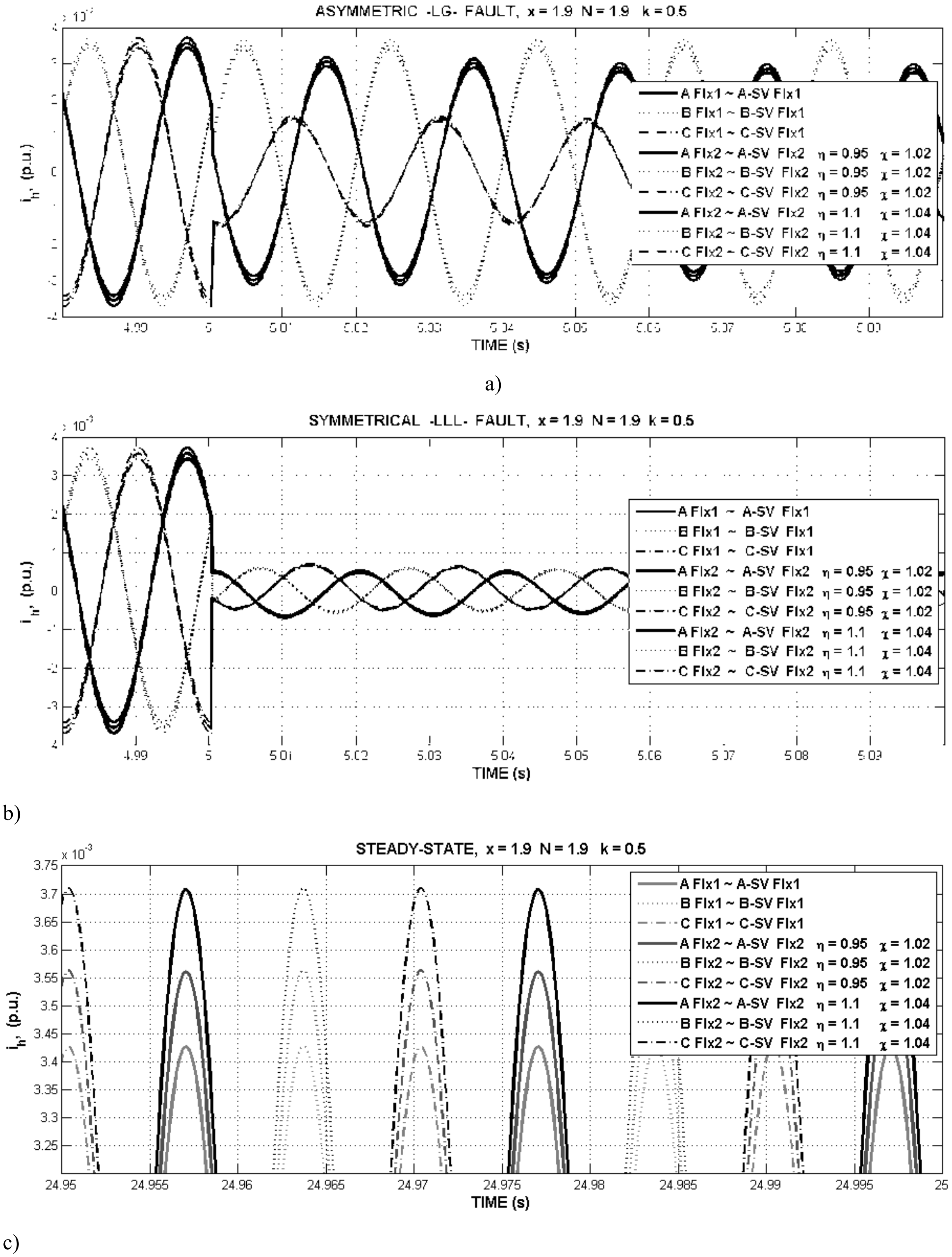

a)

b)

c)

Figure 6.9 Per-phase total iron-losses current response, a) a short part of the fault interval showing the waveform change once the LG fault is inserted, b) similar time-window for the case of LLL fault, and c) the steady-state response.

distortion during the fault interval. Also, although not shown, once the fault is cleared they keep on being sinusoidal too. In this way and relative to the **Flx2** model including the power converter effects for a specific η-χ couple, they are proportional to the dominant time-varying applied voltage.

The *ABC* and RMS responses match the corresponding *ABC* currents when SV formulation is used, for both **Flx1** and **Flx2** iron-losses models. This is true even if power converter effects are introduced. Comparing the responses amplitude, it can be inferred that the effect of eddy-current losses is dominant.

As shown in Figure 6.9(c), in the steady-state there is a similar trend to the already observed in models groups where phase currents match each other. As the iron-losses increases, the current amplitudes increase too. This corresponds with the decrement in iron-loss resistance already explored, and the power converter effects of Figure 6.1.

6.6 Conclusion

This Chapter have presented the step by step construction of a time-varying non-linear iron-losses resistance model. Three modelling alternatives are presented **Slip model, Flx1 model** and **Flx2 model,** and in a two way formulation: one uses the (RMS) values to represent stator *ABC* voltages and fluxes, and another represents them by spatial vectors (SV).

Simulation results allow observing:

- The time-varying resistance parameter representing iron-losses is widely oscillatory as influenced by the hysteresis effects. This feature is more evident in transient asymmetrical operating conditions and using SV formulation. In this case, the RMS formulation acts as a limiting profile of the SV response. Under transient symmetrical operating conditions, the hysteresis effect is hidden or negligible. It besides softly follows the voltage drop which effect appears dominant. In this case, the RMS formulation looks competitive with the SV formulation,

- The *ABC* combined iron-loss resistance parameter response, hides asymmetrical phase contributions from asymmetric operating conditions, resulting with relatively small amplitude.
- With symmetrical operating conditions even under fault conditions, the iron-loss resistance parameter behaviour, as *ABC* combination or with individual effects, basically follows the dominant effect of the voltage drop.
- For the representation of non-sinusoidal voltages supply, the proposed methodology and model adjustment based on voltages ratios delivered by the power converter, substantially and logically affects the iron loss resistance. In fact if iron losses increases, it is observed that iron-losses resistance decreases, and vice versa.
- The small current in the hysteresis branch appears highly distorted during the fault interval with asymmetric fault. It does not happen with symmetric fault. In the steady-state, the amplitude results modelling dependent. The total iron losses current is not distorted and also results modelling dependent.

* * *

THIS PAGE IS INTENTIONALLY LEFT BLANK

7

Time-Varying and Slip Dependent Deep-Bar *abc* Function

7.1 Introduction

The deep-bar effect modelling in squirrel cage induction machines, has been traditionally proposed adding branches to the rotor circuit, with slip dependent parameters [Macek-Kamniska 1995], [Eigenmann 1998], [Dymond 2000], [Grantham 2003]. Although this representation is a more exact way to take into account the cage and thus it is a trustable mathematical model [Babau *et al*. 2007], it increments the computational complexity of the whole induction machine model. Some modelling variants are: i) to add parameters which are related to specific parts of the cage, or ii) to include bar dimensions and its physical construction.

It is also widely known that, in technical reports rotor parameters behaviour is registered as approximately linear. This approach is usually made for small, medium and even large size induction machines [Akbaba and Fakhro 1992].

In the year 2007 an experimental influence to this paradigm is reported in [Babau *et al*. 2007] for a 7.5 MW induction machine. It allows identifying rotor parameters behaviour with at least two linear zones with a brake at the breakdown slip. Following practical test techniques like no-load direct-on-line start-up and slow-down, together to efficient instrumentation, authors make explicit their satisfaction with the meaningful results for large machines with 1/10 relationship between wide and depth of a cage-bar. In this doctoral research, these Babau's results are interpreted presenting two zones with almost linear behaviour, and separated by a non-linear region at the neighbourhood of the breakdown slip.

Also saturation and iron losses are included improving the original work [Babau *et al*. 2007], where authors neglect them.

Based on these results, the following hypothesis is enounced: the known computed or recorded rotor resistance and leakage reactance parameters of large size induction machine, can be taken as a technical reference for any paradigm trying to represent those parameters in any large machine. The basin of this hypothesis rests on the fact that two mandatory points belong to those characteristics. One is related to the start-up point where the slip = 1.0. The other, relates the rotor parameters with the full-load operational point, as obtained from the standard load-test.

In this chapter, this modelling hypothesis is developed and it is demonstrated that it satisfactorily represents the deep-bar effect. It is practical for the steady-state induction machine operation, as well as during transient symmetrical or asymmetrical operative conditions.

7.2 Test Based Rotor Parameters Modelling. The Reference Machine

In [Babau *et al*. 2007], main parameters and variables were identified by test, for several tents of large induction machines. Their power range was between 1 and 7.5 MW, and some innovative procedures were used like No-Load Direct-On-Line (DOL) Startup and Natural Slowdown. These methods are widely described there, and reveal a better and cheaper way to replace the traditional no-load and load standard tests [IEEE Std-112 2004].

What this research concerns, rotor resistance and leakage reactance parameters are computed as slip dependent functions, for a specific 7.5 MW, 6 kV, 1500 rpm, 50 Hz, induction machine. For this research, appropriate A, B, C, D, E and F pilot points are selected, and their corresponding rotor parameter-slip pairs, are summarized in Table 7.1 in ohm values.

Two test-based points are mandatory. The first corresponds to the rotor parameter values at the start-up point *F*, and it is obtained from blocked-rotor test, subtracting the stator parameter from the short-circuit value. The second agrees to the full-load point *A*, and it can be computed from the standard load-test conditions.

Table 7.1 Resistance and leakage reactance pilot points, as extracted from the rotor parameters graph in [Babau *et al.* 2007].

			Resistance R_r		**Leakage Reactance X_r**		
Points		**Slip**	**ohm**	**R_r/RfL**	**ohm**	**Xr/XfL**	**X_r/R_r**
F	Start-up	1	0.1222	5.25	0.1245	0.155	1.0188
E	Pull-out T_e	0.5432	0.0867	3.72	0.1727	0.215	1.99
D		0.24	0.0489	2.099	0.2	0.249	4.09
C	Breakdown T_e	0.0682	0.0422	1.81	0.2367	0.29	5.61
B		0.0455	0.0314	1.35	0.2980	0.37	9.49
A	Full load	0.0067	0.0233	1.0	0.804	1.0	34.51

They are obtained by subtracting the stator parameter values from the short circuit parameters. The second point corresponds to the parameters at full-load operation point *A*, R_{r-fL} and X_{r-fL}, the rotor resistance and leakage reactance respectively. Two additional points, also constituting particular operation pairs are essential. The point *E*, associated to the pull-out electromagnetic torque, and the point *C*, as associated to the breakdown electromagnetic torque. Their corresponding slips can be measured or computed. Furthermore, in the points *B* and *D*, although arbitrary, slope changes occur and they have been included in the list.

Three columns are suitably added to Table 7.1. Two of them relate R_r and X_r parameters to their respective R_{r-fL} and X_{r-fL} values. The resistance ratio R_r / R_r results very large and decreases from start-up to full load. The reactance ratio X_r / X_{r-fL} is smaller and increases in the same interval. A third column presents the X_r/R_r ratio. Given the large X_r values, it well represents the variation of the rotor impedance along the start-up process.

Relating Table 7.1 and the original draws in [Babau *et al*. 2007] already synthetized in Figure 7.1, it is observed that, once the machine starts, rotor parameters and parameters ratios here proposed, present an almost linear behaviour up to the neighbourhood of the breakdown slip, where a soft slope change occurs looking for the full-load point. Anyway, this feature is softer in the rotor resistance.

This mathematically obtained characteristics presents: i) soft start-up process without some impulses, and ii) parameter values at zero speed. The machine test in [Babau *et al*. 2007] report at 4 MW peak at the start-up (slip = 1), and thus, sudden small low frequency oscillations can appear. Otherwise, rotor parameter values at full-load can be taken out from the load test, but not beyond it in the neighbourhood of zero speed.

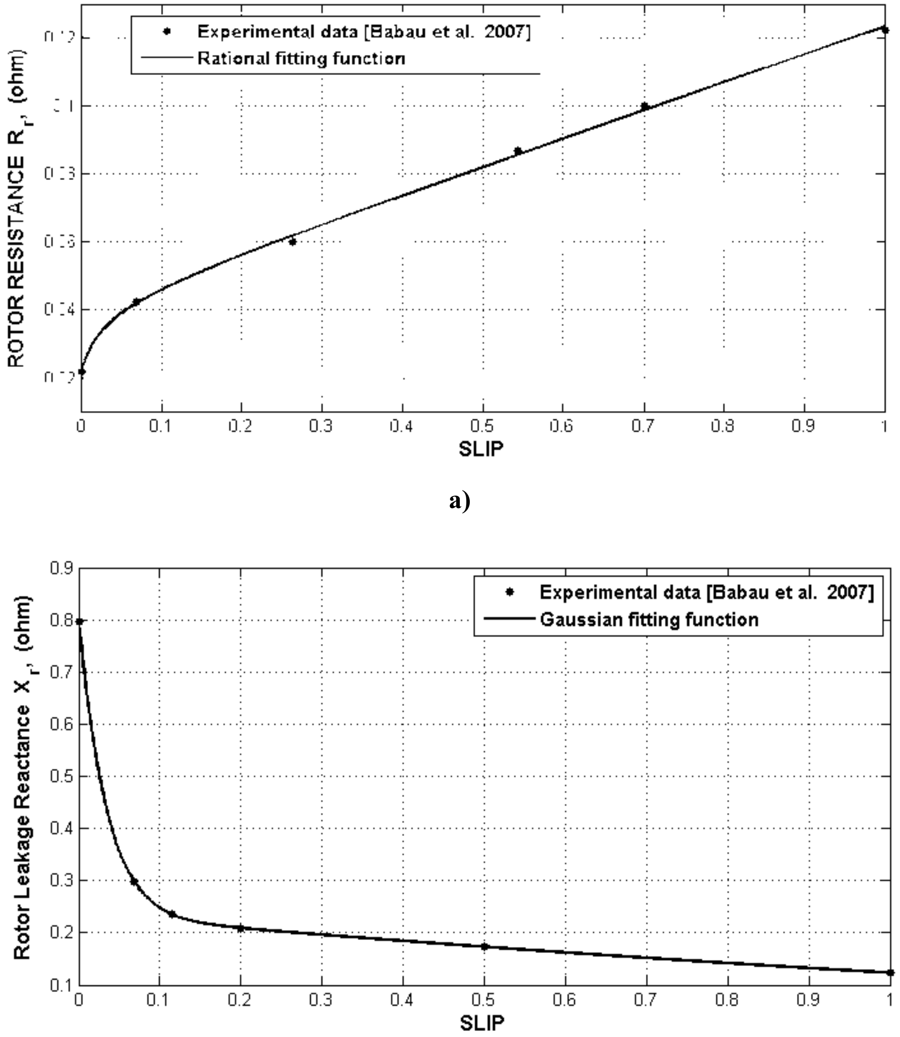

a)

b)

Figure 7.1 Synthesis of the rotor parameter behaviour , as reported in [Babau *et al.* 2007]: a) Rotor resistance, b) Rotor leakage reactance.

Test results in [Babau *et al.* 2007] reveal that, the rotor resistance and leakage reactance have a non-linear behaviour, with emphasis in the machine operation zone, in the neighbourhood of the breakdown slip, and they have significant almost linear variation between start-up and full load operational conditions. Authors establish that, these features in rotor parameters reinforce what is expected in large machines, with 1/10 relationship between width and depth of the bar, in a deep-bar construction.

According to this observation, the linear or almost-linear functions proposed in several publications and additionally enclosed to the interval where slip is greater than breakdown slip only [Akbaba and Fakhro 1992], [Iov *et al.* 2004], seems to be a sort of thick approximation.

Given this almost complete information about rotor resistance parameters, as extracted from the test machine in [Babau *et al.* 2007], it will be cited as reference machine from hereafter.

7.3 Modelling Strategy

The classical approach tries to represent the results in Figure 7.1 with two, three or multiple elementary rotor cages, with constant resistance parameter over slip [Macek-Kamniska 1995], [Eigenmann 1998], [Dymond 2000], [Grantham 2003]. It is common in these cases to use the Levenberg-Marquandt regression method [Mondragon 2003]

If the expected model should behaves as synthesized in Figure 7.1, it is apparent that any other paradigm reproducing the trend in the rotor parameters as slip dependent, is competitive. In this way, an electrical and geometric point of view of the results in [Babau *et al.* 2007], is proposed in this investigation.

In order to construct this paradigm and to illustrate it for a specific induction machine, the following computational strategy is proposed:

a) Based on load / blocked-rotor standard test, identify the point *F* at the start-up and the point *A* at full-load operational conditions. These two points are the basin to enclose a consistent zone, where a more general function operates. At the point *F* belongs the rotor resistance at the start-up R_{st} and the slip = 1. At the point *A* belongs the full-load resistance $R_{r\text{-}fL}$ and the slip = S_{fL}.

b) Suitably but realistically, identify rotor resistance values candidates to establish the $R_r/R_{r\text{-}fL}$ ratio. They should belong to the consistent zone.

c) Carefully establish the X_r/R_r ratio, which will allow computing the rotor leakage reactance, as related to the rotor resistance at any slip. An increasing leakage reactance value from 1 to 0 slip, is required, according to Table 7.1.

7.3.1 The machine in this investigation

For the 2 MW induction machine data used in this research, rotor resistance parameters are only partially known, to be consistent with the list of trial A to F points in Section 7.2. There is an entire certain on R_{st} and $R_{r\text{-}fL}$ parameters and their corresponding slips at start-up *F* and full-load *A*. These points are assumed available. Meanwhile there is only partial certain on *E* and *C* points and complete uncertain on points *B* and *D*.

Table 7.2 is one proposed synthesis for all A to F trial points, as associated to this research machine. In light gray background appear assumed slip and candidate resistance values. With these, the resistance $R_r/R_{r\text{-}fL}$ and reactance X_r/R_r ratios are suitably chosen to fulfil the trend in the reference machine. The column containing reactance X_r values, is used as a first sight of the expected values.

Table 7.2 Resistance and Leakage Reactance points for the 2 MW induction machine in this research, as closed to the 7.5 MW machine in [Babau *et al.* 2007]

		Resistance R_r		**Leakage Reactance X_r**	
Points	**Slip**	**ohm**	**$R_r/R_{r\text{-}fL}$**	**ohm**	**X_r/R_r**
F (start up)	1	0.025415	2.8557	0.06023	2.37
E (pull-out Te)	0.5	0.023	2.5843	0.06095	2.65
D	0.2	0.02	2.2472	0.062	3.1
C (max Te)	0.04	0.01566	1.7596	0.06374	4.07
B	0.02	0.011	1.236	0.06545	5.95
A (full load)	0.00845	0.0089	1	0.09407	10.57

The selected resistance and reactance ratios are displayed in Figure 7.2, and compared to those corresponding to the reference machine, according to Table 7.1. Following the trend in the reference machine, $R_r/R_{r\text{-}fL}$ ratio for this research machine in Figure 7.2(a) results too much close to the reference machine at the non-linear zone with small slips less than 0.3, and presents a progressively increasing separation above this value. While the X_r/R_r ratio in Figure 7.2(b), results relatively close to that of the reference machine, all along the slip range, before and after the breakdown slip.

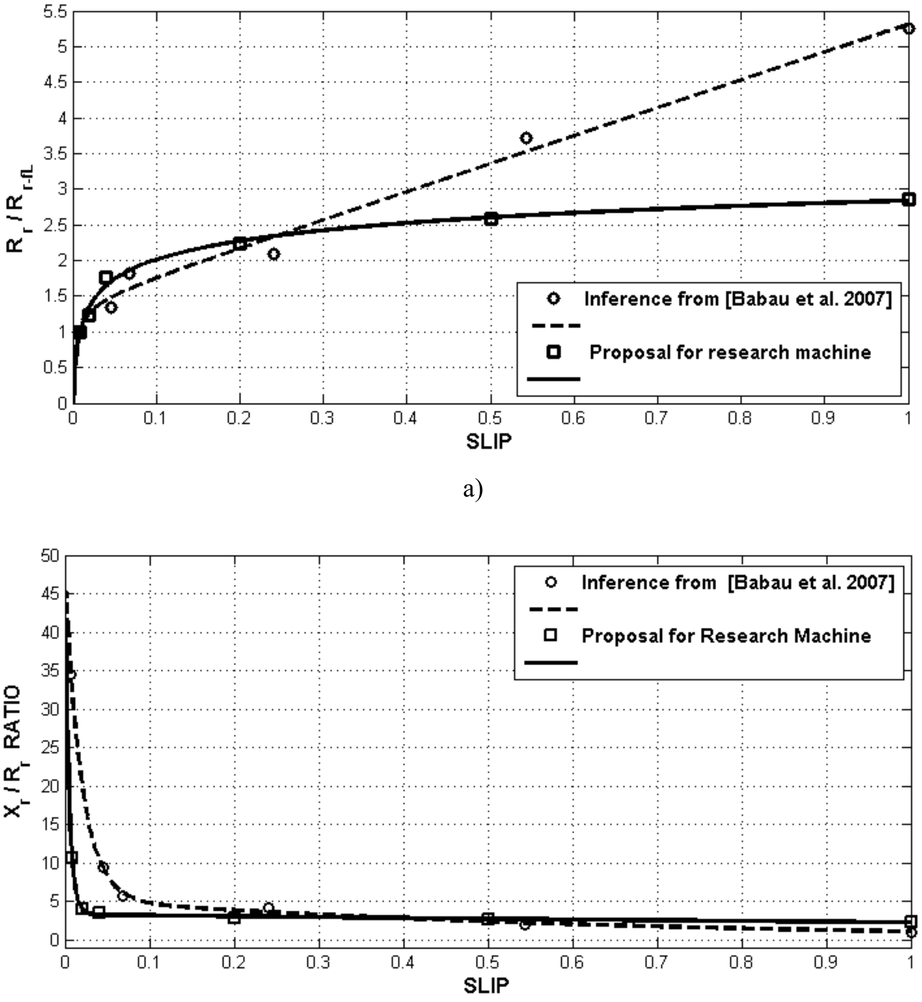

a)

b)

Figure 7.2 Comparison of rotor parameter ratios for the 2 MW induction machine in this research and those of the 7.5 MW test machine in [Babau *et al.* 2007], a) Rotor Rr/RfL ratio, b) Rotor Xr/Rr ratio

From Figure 7.2, the X_r/R_r ratio appears to be a much more standard relationship that the $R_r/R_{r\text{-}fL}$ ratio, in real large machines. In order to make easy the selection of the rotor resistance candidates, Figure 7.3 presents a geometrical interpretation of the rotor parameters, as applied to this research 2 MW induction machine. Three aspects are highlighted:

i) Points *A* and *F* are mandatory to be initially settled. They determine the consistency zone inside the triangle *AZF*, where any candidate value must be. The *OA* segment is a complementary linear function to include the slip interval involving the zero crossing,

ii) Circle, square and cross symbols are used to identify the probable rotor resistance candidates at pilot points. The set of points with square symbols are the selected rotor resistances in this investigation, and reported in Table 7.2 and Figure 7.2,

iii) Classical or up to date methods to register the electromagnetic torque allow identifying the slip at point *E*, where the corresponding rotor resistance value should be between the start-up and breakdown resistance values. In this way, *C* and *E* points are relatively easy to identify.

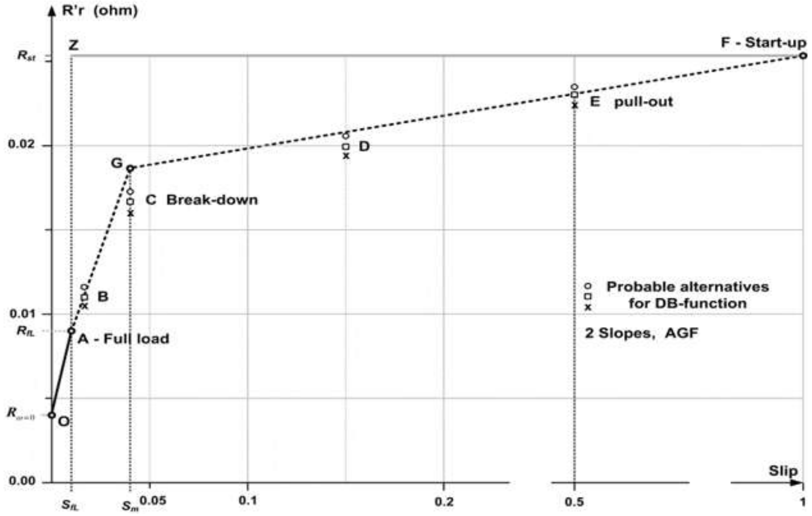

Figure 7.3 Geometric interpretation of the results in [Babau *et al.* 2007] for rotor resistance selection.

Once the resistance values candidates are available, the resistance $R_r/R_{r\text{-}fL}$ ratio is straightforward. Note in Figure 7.3 that the rotor resistance does not cross by zero, but it has a zero slip value. Then in the *O* point, there is a mirror image effect between motor and generator operation modes. As a consequence, slope change is expected when the machine oscillates from generator mode with negative slip to motor mode with positive slip. Identical comment is valid for the resistance $R_r/R_{r\text{-}fL}$ ratio in Figure 7.2(a). It is underlined that the slip in this investigation is a time dependent variable, which can be perturbed by symmetrical or asymmetrical electro-mechanical events, coming from internal or external fault sources.

7.3.2 One-Slope Reference Model

A near-linear model, which has been widely probed and reported in [Akbaba and Fakhro 1992], [Iov *et al*. 2003], [Iov *et al*. 2004], is selected as the linear reference model. It was selected as the first research stage and carefully used as *abc* approach in [Fajardo *et al*. 2007a] and [Fajardo *et al*. 2007b]. Furthermore, in this final thesis report, its original requirement of being active only if slip is greater than breakdown slip, is removed. This decision is made consistently with the rotor parameters behaviour in [Babau *et al*. 2007], which is used here as a reference research. In this way, rotor parameters are active all along the whole slip range. For research comparison, this model is symbolized as one-slope (*) model, where the recursive symbol (*) emphasizes the modification announced to the original model.

7.3.3 Two-Slope Model

In addition to *A* (full-load (*fL*), S_{fL}) and *F* (start-up (*su*), S_{su}) points in Figure 7.3, a third point *G* is chosen matching the breakdown slip S_m and it should be in the neighbourhood of the point *C*. Point *G* can be computed from the machine parameters or measured from test [Krause *et al*. 2002], [Babau *et al*. 2007].

By conventional formulation, two linear functions constitute the two-slope rotor resistance model. Including the deep-bar effect (*db*) correction, it is proposed by,

$$\begin{aligned} R_{r-db,abc} = {} & Slip(R_{r-su,abc} - R_{r-Sm,abc})/(1-s_m) + \\ & R_{r-Sm,abc} - s_m(R_{r-su,abc} - R_{r-Sm,abc})/(1-s_m), \quad S_m < Slip < 1.0 \end{aligned} \tag{7.1}$$

and,

$$\begin{aligned} R_{r-db,abc} = {} & Slip(R_{r-Sm,abc} - R_{r-SfL,abc})/(s_m - s_{fL}) + \\ & R_{r-fL,abc} - s_{fL}(R_{r-Sm,abc} - R_{r-SfL,abc})/(s_m - s_{fL}), \quad S_{fL} < Slip < S_m \end{aligned} \tag{7.2}$$

Once the resistance value is computed in agreement to Section 7.3.1, the corresponding slip dependent rotor leakage reactance $X_{r\text{-}db,abc}$, should be related to the previously and suitably selected X_r/R_r ratio, which is presented in the next Section.

Note that the standard test characteristics miss *abc* results in the blocked rotor test. If they were available, (7.1) and (7.2) should be straightforward to take into account the *abc* goal in this research. Anyway, these equations are ready to be used in case of.

7.3.4 Non-Linear Model

Following the modelling strategy, a more general function joining the trial points from *A* to *F*, can be constructed. In the Section 7.3.1 a rational strategy to identify these points was proposed, where in addition, point *G* can be used as a guide to reasonably assume *B* and *D* points. Starting from the trial points, their corresponding $R_r/R_{r\text{-}fL}$ values can be easily computed, and also their associated trial values for the reactance X_r/R_r can be reasonably assumed. The **cftool** in Matlab/Simulink is used to produce the closest continuous fitting functions representing the by deep-bar (*db*) effect corrected $R_{r\text{-}db,abc}$ and $X_{r\text{-}db,abc}$, resistance and leakage reactance rotor parameters, respectively.

In order to generalize the modelling, two possible additional alternatives to those in Table 7.2 for $R_r/R_{r\text{-}fL}$ and X_r/R_r ratios, are shown in Figure 7.4. In Figure 7.4(a), R-ratio-2 represents the *n* probable $R_r/R_{r\text{-}fL}$ ratios appearing above the basin alternative R-ratio-1 in Table 7.2, and R-ratio 3 represents all *n* probable alternatives below R-ratio-1. The basin alternative R-ratio-1 is represented in Figure 7.3 and Figure 7.4(a) by square symbols. In the same way, *m* probable alternatives XR-ratio, associated to a specific R-ratio alternative, are possible. In Figure 7.4(b) the three XR-ratio showed, are all associated to R-ratio-1 only.

Figure 7.4 proposes that, given a slip value, Rr is computed from the $R_r/R_{r\text{-}fL}$ ratio, and then Xr is computed from the X_r/R_r ratio, as a function of the already determined R_r value.

In this way rotor resistance and leakage reactance as slip dependent induction machine rotor parameters, can be easily and efficiently computed to take into account the deep-bar effect, without any complex formulation.

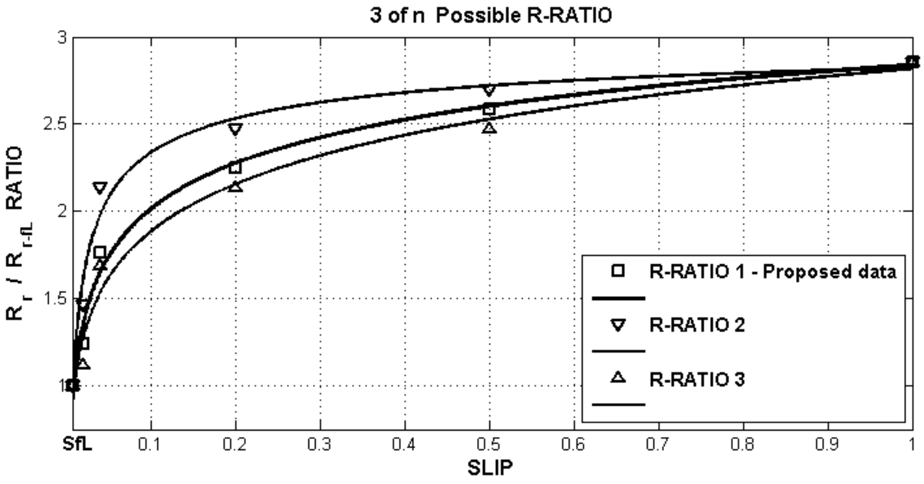

a)

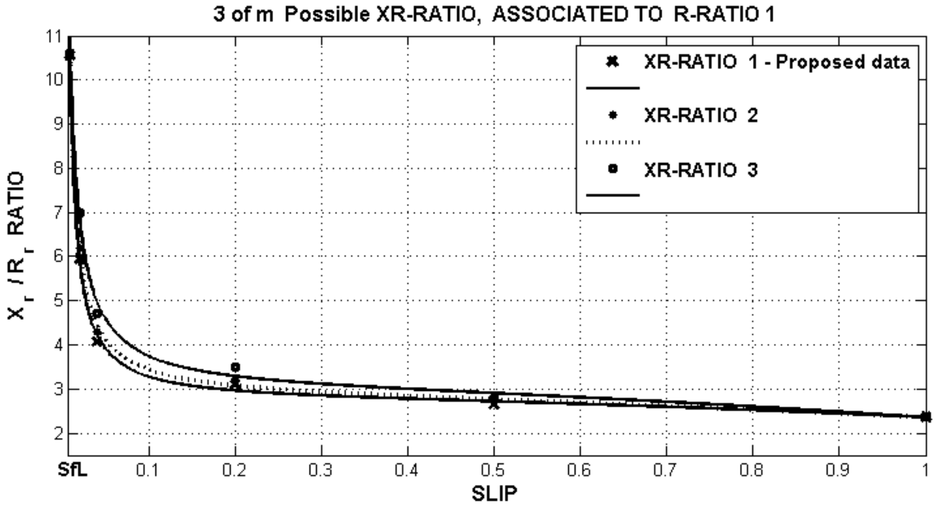

b)

Figure 7.4 Expanding the number of rotor parameter ratios for the 2 MW research machine, following the proposal in Table 7.2, Figure 7.2 and Figure 7.3: a) rotor resistance Rr/Rr-fL, b) rotor reactance to resistance Xr/Rr.

7.4 Analysis and Results

The slip dependency of rotor resistance and leakage reactance parameters has been presented above. From other point of view, in this research slip is a time-varying variable. In this way, rotor parameters and related variables are expected to be time-varying too. Results in Figures 7.5 to 7.8 correspond to symmetrical three-phase fault excitation at PCC. In order to make easy the reading in their legends, some short strings are used. The No-DB effect response relates a constant parameter model with no deep-bar effect, One-slope (*) corresponds to Section 7.3.2, the three different two-slope alternatives ($R_r = 0.023$, 0.0185, 0.013 ohm at breakdown slip), relates the two-slope model proposal in Section 7.3.3, and the DB-function corresponds to the modelling proposal in Section 7.3.4. By its structure, the DB-function model is taken as the exact model, against what other models are compared.

7.4.1 Time-varying rotor parameters when the induction machine is symmetrically perturbed.

A) The time-varying slip variable is presented in Figure 7.5. Deep-bar modelling response is segmented for a time-window during the fault interval in Figure 7.5(a) and a post-fault time-window in Figure 7.5(b). Relevant aspects are highlighted:

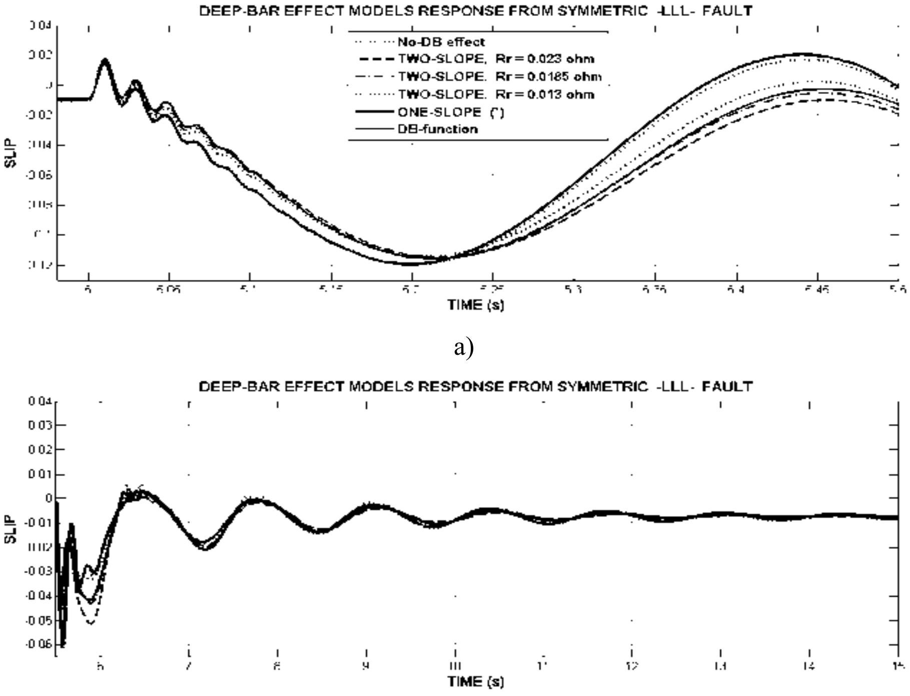

a)

b)

Figure 7.5 Time-varying slip response, due to the application of a three-phase fault (LLL) at PCC, a) slip behaviour at the fault interval, b) slip behaviour after the fault is cleared

i) The steady-state value as measured at 20 s suitably extrapolating what is shown in Figure 7.5(b), is around of -0.008 from the No-DB effect model, -0.0075 from one-slope model, 0.007441 from two-slope models, and -0.00734 from the DB-function model. Respect to the input -0.00854 slip value, there is a maximum deviation nearby 14 % associated to the DB-function model. Mechanically this deviation means that the rotor speed is nearer to the synchronous speed. In addition, it is also the largest error in the steady-state slip value, if deep-bar effect is not modelled,

ii) Relative to their practically common steady-state value, the largest slip deviation in the transient process is seen at 5.2 s in Figure 7.5(a), as given by the No-DB effect and one-slope models. It is around 15.13 times the steady-state value. All other models deviate around 14.43 times.

iii) During the interval when the fault in inserted and also after the fault is released, No-DB effect and one-slope models run practically together, describing a less damped path than DB-function and two-slope models,

iv) Just when the fault is applied, deviations start oscillating and then they are damped. Because stator voltages suddenly drop with identical amplitude, oscillations are intended to be the result of the symmetrical inductive effect between stator and rotor, trying to avoid stator and rotor currents change. Once the fault is released, the demagnetization progressively recovers and responses relax, looking for the steady-state with damped low frequency oscillation.

These observations allow inferring that, solving the induction machine dynamic equations leaves a time-varying rotor speed and thus a time-varying slip variable, due to the rotor parameters change originated by the deep-bar effect. Two-slope slip models look as efficient as DB-function model, despite their large differences in basin resistance. The one-slope model looks very inefficient and practically matches the No-DB effect model.

B) The time-varying breakdown slip performs in almost similar way, as shown in Figure 7.6. But in this case the rotor resistance is directly involved [Krause *et al*. 2002], and thus, deep-bar effects are expected. Relevant aspects are:

i) In Figure 7.6(b), the steady-state value from No-DB effect is around -0.04066 and it is computed following [Krause *et al*. 2002], with the input constant parameters. From one-slope model is read -0.03806 value, from two-slope model a common -0.03694 value and from DB function -0.03748. The largest slip deviation related to the No-DB effect model, corresponds to two-slope models with 9.15 %. The DB-function presents 7.82 %. Note that between one-slope model and two-slope and DB-function models, the deviation is less than 3 %. These results show that the breakdown slip can have different values, as computed from different deep-bar models, and the deviations can be meaningful. Being this fact relevant for rotor speed control, it makes evident that during tests, extreme careful should be taken on the instrumentation for measuring purposes.

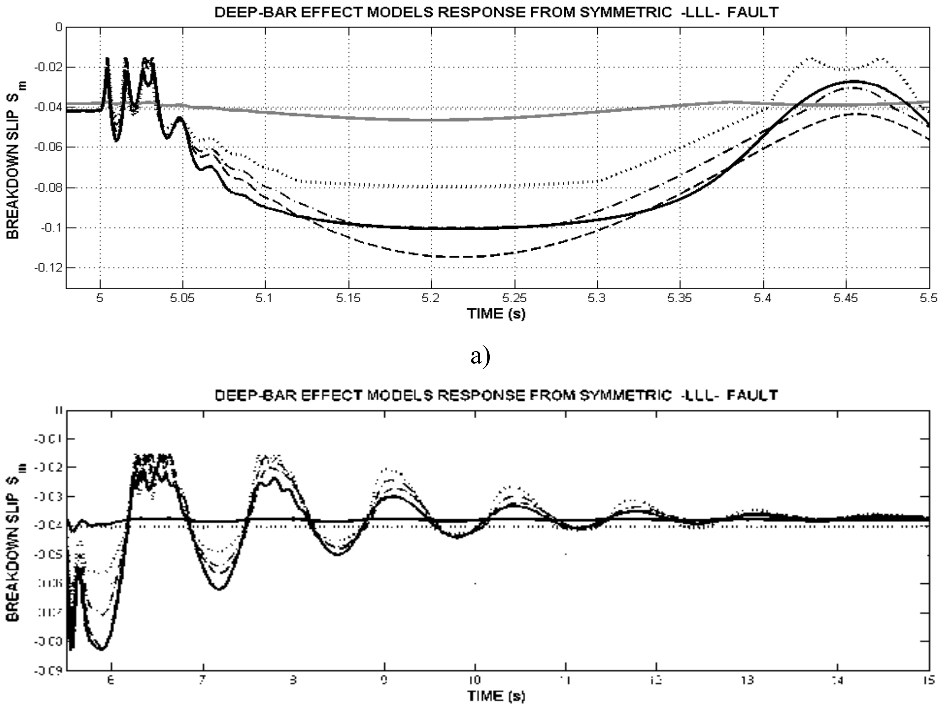

a)

b)

Figure 7.6 Time-varying breakdown slip response, by applying a three-phase fault (LLL) at the PCC. Line conventions are similar to Figure 7.5. a) at the fault interval, b) after the fault is cleared.

It will allow selecting test points closed to an exact modelling, for prediction purposes. It is also to highlight that, although two-slope models have been constructed with three different rotor resistances at the point G, they converge to a common steady-state value. It is probably due to the location of point G, which is selected at the breakdown slip.

ii) In the interval when the fault is inserted, maximum deviation at around 5.215 s is between 14.2 % from the one-slope model and 181.6 % from two-slope model with Rr = 0.023. All other deep-bar model responses are within this range. It is to highlight that, when the machine speed oscillations changes from negative slip to positive slip or vice versa, an abrupt change occurs in the breakdown slip. This is computed from actual rotor parameter values, as slip dependent. As a consequence and according to the note in Section 7.3.1, is the zero slip crossing which makes the slope of the breakdown slip suddenly changes.

iii) Once the fault is cleared, the breakdown slip non-linear response recovery is more damped from the DB-function model. From two-slope models it is observed that, the smaller rotor resistance the larger damped oscillating amplitude. While the one-slope model tends to the steady-state almost immediately, missing these damped oscillations.

Knowing that the breakdown slip displacements constitute a measure for variable-speed wind turbine applications, the observation above reveals that for control purposes if deep-bar effect is missed, the wide breakdown slip displacements during a symmetrical fault event are missed too. Two-slope models appear in certain way less efficient, producing larger deviations and amplitude oscillations, than the DB-function model. Meanwhile, the one-slope model produces very small and almost negligible breakdown slip variations, as compared to other models.

C) The time-varying rotor resistance response is shown in Figure 7.7. Being this response the heart of the research about deep-bar effect, some meaningful aspects are highlighted:

i) It is the direct result of the first step, which is to select rotor resistance candidate values. They have been selected between start-up and full-load resistance values, follow the trend observed in the reference machine and appear in Table 7.2. With the pilot points for these ratios, a fitting tool is used to identify the slip dependent continuous function linking them. For the case of this investigation a rational function of the type,

$$\frac{R_r}{R_{fL}}(S) = (p_1 S(t)^2 + p_2 S(t) + p_3) / (S(t) + q_1) \quad (7.3)$$

was chosen, where p_i, q_1 are constants and $S(t)$ is the time-varying slip variable. If at least one the trial point is moved, the fitting function (7.3) can change not only in the parameters but also in the type. Power, rational and exponential functions types were probed, and they are candidates to fit the trial points in a wide variety of alternatives withim the consistent zone, according to Figure 7.3.

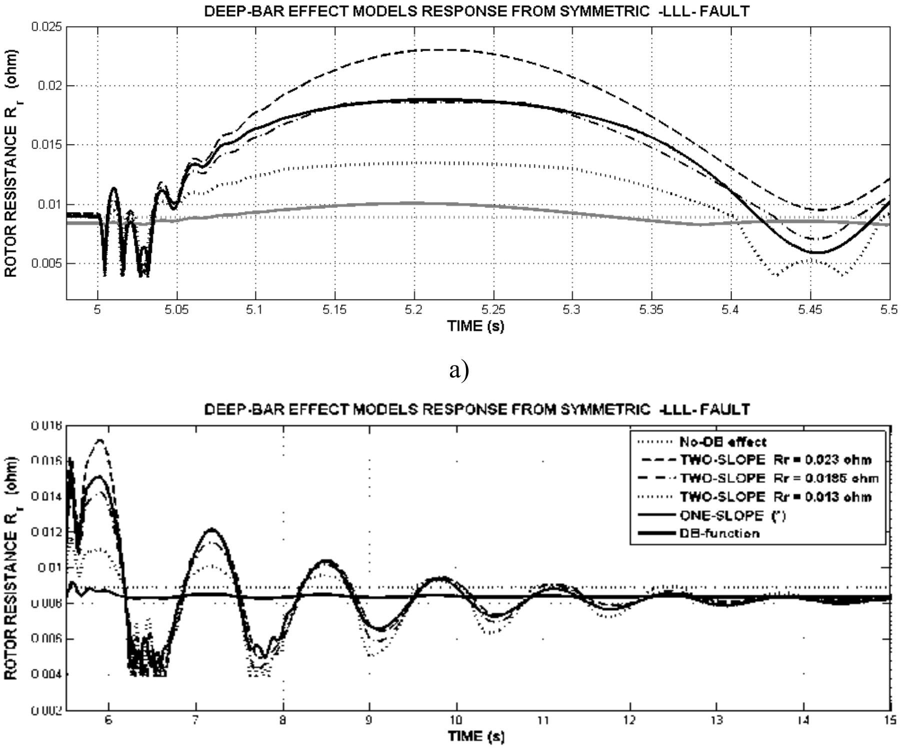

a)

b)

Figure 7.7 Time-varying rotor resistance, by applying a three-phase (LLL) fault at PCC, a) fault interval, b) after the fault is cleared

ii) Looking at Figure 7.7(b) and relative to the RfL input value (8.9 milliohm), the maximum deviation at the steady-state comes from the DB-function model, with around 8.5 % (~0.8 milliohm). From other models the decrement is less than this value. Note that relative to the RfL input value, all deep-bar models produce smaller values.

iii) At any time, the rotor resistance increases as the slip increases in the motor mode or the slip decreases in the generator mode, and vice versa. It is in agreement to [Babau *et al.* 2007].

iv) During the fault interval, after some initial oscillations, the rotor resistance increases to a maximum value (closed to the absolute slip value) in dependence of the deep-bar model, as shown in Figure 7.7(a). The minimum deviation is expected from the one-slope model with 13 %, and the maximum deviation comes from the two-slope model when Rr = 0.023 ohm, with 158.4 % (~14.1 milliohm). Other model responses are inside this range. It is to highlight the sudden slope changes, visible in one-slope and two-slope model responses, which correspond to the zero slip crossing.

v) Once the fault is cleared, rotor resistance responses from all models settle to the steady-state, with low frequency damped oscillation. Two-slope models present larger amplitudes than the non-linear DB-function, and one-slope model with relative almost negligible amplitude.

The rotor resistance parameter present in the steady-state smaller values than the input RfL, from all deep-bar models. The maximum deviation observed is from the non-linear DB-function, with the selected candidates of resistance values in Table 7.2. As expected following the proposed methodology, rotor resistance responses reply the trend in the reference machine, from all deep-bar models. But the aspect to underline is that, all deep-bar models are very close to the one-slope model response, which has nothing to do with the proposed methodology. This observation is extended to other responses in this report. It means that the proposed methodology results very consistent and reliable.

D) The time varying rotor leakage reactance Xr is highly dependent on the selected Xr/Rr ratio. Once the rotor $R_r/R_{r\text{-}fL}$ ratio is computed, a very careful selection of the X_r/R_r ratio is needed, following as closed as possible the tendency observed in the reference machine. In this investigation, pilot X_r/R_r values are shown in Table 7.2. They are selected taking into account that two of them are known, at the start-up and full-load, respectively. They are the guide to select other X_r/R_r values for the trial points B, C, D, E. At this stage, true Xr values are not known for computational purposes, and that is why the respective Xr values appear highlighted in grey background colour in Table 7.2. What it is really known for computational purposes is R_{fL}, and ratios $R_r/R_{r\text{-}fL}$ and X_r/R_r. Taking into account the input X_{fL} = 0.094 ohm for comparison purposes, it is to highlight:

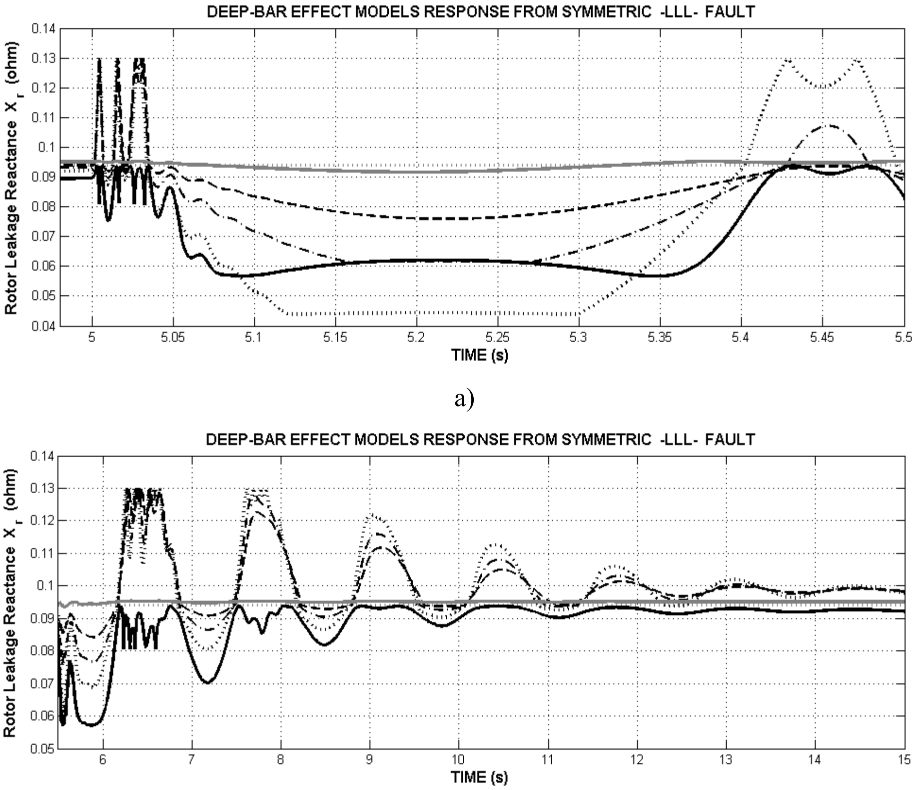

a)

b)

Figure 7.8 Time-varying rotor leakage reactance, when a three-phase (LLL) is applied at PCC, a) fault interval, b) after the fault is cleared

i) Due to the starting oscillations in R_r, X_r also oscillates, as shown in Figure 7.8(a). Relative to X_{fL}, these oscillations are moderate and of the order of 20.2 % (~ 19 milliohm), while the two-slope models produce oscillations up to of the order of 38.3 % (~ 36 milliohm) including the zero-crossing slope change, and the one-slope model produce oscillations of the order of 1.33 % (~ 1.3 milliohm) only.

ii) As the slip decreases in the generator mode, X_r decreases, which is in agreement to [Babau *et al*. 2007]. The largest deviation is seen from two-slope model with $R_r = 0.013$ ohm, with X_r deviation around 52.8 % (~ 49.6 milliohm). The smallest deviation is produced by the one-slope model with only 2.5 % (~ 2.4 milliohm). Deviation from other models is inside this range, including the DB-function. In this way, the proposed non-linear modelling produces more significant rotor parameter deviations that the traditional linear one.

iii) Once the fault is released as shown in Figure 7.8(b), the DB-function model goes to the steady-state with damped oscillations below the X_{fL} value. The two-slope models present larger amplitude oscillations than the DB-function model, they run above the Xfl value and as the R_r value decreases, their oscillations are magnified.

iv) In the steady-state and relative to the X_{fL} input value, the rotor leakage reactance from one-slope model deviates above around 1.15 % (~ 1.1 milliohm), the two-slope models also above around 4.93 % (~ 4.6 milliohm), and the DB-function model deviates below the X_{fL} value around 1.7 % (~ 1.6 milliohm). Note that the DB function produces a relative decrement while other deep-bar models produce a relative increment.

As expected, comparing Figures 7.5 and 7.8, X_r responses result in agreement to the trend in the reference machine, this is, X_r decreases as the absolute slip value increases and vice versa. Also note that this is 'one' result of several possible for each X_r/R_r ratio selected, according to Figure 7.4.

7.4.2 Time-Varying Rotor Parameters when the Induction Machine is Asymmetrically Perturbed.

An analysis similar to Section 7.4.1, is followed here. It allows comparing the same parameters, relative to those obtained there. Figures 7.9, 7.10, 7.11 and 7.12, have analogue results of Figures 7.5, 7.6, 7.7 and 7.8, respectively. It is observed that an oscillatory feature is common for all parameter responses, during the fault interval. It comes from the electromagnetic dynamics due to the asymmetrical operation, and has no direct relation to deep-bar modelling. The proof is that these oscillations are not present at the pre-fault time and they disappear once the fault is released. Thus, observations will be made at the centre of these waveforms.

A) The slip value in the steady-state, as measured at 20 s extrapolating what is shown in Figure 7.9(b) is effectively identical to the ones measured for the case of LLL fault, from every deep-bar model. The apparent differences in magnitude in Figures 7.5(b) and 7.9(b) are due to i) the oscillations introduced by the fault type and its associated recovery time, and ii) the suitably selected different vertical scale. Once the fault is released, the asymmetrical demagnetization progressively recovers to a symmetrical again and responses relax, going to the steady-state with damped low frequency oscillation.

B) As expected, the breakdown slip in the steady-state has identical values like those from LLL fault. In this way, the corresponding comments are identical too. During the fault interval, responses present also smaller deviation from their respective steady-state values than in the case of LLL fault. Once the fault is cleared, the damped oscillatory response is larger than in the case of LLL fault, from two-slopes and DB-function models.

C) The time-varying rotor resistance response as shown in Figure 7.11(a), during the fault interval runs with very low frequency of the order of 0.22 Hz, oscillating with small amplitude relative to the deviation from the R_{fL} value (8.9 mili-ohm). The largest rotor resistance average deviation, as measured at the centre of an oscillatory waveform, is obtained from the two-slope model when R_r = 0.023 ohm and with around 45 % (~ 4 mili-ohm), above the input R_{fL} value. The minimum deviation comes from one-slope model, with only 1.8 % (~ 0.16 mili-ohm). Once the fault is cleared as shown in Figure 7.11(b), rotor resistance responses settle to the steady-state with damped oscillation, where the DB-function model presents the smallest amplitude if compared to two-slope responses. The one-slope model response oscillation has practically negligible amplitude.

The time-varying rotor leakage reactance response X_r, follows the trend of X_r with LLL fault, as shown in Figure 7.12(a), but now at the centre of one oscillatory waveform. The maximum average deviation comes from the DB-function model with around 25.5 % (~ 24 milliohm). With the two-slope models, as the selected R_r increases, their respective maximum deviations decreases. Note that the one-slope model produces a slightly 1 % (~ 1 milliohm) larger X_r value above the X_{fL} input value, and its deviation due to LG fault looks negligible.

D) Once the fault is cleared as shown in Figure 7.12(b), all deep-bar models go to the steady-state with a softer waveform like in the case of LLL fault. Again the DB-function model runs below the X_{fL} value and two-slope models above it. The one-slope model runs practically constant.

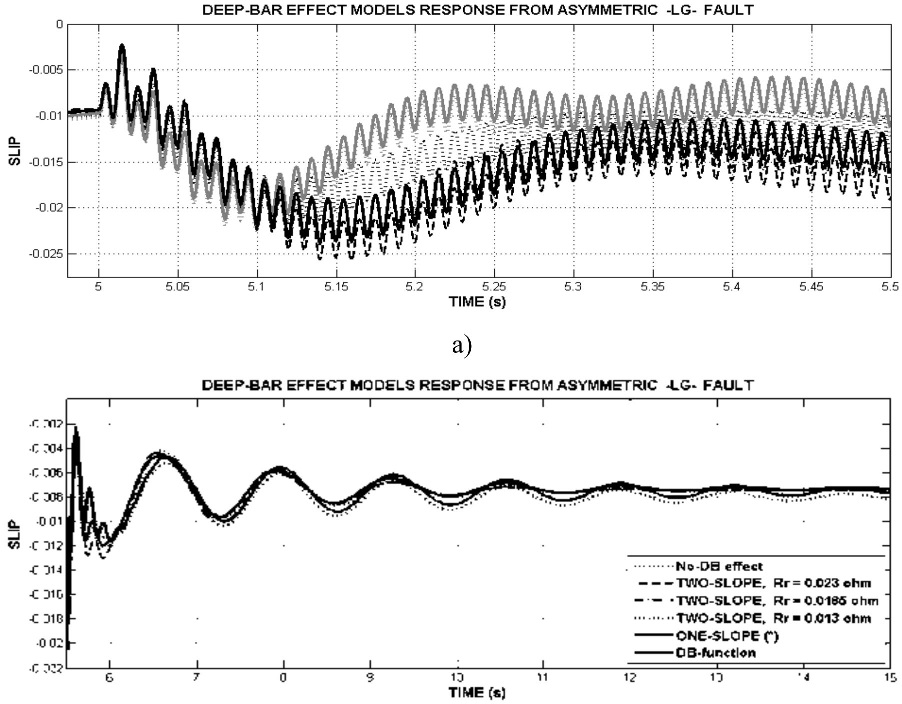

a)

b)

Figure 7.9 Time-varying slip response, due to the application of a line-to-ground (LG) fault at PCC, a) fault interval, b) after the fault is cleared

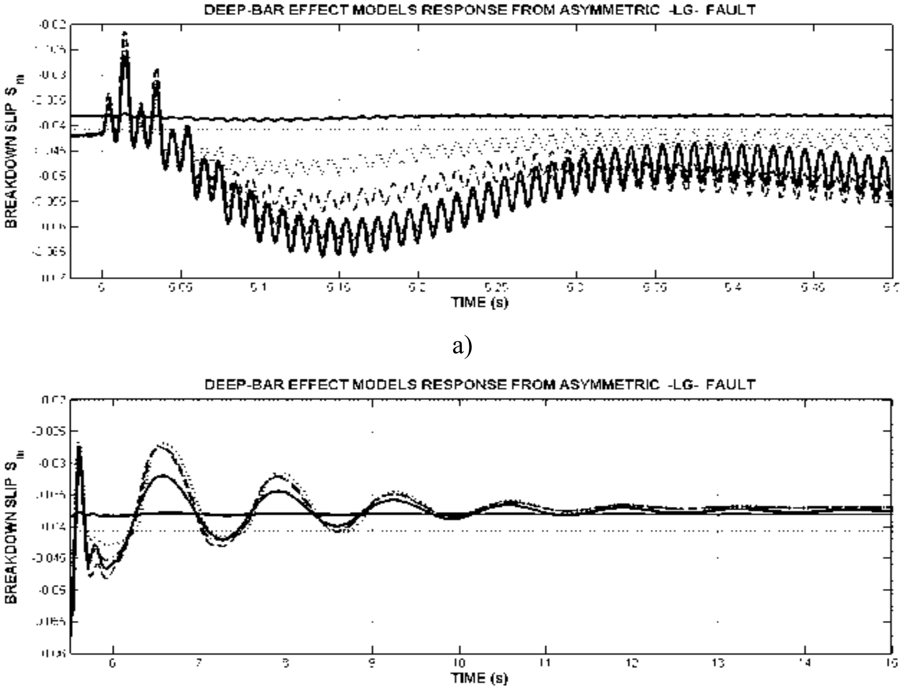

a)

b)

Figure 7.10 Time-varying breakdown slip response, by applying a line-to-ground (LG) fault at PCC, a) fault interval, b) after the fault is cleared

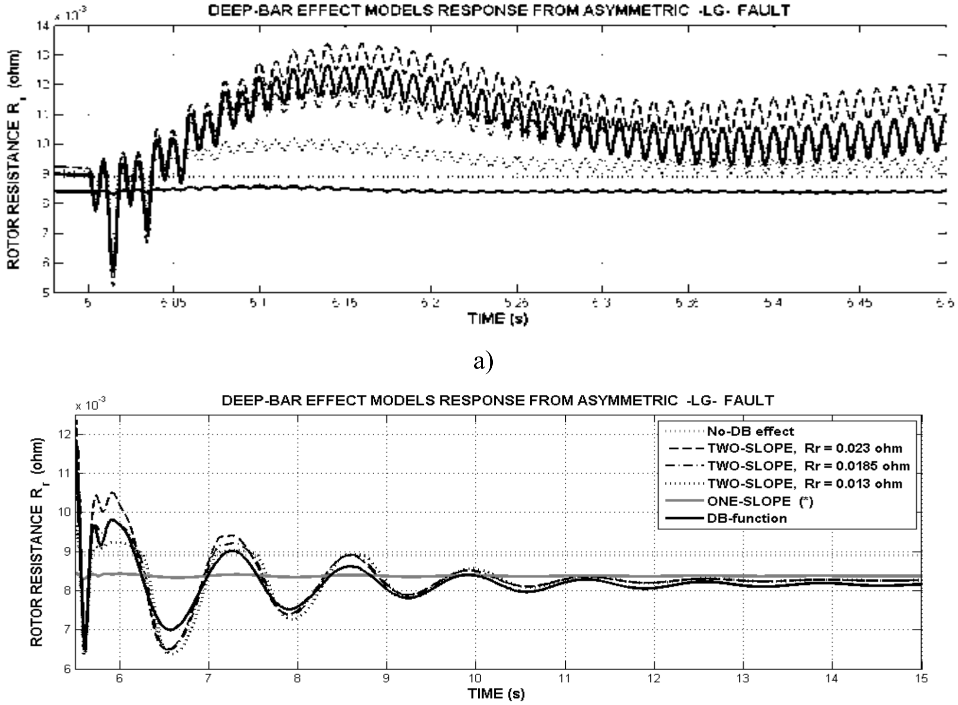

a)

b)

Figure 7.11 Time-varying rotor resistance, by applying a line-to-ground (LG) fault at PCC, a) fault interval, b) after the fault is cleared

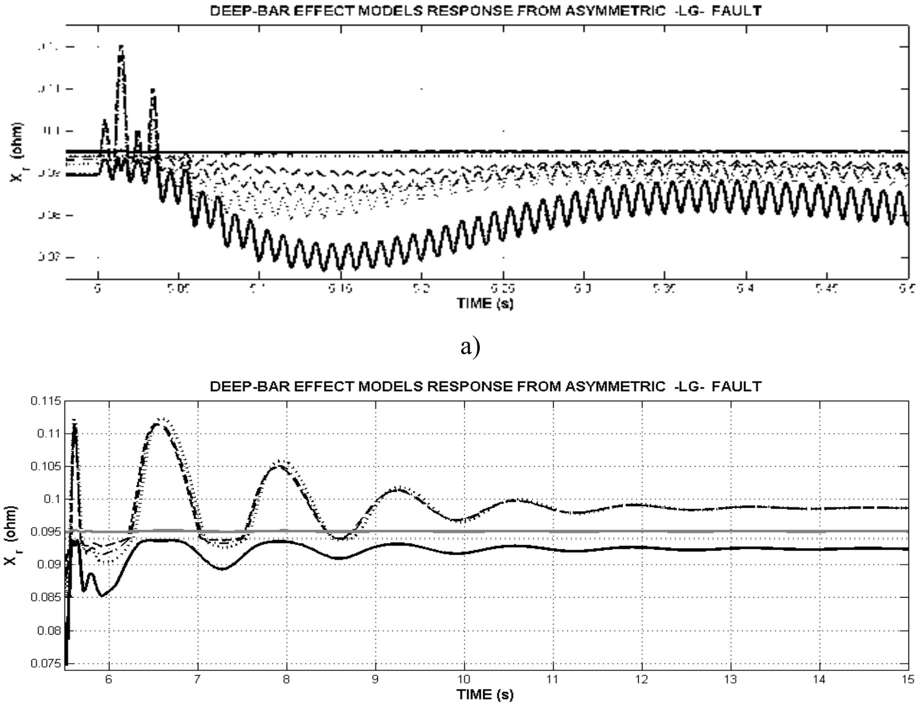

a)

b)

Figure 7.12 Time-varying rotor leakage reactance, by applying a line-to-ground (LG) fault at PCC, a) fault interval, b) after the fault is cleared

7.4.3 Deep-Bar Effect on the Electromagnetic torque

This is the directly influenced variable due to rotor parameter changes, as affected by deep-bar effect. Figure 7.13 shows the electromagnetic torque for identical operating conditions and different deep-bar models. Observations allow establishing the following:

i) Due to the very low speed starting time, all models report a positive starting torque in motor mode,

ii) All models look for the maximum positive torque but each one achieves it at different times. Without deep-bar effect, this time is approximately 7.782 s, while from the one-slope deep-bar model is around 4.358 s, from the two-slope models is 3.237 s and from the DB-function model is around 3.205 s. If the DB-function is taken as a truth reference, the deviation time from other models is: 32 ms relative to two-slope models, 1.153 s from one-slope model and 4.577 s from the No-DB effect model.

iii) The maximum value from No-DB effect model is around of 1.38 p.u. from one-slope model is around of 1.95 p.u., from two-slopes around of 3.03 p.u. and from the DB-function model is around of 2.57 p.u. It demonstrates that the deep-bar effect significantly influence the maximum torque occurrence and value. If the DB-function is taken as a truth reference, the error from other models is: 46 % relative to two-slope models, 62 % relative to the one-slope model and 119 % relative to the No-DB effect model.

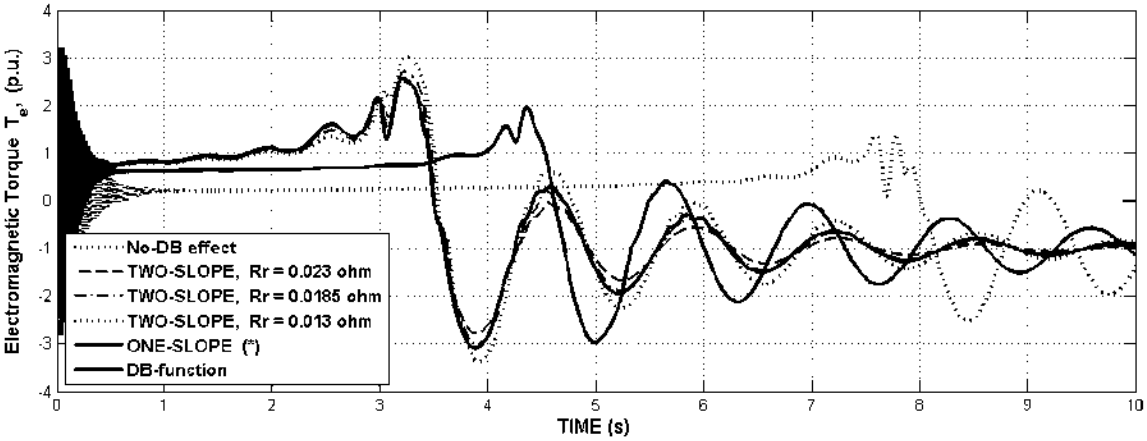

a)

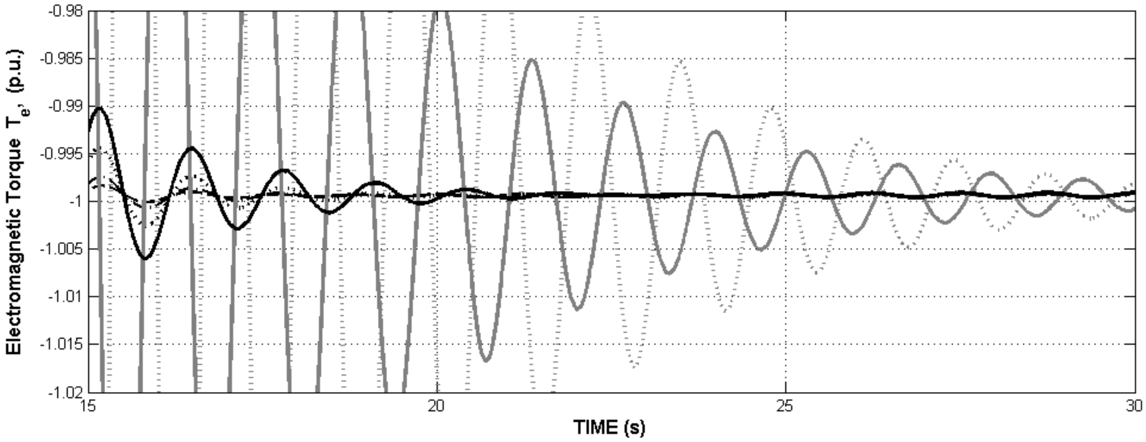

b)

Figure 7.13 Electromagnetic torque response from various deep-bar effect models: a) at the start-up, b) process toward the steady-state

iv) Once the maximum positive value is reached, all models look for the negative maximum,

v) Despite the heterogeneous transient state, there is a trend to a common steady-state from all deep-bar models, as measured at 30 s and shown in figure 7.13(b). In addition it is observed that the DB-function model is slightly less damped than the two-slope models and try to match the corresponding to R_r = 0.0185 ohm. The one-slope model presents the less damped response only exceeded by the No-DB effect model.

It is inferred that, the non-linear DB-function model produces the most significant effect on the electromagnetic torque, making the response much more in advance relative to other models responses and incrementing the maximum value at the motor operating mode. The 2-slope approach produces almost identical responses like the DB-function, and they go closed to it, as the pilot rotor resistance value increases. The one-slope model is an intermediate response closer to deep-bar effect with DB-function than that ignoring it. Once the machine goes to the generator operating mode, the maximum oscillation belongs also to the DB-function and 2-slope models. Also the 2-slope models have competitive convergence process, as compared to the DB-function response, going to the steady-state. The one-slope and the response neglecting the DB effect converge with larger oscillations.

7.5 Conclusion

Taking into account an experimental report for a 7.5 MW induction machine test, it has been inferred a suitable methodology to produce rotor parameters as slip dependent functions, for a 2 MW large machine. Being the slip a time domain variable, it allows computing time domain responses for rotor resistance and leakage reactance parameters as well as any electro-mechanical variable.

The proposed methodology is based in the careful selection of a set of six rotor resistance values, within a consistent test zone. Two mandatory trial points match the start-up and full-load conditions. Other two match the slips at pull-out and breakdown torques. Two additional points are above and below the breakdown slip. About the first four points there is high certainty from standard tests. The last two points are completely uncertain but they can be reasonable chosen once the breakdown slip is computed.

From these six points, a continuous slip dependent function can be easily identified, using any fitting tool. Also two-slope slip dependent model is perfectly located and justified.

For comparison purposes and in order to reference the classical procedure, a known one-slope model is used and also a model without deep-bar effect.

Results demonstrate that the proposed methodology works well, reproducing the steady-state for the research machine, the observed trend in the rotor parameters in the reference machine. The model is probed with the electromagnetic torque, where the non-linear DB-function model produces the most significant effect, making the response much more in advance, relative to other deep-bar models responses and incrementing the magnitude of the breakdown torque.

The time domain methodology here proposed to take into account the deep-bar effect, appears to be computationally efficient to be extended to any large machine.

* * *

THIS PAGE IS INTENTIONALLY LEFT BLANK

8

Conclusion and Recommendations for Future Work

8.1 Conclusion

An advanced non-linear, time-domain, 123 ↔ *abc* wind turbine electromechanical modelling has been presented.

The mechanical sub-model*,* which involves large pre-bent blades, makes possible the detection of individual *123* blade disturbances. It produces more significant waveform of the effective per-blade wind speed, taking into account wind shear and tower transference effects, with feedback from blade mechanical loading. This improves the assessment of individual blade contributions to the mechanical torque computation. The sub-model also allows defining an operational per-blade inertia moment, and thus, a more reliable blade-based 2-mass model has been proposed. As a consequence of these integrated effects, individual per-blade 123 rotational speeds contributions can also be evaluated to compose the resultant rotational speed at the low-speed shaft.

The electric generator sub-model in phase coordinates ABC/*abc*, reinforced with relevant electromagnetic phenomena as valid for large machines, directly detects and transfers either electric sinusoidal or non-sinusoidal phase voltage disturbances. They produce stator and rotor phase currents with all the disturbance information to produce consequent stator and rotor fluxes state variables. Furthermore, the representation of main path magnetic saturation by mean of three *ABC* saturation characteristics makes significantly sensible this path to phase contributions. If similar conception is involved to represent *ABC* iron losses and *abc* deep-bar effect, they produce a whole induction generator model very sensible to asymmetrical electrical disturbances. It has been demonstrated that the averaging of these results produce the expected results, as obtained from the traditional modelling.

The resultant electromagnetic torque, as made with individual phase magnetizing inductance and currents effects, is going to interact with the wind turbine mechanical torque in the shaft system, as composed by individual blade effects.

As it is evident, the individual *abc* ↔ *123* electro-mechanical effects are combined in the low and high-speed shafts, but now with the contribution of individual components. Due to this interaction, the respective rotational speeds are influenced.

This wind turbine modelling makes possible to assess symmetrical and asymmetrical, mechanical and electrical disturbances. It results significantly more robust for dynamic studies than the traditional one, particularly when the wind power plant is interconnected with conventional power plants.

8.2 Recommendations for Future work

The wind turbine electro-mechanical model presented in this thesis should be suitably supplemented with a power electronic based reactive power source. The control strategy expected for the whole wind turbine setup should include the individual blade dynamics into the individual pitch angle control, and it should safeguard the *abc* ↔ *123* interaction characteristics here found, improving or replacing the classical PID controller. These will also enable the construction of a detailed and suitably aggregated power plant model. Given the no possibility to properly validate this thesis results, it should be done against experimental data.

The computational characteristics of the Simulink blocks in the present model should be revisited in order to improve the efficiency of the inherent expensive computational time. Starting from this detailed wind turbine modelling together to the operative conditions, this modelling will contribute to the limited experience on making reduced order models of wind turbines. This modelling is also estimated to will enable the construction of dedicated power system arrangements, to represent either area control zones or whole power systems, for power system dynamic studies.

◆

Appendix A.

Background and Supplements for the Wind Modelling

A.1 Logarithmic law: wind profile model with atmospheric stability

The logarithmic law approach is based on Monin-Obukhov similarity theory (MOST) [Monin and Obukhov 1954]. Given an horizontal motion of the flow in the Atmospheric Boundary Layer (ABL) and assuming barotropic conditions and horizontal homogeneity, a direct consequent definition of wind speed gradient is [Large and Pound 1981], [Andreas *et al*. 2006], [Peña *et al*. 2008],

$$\frac{du_z}{dz} = \frac{u_*}{\kappa}\frac{1}{\ell} \tag{A.1}$$

where $\ell = \ell_{SL}\phi_m^{-1}$ is the local length scale, κ is the Von-Karman constant, u_* is the surface friction velocity and $\phi_m(\zeta)$ is a universal function also named atmospheric stability correction, or dimensionless wind shear, introduced in MOST. In [Dyer 1974], [Large and Pound 1981] $\phi_m(\zeta)$ is defined with $\zeta = z/L$, being L the Obukhov's length as,

$$\phi_m(\zeta) = \begin{cases} 1 + a\zeta, & \zeta > 0 \\ 1 + b\zeta + c\zeta^2, & -0.1 < \zeta < 0.1 \\ (1 + d\zeta)^p, & \zeta < 0 \end{cases} \tag{A.2}$$

with *a*, *b*, *c* and *p* constants are according to [Businger *et al.* 1971]. In a general case the length scale in the surface layer is,

$$\ell_{SL} = z - d_{om} \tag{A.3}$$

where z is the height of interest, d_{om} is the displacement height measured in length units and used for the surface layer applications [Yanlian *et al*. 2006], [Zilitinkevich *et al*. 2008]. This length suitably displaces the vertical axis origin [Monin and Yaglow 1971], [Garratt 1992] as associated with the aerodynamic roughness length z_{om}. Once integrated (2.3), the result can be written as,

$$u_z = \frac{u_*}{\kappa} Z_\psi \tag{A.4}$$

with the Z_ψ factor as defined in [McBean and Miyake 1972], [Holstlag *et al*. 1990], [Yanlian *et al*. 2006], [Zilitinkevich *et al*. 2006] as,

$$Z_\psi = Z_1 + Z_2 + Z_3 \tag{A.5}$$

with

$$Z_1 = \ln\left(\frac{z - d_{om}}{z_{om}}\right), \quad Z_2 = -\Psi_m\left(\frac{z - d_{om}}{L}\right), \quad Z_3 = \Psi_m\left(\frac{z_{om}}{L}\right)$$

In Marine Atmospheric Boundary Layer d_{om} is usually neglected [Peña *et al*. 2008] and it is reserved for land applications. As it will be demonstrated later and maybe without computation, a very small value for the Z_3 term is expected. The Ψ_m function results from the integration process applied to (2.3) [Large and Pound 1981]. For stable conditions ($\zeta > 0$) it gives,

$$\Psi_m\left(\frac{z}{L}\right) = -a\frac{z}{L} \tag{A.6}$$

And for unstable conditions ($\zeta < 0$) it gives,

$$\Psi_m\left(\frac{z}{L}\right) = 2\ln\left(\frac{1+\chi}{2}\right) + \ln\left(\frac{1+\chi^2}{2}\right) - 2\tan^{-1}\chi + \frac{\pi}{2} \tag{A.7}$$

with,

$$\chi = \left(1 + d\frac{z}{L}\right)^p$$

A more closed approach to near to neutral stability conditions is,

$$\Psi_m\left(\frac{z}{L}\right) = -\left(b\frac{z}{L} + \frac{c}{2}\left[\frac{z}{L}\right]^2\right) \tag{A.8}$$

Parameters a, b,d, and p are selected according to the theoretical limit for convective conditions [Carl *et al*. 1973], [Grachev *et al*. 2000], [Gryning *et al*. 2007].

A.2 Logarithmic law: three-layer wind profile model

In 2007, an extension of the wind profile formulation valid for homogeneous terrain and beyond the surface boundary layer was presented in [Gryning *et al.* 2007]. The length scale l in (A.1) is composed of three layers, the surface, middle and upper part of the boundary layer. For stable conditions ($L > 0$) the three-layer length scale results,

$$\frac{1}{\ell} = \frac{1}{z}\left(1 + b\frac{z}{L}\right) + \frac{1}{\ell_{MBL}} + \frac{1}{z_i - z} \tag{A.9}$$

and for unstable conditions ($L < 0$),

$$\frac{1}{\ell} = \frac{1}{z}\left(1 - 12\frac{z}{L}\right)^{-1/3} + \frac{1}{\ell_{MBL}} + \frac{1}{z_i - z} \tag{A.10}$$

and z_i could be calculated or measured [Peña *et al.* 2010]. In [Gryning *et al.* 2007],

$$z_i = \frac{c u_{*_o}}{f_c} \tag{A.11}$$

Because of determining c constant is computationally complex, it is approached to 0.25 in [Tennekes 1982] and 0.1 in [Gryning *et al.* 2007]; f_c is the Coriolis parameter computed as,

$$f_c = \left|2\Omega \sin \phi_f\right| \tag{A.12}$$

with Ω being the earth's angular velocity, ϕ_f the latitude angle and

$$\ell_{MBL} = \frac{u_{*o} / f_c}{55 - 2\ln\left(u_{*o} / (f_c z_{om})\right)} \tag{A.13}$$

Wind profile for stable and stable conditions is then built. Results were already presented in Chapter 2, Section 2.1. The specific resultant atmospheric stability Ψ_{mG} function is,

$$\Psi_{mG}\left(\frac{z}{L}\right) = \frac{3}{2}\ln\left(\frac{1+\chi_G+\chi_G^2}{3}\right) - \sqrt{3}\arctan\left(\frac{1+2\chi_G}{\sqrt{3}}\right) + \frac{\pi}{\sqrt{3}} \tag{A.14}$$

where,

$$\chi_G = \left(1 + a\frac{z}{L}\right)^p$$

A.3 Aerodynamic roughness length based on Charnock parameter

The aerodynamic roughness length research is based on the Charnock parameter α_c using experimental constants A, B, C, D [Lange an Højstrup 2000], [Saint-Drenan 2009]. These constants try to describe the general trend of a very scattered on-site measuring data. Despite of the 50's constant value in [Charnock 1955], in the 90's and using a subset data from the HEXMAX experiment, [Maat *et al*. 1991], [Smith *et al*. 1992] a general Charnock model also called the HEXOS relationship [Taylor and Yelland 2001] was proposed as,

$$\alpha_c = A\left(\frac{C_p}{u_*}\right)^B \tag{A.15}$$

from which the aerodynamic roughness length is defined as,

$$z_{om} = \alpha_c \frac{u_*^2}{g} \tag{A.16}$$

This implies that younger waves are rougher than older waves; z_{om} is the height (m) where wind speed becomes zero when extrapolated downward from the surface boundary layer. It is expected from this modelling that z_{om} proportionally reflects the strongest wind stress which results in high waves; g is the gravity acceleration. The friction velocity u_* is closed to the water surface and in this research it is assumed less than 0.32 ms^{-1} which has been found the lowest value for smooth low height rural terrain [Gryning *et al.* 2007].

For coastal areas and in the ocean, it has been established that Charnock's parameter is greatly influenced by the wave age C_p/u_* generation process (being C_p the phase speed), its steepest characteristics, its distance to the shore, its frequency, and the wind speed and direction. Another fundamental research agreement is the Kitaigorodskii's ratio established in 1962, which relates inverse wave age and fetch x given by [Kitaigorodskii 1962],

$$\frac{u_*}{C_p} = C\left(\frac{g}{u_*^2}x\right)^D \tag{A.17}$$

The left term comes from the wave frequency in rad/s [Johnson *et al.* 1998] and it matches the definition $w_p = g/C_p$ [Stewart 2008]. It is also presented in [Hasselmman *et al.* 1973] with the frequency in Hz. In neutral atmospheric conditions, the drag coefficient $C_d(z)$

relates u_* and u_z wind speeds according to [Csanady 1967], [Garrat 1977], [Taylor and Yelland 2001] is,

$$C_d(z) = \left(\frac{u_*}{u_z} \right)^2 \tag{A.18}$$

A.4 Wind shear constants.

In Section 2.2.5.1 the Taylor series expansion applied to the power law, leaves the following constants:

$$\begin{aligned}
C_{P0} &= h^{\alpha} - O_{vh} K_1 \sin\gamma + O_{vh}^2 K_2 \sin^2\gamma - O_{vh}^3 K_3 \sin^3\gamma + O_{vh}^4 K_4 \sin^4\gamma \\
&\quad - O_{vh}^5 K_5 \sin^5\gamma + O_{vh}^6 K_6 \sin^6\gamma \\
C_{P1} &= -K_1 + 2O_{vh} K_2 \sin\gamma - 3O_{vh}^2 K_3 \sin^2\gamma \\
&\quad + 4O_{vh}^3 K_4 \sin^3\gamma - 5O_{vh}^4 K_5 \sin^4\gamma + 6O_{vh}^5 K_6 \sin^5\gamma \\
C_{P2} &= K_2 - 3O_{vh} K_3 \sin\gamma + 6O_{vh}^2 K_4 \sin^2\gamma \\
&\quad - 10O_{vh}^3 K_5 \sin^3\gamma + 15O_{vh}^4 K_6 \sin^4\gamma \\
C_{P3} &= -K_3 + 4O_{vh} K_4 \sin\gamma - 10O_{vh}^2 K_5 \sin^2\gamma + 20O_{vh}^3 K_6 \sin^3\gamma \\
C_{P4} &= K_4 - 5O_{vh} K_5 \sin\gamma + 15O_{vh}^2 K_6 \sin^2\gamma \\
C_{P5} &= -K_5 + 6O_{vh} K_6 \sin\gamma \\
C_{P6} &= K_6
\end{aligned} \tag{A.19}$$

with,

$$K_1 = \alpha z^{\alpha-1}$$

$$K_2 = \frac{1}{2}\alpha(\alpha-1) z^{\alpha-2}$$

$$\begin{aligned}
K_3 &= \frac{1}{6}\alpha(\alpha-1)(\alpha-2)z^{\alpha-3} \\
K_4 &= \frac{1}{24}\alpha(\alpha-1)(\alpha-2)(\alpha-3)z^{\alpha-4} \\
K_5 &= \frac{1}{120}\alpha(\alpha-1)(\alpha-2)(\alpha-3)(\alpha-4)z^{\alpha-5} \\
K_6 &= \frac{1}{720}\alpha(\alpha-1)(\alpha-2)(\alpha-3)(\alpha-4)(\alpha-4)z^{\alpha-6}
\end{aligned} \tag{A.20}$$

In Section 2.2.5.1, the Taylor's series expansion applied to the logarithmic law with atmospheric stability, leaves the following constants: For the stable case (L>0),

$$\begin{aligned}
C_{S0} = Z_{\psi o} &+ O_{vh}(aL^{-1}-(z-d_{om})^{-1})\sin\gamma \\
&- O_{vh}^2\frac{(z-d_{om})^{-2}}{2}\sin^2\gamma - O_{vh}^3\frac{(z-d_{om})^{-3}}{3}\sin^3\gamma - O_{vh}^4\frac{(z-d_{om})^{-4}}{4}\sin^4\gamma \\
&- O_{vh}^5\frac{(z-d_{om})^{-5}}{5}\sin^5\gamma - O_{vh}^6\frac{(z-d_{om})^{-6}}{6}\sin^6\gamma + \ldots
\end{aligned}$$

$$\begin{aligned}
C_{S1} = -(z-d_{om})^{-1} &+ aL^{-1} - O_{vh}(z-d_{om})^{-2}\sin\gamma \\
&- O_{vh}^2(z-d_{om})^{-3}\sin^2\gamma - O_{vh}^3(z-d_{om})^{-4}\sin^3\gamma \\
&- O_{vh}^4(z-d_{om})^{-5}\sin^4\gamma - O_{vh}^5(z-d_{om})^{-6}\sin^5\gamma
\end{aligned}$$

$$\begin{aligned}
C_{S2} = -\frac{(z-d_{om})^{-2}}{2} &- O_{vh}(z-d_{om})^{-3}\sin\gamma - 3O_{vh}^2\frac{(z-d_{om})^{-4}}{2}\sin^2\gamma \\
&- 2O_{vh}^3(z-d_{om})^{-5}\sin^3\gamma - 15O_{vh}^4\frac{(z-d_{om})^{-6}}{6}\sin^4\gamma
\end{aligned}$$

$$\begin{aligned}
C_{S3} = -\frac{(z-d_{om})^{-3}}{3} &- O_{vh}(z-d_{om})^{-4}\sin\gamma - 2O_{vh}^2(z-d_{om})^{-5}\sin^2\gamma \\
&- 10O_{vh}^3\frac{(z-d_{om})^{-6}}{3}\sin^3\gamma
\end{aligned} \tag{A.21}$$

$$C_{S4} = -\frac{(z-d_{om})^{-4}}{4} - O_{vh}(z-d_{om})^{-5}\sin\gamma - 15O_{vh}^2\frac{(z-d_{om})^{-6}}{6}\sin^2\gamma$$

$$C_{S5} = -\frac{(z-d_{om})^{-5}}{5} - O_{vh}(z-d_{om})^{-6}\sin\gamma$$

$$C_{S6} = -\frac{(z-d_{om})^{-6}}{6}$$

And for the unstable case,

$$\begin{aligned}
C_{U0} &= Z_{\psi o} - O_{vh}[(z-d_{om})^{-1} + C'_{wsU}]\sin\gamma + O_{vh}^2\frac{(-(z-d_{om})^{-2} + C''_{wsU})}{2}\sin^2\gamma \\
&\quad - O_{vh}^3\frac{2(z-d_{om})^{-3} + C'''_{wsU}}{6}\sin^3\gamma \\
C_{U1} &= -[(z-d_{om})^{-1} + C'_{wsU}] + 2O_{vh}\frac{(-(z-d_{om})^{-2} + C''_{wsU})}{2}\sin\gamma \\
&\quad - 3O_{vh}^2\frac{2(z-d_{om})^{-3} + C'''_{'wsU}}{6}\sin^2\gamma \\
C_{U2} &= \frac{(-(z-d_{om})^{-2} + C''_{wsU})}{2} - 3O_{vh}\frac{R_b^4 - r_{ob}^4}{4}\frac{2(z-d_{om})^{-3} + C'''_{'wsU}}{6}\sin\gamma \\
C_{U3} &= \frac{2(z-d_{om})^{-3} + C'''_{'wsU}}{6}
\end{aligned} \tag{A.22}$$

In Section 2.2.5.1 the Taylor series expansion applied to the logarithmic law with atmospheric stability, leaves the following constants. For the stable case (L>0),

$$\begin{aligned}
C_{GS0} &= Z_{\psi o} \\
&\quad - O_{vh}[(z-d_{om})^{-1} - aL^{-1} + \frac{b}{L}\left(1 + \frac{d_{om}}{2z_i}\right) - \frac{b}{z_i L}z + \ell_{MBL}^{-1} + (z-d_{om})(z_i\ell_{MBL})^{-1}]\sin\gamma \\
&\quad - O_{vh}^2\frac{(z-d_{om})^{-2} - b/(Lz_i)^{-1} + (z_i\ell_{MBL})^{-1}}{2}\sin^2\gamma \\
&\quad + O_{vh}^3\frac{(z-d_{om})^{-2} - b/(Lz_i)^{-1} + (z_i\ell_{MBL})^{-1}}{2}\sin^3\gamma \\
&\quad - O_{vh}^4\frac{(z-d_{om})^{-4}}{4}\sin^4\gamma - O_{vh}^5\frac{(z-d_{om})^{-5}}{5}\sin^5\gamma - O_{vh}^6\frac{(z-d_{om})^{-6}}{6}\sin^6\gamma
\end{aligned}$$

$$
\begin{aligned}
C_{GS1} &= -[(z-d_{om})^{-1} - aL^{-1} + \frac{b}{L}\left(1+\frac{d_{om}}{2z_i}\right) - \frac{b}{z_i L}z + \ell^{-1}_{MBL} + (z-d_{om})(z_i \ell_{MBL})^{-1}] \\
&\quad - O_{vh}[(z-d_{om})^{-2} - b/(Lz_i)^{-1} + (z_i \ell_{MBL})^{-1}]\sin\gamma - O_{vh}^2 (z-d_{om})^{-3}\sin^2\gamma \\
&\quad - O_{vh}^3 (z-d_{om})^{-4} r_b^2 \sin^3\gamma - O_{vh}^4 (z-d_{om})^{-5}\sin^4\gamma \\
&\quad - O_{vh}^5 (z-d_{om})^{-6}\sin^5\gamma \\
\\
C_{GS2} &= -\frac{(z-d_{om})^{-2} - b/(Lz_i)^{-1} + (z_i \ell_{MBL})^{-1}}{2} - O_{vh}(z-d_{om})^{-3}\sin\gamma \\
&\quad - 3O_{vh}^2 \frac{(z-d_{om})^{-4}}{2}\sin^2\gamma - 2O_{vh}^3 (z-d_{om})^{-5}\sin^3\gamma - 15O_{vh}^4 \frac{(z-d_{om})^{-6}}{6}\sin^4\gamma \\
C_{GS3} &= -\frac{(z-d_{om})^{-3}}{3} - O_{vh}(z-d_{om})^{-4}\sin\gamma - 2O_{vh}^2 (z-d_{om})^{-5}\sin^2\gamma \\
&\quad - 10O_{vh}^3 \frac{(z-d_{om})^{-6}}{3}\sin^3\gamma \\
\\
C_{GS4} &= -\frac{(z-d_{om})^{-4}}{4} - O_{vh}(z-d_{om})^{-5}\sin\gamma - 15O_{vh}^2 \frac{(z-d_{om})^{-6}}{6}\sin^2\gamma \\
\\
C_{GS5} &= -\frac{(z-d_{om})^{-5}}{5} - O_{vh}(z-d_{om})^{-6}\sin\gamma \\
\\
C_{GS6} &= -\frac{(z-d_{om})^{-6}}{6}
\end{aligned}
\tag{A.23}
$$

and for the unstable case (L<0),

$$
\begin{aligned}
C_{GU0} &= Z_{\psi o} - O_{vh}\left((z-d_{om})^{-1} + C'_{wsU} + \ell^{-1}_{MBL} + \frac{z-d_{om}}{z_i \ell_{MBL}}\right)\sin\gamma \\
&\quad + O_{vh}^2\left(\frac{-(z-d_{om})^{-2} + C''_{wsU} + (z_i \ell_{MBL})^{-1}}{2}\right)\sin^2\gamma \\
&\quad - O_{vh}^3\left(\frac{2(z-d_{om})^{-3} + C'''_{wsU}}{6}\right)\sin^3\gamma
\end{aligned}
$$

$$
\begin{aligned}
C_{GU1} = &-\left((z-d_{om})^{-1} + C'_{wsU} + \ell_{MBL}^{-1} + \frac{z-d_{om}}{z_i \ell_{MBL}} \right) \\
&+ O_{vh} \left(-(z-d_{om})^{-2} + C''_{wsU} + (z_i \ell_{MBL})^{-1} \right) \sin\gamma \qquad \text{(A.24)} \\
&- O_{vh}^{2} \left(\frac{2(z-d_{om})^{-3} + C'''_{'wsU}}{2} \right) \sin^2\gamma
\end{aligned}
$$

$$
C_{GU2} = \left(\frac{-(z-d_{om})^{-2} + C''_{wsU} + (z_i \ell_{MBL})^{-1}}{2} \right) - O_{vh} \left(\frac{2(z-d_{om})^{-3} + C'''_{'wsU}}{2} \right) \sin\gamma
$$

$$
C_{GU3} = -\frac{2(z-d_{om})^{-3} + C'''_{'wsU}}{6}
$$

A.5 Blade mechanical loading

Three loading sources at every blade body-section are identified [Hansen 2008].

1. **Gravitational source** due to earth’s gravitational field, produces a load associated to the blade mass density distributed along the blade, which is an available manufacturer datum [Hansen 2008], [Jonkman *et al*. 2009]. This force is wind turbine speed rotor dependant.

2. **Inertial source** due to blade acceleration / deceleration produces a load associated to wind changes, breaking torque and centrifugal effects. These load are wind turbine rotor speed dependent.

3. **Aerodynamic source** producing aerodynamic tangential (y-axis) p_T and normal (z-axis) p_N loads acting in the rotor plane and perpendicular to it respectively. These loads are the natural consequence of the blade structure [Madsen *et al*. 1984], [Jonkman *et al*. 2009], [Hansen 2008], and depend on wind characteristics, blade aerodynamic characteristics and wind turbine speed rotor.

The corresponding forces combination acting in the rotor plane (y-axis) produce an edgewise bending moment M_{edg} , which delivers the shaft torque that turns the rotor. While the forces combination acting perpendicular to the rotor plane (z-axis) produce a flapwise bending moment M_{flp} , which try to deflect the blades out of the rotor plane.

In [Jonkman *et al*. 2009] large-blade structural and dynamic data is provided from laboratory tests laid on software like AeroDyn, FAST and ADAMS. It is furthermore emphasized there that this data is obtained by re-processing some before wind turbine prototypes from MULTIBRID - M5000, REpower, WindPACT, RECOFF and DOWEC projects. All of them are at least 5 MW capacity size and 60 m blade length. In [Jonkman *et al*. 2009], data target reference is the REpower one published in 2005. Tabulated data relating several parameters to blade body section is presented. This list together to the data in [Hansen 2008] and [Kallesøe and Hansen 2008], matches the needed data to apply the beam theory, which are as follows:

- Distance from the zero blade-root to each blade body section and the respective:
- Chord (m)
- Twist angle (deg)
- ν angle to be used in (2-39)-(2.42)
- Mass density (kg/m)
- Flap Stiffness (Nm^2)
- Edge Stiffness (Nm^2)
- Torsional Stiffness (Nm^2)
- Flap Inertia (kgm)
- Edge Inertia (kgm)
- Aeroelastic frequency for first flapwise function (Hz)
- Aeroelastic frequency for first edgewise function (Hz)

In [Kallesøe and Hansen 2008] functions relating first flapwise and edgewise frequencies to wind turbine rotor speed are published. With this information, the Matlab curve fitting tool **cftool** is called on to build or reply according to the case, respective mathematical functions.

Wind force T in N-m is a function of wind load p, mass density m and blade deflection $\delta_{y,z}$. They are expressed by,

$$\frac{dT_y}{dr} = -p_y(r) + m(r)\ddot{\delta}_y(r)\ ,\quad \frac{dT_z}{dr} = -p_z(r) + m(r)\ddot{\delta}_z(r) \tag{A.25}$$

Bending moments M in N-m^2 as a consequence result to be,

$$\frac{dM_y}{dr} = T_z\ ,\quad \frac{dM_z}{dr} = -T_y \tag{A.26}$$

Blade angle deformations $\boldsymbol{\theta}_{yz}$ in radians as a function of factors K_k ($k = y$, z), as defined in (A.11) and (A.12) outcome,

$$\frac{d\theta_y}{dr} = K_y\ ,\quad \frac{d\theta_z}{dr} = K_z \tag{A.27}$$

In consequence, blade deflections $\boldsymbol{\delta}_{yz}$ in meters,

$$\frac{d\delta_y}{dr} = \theta_z\ ,\quad \frac{d\delta_z}{dr} = -\theta_y \tag{A.28}$$

where, $m(r)$ is the blade mass density associated to a blade body-section at a r distance from the blade-root. A symbol ($\ddot{\mathbf{x}}$) means d^2/dt which applied over a length in the case of δ_{yz} it means acceleration as in the case of (A.4). Since for an eigen-mode the associated deflection is $\delta_l = A\sin(w_*t)$, the acceleration results proportional to the deflection,

$$\ddot{\delta}_{yz} = -w_{*yz}^2 \delta_{yz} \tag{A.29}$$

where w_{*yz} is frequency mode associated to blade flapwise (z-axis) or edgewise (y-axis) move. Transforming the bending moments M_y and M_z to the principal axis it results,

$$M_1 = M_y \cos(\beta_E + \upsilon) - M_z \sin(\beta_E + \upsilon) \tag{A.30}$$

$$M_2 = M_y \sin(\beta_E + \upsilon) + M_z \cos(\beta_E + \upsilon) \tag{A.31}$$

Expressing the curvatures κ_k/M_i ($i = 1, 2$) about the principal axis, back on y and z axis,

$$\kappa_y = \frac{M_1}{(EI)_1}\cos(\beta_E + \upsilon) + \frac{M_2}{(EI)_2}\sin(\beta_E + \upsilon) \tag{A.32}$$

$$\kappa_z = -\frac{M_1}{(EI)_1}\sin(\beta_E + \upsilon) + \frac{M_2}{(EI)_2}\cos(\beta_E + \upsilon) \tag{A.33}$$

where $\kappa_{y,z}$ is a dummy variable. In the above expressions (A-9)-(A.12) [Hansen 2008], the twist angle $\boldsymbol{\beta_E}$ combined with the relatively usually small $\boldsymbol{\upsilon}$ angle, nearly negative at the blade-end, determine the angle difference between the y-axis and the first principal axis which is assumed along the chord of a 'symmetrical' airfoil as given in Figure A.1. Despite a real situation presents different asymmetrical airfoil for blade sections from the root to the blade-end, it is expected of negligible influence. Also being β_E negative for a normally twisted blade, $\beta_E+\upsilon$ is assumed positive. E is the modulus of elasticity depending on the materials used and *I* is the moment of inertia depending on the shape, both of them at each blade airfoil and in this research, for each blade body-section.

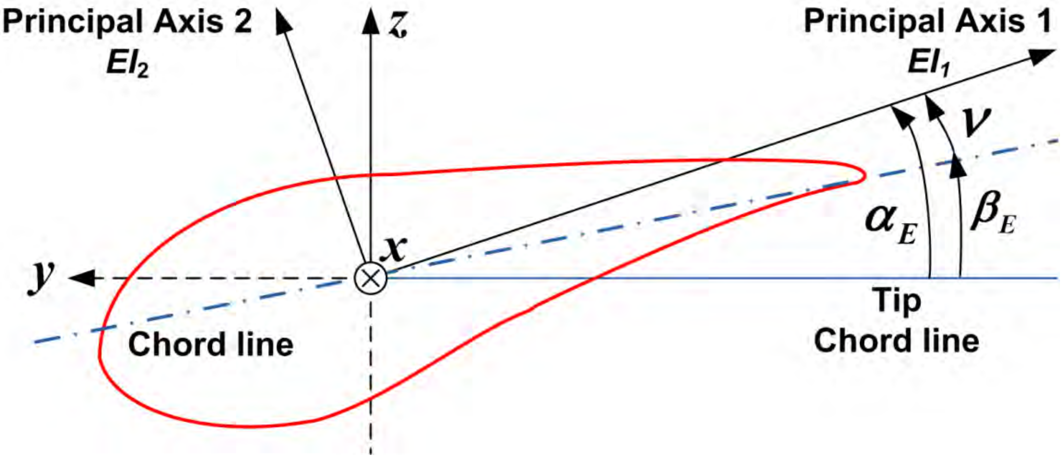

Figure A.1 Blade section to identify axis convention and the principal axis [Hansen 2008]

Additionally after data comparison between Table 11.1 in [Hansen 2008] and Appendix A2 in [Jonkman *et al*. 2009], the factors $(EI)_1$ and $(EI)_2$ in (A.11), (A.12) representing the moment of stiffness inertia about principal axis 1 and 2, are assumed to be related to the flap stiffness and edge stiffness respectively, through the α_E angle between tip chord line and first principal axis, which is assumed to be closed to but not necessarily equal to β+υ. In the absence of additional information about this α_E angle and computation details in [Jonkman *et al*. 2009], in this research that comparison is assumed to match each other.

Agreeing the suggestion in [Hansen 2008], for computational purposes a blade is discretized in *N* body-sections. Figure A.2 illustrates a general case about how to proceed with sectioning. The length of every body-section is arbitrary. In this research it has been suitably chosen close to 1 m. Linear behaviour is assumed for all variables between two adjacent nodes. At any blade body-section between nodes r^{i-1} and r^i, forces, moments, angle deformation and deflections are obtained by integrating the corresponding models. In this way, Simpson's trapezoidal rule for definite integrals is applied to integrate the ordinary differential equations.

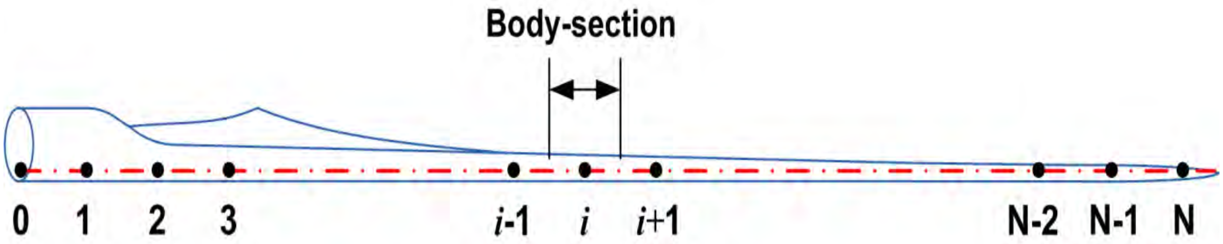

Figure A.2 Discretizing and ordering of blade body-sections as a cantilever beam [Hansen 2008]

A first run covers the blade from the blade-end at the section *N* to the blade-root at section 1, computing forces and moments, P_1, at any blade section. It means,

$$\int_{r^i}^{r^{i-1}} P_1(x)dx = P_1^{i-1}(x) - P_1^i(x) \approx 0.5(r^{i-1} - r^i)[f(r^i) + f(r^{i-1})] \qquad \text{(A.34)}$$

where

$$P_1^{i-1}(x) \approx P_1^i(x) + 0.5(r^{i-1} - r^i)[f(r^i) + f(r^{i-1})] \qquad \text{(A.35)}$$

A second run starting in the blade-root at section 1, computes angle deformations and deflections, P_2, at any blade section, until reaching again the blade-end at section *N*. As a general rule it means,

$$\int_{r^{i-1}}^{r^i} P_2(x)dx = P_2^i(x) - P_2^{i-1}(x) \approx 0.5(r^i - r^{i-1})[f(r^{i-1}) + f(r^i)] \qquad \text{(A.36)}$$

and as a consequence,

$$P_2^i(x) \approx P_2^{i-1}(x) + 0.5(r^i - r^{i-1})[f(r^{i-1}) + f(r^i)] \qquad \text{(A.37)}$$

Following this methodology, mechanical loads can be computed. Although in a not canonical order, they are completely specified in [Hansen 2008].

* * *

Appendix B

Induction Generator Modelling Background, Wind Turbine System Setup and Data

B.1 Briefs About Basic *abc* Formulation of the Induction Machine Model

In this Section, a basic *abc* constant parameters induction machine model with fluxes as state variables, is introduced. This modelling agrees with technical research reports, which illustrates advances to the modelling itself and they are also used together to *dq* based control systems in experimental setups. It accumulates at least 50 years of industry and research experience, and it was used as a base in order to introduce *d-q* modelling closed to switching devices in [Krause and Thomas 1965], some usual approaches are presented in, [Pillay and Levin 1995], [Goldemberg *and* de Arruda-Penteado 1999], [Krause *et al*. 2002], a generalized approach in [Ghani 1988] and its discretization in [Macbahi *et al*. 2000]. Most of them cites [Park 1929] as the most relevant source.

Following the motor operation mode convention and applying voltage Kirkchoff law, a set of six non-linear ordinary differential equations, represent the electrical behaviour of an induction machine. In short it results as in [Krause *et al*. 2002],

$$\boldsymbol{v}_{abc} = \boldsymbol{R}_{abc}\boldsymbol{i}_{abc} + \boldsymbol{p}\boldsymbol{\psi}_{abc} \tag{B.1}$$

where p is the Heaviside operator (d(.)/dt), the stator (*s*) and rotor (*r*) currents are included in the vector $\boldsymbol{i} = [\boldsymbol{i}_s, \boldsymbol{i}'_r]$, flux linkage in the vector $\boldsymbol{\psi} = [\boldsymbol{\psi}_s, \boldsymbol{\psi}_r]$, the applied voltage in the vector

$\boldsymbol{v} = [\boldsymbol{v}_s, \boldsymbol{v}_r]$ and R is the resistance matrix. All of them in the *abc* reference frame. A linear function relates flux linkage and currents as,

$$\psi_{abc} = \boldsymbol{L}_{abc}\boldsymbol{i}_{abc} \tag{B.2}$$

through the inductance matrix $\boldsymbol{L}$. The traditional combination of (B.1) and (B.2) with fluxes as the state variables yields,

$$p\psi_{abc} = -\boldsymbol{R}_{abc}\boldsymbol{L}_{abc}^{-1}\psi_{abc} + \boldsymbol{v}_{abc} \tag{B.3}$$

and assuming currents as state variables it results

$$p\boldsymbol{i}_{abc} = -\boldsymbol{L}_{abc}^{-1}\left(\boldsymbol{R}_{abc} + \boldsymbol{w}_r \frac{d}{d\theta_r}\boldsymbol{L}_{abc}\right)\boldsymbol{i}_{abc} + \boldsymbol{L}_{abc}^{-1}\boldsymbol{v}_{abc} \tag{B.4}$$

Additional necessary definitions are:

$\boldsymbol{R}_{abc}$ is a diagonal matrix with stator R_s and rotor R_r resistance parameters in ohms. The decomposed stator and rotor flux linkage vector in (B.2) can be expressed by,

$$\begin{bmatrix} \boldsymbol{\psi}_{s,abc} \\ \boldsymbol{\psi}'_{r,abc} \end{bmatrix} = \begin{bmatrix} \boldsymbol{L}_s & \boldsymbol{L}_{sr} \\ \boldsymbol{L}'_{sr} & \boldsymbol{L}'_r \end{bmatrix} \begin{bmatrix} \boldsymbol{i}_{s,abc} \\ \boldsymbol{i}'_{r,abc} \end{bmatrix} \tag{B.5}$$

where the inductance matrix has the form [Krause *et al*. 2002],

$$
\boldsymbol{L_{abc}} = \begin{array}{c|ccc|ccc|c}
 & \mathbf{A} & \mathbf{B} & \mathbf{C} & \boldsymbol{a} & \boldsymbol{b} & \boldsymbol{c} & \\
\hline
\mathbf{A} & L_s & L_{AB} & L_{AC} & a_1 L_{Aa} & a_2 L_{Ab} & a_3 L_{Ac} & \\
\mathbf{B} & L_{BA} & L_s & L_{BC} & a_3 L_{Ba} & a_1 L_{Bb} & a_2 L_{Bc} & \mathbf{STATOR} \\
\mathbf{C} & L_{CA} & L_{CB} & L_s & a_2 L_{Ca} & a_3 L_{Cb} & a_1 L_{Cc} & \\
\hline
\boldsymbol{a} & a_1 L_{aA} & a_3 L_{aB} & a_2 L_{aC} & L_r & L_{ab} & L_{ac} & \\
\boldsymbol{b} & a_2 L_{bA} & a_1 L_{bB} & a_3 L_{bC} & L_{ba} & L_r & L_{bc} & \mathbf{ROTOR} \\
\boldsymbol{c} & a_3 L_{cA} & a_2 L_{cB} & a_1 L_{cC} & L_{ca} & L_{cb} & L_r & \\
\hline
 & \multicolumn{3}{c|}{\mathbf{STATOR}} & \multicolumn{3}{c|}{\mathbf{ROTOR}} &
\end{array} \qquad \text{(B.6)}
$$

where $\boldsymbol{L_{abc}}$ is a full 6th order, symmetric, with L_s , L_r constant parameters. Following the nomenclature for stator and rotor in (B.6), for each couple X-Y of stator windings, L_{XY} is the stator mutual inductance. And for each couple x-y of rotor windings, L_{xy} is the rotor mutual inductance. By extension, L_{Xy} or L_{xY} is the stator-rotor mutual inductance. Stator-rotor mutual inductances are sinusoidal varying parameters according with their rotor position dependence and taking into account the assumption for air-gap flux. Equation (B.6) assumes electrical and magnetic symmetry, and excludes any stator/rotor, slot and winding real characteristics [Pillay and Levin 1995]. Inductance elements are in Henry units. In relation to (B.3) and (B.4), it is established that $\boldsymbol{L^{-1}_{abc}}$ can be explicitly or implicitly calculated. Furthermore,

p_p is the number of pole pairs

$w_r = w_{rm} p_p = p\theta_r$, is the instantaneous induction generator rotor speed (el. rad/s)

θ_r , is the instantaneous electrical rotor position (el. rad).

$$a_1 = \cos\theta_r , \quad a_2 = \cos(\theta_r + 2\pi/3), \quad a_3 = \cos(\theta_r - 2\pi/3)$$

$L_{ms} = L'_{mr}$ is the measured no-load test magnetizing inductance value.

$L_s = L_{\sigma s} + L_{ms}$, is the per-phase inductance at the stator

$L'_r = L'_{\sigma r} + L_{ms}$, is the per-phase inductance at the rotor, as seen (′) from the stator

$L_{\sigma s}$ and $L'_{\sigma r}$ are the stator and rotor leakage inductances, as seen from the stator, respectively.

In (B.6) the magnetic coupling between magnetizing flux and stator leakage flux is included in $\boldsymbol{L_s}$ elements, and the magnetic coupling between magnetizing flux and rotor leakage flux in $\boldsymbol{L_r}$ elements. The mutual magnetic coupling between stator and rotor is taken in $\boldsymbol{L_{sr}}$, $\boldsymbol{L_{rs}}$, sub-matrices, as a whole.

Some practical and usual constraints about $\boldsymbol{L_{abc}}$ matrix for symmetrical machines are [Krause and Thomas 1965], [Ghani 1988]:

i) Stator and rotor mutual inductances have magnetic reciprocity property, then $L_{XY} = L_{YX}$, $L_{xy} = L_{yx}$ and $L_{Xy} = L_{xY}$. In [Krause *et al*. 2002] it is besides established that

$$L_{XY} = L_{xy} = -0.5 L_{ms} \tag{B.7}$$

$$L_{Xy} = L_{xY} = L_{ms} \tag{B.8}$$

ii) Winding structures for the stator and rotor are symmetrical identical groups,

Anyway, the instantaneous electromagnetic torque T_e due to the co-energy for an *abc* reference frame [Krause *et al*. 2002], is expressed as,

$$T_e = p_p \left(i_{s,abc} \right)^t \frac{\partial}{\partial \theta_r} [L_{sr}] i'_{r,abc} \tag{B.9}$$

In the case of the exact solution knowing the mutual inductances [Ghani 1988], T_e results to be,

$$\begin{aligned} T_e = {} & \\ -\frac{1}{2}\Big[& i_A\left(i_a(L_{Aa}+L_{aA})\sin\theta_r + i_b(L_{Ab}+L_{bA})\sin(\theta_r+2\pi/3) + i_c(L_{Ac}+L_{cA})\sin(\theta_r-2\pi/3)\right) \\ & + i_B\left(i_a(L_{Ba}+L_{aB})\sin(\theta_r-2\pi/3) + i_b(L_{Bb}+L_{bB})\sin\theta_r + i_c(L_{Bc}+L_{cB})\sin(\theta_r+2\pi/3)\right) \\ & + i_C\left(i_a(L_{Ca}+L_{aC})\sin(\theta_r+2\pi/3) + i_b(L_{Cb}+L_{bC})\sin(\theta_r-2\pi/3) + i_c(L_{Cc}+L_{cC})\sin\theta_r\right)\Big] \end{aligned} \tag{B.10}$$

and taking into account the above $\boldsymbol{L_{abc}}$ matrix constraints [Ghani 1988], [Krause *et al*. 2002], it is,

$$\begin{aligned} T_e = -L_{ms}\Big[& \left(i_a i_A + i_b i_B + i_c i_C\right)\sin\theta_r \\ & \left(i_a i_B + i_b i_C + i_c i_A\right)\sin(\theta_r - 2\pi/3) \\ & \left(i_a i_C + i_b i_A + i_c i_B\right)\sin(\theta_r + 2\pi/3)\Big] \end{aligned} \tag{B.11}$$

Note that from (B.10) or (B.11), it is perfectible possible to define a per-phase Te.

Using a space vector based approach, the time dependent active *P(t)* and reactive *Q(t)* power supply, from the induction generator and in phase coordinates, result:

$$P(t) = v_a i_a + v_b i_b + v_c i_c \tag{B.12}$$

$$Q(t) = \frac{\sqrt{3}}{3}\left(v_{bc} i_a + v_{ca} i_b + v_{ab} i_c\right) \tag{B.13}$$

where v_j and i_j ($j = a,b,c$) are time dependent voltages and currents variables.

B.2 Simulink Block Structure and Computational Setup

The general Matlab/Simulink arrangement for this investigation looks as depicted in Figure B.1. As it is shown, blocks for the short-circuit *abc* source, *abc* power transformer, *abc* Induction Generator, *123* Wind and Drive-train, constitutes the fundamental structure.

All blocks are supported by S-functions in C-code. This physical based wind turbine arrangement is proposed in [Akhmatov 2003].

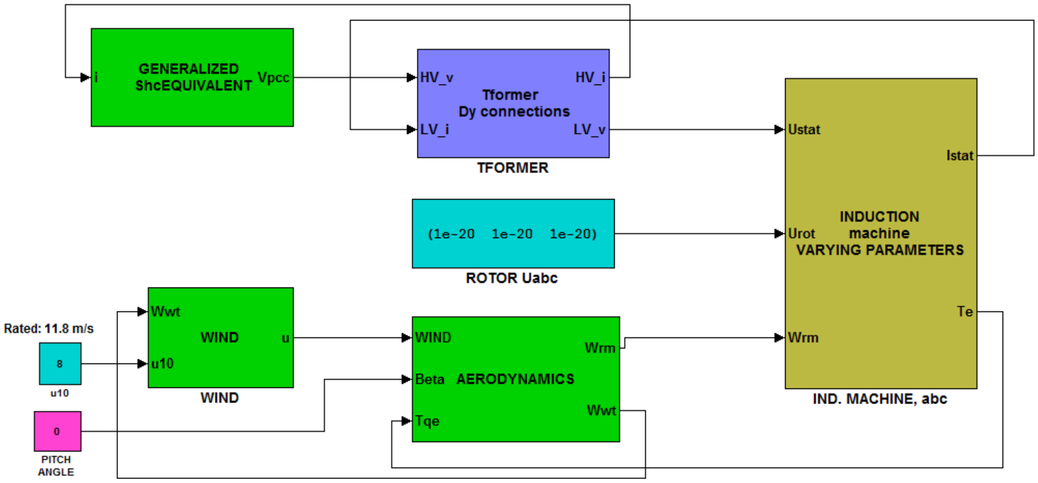

Figure B.1 Matlab/Simulink Blocks for the Wind Turbine Model.

Inputs u_{10} wind speed and pitch angle are specific values, for each simulation case.

In Figure B.2 a wind turbine is grid connected at the Point of Common Coupling (PCC). The voltage level at this point is 31.5 kV and other relevant information about the network is associated to the Generalized Short Circuit Source block.. The 2 MW / 31.5/0.96/$\sqrt{3}$ kV/ 50 Hz./ Dy11 power transformer is between PCC and the induction generator. The 2 MW / 0.96 kV / 50 Hz. induction generator, has the option to be used as squirrel cage or wound rotor. At 5 seconds of the simulation time, a 4 ohm fault resistance is inserted at PCC and the fault is cleared 0.5 s after, in the most critical case, according to grid code for low voltage fault ride-through [Hansen *et al*. 2011.]

RMS phase voltages at induction generator terminals are presented in Figures B.3(a) for symmetrical three-phase LLL fault and in Figure B.3(b) for asymmetrical line-to-ground LG fault, respectively. These voltages are computed after the effect of Dy11 power transformer connection.

Wind, Fault at the PCC, Transformer, Drive-train and Induction generator input data, appears in Section B.2. Fault impedance is equal to 4 ohm per/phase.

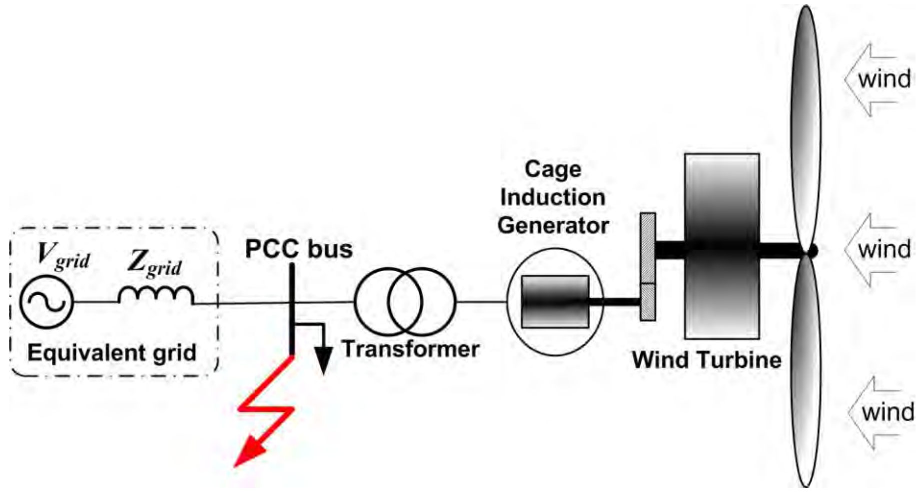

Figure B.2 Wind Turbine Power System setup

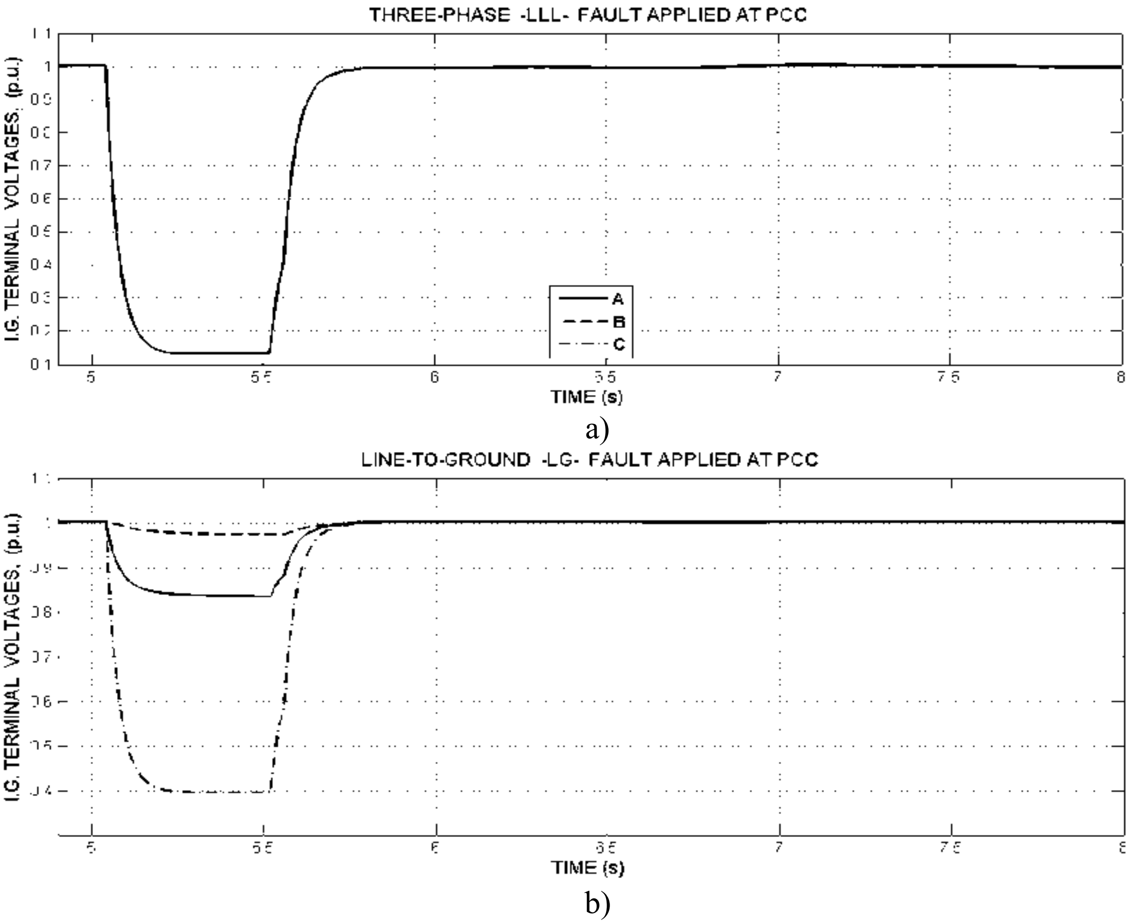

Figure B.3 Faulted *abc* RMS voltages in p.u at the PCC on the base of the rated voltage.: a) from symmetrical LLL fault, and b) from asymmetrical LG fault.

B.3 Input Data.

B.3.1 Short-Circuit Voltage Source Model Data

The voltage source is appropriately designed to represent a grid equivalent. It comprehends an infinite bus, a network defined by the short circuit data at PCC and fault data at PCC too. It can supply voltage unbalance and harmonics. Figure B.4 presents the Simulink mask to enter this voltage source data.

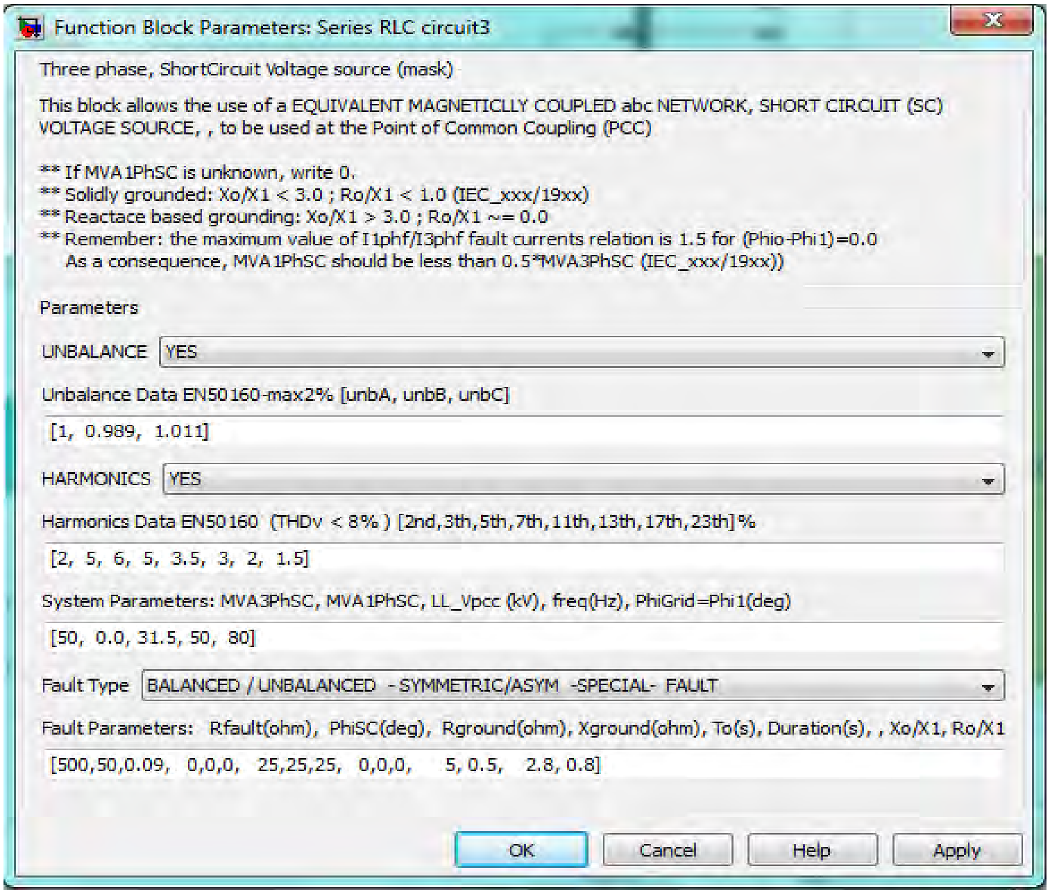

Function Block Parameters: Series RLC circuit3

Three phase, ShortCircuit Voltage source (mask)

This block allows the use of a EQUIVALENT MAGNETICLLY COUPLED abc NETWORK, SHORT CIRCUIT (SC) VOLTAGE SOURCE, , to be used at the Point of Common Coupling (PCC)

** If MVA1PhSC is unknown, write 0.
** Solidly grounded: Xo/X1 < 3.0 ; Ro/X1 < 1.0 (IEC_xxx/19xx)
** Reactace based grounding: Xo/X1 > 3.0 ; Ro/X1 ~= 0.0
** Remember: the maximum value of I1phf/I3phf fault currents relation is 1.5 for (Phio-Phi1)=0.0
As a consequence, MVA1PhSC should be less than 0.5*MVA3PhSC (IEC_xxx/19xx))

Parameters

UNBALANCE: YES

Unbalance Data EN50160-max2% [unbA, unbB, unbC]
[1, 0.989, 1.011]

HARMONICS: YES

Harmonics Data EN50160 (THDv < 8%) [2nd,3th,5th,7th,11th,13th,17th,23th]%
[2, 5, 6, 5, 3.5, 3, 2, 1.5]

System Parameters: MVA3PhSC, MVA1PhSC, LL_Vpcc (kV), freq(Hz), PhiGrid=Phi1(deg)
[50, 0.0, 31.5, 50, 80]

Fault Type: BALANCED / UNBALANCED - SYMMETRIC/ASYM -SPECIAL- FAULT

Fault Parameters: Rfault(ohm), PhiSC(deg), Rground(ohm), Xground(ohm), To(s), Duration(s), , Xo/X1, Ro/X1
[500,50,0.09, 0,0,0, 25,25,25, 0,0,0, 5, 0.5, 2.8, 0.8]

Figure B.4 Simulink mask to input short-circuit voltage source data

B.3.2 Power Transformer Model Data

Figure B.5 presents the Simulink mask to enter the transformer and Short-circuit source data. The power transformer is not a modelling target in this investigation, and thus, a simple model is used with detailed Dy connectivity.

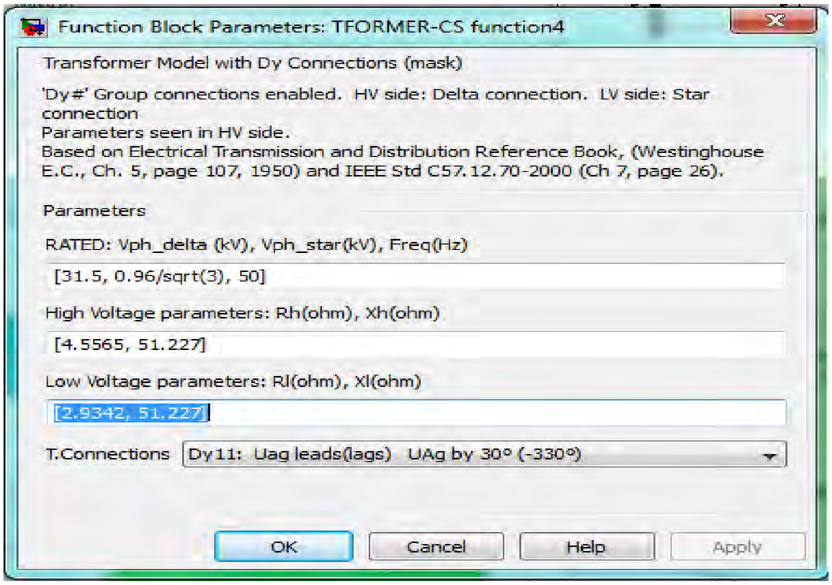

Transformer Model with Dy Connections (mask)

'Dy#' Group connections enabled. HV side: Delta connection. LV side: Star connection
Parameters seen in HV side.
Based on Electrical Transmission and Distribution Reference Book, (Westinghouse E.C., Ch. 5, page 107, 1950) and IEEE Std C57.12.70-2000 (Ch 7, page 26).

Parameters

RATED: Vph_delta (kV), Vph_star(kV), Freq(Hz)
[31.5, 0.96/sqrt(3), 50]

High Voltage parameters: Rh(ohm), Xh(ohm)
[4.5565, 51.227]

Low Voltage parameters: Rl(ohm), Xl(ohm)
[2.9342, 51.227]

T.Connections: Dy11: Uag leads(lags) UAg by 30° (-330°)

Figure B.5 Simulink mask to input power transformer data

B.3.3 Wind Model Data

Figure B.6 displays the Simulink mask to enter wind data. The fundamental information around which this research results are obtained, appear in it.

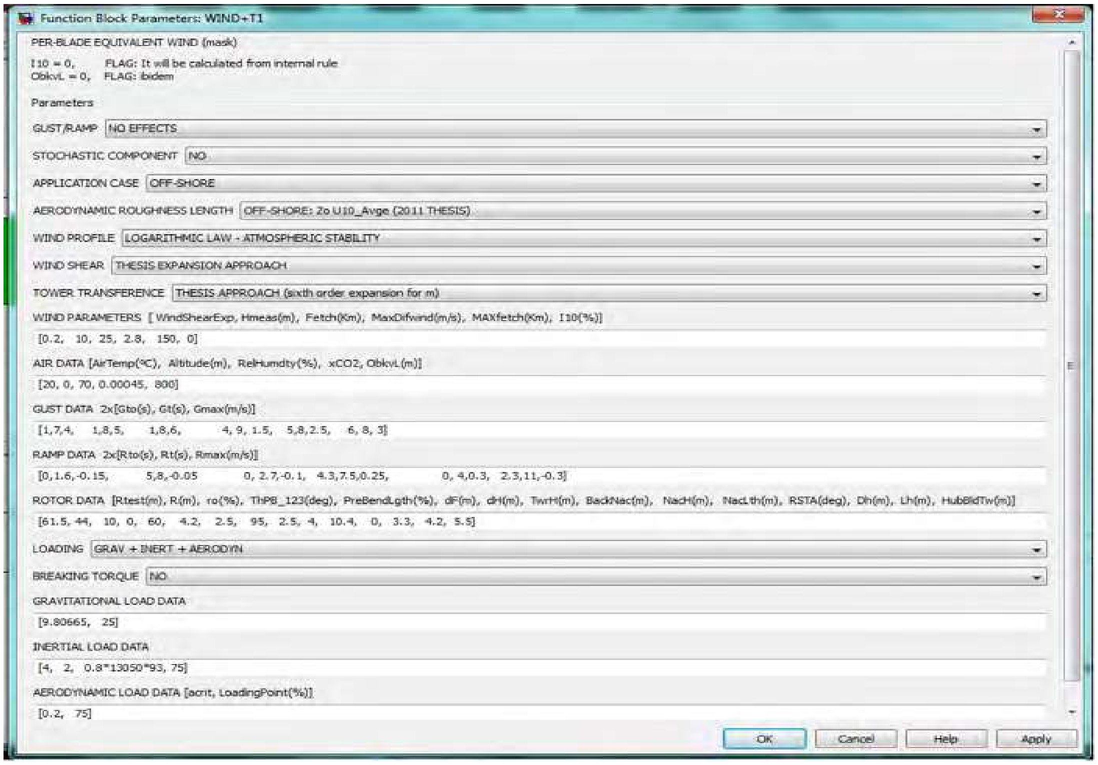

PER-BLADE EQUIVALENT WIND (mask)

I10 = 0, FLAG: It will be calculated from internal rule
ObkvL = 0, FLAG: ibidem

Parameters

GUST/RAMP: NO EFFECTS
STOCHASTIC COMPONENT: NO
APPLICATION CASE: OFF-SHORE
AERODYNAMIC ROUGHNESS LENGTH: OFF-SHORE: Zo U10_Avge (2011 THESIS)
WIND PROFILE: LOGARITHMIC LAW - ATMOSPHERIC STABILITY
WIND SHEAR: THESIS EXPANSION APPROACH
TOWER TRANSFERENCE: THESIS APPROACH (sixth order expansion for m)

WIND PARAMETERS [WindShearExp, Hmeas(m), Fetch(Km), MaxDifwind(m/s), MAXfetch(Km), I10(%)]
[0.2, 10, 25, 2.8, 150, 0]

AIR DATA [AirTemp(°C), Altitude(m), RelHumdty(%), xCO2, ObkvL(m)]
[20, 0, 70, 0.00045, 800]

GUST DATA 2x[Gto(s), Gt(s), Gmax(m/s)]
[1,7,4, 1,8,5, 1,8,6, 4, 9, 1.5, 5,8,2.5, 6, 8, 3]

RAMP DATA 2x[Rto(s), Rt(s), Rmax(m/s)]
[0,1.6,-0.15, 5,8,-0.05 0, 2.7,-0.1, 4.3,7.5,0.25, 0, 4,0.3, 2.3,11,-0.3]

ROTOR DATA [Rtest(m), R(m), ro(%), ThPB_123(deg), PreBendLgth(%), dF(m), dH(m), TwrH(m), BackNac(m), NacH(m), NacLth(m), RSTA(deg), Dh(m), Lh(m), HubBldTw(m)]
[61.5, 44, 10, 0, 60, 4.2, 2.5, 95, 2.5, 4, 10.4, 0, 3.3, 4.2, 5.5]

LOADING: GRAV + INERT + AERODYN
BREAKING TORQUE: NO

GRAVITATIONAL LOAD DATA
[9.80665, 25]

INERTIAL LOAD DATA
[4, 2, 0.8*13050*93, 75]

AERODYNAMIC LOAD DATA [acrit, LoadingPoint(%)]
[0.2, 75]

Figure B.6 Simulink mask to input wind data

B.3.4 Aerodynamic Model Data

Figure B.7 illustrates the Simulink mask to enter drive-train data. The fundamental information around appears in it.

B.3.5 Induction Generator Model Data

Figure B.8 shows the Simulink mask to enter induction generator data. The fundamental information around which this research results are obtained, appear in it.

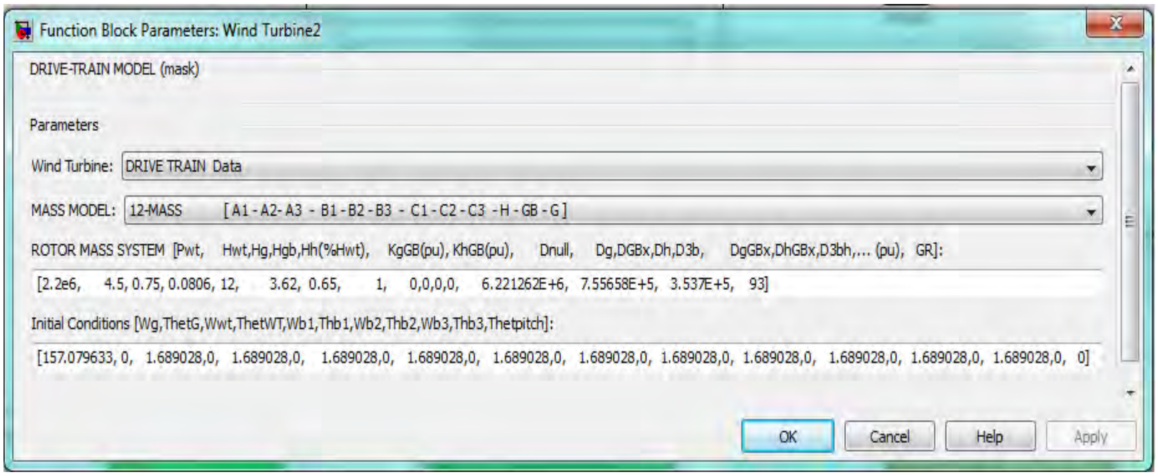

Function Block Parameters: Wind Turbine2

DRIVE-TRAIN MODEL (mask)

Parameters

Wind Turbine: DRIVE TRAIN Data

MASS MODEL: 12-MASS [A1 - A2- A3 - B1 - B2 - B3 - C1 - C2 - C3 -H - GB - G]

ROTOR MASS SYSTEM [Pwt, Hwt,Hg,Hgb,Hh(%Hwt), KgGB(pu), KhGB(pu), Dnull, Dg,DGBx,Dh,D3b, DgGBx,DhGBx,D3bh,... (pu), GR]:

[2.2e6, 4.5, 0.75, 0.0806, 12, 3.62, 0.65, 1, 0,0,0,0, 6.221262E+6, 7.55658E+5, 3.537E+5, 93]

Initial Conditions [Wg,ThetG,Wwt,ThetWT,Wb1,Thb1,Wb2,Thb2,Wb3,Thb3,Thetpitch]:

[157.079633, 0, 1.689028,0, 1.689028,0, 1.689028,0, 1.689028,0, 1.689028,0, 1.689028,0, 1.689028,0, 1.689028,0, 1.689028,0, 1.689028,0, 1.689028,0, 0]

Figure B.7 Simulink mask to input aerodynamic data

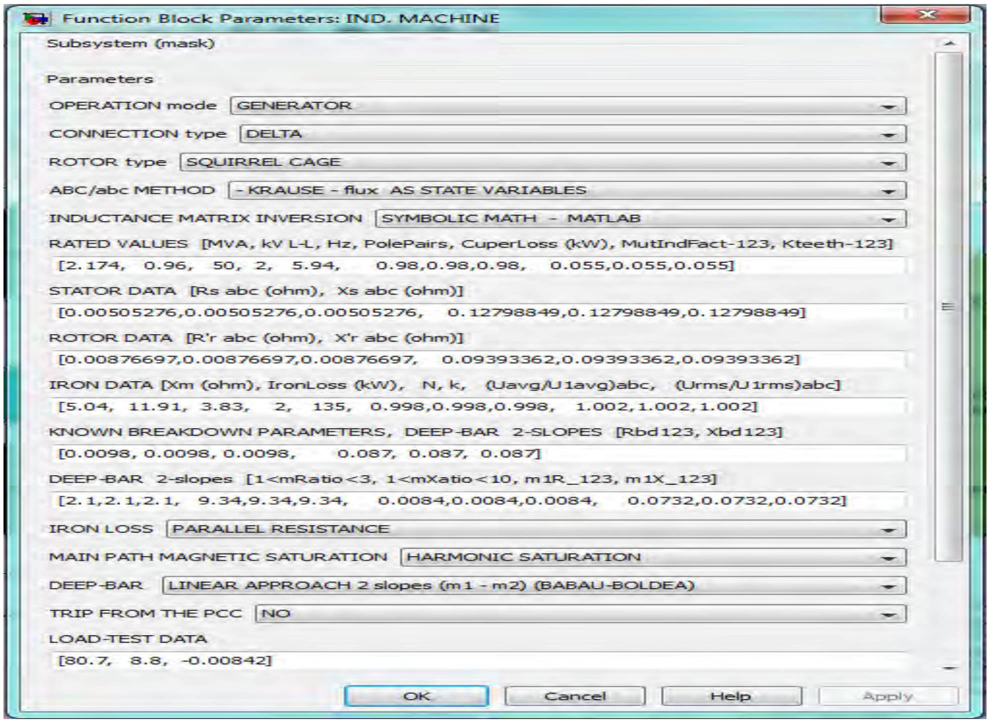

Function Block Parameters: IND. MACHINE

Subsystem (mask)

Parameters

OPERATION mode GENERATOR

CONNECTION type DELTA

ROTOR type SQUIRREL CAGE

ABC/abc METHOD - KRAUSE - flux AS STATE VARIABLES

INDUCTANCE MATRIX INVERSION SYMBOLIC MATH - MATLAB

RATED VALUES [MVA, kV L-L, Hz, PolePairs, CuperLoss (kW), MutIndFact-123, Kteeth-123]

[2.174, 0.96, 50, 2, 5.94, 0.98,0.98,0.98, 0.055,0.055,0.055]

STATOR DATA [Rs abc (ohm), Xs abc (ohm)]

[0.00505276,0.00505276,0.00505276, 0.12798849,0.12798849,0.12798849]

ROTOR DATA [R'r abc (ohm), X'r abc (ohm)]

[0.00876697,0.00876697,0.00876697, 0.09393362,0.09393362,0.09393362]

IRON DATA [Xm (ohm), IronLoss (kW), N, k, (Uavg/U1avg)abc, (Urms/U1rms)abc]

[5.04, 11.91, 3.83, 2, 135, 0.998,0.998,0.998, 1.002,1.002,1.002]

KNOWN BREAKDOWN PARAMETERS, DEEP-BAR 2-SLOPES [Rbd123, Xbd123]

[0.0098, 0.0098, 0.0098, 0.087, 0.087, 0.087]

DEEP-BAR 2-slopes [1<mRatio<3, 1<mXatio<10, m1R_123, m1X_123]

[2.1,2.1,2.1, 9.34,9.34,9.34, 0.0084,0.0084,0.0084, 0.0732,0.0732,0.0732]

IRON LOSS PARALLEL RESISTANCE

MAIN PATH MAGNETIC SATURATION HARMONIC SATURATION

DEEP-BAR LINEAR APPROACH 2 slopes (m1 - m2) (BABAU-BOLDEA)

TRIP FROM THE PCC NO

LOAD-TEST DATA

[80.7, 8.8, -0.00842]

Figure B.8 Simulink mask to input Induction Generator data

Bibliography

[Ackermann 2005]
Ackermann T., ‘Wind power in power systems’, John Wiley & Sons Ltda – Royal Institute of Technology, England, 2005

[Akbaba and Fakro 1992]
Akbaba M. and Fakro S.Q., ‘New model for single-unit representation of induction motor loads, including skin-effect, for power system transient stability studies’, IEE Proceedings-B, vol 139, No 6, November 1992.

[Akhmatov 2003]
Akhmatov V., ‘Analysis of dynamic behaviour of electric power systems with large amount of wind power’, PhD thesis, Electric Power Engineering, Ørsted-DTU, Technical University of Denmark, Kgs. Lingby, Denmark, 2003

[Akiror 2012]
Akiror J.C., ‘Model for core loss prediction at high frequency and high flux density’, MSc thesis, Department of Electrical Engineering, Concordia University, Montreal, Quebec, Canada, 2012.

[Arshad *et al*. 2008a]
Arshad W.M., Kanerva S., Menescardi B. and Savinovic D., ‘Static breakdown torques from run-up dynamic tests in medium-large induction motors’, 4th IET Conference on Power Electronics Machines and Drives, 2008, pp. 362-366.

[Babau *et al*. 2007]

Babau R., Boldea I., Miller T.J.E. and Muntean N., 'Complete Parameter Identification of Large Induction Machines From No-Load Acceleration-Deceleration Tests', IEEE Transactions on Industrial Electronics, Vol 54, No 4, pp. 1962-1972, August 2007.

[Boglietti *et al*. 1996]

Boglietti A., Ferraris P., Lazzari M. and Pastorelli M., "Influence of modulation techniques on iron losses with single phase DC/AC converter", *IEEE Transactions on Magnetics*, Vol. 32, No. 5, September 1996

[Boglietti *et al*. 2001]

Boglietti A., Cavagnino A., Lazzari M., Pastorelli M., "Two simplified methods for the iron losses prediction in soft magnetic materials supplied by PWM inverter", Conf. Rec. IEEE International Electric Machines and Drives Conference 2001, IEMDC'01, 17-20 June 2001, Boston, USA.

[Boglietti *et al*. 2003]

Boglietti V, Cavagnino A., Lazzari M., Pastorelli M., "Predicting iron losses in soft magnetic materials with arbitrary voltage supply: an engineering approach", *IEEE Transactions on Magnetics*, Vol. 39, March 2003, pp. 981-989.

[Boglietti *et al*. 2007]

Boglietti A., Cavagnino A., Knight A.M., 'Factors affecting Losses in Induction Motors with no-sinusoidal supply', 2007

[Boglietti *et al*. 2010]

Boglietti A., Bojoi R., Cavagnino A., Ferraris P., 'No-load operations of Induction Motors PWM supply', 2010.

[Bolik 2004]

Bolik, S.M., ‘Modelling and analysis of variable speed wind turbines with induction generator during grid fault’, PhD Thesis, Aalborg University, October 2004.

[Carvalho 2003]

Carvalho R.P.A., ‘Dynamic influences of wind power on the power system’, PhD thesis, Electric Power Engineering, Ørsted-DTU, Technical University of Denmark & Risø National Laboratories, Kgs. Lingby, Denmark, 2003

[Charnock 1955]

Charnock, H.: ‘Wind stress over a water surface’, Quarterly Journal of the Royal Meteorological Society, Vol. 81, 1955, pp 639-640.

[Chua *et al*. 1970]

Chua L. O. and Stromsmoe K. A., “Lumped-circuit models for nonlinear inductors exhibiting hysteresis loops,” *IEEE Trans. Circuit Theory*, vol. CT-17, no. 4, pp. 564–574, Nov. 1970

[Chua *et al*. 1971]

Chua L. O. and Stromsmoe K. A., “Mathematical model for dynamic hysteresis loops,” *Int. J. Eng.Sci.*, vol. 9, no. 5, pp. 435–450, May 1971.

[Colin *et al*. 2010]

Colin J., Faibre R. and Menenti M., ‘Aerodynamic roughness length estimation for very high-resolution imaging LIDAR observations over the Heihe basin in China’, Journal on Hydrology and earth systems science discussions, 2010, pp. 3397-3421.

[Dolan and Lehn 2006]

Dolan D.S.L. and Lehn P.W., ‘Simulation model of wind turbine 3p torque oscillations due to wind shear and tower shadow,’ *IEEE Transactions on Energy Conversion*, Vol. 21, No 3, pp. 717-724, September 2006.

[Donescu *et al*. 1999]

Donescu V., Charette A., Yao Z. and Ragajopalan V., ‘Modelling and Simulation of Saturated Induction Motors in Phase Quantities’, IEEE Transactions on Energy Conversion, Vol. 14, No. 3, pp. 386-393, September 1999.

[Dyer 1974]

Dyer, A. J.: ‘A review of flux profile relationships’, Boundary-Layer Meteorology, Springer, 7, 1974, pp 363-372

[Fairal and Bradley 2003]

Fairal, C.W. and Bradley, E.F., Bulk parameterization of air-sea fluxes: updates and verification for the COARE algorithm, Journal of Climate of the American Meteorological Society, 2003, pp 571-591.

[Fajardo *et al*. 2009]

Fajardo-R L.A., Medina A. and Iov F., ‘Transient stability with grid-connection and wind turbine drive-train effects’ EPEC’09, Montreal, Canada, 2009.

[Ghani 1988]

Ghani S.N., ‘Digital computer simulation of three-phase induction machine dynamics – A generalized approach’, IEEE transaction on Industry Applications, Vol 24, No 1, January/February 1988, pp. 106-114

[Grantham and McKinnon 2003]

Grantham C., and McKinnon D.J., ‘A novel method for load testing and efficiency measurements of three phase induction motors’

[Goldemberg and De Arruda-Penteado 1999]

Goldemberg C. and de Arruda-Penteado A., ‘Improvements on the inductance matrix inversion simplifying the use of ABC/abc induction machine model’, International Conference IEMD’99, on Electric Machines and Drives, May 1999, pp. 422-424.

[Gryning *et al*. 2007]

Gryning, S.E., Batchvarova, E., Brumer, E., Jorgensen, H. and Larsen, S.: 'On the extension of the wind profile over homogeneous terrain beyond the surface boundary layer', Riso National Laboratory, 2007.

[Hansen 2008]

Hansen M.O.L., 'Aerodynamics of wind turbines', Second edition, EARTHSCAN, London, U.K., 2008.

[Hasager *et al*. 2008]

Hasager, Ch. B., Peña, A., Christiansen, M. B., Astrup, P., Nielsen, M., Monaldo, F., Thompson, D. and Nielsen, P.: 'Remote sensing observation used in offshore wind energy', IEEE Journal on Selected topics in applied earth observations and remote sensing, Vol 1, No 1, March 2008, pp 67-79.

[Hinrichsen and Nolan 1982]

Hinrichsen E.N. and Nolan P.J., 'Dynamics and stability of wind turbine generators', IEEE Transactions on Power Systems, Vol PAS 101, No 8, August 1982, pp. 2640-2648

[Ionel *et al*. 2008]

Ionel D.M., Popescu M., Cossar C., McGilp M. I., Boglietti A., Cavagnino A., "A General Model of the Laminated Steel Losses in Electric Motors with PWM Voltage Supply*",* Conf. Rec. IEEEIAS' 08. IEEE, 5-9 Oct. 2008, pp. 1-7

[Iov *et al*. 2003]

Iov F., Hansen A.D., Sørensen P. and Blaabjerg F., 'Wind Turbine Blockset in Matlab/Simulink: general overview and description of the models', Aalborg University - RIS∅, December 2003. Available at: www.et.aau.dk

[Iov *et al*. 2004]

Iov F., Hansen A.D., Jauch C., Sørensen P. and Blaabjerg F., ‘Advanced tools for modelling, design and optimization of wind turbine systems’, Nordic Wind Power Conference, halmers University, 2004, pp. 1-12

[Iov *et al*. 2007]

Iov F., Hansen A.D., Sørensen P. and Cutululis N.A., ‘Mapping of grid-faults and grid codes’, Risø-R-1617(EN), Risø National Laboratory, Technical University of Denmark, Røskilde, Denmark, July 2007.

[IEEE Std-112 2004]

IEEE Standard test procedure for polyphase induction motors and generators, IEEE power Engineering Society, 2004.

[IEC 60034-2-1 2007]

International Standard IEC, ‘Rotating Electrical Machines, Part 2-1. Standard methods for determining losses and efficiency from tests, 2007’

[Jonkman *et al*. 2009]

Jonkman J., Butterfield S., Musial W. and Scott G., ‘Definition of a 5MW reference wind turbine for offshore system development’, National Renewable Laboratory NREL/TP 500-3860, February 2009

[Johnson *et al*. 1998]

Johnson, H. K., Højstrup, J., Vested, H. J. and Larsen, S. E.: ‘On the dependence of sea surface roughness on wind waves’, Journal of Physical Oceanography, Vol, 28, 1998, pp 1702-1716.

[Khalig *et al*. 2005]

Khalig A., Nagel N. and Emadi A., ‘A detailed modular approach for induction machines considering iron losses’, IEEE IECON’05, Industrial Electronics Society, 2005

[Kitaigorodskii 1962]

Kitaigorodskii, S. A.: 'Applications of the theory of similarity to the analysis of wind-generated wave motion as a stochastic process', Bulletin of the academy of science USSR geophysics series, No 1, 1962, 73.

[Klaes 1993]

Klaes N.R., 'Parameter identification of an induction machine with regard to dependencies on saturation', IEEE Transactions on Industry Applications, Vol. 29, No. 6, Nov/Dec 1993, pp. 1135-1140

[Krause *and* Thomas 1965]

Krause P.C., and Thomas C.H.: 'Simulation of symmetrical induction machinery', IEEE Transaction on PAS, PAS-84, No 11, Nov1965, pp 1038-1053.

[Krause *et al*. 2002]

Krause P.C., Wasynczuk O., Sudhoff S.D.: 'Analysis of electric machinery and drive systems', Second Edition, IEEE series on Power Engineering, Wiley Interscience, NY-USA, 2002.

[Lange *et al*. 2002]

Lange, B., Larsen, S., Højstrup, J., Barthelmie, R. and Focken, U.: 'Modelling the vertical wind speed and turbulence intensity profiles at prospective offshore wind farm sites', World Wind Energy Conference, Berlin, Germany, 2002

[Lange *et al*. 2004]

Lange, B., Larsen, S. E., Højstrup, J. and Barthelmie, R.: 'The influence of thermal effects on the wind speed profile of the coastal marine boundary layer', Boundary-Layer meteorology, 112, 2004, 587-617.

[Large and Pound 1981]
Large, W. G. and Pound, S.; 'Open ocean momentum flux measurements in moderate to strong winds', Journal of Physical Oceanography, Vol. 11, 1981, pp 324-336.

[Li and Chen 2008]
Li H. and Chen Z., 'Overview of different wind generator systems and their comparisons', IET Renewable Power Generation, Vol. 2, No, 2, 2008, pp. 123-138

[Larsen and Hansen 2007]
Larsen T.J. and Hansen A.M., 'How 2 HAWC2, the user's manual', Risø National Laboratories, Technical University of Denmark, Risø-R-1597(Ver. 3-1)(EN)

[Maat *et al*. 1991]
Maat, N., Kran, C. and Oost, W. A.: 'The roughness of wind waves, Boundary-Layer Meteorology', Springer, 54, 1991, pp 89-103

[Madsen *et al*. 1984]
Madsen P.H., Frandsen S., Holley W.E. and Hansen J.C., 'Dynamics and fatigue damage of wind turbine rotors during steady operation', Risø National Laboratories, Risø-R-512, Denmark, July 1984

[Marsaglia and Tsang 2000]
Marsaglia G. and Tsang W.W., 'The Ziggurat method for generating random variables', Journal of Statistical software, vol 5, No 8, 7pp, 2000

[Masters 2004]
Masters G.M., 'Renewable and efficient electric power systems', John Wiley & Sons Inc., 2004.

[Macbahi *et al*. 2000]

Macbahi H., Ba-razzouk A, Xu J., Cheriti A. and Rajagopalan V., ‘A unified method for modelling and simulation of three-phase induction motor drives’, 2000

[McKinnon *et al*. 2004]

McKinnon D.J., Seyoum D., Grantham C., ‘Investigation of parameter characteristics for induction machine analysis and control’, IEE Second International Conference on Power Electronics Machines and Drives, 2004, Vol 1, pp. 320-325

[Mondragon 2003]

Mondragon P.F.. ‘A comparison of non-linear regression codes’ MSc in mathematics with Operation Research and Statistics Option, Institute of Mining and Technology, Socorro, New Mexico, USA, May 2003.

[Monin and Obukhov 1954]

Monin, A. S. and Obukhov, A. M.: ‘Dimensionless characteristics of turbulence in the surface layer’, Akad. Nauk. SSSR Geofiz. Inst., Tr, No 24, 1954, pp 163-187.

[Muyeen *et al*. 2007]

Muyeen S.M., Hasan A. Md., Takahashi R., Murata T., Yomaki Y., Sakahara A. and Sasano E., ‘Comparative study of transient stability analysis of wind turbine generator system using different drive-train models’, IEEE-IET Renewable Power Generation, 2007, 1, (2), pp. 131-141

[Novotny and Wouterse 1976]

Novotny D.W. and Wouterse J.H., ‘Induction machine transfer function and dynamic response by means of complex time variables’, IEEE-PAS, Vol PAS-95, No 4, Jul/Aug 1976, pp 1325-1335.

[Olesen *et al*. 2012]

Olesen E.E., Koefoed S. M., Pedersen S.H., Jespedersen K. and Jeno J.J., ‘Method of manufacturing pre-bent wind turbine blades’. US patent publication US 2012/007269 A1,

[Park 1929]

Park, R.H., ‘Two-reaction theory of synchronous machines. Generalized method of analysis - Part I’, Transactions AIEE, vol 48, pp. 716-730, July 1929.

[Pedersen *et al*. 2000]

Pedersen J.K., Akke M., Poulsen N.K. and Helgelsen-Pedersen K.O., ‘Analysis of wind farm islanding experiment’, IEEE Transaction on Energy Conversion, Vol 15, No 1, March 2000, pp. 110-115

[Pedersen *et al*. 2003]

Pedersen J.K., Helgelsen-Pedersen K.O., Poulsen N.K., Akhmatov V., and Nielsen A.H., ‘Contribution to a wind turbine model validation from a wind farm islanding experiment’, ELSEVIER Science, Electric Power System Research, 64 (2003), pp. 41-51.

[Peña and Gryning 2008]

Peña, A. and Gryning, S. E.: ‘Charnock roughness length model and non-dimensional wind profiles over the sea’, Riso National Laboratory, 2008, pp 1-12

[Picard *et al*. 2008]

Picard A., Davis R.S., Gläser M. and Fujji K., ‘Revised formula for the density of moist air (CIPM-2007)’, Metrologia, Bureau international des poids et mesures, IOP Publishing, UK, pp 149-155, 2008.

[Pillay and Levin 1995]

Pillay P. and Levin V., ‘Mathematical models for induction machines’, IEEE Thirtieth IAS annual meeting, Industry Applications Conference, 1995, pp 606-616.

[Popescu *et al*. 2010]

Popescu M., Dorrell D.G., Ionel D.M., "A Study of the Engineering Calculations for Iron Losses in 3-phase AC Motor Models", Conf. Rec. 33rd IECON 2007, 5-8 Nov. 2007, pp. 169 – 174.

[Ranta *et al*. 2009]

Ranta M., Hinkkanen M., Dlala E., Repo A.K. and Luomi J., 'Inclusion of Hysteresis and Eddy Current losses in Dynamic Induction Machine Models', IEEE International Electric Machines and Drives Conference IEMDC'09, pp. 1387-1392, May 2009.

[Saint-Drenan 2009]

Saint-Drenan Y.M.: 'Comparison of different Charnock models for the determination of the vertical wind profile', R&D Division Energy Economy and Grid Operation, Kassel, Germany, 2009.

[Salman *et al*. 2000]

Salman S.k., Teo A.L.J. and Rida I.M., 'The effect of shaft modelling on the Assessment of fault CCT and the power quality of a wind farm', Proceedings of the Ninth International Conference on Harmonics and Power Quality, Vol 3, 2000, pp. 994-998

[Salman and Teo 2002]

Salman S.K. and Teo A.L.J., 'Investigation into the estimation of the critical clearing time of a grid connected wind power based embedded generator', Asia/Pacific Transmission and Distribution Conference and exhibition 2002, Vol 2, pp. 975-980

[Seman *et al*. 2003]

Seman S., Saitz J. and Arkkio A., 'Dynamic Model of Cage Induction Motor considering saturation and skin effect', VI international Conference on Electrical Machines and Systems, ICEMS'03, Vol 2, pp. 710-713, November 2003.

[Seman and Arkkio 2003]
Seman S., Saitz J., Arkkio A., 'Dynamic model of cage induction motor considering saturation and skin effects', 2003

[Seyoum *et al*. 2003]
Seyoum D., Grantham C. and Rahman M.F., 'The Dynamic Characteristics of an Isolated Self-Excited Induction Generator Driven by a Wind Turbine', IEEE Transactions on Industry Applications, Vol. 39, No. 4, pp. 936-944, July/August 2003.

[Sørensen *et al*, 2002]
Sørensen P., Hansen A.D. and Carvalho R.P.A., 'Wind models for simulation of power fluctuations from wind farm', ELSEVIER-Journal of Wind Engineering and Industrial Aerodynamics, Vol 90, pp 1381-1402, 2002

[Slootweg 2003]
Slootweg J. G., Wind Power: Modelling on impact of Power System Dynamics, PhD Thesis, Technische Universiteit Delft, December 2003

[Smith *et al*. 1992]
Smith, S. D., Anderson, R. J., Oost, W. A., Kraan, C., Maat, N., DeCosmo, J., Katsaros, K. B., Davidson, K. L., Bumke, K., Hasse, L. and Chadwick, H. M.: 'Sea surface wind stress and drag coefficients; The HEXOS results', Boundary-Layer Meteorology, 60, 1992, 109-142.

[Taylor and Yelland 2001]
Taylor, P.K. and Yelland, M. J.: 'The dependence of sea surface roughness on the height and steepness of the waves', Journal of Physical Oceanography, Vol. 31, 2001, pp 572-590.

[Tsili and Papathanassiou 2009]
Tsili M. and Papathanassiou S., 'Review of grid-code technical requirements for wind farms', IET renewable power generation, 2009, pp. 1-25

[Tu *et al*. 2008]

Tu X., Dessiant L.A., Champagne R. and Al-Haddad K., 'Transient Model of Squirrel-Cage Induction Machine considering Air-Gap Flux Saturation Harmonics', IEEE Transactions on Industrial Electronics, Vol 55 No 7, pp 2798-2809, July 2008.

[VESTAS wind systems 2013]

VESTAS wind systems. http://www.vestas.com/en/media/brochures.aspx

[Westlake *et al*. 1996]

Westlake A.J.G., Bumby J.R., Spooner E., 'Damping the power angle oscillations of PM synchronous generator with particular reference to wind turbine applications', IEE Proceedings on Electric Power Applications, vol 143, No 3, pp 269-280, 1996.

[Zilikentevich and Essau 2007]

Zilikentevich, S.S. and Essau, I. N.: 'Similarity theory and calculation of turbulent fluxes at the surface for the stably stratified atmospheric boundary layer', Journal of Atmospheric Boundary Layer, Springer, 2007, pp 37-49.

* * *